frontiers | Research Topics

Wave-induced particle motions in the ocean

Edited by
Henrik Kalisch, Ton Van Den Bremer, John Carter,
Nick Pizzo and Yan Li

Published in
Frontiers in Marine Science

ISSN 1664-8714
ISBN 978-2-8325-5920-8
DOI 10.3389/978-2-8325-5920-8

About Frontiers

Frontiers is more than just an open access publisher of scholarly articles: it is a pioneering approach to the world of academia, radically improving the way scholarly research is managed. The grand vision of Frontiers is a world where all people have an equal opportunity to seek, share and generate knowledge. Frontiers provides immediate and permanent online open access to all its publications, but this alone is not enough to realize our grand goals.

Frontiers journal series

The Frontiers journal series is a multi-tier and interdisciplinary set of open-access, online journals, promising a paradigm shift from the current review, selection and dissemination processes in academic publishing. All Frontiers journals are driven by researchers for researchers; therefore, they constitute a service to the scholarly community. At the same time, the *Frontiers journal series* operates on a revolutionary invention, the tiered publishing system, initially addressing specific communities of scholars, and gradually climbing up to broader public understanding, thus serving the interests of the lay society, too.

Dedication to quality

Each Frontiers article is a landmark of the highest quality, thanks to genuinely collaborative interactions between authors and review editors, who include some of the world's best academicians. Research must be certified by peers before entering a stream of knowledge that may eventually reach the public - and shape society; therefore, Frontiers only applies the most rigorous and unbiased reviews. Frontiers revolutionizes research publishing by freely delivering the most outstanding research, evaluated with no bias from both the academic and social point of view. By applying the most advanced information technologies, Frontiers is catapulting scholarly publishing into a new generation.

What are Frontiers Research Topics?

Frontiers Research Topics are very popular trademarks of the *Frontiers journals series*: they are collections of at least ten articles, all centered on a particular subject. With their unique mix of varied contributions from Original Research to Review Articles, Frontiers Research Topics unify the most influential researchers, the latest key findings and historical advances in a hot research area.

Find out more on how to host your own Frontiers Research Topic or contribute to one as an author by contacting the Frontiers editorial office: frontiersin.org/about/contact

Wave-induced particle motions in the ocean

Topic editors

Henrik Kalisch — University of Bergen, Norway
Ton Van Den Bremer — Delft University of Technology, Netherlands
John Carter — Seattle University, United States
Nick Pizzo — University of California, San Diego, United States
Yan Li — University of Bergen, Norway

Citation

Kalisch, H., Van Den Bremer, T., Carter, J., Pizzo, N., Li, Y., eds. (2025). *Wave-induced particle motions in the ocean*. Lausanne: Frontiers Media SA. doi: 10.3389/978-2-8325-5920-8

Table of contents

frontiers | Frontiers in Marine Science

TYPE Original Research
PUBLISHED 27 October 2022
DOI 10.3389/fmars.2022.982333

OPEN ACCESS

EDITED BY
Henrik Kalisch,
University of Bergen, Norway

REVIEWED BY
Evgueni Dinvay,
Inria Rennes - Bretagne Atlantique Research Centre, France
Sergey Gavrilyuk,
Aix-Marseille Université, France

*CORRESPONDENCE
Hung-Chu Hsu
hchsu@mail.nsysu.edu.tw

SPECIALTY SECTION
This article was submitted to Physical Oceanography, a section of the journal Frontiers in Marine Science

RECEIVED 30 June 2022
ACCEPTED 07 October 2022
PUBLISHED 27 October 2022

CITATION
Hsu H-C and Li M-S (2022) Particle trajectory of nonlinear progressive flexural-gravity waves in Lagrangian coordinates. *Front. Mar. Sci.* 9:982333. doi: 10.3389/fmars.2022.982333

Particle trajectory of nonlinear progressive flexural-gravity waves in Lagrangian coordinates

Hung-Chu Hsu[1]* and Meng-Syue Li[2]

[1]Department of Marine Environment and Engineering, The Center for Water Resources Studies, National Sun Yat-Sen University, Kaohsiung, Taiwan, [2]Marine Science and Information Research Center, National Academy of Marine Research, Kaohsiung, Taiwan

In this paper, we study the particle dynamics of nonlinear flexural-gravity waves propagating in a finite water depth, which is the interaction between ice sheets and water flows. The nonlinear deformation of a floating elastic sheet is modeled by the Cosserat shell theory. The theoretical analysis is performed by a uniform asymptotic perturbation expansion. A third-order explicit parametric solution of particle trajectories in Lagrangian coordinates is presented. Taking the time average of particle motion, the mass transport velocity and the Lagrangian surface setup are also derived. Numerical simulations are computed. The influences of flexural rigidity on the water particle orbits and the mass transport velocity of nonlinear flexural-gravity waves are first discussed.

KEYWORDS

lagrangian, flexural wave, particle trajectory, mass transport, perturbation

Introduction

The study of the flexural-gravity wave problem has important contributions to floating ice sheet, climate change, and engineering applications such as manmade floating structures in polar oceans. Such hydroelastic waves have been measured in many cold regions of the Arctic (Squire and Moore, 1980; Wadhams and Holt, 1991; Squire et al., 1995). A variety of linear and nonlinear elastic sheet models are used according to the proposed linear equation (Greenhill, 1886), the Kirchhoff–Love plate theory or Cosserat theory (Toland, 2007). Previously, the linear and nonlinear theoretical solutions as well as numerical simulations were developed to study the propagation of flexural-gravity waves and were compared with field investigations (Greenhill, 1916; Forbes, 1986; Marko, 2003; Vanden-Broeck and Părău, 2011; Gao et al., 2016; Gao et al., 2019). Toland (2008) further proved the existence of progressive flexural-gravity waves using a Lagrangian method.

There are fewer studies of the particle trajectories beneath the flexural-gravity waves. It is important to understand the transport mechanism of nonlinear water waves. Linearized solution patterns of flexural-gravity waves with uniform current have been

presented in Ref (Bhattacharjee and Sahoo, 2007).. Wang et al. (Wang et al., 2020) calculated particle paths numerically for the fully nonlinear equations of flexural-gravity waves with constant vorticity. They studied the fluid particle motion based on integrating the water particle velocity derived by the Eulerian coordinates. This method was often used to trace the particle path and the steady streaming velocity on water waves (Stokes, 1847; Longuet-Higgins, 1953). However, the above studies cannot show some important properties of particle dynamics such as the Lagrangian wave period, a Lagrangian setup that is different from the wave properties in the Eulerian frameworks (Longuet-Higgins, 1986; Ng, 2004).

The first linear Lagrangian exact solution describing a flow of non-constant vorticity in water of infinite depth was presented by Gerstner (1802). Using a rigorous mathematical analysis, Constantin (2006) showed that the exact solution by Gerstner is dynamically possible. He then successfully extended Gerstner's solution to the problem of edge and geophysical waves (Constantin, 2012a; Constantin, 2013). Chen and Hsu (2009) provided a method of modified Euler–Lagrange transformation to obtain the third-order approximation for the particle motion in nonlinear Stokes waves. Some asymptotic solutions for the nonlinear progressive or short-crested waves in the Lagrangian approach have been developed (Pierson, 1962; Buldakov et al., 2006; Clamond, 2007; Hsu et al., 2010; Chen et al., 2010; Chen and Chen, 2014). More recently, analytical solutions that provide a detailed mechanism of the water particle orbits for water waves were presented in Refs (Constantin and Villari, 2008; Constantin and Escher, 2011; Constantin, 2012b). These works proved that there exist open orbits in two-dimensional nonlinear irrotational and inviscid flows.

The focus of this work is to describe the particle dynamics in flexural-gravity waves in Lagrangian coordinates. To our knowledge, it has not been studied yet. We introduce the equations of motion together with their boundary conditions in Section 2. A Lindstedt–Poincare perturbation method used to obtain a third-order asymptotic parametric solution for the particle trajectories in the Lagrangian framework will be discussed in Section 3. In Section 4, we will analyze the particle trajectory, drift velocity, and Lagrangian surface setup of flexural-gravity waves under the influences of ice sheet thickness, water depth, and wave steepness. Finally, in Section 5, we give a short conclusion.

Formulations

We consider a two-dimensional irrotational, inviscid, and incompressible fluid for the steady finite-amplitude progressive flexural-gravity waves. The water depth h is finite with an impermeable bottom. The Cartesian coordinates are introduced where the x-axis is taken at the undisturbed ice sheet, and y is the upward positive vertical axis. The wave is periodic with the wave number $k = 2\pi / L$ and wave frequency $\sigma_w = 2\pi / T_w$. Following Toland (Toland, 2007; Toland, 2008) and Wang et al. (2020), the nonlinear Cosserat model of hyperelastic sheets is used to express the deformation of floating ice sheets, which is assumed as

$$p = D \cdot \left(\partial_{ss}\kappa + \frac{1}{2}\kappa^3\right) \tag{2.1}$$

where p is the pressure across the elastic sheet, $D = \frac{E \cdot d^3}{12 * (1 - \nu^2)}$ is the flexural rigidity, E is Young's modulus, ν is Poisson's ratio, d is the thickness of the ice sheet, κ is the curvature of the sheet, and s is the arc length. Since the thickness of the elastic sheet is small compared with the wavelength of the flexural wave, the sheet density is neglected in this paper.

In the Lagrangian coordinates, the mathematical description of fluid particle motion ($x(a,b,t)$, $y(a,b,t)$) is expressed in two horizontal and vertical variables a and b labeling individual fluid particles at time $t = 0$, where the vertical label $b = 0$ corresponding to the free surface η and $b = -h$ is on the impermeable sea bottom. For an incompressible and inviscid fluid, the continuity equation that sets the invariant condition on the total volume variation of a water particle in the Lagrangian framework is

$$x_a y_b - x_b y_a = 1 \tag{2.2}$$

Taking the partial differentiating Eq. (2.3) with respect to t yields

$$x_{at}x_b - x_{bt}x_a + y_{at}y_b - y_{bt}y_a = 0 \tag{2.3}$$

and the irrotational flow conditions are (Chen et al., 2010; Chen and Chen, 2014)

$$\phi_a = x_t x_a + y_t y_a,\ \phi_b = x_t x_b + y_t y_b \tag{2.4}$$

The Bernoulli equation (Chen et al., 2010; Chen and Chen, 2014) including the term of flexural rigidity of the elastic ice sheet in the Lagrangian description can be written as

$$\frac{p}{\rho} = -\phi_t - g\,y + \frac{1}{2}\left(x_t^2 + y_t^2\right) - \frac{1}{2}\frac{D}{\rho}\left[\frac{\kappa_{aa}}{J} + \left(\frac{\kappa_a}{J}\right)_a + \kappa^3\right] \tag{2.5}$$

where $J = x_a^2 + y_a^2$ and $\kappa = (x_a y_{aa} - x_{aa} y_a)/J^{3/2}$.

The boundary conditions of zero pressure at the upper boundary and zero vertical velocity at the rigid and impermeable sea bed for water particles are

$$p = 0,\ b = 0, \tag{2.6}$$

$$v = y_t = 0,\ b = -h, \tag{2.7}$$

where the subscripts a, b, and t denote partial differentiation with respect to the specified variable; g is the constant gravitational acceleration; and $\phi(a, b, t)$ is a Lagrangian velocity potential function introduced by (2.4). Therefore, the governing equations and boundary conditions of two-dimensional irrotational progressive flexural-gravity water waves in the Lagrangian coordinates are established, which consist of the continuity equations (2.2) and (2.3), vorticity conservation equation (2.4), energy equation (2.5), dynamic boundary condition (2.6) under the sheet, and condition (2.8) at the bottom.

Asymptotic solutions

We used the Lindstedt–Poincare technique to solve the nonlinear boundary value equations (2.2)–(2.5) with boundary conditions (2.6) and (2.7) in the Lagrangian coordinates. Following Chen and Hsu (Chen et al., 2010) and Chen and Chen (2014), the solutions of the particle displacements x and y, the potential function ϕ , and the pressure p are sought in the power series as

$$x(a, b, t) = a + \epsilon(f_1 + f_1') + \epsilon^2(f_2 + f_2') + \epsilon^3(f_3 + f_3') + \cdots, \quad (3.1)$$

$$y(a, b, t) = b + \epsilon(g_1 + g_1') + \epsilon^2(g_2 + g_2') + \epsilon^3(g_3 + g_3') + \cdots, \quad (3.2)$$

$$\phi(a, b, t) = \epsilon(\phi_1 + \phi_1') + \epsilon^2(\phi_2 + \phi_2') + \epsilon^3(\phi_3 + \phi_3') + \cdots, \quad (3.3)$$

$$p(a, b, t) = -\rho g b + \epsilon p_1 + \epsilon^2 p_2 + \epsilon^3 p_3 + \cdots, \quad (3.4)$$

$$\sigma(b) = 2\pi / T_L = \sigma_0 + \epsilon\sigma_1 + \epsilon^2\sigma_2 + \cdots, \quad (3.5)$$

where ϵ is an ordering parameter that is used to identify the order of the perturbation expansion. In these expressions, f_n, g_n, ϕ_n , and p_n are the nth-order periodic harmonic function solutions. f_r^n and ϕ_r^n are the non-periodic functions that are a function of time t. g_r^n is related to the Lagrangian wave mean level and is a function of the vertical label b. $\sigma = 2\pi / T_L$ is the Lagrangian angular frequency of a particle reappearing at the same elevation where T_L is the particle motion period. Substituting the power series functions (3.1)–(3.5) into (2.3)–(2.8), and equating the equal order terms of ϵ up to the third order, we obtain a recursive series of nonhomogeneous linear partial differential equations that can be solved successively.

First-order solution

At the first order ϵ , the governing equations (2.3)–(2.6) yield

$$f_{1a} + f_{1a}' + g_{1b} + g_{1b}' + \sigma_{ob}(g_{1\sigma t} + g_{1\sigma_o t}') t = 0 \quad (3.6a)$$

$$\sigma_o(f_{1b\sigma t} + f_{1b\sigma_o t}' - g_{1a\sigma t} - g_{1a\sigma_o t}') + \sigma_{ob}(f_{1\sigma t} + f_{1\sigma_o t}') + \sigma_o\left\{\sigma_{ob}[f_{1(\sigma t)^2} + f_{1(\sigma_o t)^2}']\right\} t = 0 \quad (3.6b)$$

$$\phi_{1a} + \phi_{1a}' = \sigma_o(f_{1\sigma t} + f_{1\sigma_o t}') \quad (3.6c)$$

$$\phi_{1b} + \phi_{1b}' + \sigma_{ob}(\phi_{1\sigma t} + \phi_{1\sigma_o t}') t = \sigma_o(g_{1\sigma t} + g_{1\sigma_o t}') \quad (3.6d)$$

$$\frac{p_1}{\rho} = -\sigma_o(\phi_{1\sigma t} + \phi_{1\sigma_o t}') - g(g_1 + g_1') - \frac{D}{\rho}(g_{1aaaa} + g_{1aaaa}') \quad (3.6e)$$

Also, the dynamic free surface boundary condition and the bottom boundary condition give

$$p_1 = 0 \quad \text{on} \quad b = 0 \quad (3.6f)$$

$$g_{1\sigma t} + g_r 1\sigma_0 t = 0 \quad \text{on} \quad b = -h \quad (3.6g)$$

From the continuity equation (3.6a) and the bottom boundary condition (3.6g), the first-order periodic solution can be obtained by the separation of variables. From (3.6b) to (3.6d) and avoiding the secular terms, the first-order analytical solution can be easily written in the form

$$f_1 = -A\frac{\cosh k(b + h)}{\cosh kh}\sin(ka - \sigma t), \quad f_1' = 0 \quad (3.7)$$

$$g_1 = A\frac{\sinh k(b + h)}{\cosh kh}\cos(ka - \sigma t), \quad g_1' = 0 \quad (3.8)$$

$$\phi_1 = A\frac{\sigma_0}{k}\frac{\cosh k(b + h)}{\cosh kh}\sin(ka - \sigma t) \quad (3.9)$$

where the parameter A represents the linear amplitude. Substituting (3.7)–(3.9) into (3.6e), we can get the wavenumber k satisfying the linear dispersion equation at the leading order

$$\sigma_0^2 = gk(1 + \frac{Dk^4}{\rho g})\tanh kh \quad (3.10)$$

The linear dispersion relation in the Lagrangian coordinates is the same as that of the leading-order progressive flexural-gravity wave in the Eulerian approach (Wang et al., 2020). By setting $b = 0$ in (3.8), we can get the first-order free surface function in the Lagrangian coordinates.

Second-order solution

At the second order ϵ^2 , we have the following set of governing equations:

$$f_{2a} + f'_{2a} + g_{2b} + g'_{2b} + f_{1a}g_{1b} - f_{1b}g_{1a} + \sigma_{1b}g_{1\sigma t}\, t = 0 \tag{3.11a}$$

$$\sigma_o\,(f_{2b\sigma t} + f'_{2b\sigma_o t} - g_{2a\sigma t} - g'_{2a\sigma_o t}) + \sigma_1(f_{1b} - g_{1a})_{\sigma t} + \sigma_{1b}f_{1\sigma t} + \sigma_o\,(f_{1a}f_{1b\sigma t} - f_{1a\sigma t}f_{1b} + g_{1a}g_{1b\sigma t} - g_{1b}g_{1a\sigma t}) + \sigma_o\sigma_{1b}f_{1(\sigma t)^2}\, t = 0 \tag{3.11b}$$

$$\phi_{2a} + \phi'_{2a} = \sigma_o\,(f_{2\sigma t} + f'_{2\sigma_o t}) + \sigma_1 f_{1\sigma t} + \sigma_o\,(f_{1a}f_{1\sigma t} + g_{1a}g_{1\sigma t}) \tag{3.11c}$$

$$\phi_{2b} + \phi'_{2b} = \sigma_o\,(g_{2\sigma t} + g'_{2\sigma_o t}) + \sigma_1 g_{1\sigma t} + \sigma_o\,(f_{1b}f_{1\sigma t} + g_{1b}g_{1\sigma t}) - \sigma_{1b}t\phi_{1\sigma t} \tag{3.11d}$$

$$\frac{p_2}{\rho} = -\,[\sigma_o\,(\phi_{2\sigma t} + \phi'_{2\sigma_o t}) + g\,(g_2 + g'_2)] - \sigma_1\phi_{1\sigma t} + \frac{1}{2}\,\sigma_o^2\,(f^2_{1\sigma t} + g^2_{1\sigma t}) - \frac{D}{\rho}\,\{(g_{2aaaa} + g'_{2aaaa}) - 5\,(f_{1aaa} + f'_{1aaa})\,(g_{1aa} + g'_{1aa}) - 4\,(f_{1aa} + f'_{1aa})\,(g_{1aaa} + g'_{1aaa}) - (f_{1aaaa} + f'_{1aaaa})\,(g_{1a} + g'_{1a}) - 2(f_{1a} + f'_{1a})\,(g_{1aaaa} + g'_{1aaaa})\} \tag{3.11e}$$

and the boundary conditions are

$$p_2 = 0 \quad \text{at} \quad b = 0 \tag{3.11f}$$

$$g_{2\sigma t} + g_f^{2\sigma_0 t} = 0 \quad \text{on} \quad b = -h \tag{3.11g}$$

eliminating the secular term yields $\sigma_{1b} = 0$ and, hence, $\sigma_1 = w_1 = \text{constant}$. Solving for the other modes that satisfy the mass conservation equation (3.11a)–(3.11b) and the bottom boundary condition (3.11g), the second-order parametric equations of water particle trajectory can be expressed as periodic harmonic functions f_2 and g_2 in the horizontal and vertical coordinates

$$f_2 = -\beta_2\,\frac{\cosh 2k\,(b+h)}{\cosh^2 kh}\,\sin 2\,(ka - \sigma t) + \frac{1}{4}\,A^2k\,\frac{1}{\cosh^2 kh}\,\sin 2\,(ka - \sigma t) - \lambda_2\,\frac{\cosh k\,(b+h)}{\cosh kh}\,\sin\,(ka - \sigma t) \tag{3.12}$$

$$g_2 = \beta_2\,\frac{\sinh 2k\,(b+h)}{\cosh^2 kh}\,\cos 2\,(ka - \sigma t) + \lambda_2\,\frac{\sinh k\,(b+h)}{\cosh kh}\,\cos\,(ka - \sigma t) \tag{3.13}$$

and non-periodic function f_f^2 and g_f^2

$$f_f^2 = \frac{1}{2}\,A^2k\,\frac{\cosh 2k\,(b+h)}{\cosh^2 kh}\,\sigma_0 t \tag{3.14}$$

$$g'_2 = \frac{1}{4}\,A^2k\,\frac{\sinh 2k\,(b+h)}{\cosh^2 kh} \tag{3.15}$$

Inserting the first-order solutions into the irrotational conditions (3.11c) and (3.11d) and eliminating the secular term, we can get $\alpha w_1 + \sigma_0\beta_{2111} = 0$. By integrating over the Lagrangian variables a or b to (3.11c) and (3.11d), the second-order Lagrangian velocity potential ϕ_2 is obtained as

$$\phi_2 = \frac{\sigma_o}{k}\,\beta_2\,\frac{\cosh 2k\,(b+h)}{\cosh^2 kh}\,\sin 2\,(ka - \sigma t) - \frac{1}{2}\,A^2\sigma_o\,\frac{\sin 2\,(ka - \sigma t)}{\cosh^2 kh} \tag{3.16}$$

Substituting (3.16) and the first-order solution into the Bernoulli equation (3.11e) and applying (3.11f), we find the coefficients as

$$w_1 = \lambda_2 = 0 \tag{3.17}$$

$$\phi'_2 = D'_2\,(\sigma_0 t) = [\frac{1}{4}\,A^2\sigma_0^2\,(\tanh^2 kh - 1) - \frac{1}{2}\,\frac{D}{\rho}\,k^5A^2\,\tanh kh] \cdot t \tag{3.18}$$

$$\beta_2 = \frac{3kA^2}{2\sigma_0^2\,\cosh 2kh - k\,(g + 16\,\frac{D}{\rho}\,k^4)\,\sinh 2kh}\,[\frac{1}{4}\,\sigma_0^2 + \frac{D}{\rho}\,k^5\,\sinh 2kh] \tag{3.19}$$

From the obtained asymptotic solution at the second-order approximation, the perturbation scheme is valid except for the singularity condition that the denominator β_2 is zero. The second-order approximation is found to break down at and near the critical value, where this singularity condition occurs. It was first pointed out by Wilton (1915) for capillary waves.

Third-order solution

The continuity, irrotational, and energy equations up to order ϵ^3 are as follows:

$$f_{3a} + f'_{3a} + g_{3b} + g'_{3b} + f_{1a}g_{2b} + f_{2a}g_{1b} - f_{1b}g_{2a} - f_{2b}g_{1a} + \sigma_{2b}g_{1\sigma t}\, t = 0 \quad (3.27a)$$

$$\sigma_o\,(f_{3b\sigma t} + f'_{3b\sigma_o t} - g_{3a\sigma t} - g'_{3a\sigma_o t}) + \sigma_2\,(f_{1b\sigma t} - g_{1a\sigma t}) + \sigma_{2b}f_{1\sigma t} + \sigma_o\sigma_{2b}f_{1\,(\sigma t)^2}t + \sigma_o\,[f_{1a}f_{2b\sigma t} + f_{2a}f_{1b\sigma t} - f_{2a\sigma t}f_{1b} - f_{1a\sigma t}f_{2b} + g_{1a}g_{2b\sigma t} + g_{2a}g_{1b\sigma t} - g_{1b}g_{2a\sigma t} - g_{2b}g_{1a\sigma t}] = 0 \quad (3.27b)$$

$$\phi_{3a} + \phi'_{3a} = \sigma_o\,(f_{3\sigma t} + f'_{3\sigma_o t}) + \sigma_2 f_{1\sigma t} + \sigma_o\,[f_{1\sigma t}f_{2a} + f_{2\sigma t}f_{1a} + g_{1\sigma t}g_{2a} + g_{2\sigma t}g_{1a}] \quad (3.27c)$$

$$\phi_{3b} + \phi'_{3b} = \sigma_o\,(g_{3\sigma t} + g'_{3\sigma_o t}) + \sigma_2 g_{1\sigma t} + \sigma_o\,[f_{1\sigma t}f_{2b} + f_{2\sigma t}f_{1b} + g_{1\sigma t}g_{2b} + g_{2\sigma t}g_{1b}] - \sigma_{2b}t\phi_{1\sigma t} \quad (3.27d)$$

$$\frac{p_3}{\rho} = -\,[\sigma_o\,(\phi_{3\sigma t} + \phi'_{3\sigma_o t}) + g\,(g_3 + g'_3)] - \sigma_2\phi_{1\sigma t} + \sigma_o^2\,[f_{1\sigma t}f_{2\sigma t} + g_{1\sigma t}g_{2\sigma t}] - \frac{D}{\rho}\,[(g_{3aa} + g'_{3aa}) - 2f_{1a}g_{2aa} - 2f_{2a}g_{1aa} - f_{2aa}g_{1a} - f_{1aa}g_{2a} + 3f_{1a}^2g_{1aa} + 3f_{1aa}f_{1a}g_{1a} - \frac{3}{2}\,g_{1aa}g_{1a}^2]_{aa} \quad (3.27e)$$

and the boundary conditions are

$$p_3 = 0 \quad >\text{at} \quad b = 0 \quad (3.27f)$$

$$g_{3\sigma t} = g'_{3\sigma_0 t} = 0 \quad \text{on} \quad b = -h \quad (3.27g)$$

On substituting the first- and second-order solutions into (3.27a–e), the third-order analytical solutions of the particle trajectory and potential function can be assumed to have the following forms:

$$f_3 = [-\beta_3\,\frac{\cosh 3k(b+h)}{\cosh^3 kh} + \frac{1}{6}\,Ak\,(5\beta_2 - \frac{1}{2}\,A^2k)\,\frac{\cosh k\,(b+h)}{\cosh^3 kh}]\,\sin 3\,(ka - \sigma t) - [\frac{1}{2}\,Ak\,(5\beta_2 + A^2k)\,\frac{\cosh 3k\,(b+h)}{\cosh^3 kh} + \lambda_3\,\frac{\cosh k\,(b+h)}{\cosh^3 kh}]\,\sin\,(ka - \sigma t) \quad (3.28)$$

$$g_3 = [\beta_3\,\frac{\sinh 3k\,(b+h)}{\cosh^3 kh} - \frac{1}{2}\,Ak\beta_2\,\frac{\sinh k\,(b+h)}{\cosh^3 kh}]\,\cos 3\,(ka - \sigma t) + [\frac{1}{2}\,Ak\,(3\beta_2 + \frac{1}{2}\,A^2k)\,\frac{\sinh 3k\,(b+h)}{\cosh^3 kh} + \lambda_3\,\frac{\sinh k\,(b+h)}{\cosh^3 kh}]\,\cos\,(ka - \sigma t) \quad (3.29)$$

$$\phi_3 = \frac{\sigma_0}{k}\,\beta_3\,\frac{\cosh 3k\,(b+h)}{\cosh^3 kh}\,\sin 3\,(ka - \sigma t) + \frac{1}{2}\,A\sigma_0\beta_2\,\frac{\cosh 3k\,(b+h)}{\cosh^3 kh}\,\sin\,(ka - \sigma t) - \frac{1}{2}\,A(3\beta_2 - \frac{1}{2}\,A^2k)\,\sigma_0\,\frac{\cosh k\,(b+h)}{\cosh^3 kh}\,\sin 3\,(ka - \sigma t) \quad (3.30)$$

Using the dynamic boundary condition (3.27f) and neglecting the secular terms that grow with time, we can obtain the second-order correction of the Lagrangian wave frequency, which is

$$\sigma_2 = -\,\frac{1}{2}\,A^2k^3\sigma_0\,\frac{\cosh 2k\,(b+h)}{\cosh^2 kh} - \frac{\sigma_0}{A}\,(1 - \tanh^2 kh)\,\lambda_3 \quad (3.31)$$

and two unknown coefficients β_3 and γ_3 , which are

$$\beta_3 = \frac{1}{3\sigma_0^2\,\cosh 3kh - (gk + 81\,\frac{Dk^5}{\rho})\,\sinh 3kd} \times \{\frac{1}{2}\,\sigma_0^2\,Ak\,(7\beta_2 - A^2k)\,\cosh kh - \frac{1}{2}\,gAk^2\,\beta_2\,\sinh kh + \frac{D}{\rho}\,k\,[(\frac{167}{2}\,k^5A\beta_2 - \frac{3}{32}\,k^6A^3)\,\sinh 3kh - (57k^5A\beta_2 + \frac{433}{32}\,k^6\alpha^3)\,\sinh kh]\} \quad (3.32)$$

$$\lambda_3 = \frac{1}{\sigma_0^2\,\cosh kh + (gk + \frac{Dk^5}{\rho})\,\sinh kh} \times \{\frac{3}{2}\,\sigma_0^2\,Ak\beta_2\,\cosh 3kh - \frac{1}{2}\,gk^2\,A\,(3\beta_2 + \frac{1}{2}\,A^2k)\,\sinh 3kh - \frac{1}{4}\,\sigma_0^2A^3k^2\,\cosh kh - \frac{Dk}{\rho}\,[(\frac{273}{32}\,k^6A^3\,\sinh 3kh - (\frac{3}{2}\,k^5A\beta_2 - \frac{333}{32}\,k^6A^3)\,\sinh kh]\} \quad (3.33)$$

The second-order correction term that only appears in the odd order asymptotic solution is different from the second-order wave frequency in the Eulerian coordinates obtained in Refs (Greenhill, 1886; Wang et al., 2020).. In Equation (3.31), the first term varies exponentially with the vertical particle label b and relative water depth, and the second term is the second-order Stokes wave frequency. Equations (3.28)–(3.33) are exactly the same as those of Chen et al. (2010) as flexural rigidity is neglected. The third-order approximation is found to break down as the denominator of β_3 is zero.

Dinvay et al. (2019) discussed the dispersion relation for moving loads on ice sheets. In Figure 1, the variation of flexural-gravity wavenumber k with the Lagrangian wave frequency from the nonlinear dispersion relation (3.31) for different values of ice sheet thickness d is presented. It is shown that for constant ice sheet thickness, the wavenumber increases with a decreasing Lagrangian wave period. Furthermore, the wavenumber decreases with an increasing thickness of ice sheet.

Computational results and discussion

The trajectory of water particles

The trajectories of particles can be directly derived from third-order parametric equations in the Lagrangian coordinates.

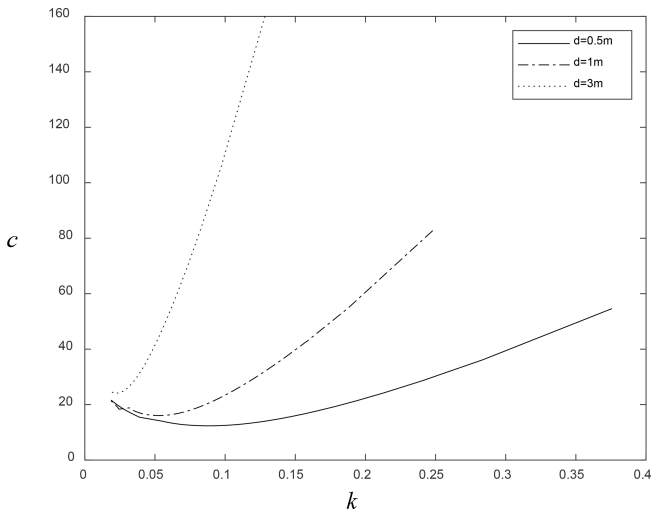

FIGURE 1
Nonlinear dispersion curve under various thicknesses of the ice sheet d = 0.5, 1, 3 m for water depth h = 100 m.

In Figures 2A–D, the particle trajectories for progressive flexural-gravity waves are plotted at five vertical levels for two Lagrangian wave frequencies under various water depths and vertical levels b for the ice sheet thickness d = 1 m and wave period T_w = 10 s. It can be seen that the horizontal and vertical displacements of water particle trajectory are larger with the shallower water depth. The vertical excursion is larger than the horizontal counterpart for the particle orbit near the free surface for the shallow water depth. The particle trajectories show an open and spiraling curve in the direction of the wave propagation.

In Figures 3A–D, the particle trajectories for nonlinear flexural-gravity waves in water depth h (=50 m) are plotted for various ice sheet thicknesses (d = 0,0.5,1,3 m) and vertical positions b. Figures 3A–D show the larger displacement amplitude of particle trajectories for the larger thickness (d = 3 m) of the ice sheet than the pure progressive gravity wave with d = 0. Increasing the thickness of the ice sheet is to increase the horizontal and vertical excursions traveled by water particles due to increasing the drift velocity. Overall, an increase in the thickness of the ice sheet and the material rigidity tends to increase the particle that moves along the orbit.

The drift velocity

In Section 3.2, we found that the mass transport velocity and the Lagrangian wave setup could be derived by taking the time average over one Lagrangian wave period to the horizontal and vertical parametric equations of the water particle that appears in the even order of our analytical solution. Taking the time average of the third-order approximation solution, the drift velocity and Lagrangian mean wave level $\bar{\eta}$ (b) over the whole range of depths can be obtained as follows:

$$\frac{k}{\sigma_0}\ \bar{x}_t = \frac{k}{\sigma_0}\ \frac{1}{T_L}\ \int_0^{T_L}\ \sum_{n=1}^{3}\epsilon^n f'_{nt}\mathrm{d}t$$

$$= \frac{1}{4}\ (2 + \frac{w_2}{\sigma_0})\ A^2k^2\ \frac{\cosh\ 2k\ (b\ +\ h)}{\cosh^2\ kh} \quad (4.1)$$

Figure 4 shows the second-order drift velocity versus the water depth and vertical label b for the ice sheet thickness d = 1 m and the wave steepness $kA = 0.03\pi$. Figure 5 shows the variation of the mass transport velocity against various ice sheet thicknesses and the vertical label b for the water depth h = 50 m and the wave steepness $kA = 0.03\pi$. From Figures 4 and 5, we can find that the mass transport velocity decays with dimensionless vertical depth for all thicknesses of the ice sheet. In Figure 5, the case d = 0 shows that the mass transport velocity is the same as that of Chen et al. (2010).

Conclusions

We extended the work of Chen et al. (2010) to include the elastic sheet effect to derive the third-order analytical

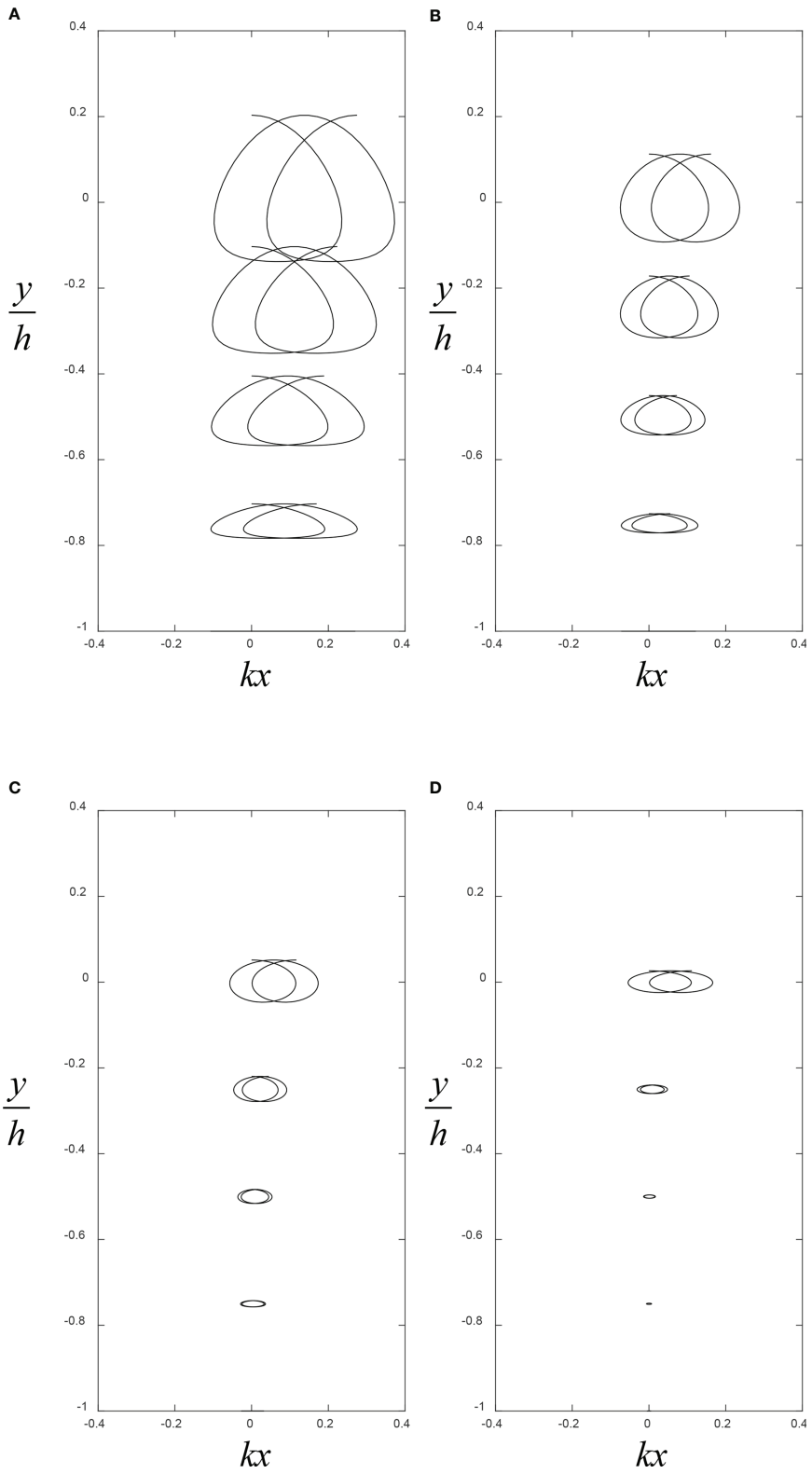

FIGURE 2
(A–D) The variation of third-order water particle trajectories at different vertical labels *b* for the thickness of the ice sheet *d* = 1 m under various water depths *h* = 10, 20, 50, 100 m.

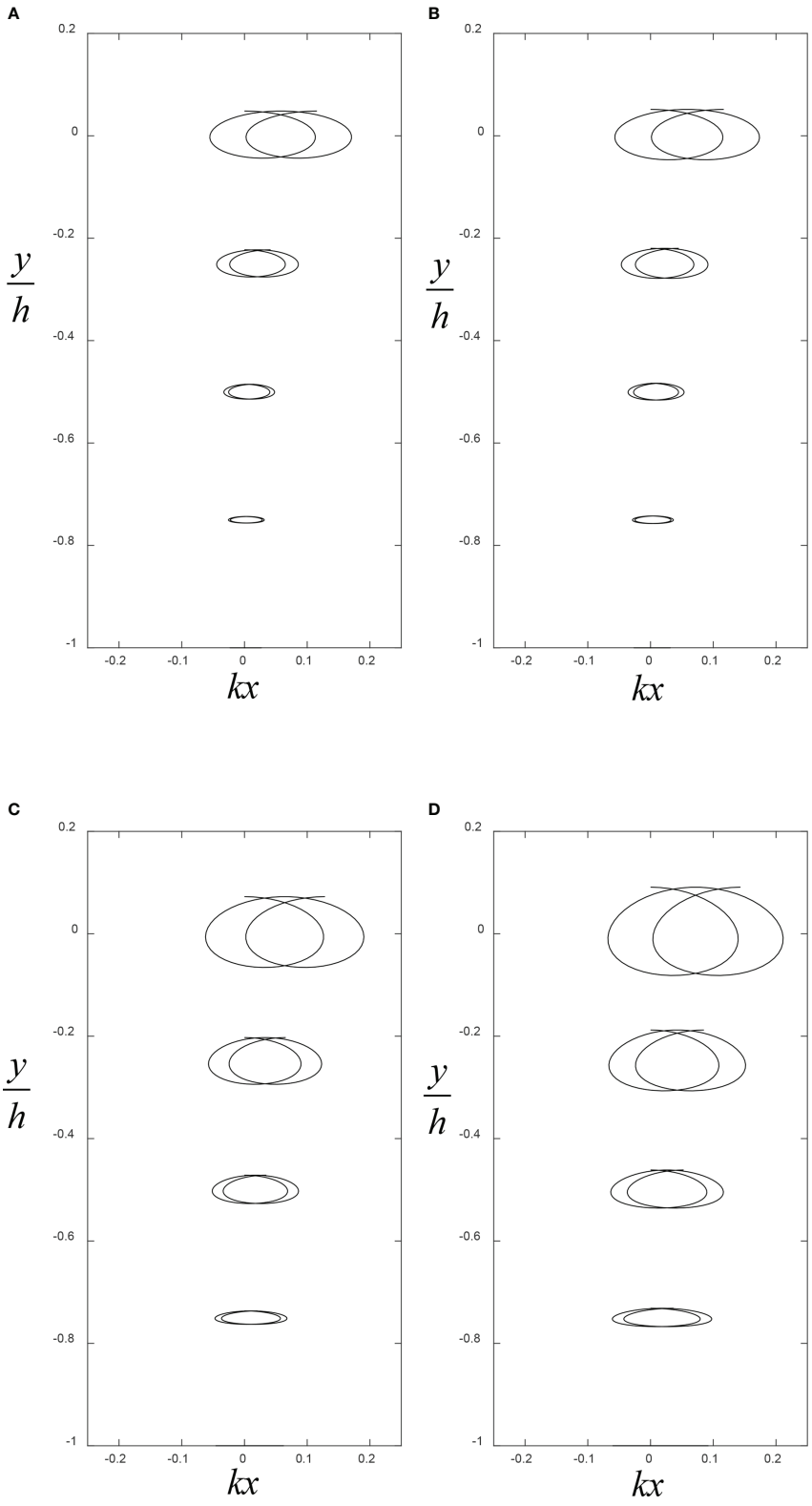

FIGURE 3
(A–D) The variation of third-order water particle trajectories at different vertical labels *b* for water depth h = 50 m under various thicknesses of the ice sheet d = 0, 0.5, 1, 3 m.

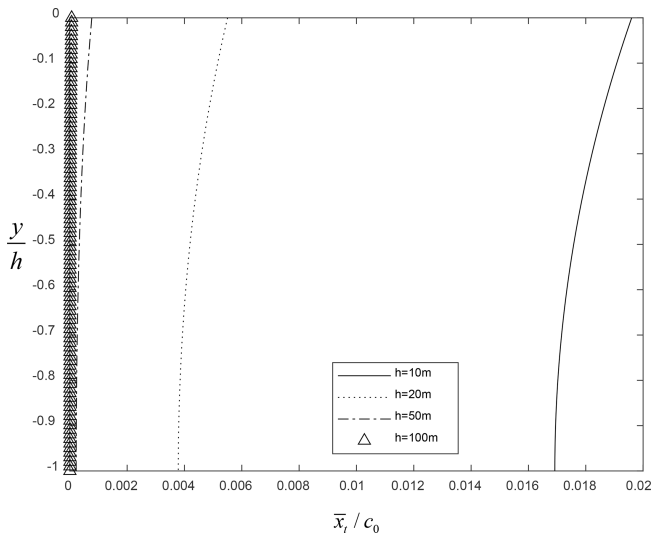

FIGURE 4
Dimensionless mass transport velocity versus vertical labels *b* for the thickness of the ice sheet *d* = 1 m under various water depths h = 10, 20, 50, 100 m.

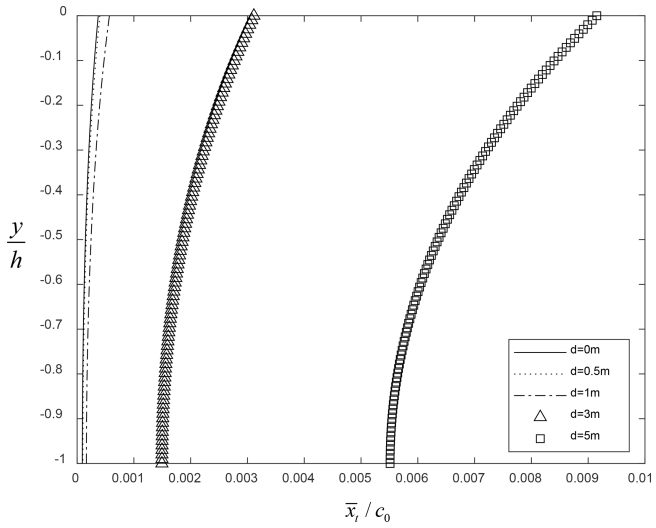

FIGURE 5
Dimensionless mass transport velocity versus vertical labels *b* for water depth h = 50 m under various thicknesses of the ice sheet d = 0, 0.5, 1, 3, 5 m.

parametric solution for nonlinear progressive flexural-gravity water waves in Lagrangian coordinates. The particle trajectories could directly be determined by the third-order Lagrangian approximation. Through the numerical simulations, the effect of the rigidity of the ice sheet on the particle dynamics of the nonlinear flexural-gravity waves was discussed. The properties of particle motion for the flexural-gravity waves are similar to the gravity-capillary waves (Hsu et al., 2016).

Data availability statement

The raw data supporting the conclusions of this article will be made available by the authors, without undue reservation.

Author contributions

H-CH: Conceptualization, Methodology, Formal analysis, Investigation, Writing-original. M-SL: software. visualization,

formal analysis. All authors contributed to the article and approved the submitted version.

Funding

The work was supported by the Research Grant of the National Science andTechnology Council, Taiwan through Project No. 110-2221-E-110-016-MY3.

Acknowledgments

The authors would like to acknowledge the referees for helpful comments.

Conflict of interest

The authors declare that the research was conducted in the absence of any commercial or financial relationships that could be construed as a potential conflict of interest.

Publisher's note

All claims expressed in this article are solely those of the authors and do not necessarily represent those of their affiliated organizations, or those of the publisher, the editors and the reviewers. Any product that may be evaluated in this article, or claim that may be made by its manufacturer, is not guaranteed or endorsed by the publisher.

References

Bhattacharjee, J., and Sahoo, T. (2007). Interaction of current and flexural gravity waves. *Ocean Eng.* 34 (11–12), 1505–1515. doi: 10.1016/j.oceaneng.2007.01.004

Buldakov, E. V., Taylor, P. H., and Eatock-Taylor, R. (2006). New asymptotic description of nonlinear water waves in Lagrangian coordinates. *J. Fluid Mech.* 562, 431–444. doi: 10.1017/S0022112006001443

Chen, Y. Y., and Chen, H. S. (2014). Lagrangian Solution for irrotational progressive water waves propagating on a uniform current: Part 1. fifth-order analysis. *Ocean Eng.* 88, 546–567. doi: 10.1016/j.oceaneng.2014.03.011

Chen, Y. Y., and Hsu, H. C. (2009). A modified Euler–Lagrange transformation for particle orbits in nonlinear progressive waves. *Ocean Eng.* 36, 747–775. doi: 10.1016/j.oceaneng.2009.04.003

Chen, Y. Y., Hsu, H. C., and Chen, G. Y. (2010). Lagrangian Experiment and solution for irrotational finite-amplitude progressive gravity waves at uniform depth. *Fluid Dyn. Res.* 42, 045511. doi: 10.1088/0169-5983/42/4/045511

Clamond, D. (2007). On the Lagrangian description of steady surface gravity waves. *J. Fluid Mech.* 589, 433–454. doi: 10.1017/S0022112007007811

Constantin, A. (2006). The trajectories of particles in stokes waves. *Invent. Math* 166, 523–535. doi: 10.1007/s00222-006-0002-5

Constantin, A. (2012a). An exact solution for equatorially trapped waves. *J. Geophys. Res. Oceans* 117, C05029. doi: 10.1029/2012JC007879

Constantin, A. (2012b). Particle trajectories in extreme stokes waves. *IMA J. Appl. Math.* 77, 293–307. doi: 10.1093/imamat/hxs033

Constantin, A. (2013). Some three-dimensional nonlinear equatorial flows. *J. Phys. Oceanogr.* 43, 165–175. doi: 10.1175/JPO-D-12-062.1

Constantin, A., and Escher, J. (2011). Analyticity of periodic traveling free surface water waves with vorticity. *Ann. Math* 173, 559–568. doi: 10.4007/annals.2011.173.1.12

Constantin, A., and Villari, G. (2008). Particle trajectories in linear water waves. *J. Math. Fluid Mech.* 10, 1–18. doi: 10.1007/s00021-005-0214-2

Dinvay, E., Kalisch, H., and Parau, E. I. (2019). Fully dispersive models for moving loads on ice sheets. *J. Fluid Mech.* 876, 122–149. doi: 10.1017/jfm.2019.530

Forbes, L. K. (1986). Surface waves of large amplitude beneath an elastic sheet. part 1. high-order series solution. *J. Fluid Mech.* 169, 409–428. doi: 10.1017/S0022112086000708

Gao, T., Wang, Z., and Milewski, P. A. (2019). Nonlinear hydroelastic waves on a linear shear current at finite depth. *J. Fluid Mech.* 876, 55–86. doi: 10.1017/jfm.2019.528

Gao, T., Wang, Z., and Vanden-Broeck, J.-M. (2016). New hydroelastic solitary waves in deep water and their dynamics. *J. Fluid Mech.* 788, 469–491. doi: 10.1017/jfm.2015.695

Gerstner, F. J. (1802). Theorie de wellen, abh. d. k. bohm. ges. wiss. *Ann. Der Phys.* 32, 412–440. doi: 10.1002/andp.18090320808

Greenhill, A. G. (1886). Wave motion in hydrodynamics. *Am. J. Math* 9 (1), 62–96. doi: 10.2307/2369499

Greenhill, A. G. (1916). Skating on thin ice. *Phil. Mag* 31, 1–22. doi: 10.1080/14786440108635465

Hsu, H. C., Chen, Y. Y., and Wang, C. F. (2010). Perturbation analysis of the short-crested waves in Lagrangian coordinates, nonlinear anal. *Real World Appl.* 11, 1522–1536. doi: 10.1016/j.nonrwa.2009.03.014

Hsu, H. C., Francius, M., Montalvo, P., and Kharif, C. (2016). Gravity-capillary waves in finite depth on flows of conatsnt vorticity. *Proc. R. London A: Math. Phys. Eng. Sci.* 472, 20160363. doi: 10.1098/rspa.2016.0363

Longuet-Higgins, M. S. (1953). Mass transport in water waves. *Phil. Trans. R. Soc Lond. A* 245, 535–581. doi: 10.1098/rsta.1953.0006

Longuet-Higgins, M. S. (1986). Eulerian and Lagrangian aspects of surface waves. *J. Fluid Mech.* 173, 683–707. doi: 10.1017/S0022112086001325

Marko, J. R. (2003). Observations and analyses of an intense waves-in-ice event in the Sea of Okhotsk. *J. Geophys. Res.* 108, 3296. doi: 10.1029/2001JC001214

Ng, C. O. (2004). Mass transport in gravity waves revisited. *J. Geophys. Res.* 109, C04012. doi: 10.1029/2003JC002121

Pierson, W. J. (1962). Perturbation analysis of the navier–stokes equations in Lagrangian form with selected linear solution. *J. Geophys. Res.* 67 (8), 3151–3160. doi: 10.1029/JZ067i008p03151

Squire, V. A., Dugan, J. P., Wadhams, P., Rottier, P. J., and Liu, A. K. (1995). Of ocean waves and sea ice. *Annu. Rev. Fluid Mech.* 27, 115–168. doi: 10.1146/annurev.fl.27.010195.000555

Squire, V. A., and Moore, S. C. (1980). Direct measurement of the attenuation of ocean waves by pack ice. *Nature* 283 (5745), 365–368. doi: 10.1038/283365a0

Stokes, G. G. (1847). On the theory of oscillatory waves. *Trans. Camb. Phil. Soc.* 8, 441–473.

Toland, J. F. (2007). Heavy hydroelastic travelling waves. *Proc. R. Soc A* 463, 2371–2397. doi: 10.1098/rspa.2007.1883

Toland, J. F. (2008). Steady periodic hydroelastic waves. *Arch. Ration. Mech. Anal.* 189, 325–362. doi: 10.1007/s00205-007-0104-2

Vanden-Broeck, J.-M., and Părău, E. I. (2011). Two-dimensional generalized solitary waves and periodic waves under an ice sheet. *Phil. Trans. R. Soc Lond. A* 369, 2957–2972. doi: 10.1098/rsta.2011.0108

Wadhams, P., and Holt, B. (1991). Waves in frazil and pancake ice and their detection on seasat synthetic aperture radar imagery. *J. Geophys. Res.* 96, 8835–8852. doi: 10.1029/91JC00457

Wang, Z., Guan, X., and Vanden-Broeck, J. M. (2020). Progressive flexural-gravity waves with constant vorticity. *J. Fluid Mech.* 905, A12–A28. doi: 10.1017/jfm.2020.750

Wilton, J. R. (1915). On ripples. *Phil. Mag.* 29 (173), 688–700. doi: 10.1080/14786440508635350

frontiers | Frontiers in Marine Science

TYPE Original Research
PUBLISHED 09 January 2023
DOI 10.3389/fmars.2022.1036381

OPEN ACCESS

EDITED BY
Wei-Bo Chen,
National Science and Technology Center for Disaster Reduction (NCDR), Taiwan

REVIEWED BY
Cihan Sahin,
Yıldız Technical University, Turkey
Wenhong Pang,
East China Normal University, China

*CORRESPONDENCE
Yongping Chen
ypchen@hhu.edu.cn
Peng Yao
p.yao@hhu.edu.cn

SPECIALTY SECTION
This article was submitted to Coastal Ocean Processes, a section of the journal Frontiers in Marine Science

RECEIVED 04 September 2022
ACCEPTED 19 December 2022
PUBLISHED 09 January 2023

CITATION
Chen Y, Pu J, Zhu Q, Su M, Zhou Z, Qiao Z, Xu C and Yao P (2023) Wind effect on sediment suspensions over silt-dominated mixtures: An experimental study.
Front. Mar. Sci. 9:1036381.
doi: 10.3389/fmars.2022.1036381

Wind effect on sediment suspensions over silt-dominated mixtures: An experimental study

Yongping Chen[1,2]*, Jinshan Pu[1,2], Qin Zhu[3], Min Su[2,4], Zeng Zhou[1,2], Zhongxing Qiao[2], Chunyang Xu[2] and Peng Yao[1,2]*

[1]State Key Laboratory of Hydrology-Water Resources and Hydraulic Engineering, Hohai University, Nanjing, China, [2]College of Harbour, Coastal and Offshore Engineering, Hohai University, Nanjing, China, [3]Research Centre of Ecology & Environment for Coastal Area and Deep Sea, Southern Marine Science and Engineering Guangdong Laboratory (Guangzhou), Guangzhou, China, [4]State Key Laboratory of Estuarine and Coastal Research, East China Normal University, Shanghai, China

A series of laboratory experiments have been conducted to explore the wind effect on Sediment Suspended Concentrations (SSCs) in fine-grained coastal systems. The paddle waves were overplayed with surface-blowing winds in a wind-wave flume to mimic offshore swells coupling with local wind waves during rough weather. Both SSCs and water turbulences under different wind and wave conditions have been investigated over two kinds of sediment beds (Sediment 1, S1, D_{50} = 52μm and Sediment 2, S2, D_{50} = 90μm). The High Concentration Layers (HCL) were formed under most of the wave-only conditions, while with the introduction of the stronger wind, more sediment suspensions were transported upward, increasing SSCs in upper water elevations. The finer sediment S1 is easier to suspend than S2 under the same conditions. The enhancement of the vertical turbulence intensity (σ_w) by winds is the main reason for the increase in SSCs. Meanwhile, because the wind-induced turbulence can hardly penetrate the HCL, the turbulence intensities outside the HCL can be further amplified compared to the experiment without a sediment bed. The wind contributes over 65% of the SSC enlargement above the HCL under a wind of 10m/s for S1, while less than 20% inside the HCL in most wind conditions. The sediment mixing coefficient (ϵ_s), a crucial parameter for suspended sediment modeling, was enhanced with stronger winds. Although the existing formulas for the vertical distribution of ϵ_s are valid under both wave-only and small winds (2.5 m/s) for both sediment beds, the enhancement of ϵ_s caused by strong winds cannot be captured, requiring further research.

KEYWORDS

suspended sediment concentration, turbulence intensity, wind effect, silt-dominated mixture, flume experiment

1 Introduction

Sediment transport has a marked influence on coastal physical processes linking feedback loops between hydrodynamics (e.g., current, wave), turbulence, and morphological evolution (Bailey and Hamilton, 1997; Wu and Hua, 2014). In shallow areas abundant in fine sediments, such as estuaries and tidal flats, the suspended load is the primary means of sediment transport. Meanwhile, suspended sediments are important agents carrying organic matter, nutrients, heavy metals, and other substances in estuarine and coastal waters, which affect coastal environmental processes (Green and Coco, 2014; Tao et al., 2020). Therefore, understanding suspended sediment dynamics is substantial for coastal morphology and ecological evolution (Cloern, 1987; Liu et al., 2014).

Sediment suspensions are primarily dependent on the turbulent motions in shallow waters, which are produced by single or combined interactions between various hydrodynamics, such as waves, currents, and winds (Bailard, 1981; Hassan and Ribberink, 2005; van Rijn, 2007; Kobayashi et al., 2008; Aagaard and Hughes, 2010; Kassem et al., 2015; Alsina et al., 2018). Bailard (1981) reported that the oscillatory wave motions performed the essential action to transport the sediment on the sandy coast. O' Hara Murray et al. (2012) reported that the wave groups, compared to a single incident wave, could generate over three times more surficial SSCs. The wave groups with varying wave heights are more active in suspending and entraining the bed sediment. Alsina et al. (2018) presented that the short-wave groups induced sediment suspended transport is dominated by horizontal advection with significant wave-swash interactions. Kassem et al. (2015) demonstrated that wave motion plays an important role in entraining sediment inside the boundary layer and high-frequency turbulence due to the momentum transfer into smaller scales supports the particles in suspension. Furthermore, Pang et al. (2020) revealed that the TKE contributed more effectively to sediment suspension at the scale of wave group than that of the incident wave, especially under broken wave conditions. Meanwhile, some research focuses on sediment suspension under complex dynamics. For example, Yao et al. (2015) conducted a series of flume experiments to explore the sediment suspension behavior under the wave and current conditions over sand-silt mixtures, discovering that current velocity can prompt the sediment suspension in upper layers compared to the wave-only condition. Meanwhile, the current direction does not significantly affect the time-averaged concentration profiles. Furthermore, much work has been done in some wind-dominated areas to explore the relationship and mechanism between wind and sediment suspension concentrations (Bailey and Hamilton, 1997; Booth et al., 2000; Su et al., 2015; Pu et al., 2022).

Apart from turbulent motions induced by various coastal hydrodynamics, the properties of sediment particles themselves, such as particle size, cohesion, and bed composition, also exert influence on sediment suspensions (van Rijn, 1989; Van Rijn et al., 1993; Mitchener and Torfs, 1996; Jacobs et al., 2011). For example, Van Rijn et al. (1993) reported that the vertical mixing process of fine sand (D_{50} = 200μm) suspension could be significantly reinforced in current and wave conditions. However, for cohesive sediment, different behaviors can be observed. Flume experiments with a wave over a consolidated mud bed have shown that the top-layer mud can be easily fluidized, generating a thin layer with large concentrations near the bottom (Maa and Mehta, 1987; Van Rijn and Louisse, 1987). Moreover, several studies have paid attention to the behavior of mixed sediment in order to predict mixed sediment transport (van Ledden et al., 2006; Sanford, 2008). Based on a validated fine sediment transport model, Waeles et al. (2008) proposed that the relative mud concentration determines the critical bed shear stress for the erosion of the superficial sediment. In addition, silt, whose size is located between sand and clay, is widely distributed in China, such as the tidal flat along the central Jiangsu coast and the modern Yellow River Delta (Gong et al., 2017; Xu et al., 2018). Silty sediment has been shown to have both cohesive and non-cohesive properties, attracting the attention of many scholars (Yao et al., 2015, Yao et al., 2022a; Yao et al., 2022b; Zuo et al., 2017; Zuo et al., 2021).

Regarding the dynamic behavior of suspension enriched in silty sediments, Zhao (2003) reported that when the cohesive fraction is low, three sediment motion forms can be identified (i.e., bed load, near-bottom high concentration layers, and suspended load in upper layers). Otherwise, the sediment transport is mainly in the suspended load. Yao et al. (2015) recognized that silty suspensions have different concentration profiles from sand under wave-only and wave-with-current conditions, respectively. Under wave-only conditions, a high concentration layer (HCL) can be formed. Inside the HCL, the silt concentration decreases logarithmically (sand-like behavior), whereas the concentration profile is distributed homogeneously outside the HCL (clay-like behavior). Zuo et al. (2021) updated existing formulations for the sand-silt mixtures to estimate depth-averaged SSCs for both vortex-rippled beds and sheet flow conditions. Several basic physical processes have been considered, such as stratification, hindered settling, and mobile beds.

It is believed that wave motion is the primary form of energy transference during wind blowing, which plays a significant role in maintaining suspensions. In addition to wave motion, Su et al. (2015) found that wind can enhance SSC directly by exerting turbulence into the water using wind-flume experiments. Furthermore, Zhu et al. (2016) found that wind would affect water turbulence in another way besides wave orbital motions based on *in-situ* field observations. Therefore, only applying wave-induced bed shear stress and mixing coefficient cannot interpret the enhancement of SSCs in a silt-dominated system during rough weather. Whether surface-generated turbulence by wind directly influences water turbulence structures, mixing processes, and thus the SSC distribution is unclear.

This study aims to explore the wind effect on fine sediment suspensions over silt-dominated mixtures. A series of experiments have been carried out in a wind-wave flume with two types of sediments under different wind and paddle wave conditions (i.e., offshore swells combined with the local wind). The addressed research questions include: (1) to what extent the wind will affect silt suspensions in shallow areas; (2) how the wind affects the mixing processes of suspended silty particles and the vertical distribution of SSCs. Section 2 describes the experimental setup, instrumentation, and analysis methods, followed by the result analyses in Section 3, including vertical distributions of SSCs and the turbulence intensities under different experimental conditions. Section 4 provides discussions followed by conclusions in Section 5.

2 Methods

2.1 Flume experiment

The laboratory experiments were performed in a wind-wave flume at Hohai University, China. The flume has a length of 80m, a width of 1m, and a depth of 1m (Figure 1). Sediment samples used in this experiment were collected from a silt-rich tidal flat in the middle of the Jiangsu coast, China. Our sampling fieldwork was carried out in mid-August 2018, and two sediment samples from the tidal flat were collected: Sediment 1 (referred to as S1) from the upper flat and Sediment 2 (referred to as S2) from the middle flat. The particle sizes of the samples (S1 and S2) were measured by a Malvern Mastersize 3000 laser particle size analyzer. S1 is a silt-enriched mixture (70% of silt content; D_{50} = 52μm) while S2 is a very fine sand-enriched mixture (30% of silt content; D_{50} = 90μm). The measured particle size distributions of the two bed sediments are shown in Figure 2.

The layout of the experimental flume, such as the wave generator, suction fan, and wave dissipator, is illustrated in Figure 1. The wave generator is located upstream of the flume, and three wave height probes are placed on the wave paddle to detect the reflected wave. By automatically adjusting the position of the wave paddle, the reflected wave can be minimized. The gravel beach slope, with a slope of 1:4.5, was also set downstream. In this study, a typical experiment duration is around 2 hours, including the time to achieve a steady state of SSC and the data collection. The active and passive wave reflection absorption systems can guarantee wave stability during long-time wave generation. Since this study focuses on SSC profiles during a steady state, the stability of the wave is essential for the measurement. Meanwhile, wave reflection is inevitable during long-time wave generation. Thus, the waves at the sediment section are combinations of the incident and reflected waves, which show a similar shape as Stokes second-order waves (See Figure S1 in Supplementary Materials). The 2nd Stokes wave represents the function of wave reflection. Therefore, the separation of wave reflection is not our primary concern. The reflection coefficients of paddle wave experiments are around 0.0626-0.2713 (based on 3-gauge method of Mansard and Funke (1980) and 0.0647-0.2034 (based on a time domain method of Sun et al. (2002)). See Table S1 in the Supplementary Materials for details. Furthermore, the present experiment methodology is consistent with existing studies on SSCs in the wave flume (such as, van Rijn and Kroon, 1992; Thorne, 2002; Yao et al., 2015; Davies and Thorne, 2016).

A suction fan was installed on the downstream side of the flume to produce wind in the same direction as waves. The wind covers were fixed on the top of the flume. Before experimenting with a sediment bed in this study, we have also done a series of experiments with a fixed bed (namely, sediment-free experiment; SFE hereinafter), keeping other experimental settings unchanged. The SFE mainly focused on wind effects on water turbulence, which showed that the surface-blowing wind intensified the turbulent kinematic energy (TKE) in the upper water column in addition to wave orbital motions.

Four Wave Height Meters (WHMs) were installed along the flume to measure the water surface elevation (Figure 1). The instantaneous water velocity was measured by the Acoustic Doppler Velocimeter (ADV). The ADV was mounted on a mobile measuring frame that can be moved vertically by a computer control system. Seven measurement points were arranged along the beam, the lowest one was 0.6 cm above the bottom, the highest one was at Z=0.6*h* (*h* is the water depth), and the other 5 points were placed at every 0.1h in between. The sampling rate was set to 50Hz. It should be noted that the

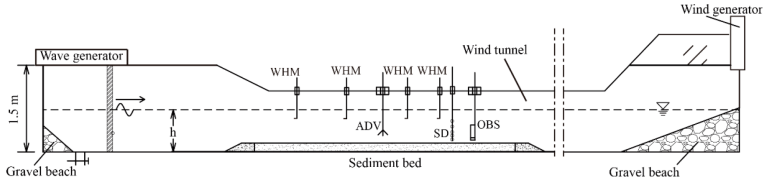

FIGURE 1
The experimental design and schematic of the wind-wave flume.

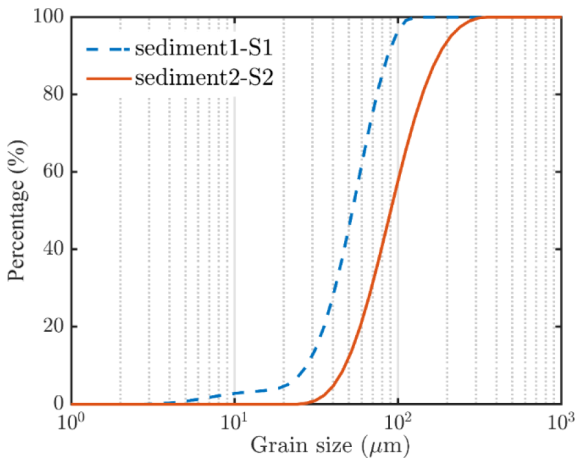

FIGURE 2
The particle size distributions of the two bed sediments.

velocity signal near the water surface, which is a blind area of the ADV, cannot be recorded. Nevertheless, substance mixing (e.g., sediment suspension) was more pronounced in the middle and lower water column. Therefore, the velocities in the middle and lower layers were analyzed and investigated in this study. The wind speed was measured by a hot-wire anemometer placed 350 mm above the motionless water surface.

Two Optical Backscatter Sensors (OBS 3+) were mounted vertically on another mobile measuring frame with a 35mm interval, providing the real-time signals on SSC development. The lens of the OBS was adjusted to be parallel to the wave direction. The initial position of the lower OBS was placed about 5 mm above the sediment bed. Our previous study has proved that the OBS signal was positively related to SSC when SSC< 40g/l (Su et al., 2016). Thus, when the OBS signal reached a steady state, the stable state of the water SSC was considered to be achieved and another function of OBS is to help us check the quality of the water SSC values during the data process. Subsequently, a specially designed siphon device was applied for the water-sediment sampling to obtain time-averaged SSC. Comparison between time-averaged OBS signals and time-averaged SSC shows a quadratic relationship, suggesting a good data quality of SSC measured by the siphon device. See Figure S2 in the Supplementary Materials for more information on OBS and SSC calibration curves. Meanwhile, the ADV started to record the velocity data as well. The siphon device (SD in Figure 1) was mounted at the left of the OBS frame at a horizontal distance of 0.6m. The lowest intake tube was set initially at 1 cm above the original flat sediment bed. During the experiment, the local bed forms were developed so that the relative height of the siphon device (i.e., SSC of each elevation) as well as the velocity data from ADV was corrected correspondingly according to the mean bed level (average of the ripple crests and troughs). Thus, under different experimental conditions, each intake tube's vertical positions differed. In each experimental case, the sediment samples were taken twice with a time interval of 10 minutes and were put into six pre-calibrated pycnometers and six glass cylinders, respectively. For the glass cylinders, the samples had to be filtered, dried and weighted to attain the time-averaged sediment concentration. For samples in the pre-calibrated pycnometers, the concentration can be calculated by weighting directly. Each experimental group was repeated twice. By averaging the two concentrations of repeated experiments, the final SSC of each experimental group can be obtained.

2.2 Experimental conditions

Instead of mimicking the field conditions on an accurate natural scale, the present study utilizes a series of controllable flume experiments with various designs. Different combinations of winds (wind speed of 0–10 m/s) and regular waves (wave heights of 6–14 cm) were designed for the experiment. The water depth (h) was 0.3m, and the wave period was kept constant, i.e., T=1.5s. Based on different experimental conditions, the resulting bed shear stresses and turbulence intensities which are important for SSCs, should be comparable to the field conditions. By these designs, the bed shear stress over the sediment bed varies in a range of 0.26-0.59 Pa over sediment S1 and 0.28-0.62 Pa over sediment S2. The bed shear stress was calculated following van Rijn (2007) by the measured near bed orbital velocity, wave period, water depth, and sediment particle size (D_{50}). The turbulence intensities (horizontal) in the laboratory are in the range of 0-0.03 m/s (details refer to section 3.2), In the tidal flat, the typical bed shear stress during windy conditions is around 0~0.8 Pa (Mariotti and Fagherazzi, 2013; Zhu et al., 2016; Hu et al., 2017), and the turbulence intensities are in the range of 0-0.06 m/s (Soulsby and Humphery, 1990). Thus, the representativeness of our experimental designs for the field conditions can be well validated.

Several pre-experimental tests have been conducted under wind-only and paddle wave-only conditions, respectively. The paddle wave shows a relatively regular shape and a narrow frequency band (see Figure S3 in the Supplementary Materials). The wave induced by surface-blowing wind depicts a wide frequency band with irregular shapes. Under 6 m/s pure wind conditions, the wave heights measured in the sediment section are around 1.77-1.93 cm, and the wave periods are 0.33-0.37s. Thus, the features of the paddle wave and wind-blowing wave generated in the flume are consistent with that of swells and wind waves in the field. In the following, the paddle wave is named swell, and the wind-blowing wave is named wind-wave, following previous studies, such as Cheng and Mitsuyasu (1992) and Mitsuyasu and Yoshida (2005).

Details of other experimental conditions are listed in Table 1. The capital letters (A, B, C) represent the experimental cases (i.e., wave height, H = 6cm, 10cm, 14cm)

and the numbers represent the corresponding wind speed level. Four levels of wind speed are designed, i.e., 0, 2.5, 6, and 10m/s. For example, S1A3 represents the experimental case with sediment S1 under a wave of 6cm and a level 3 wind speed (i.e., 10m s^{-1}). As mentioned before, the waves generated by wind only are tiny, and no sediment is initiated into motion. Therefore, the experimental conditions do not include wind-only conditions. The impacts of wind-induced turbulence on the sediment suspension can be obtained by comparing SSCs under wave-only and wave-wind combined conditions. Subsequently, the relative contribution of wind-induced and wave-induced turbulence on SSC under different conditions can be deduced.

2.3 Data analyses

The data analyses in the present study include the vertical distributions of the SSC, the calculation of turbulence parameters of the water column as well as the sediment mixing coefficient. For the vertical distributions of SSC, the method has been described in 2.1. The turbulence component needs to be separated from the original velocity signal to get the turbulence intensity. Then, the horizontal intensity σ_u and the vertical intensity σ_w can be calculated.

The instantaneous water velocities in horizontal and vertical directions are typically divided into:

$$u = \bar{u} + \tilde{u} + u', \tag{1}$$

$$\mathbf{w} = \bar{\mathbf{w}} + \tilde{\mathbf{w}} + \mathbf{w}', \tag{2}$$

where u and w are the instantaneous velocity in the horizontal and vertical direction, respectively; $\bar{u}$ and $\bar{w}$ are the time-averaged components of u' and w', respectively, $\tilde{u}$ and $\tilde{w}$ are the periodical components, and u' and w' represent the turbulent fluctuations (Benilov et al., 1974; Cheung and Street, 1988). To investigate the variation of the turbulence intensities, the time-averaged and periodical components of u and w must be removed. There are several methods for decomposing raw velocity data to extract turbulent velocities, such as the tenth-order Butterworth filter method (Lamb, 2004; Hooshmand et al., 2015), the linear filtering technique, the triple decomposition method (Olfateh et al., 2017), the phase-average method (Thais and Magnaudet, 1996; Su et al., 2015; Qiao et al., 2016). In this study, the phase-averaged method was adopted, which has already been validated by Cheung and Street (1988) and Qiao et al. (2016) using similar instrumentations and experimental settings. The turbulence intensities between the present study and the results of Cheung and Street (1988) show similar variation patterns and the same magnitude. Furthermore, the decomposed turbulent velocities of this study are 10^{-3} to 10^{-2} m/s, which are in the same magnitude as Su et al. (2015), who also chose the phase average method, and Olfateh et al. (2017), who chose the Linear Filter Technique (LFT) method. The principle of the phase-averaged method is illustrated in Figure 3 (taking the horizontal velocity u as an example). The details refer to Cheung and Street (1988) and Su et al. (2015).

TABLE 1 Basic measurements and derived data for S1 and S2.

Case	U_r (m s^{-1})	H (cm)		λ (cm)		U_m (m s^{-1})		v-σ_u (cm s^{-1})		v-σ_w (cm s^{-1})		v-σ'_u (cm s^{-1})	v-σ'_w (cm s^{-1})
		S1	S2	S1	S2	S1	S2	S1	S2	S1	S2	SFE	SFE
A0	0	5.98	5.94	0.67	0.80	0.14	0.13	0.20	0.16	0.21	0.19	0.53	0.15
A1	2.5	5.75	5.64	0.57	0.73	0.13	0.13	0.22	0.27	0.30	0.32	0.78	0.36
A2	6	6.28	6.18	0.47	0.63	0.12	0.13	0.54	0.47	0.53	0.51	1.05	0.59
A3	10	7.27	7.76	0.50	0.63	0.12	0.15	0.78	1.00	0.96	0.77		
B0	0	9.94	9.37	0.50	0.75	0.22	0.19	0.30	0.27	0.33	0.30	0.62	0.24
B1	2.5	9.63	9.40	0.60	0.83	0.22	0.20	0.47	0.30	0.46	0.35	0.72	0.33
B2	6	10.03	9.49	0.67	1.01	0.22	0.21	0.97	0.63	0.91	0.73	1.15	0.71
B3	10	10.84	11.36	0.50	0.93	0.21	0.23	1.12	1.03	1.12	0.95		
C0	0	13.12	13.20	0.43	0.83	0.27	0.28	0.75	0.46	0.62	0.43	1.06	0.55
C1	2.5	12.90	12.46	0.30	0.97	0.27	0.27	0.84	0.57	0.64	0.57	1.14	0.56
C2	6	14.05	13.29	0.43	0.83	0.28	0.26	1.33	0.93	1.27	0.85	1.12	0.59
C3	10	14.76	14.14	0.50	0.83	0.28	0.30	1.65	1.89	1.48	1.39		

H represents the wave height, averaged by the two wave gauges near the OBS and siphon device. Ur represents the reference wind speed, v-σ_u and v-σ_w represent the vertical-averaged horizontal and vertical turbulence intensity, respectively. λ represents the wave height of the bed ripples. U_m represents the near bed peak orbital velocity, v-σ'_u and v-σ'_w are the vertical-averaged horizontal and vertical turbulence intensity of the SFE, respectively.

Subsequently, the horizontal and vertical turbulence intensities (σ_u and σ_w) can be calculated as follows:

$$\sigma_u = \sqrt{\overline{u'^2}}, \tag{3}$$

$$\sigma_w = \sqrt{\overline{w'^2}}. \tag{4}$$

As mentioned earlier, the vertical distributions of SSC were measured during a steady state according to the OBS signal. By applying the time-averaged (over the wave period) advection-diffusion equation during a steady state, the sediment mixing coefficient (ϵ_s) can be derived based on measured SSCs and settling velocity ω_s (Ogston and Sternberg, 2002; van Rijn, 2007):

$$C(z)\omega_s + \epsilon_s \frac{dC}{dz} = 0, \tag{5}$$

where $C(z)$ is the time-averaged concentration at height z above the sediment bed, ϵ_s is the sediment mixing coefficient and ω_s is the settling velocity of the suspended sediment particles, which can be determined from the following formulations (van Rijn, 1990; te Slaa et al., 2013):

$$\omega_s = \begin{cases} \frac{(s-1)gd^2}{18\nu} & \text{for} 1 < d \le 100\mu m \\ \frac{10\nu}{d}\left[\left(1+\frac{0.01(s-1)gd^3}{\nu^2}\right)^{0.5}-1\right] & \text{for} 100 < d \le 1000\mu m \\ 1.1[(s-1)gd]^{0.5} & \text{for} d \ge 1000\mu m \end{cases} \tag{6}$$

in which d is the median size of the suspended sediment particles and can be measured by sampling method, s is the sediment relative density (= 2.65), and ν is the kinematic viscosity coefficient. It is well known that the settling velocity can be affected by various factors, such as particle shape, flocculation, and the sediment concentration itself. The percentages of fine-grained particles (i.e., grain size smaller than 8 μm) of both sediment S1 and S2 are 0.8%-4% (Figure 2). van Ledden et al. (2004) suggested that the sediment mixture behaves as non-cohesive when the clay content (grain size smaller than 2 μm) is smaller than 5%-10%. Thus, both sediment S1 and S2 are considered non-cohesive. Meanwhile, previous settling experiments also showed no flocculation for suspended silt (te Slaa et al., 2013; te Slaa et al., 2015; Xu et al., 2022). Furthermore, Yao et al. (2022a) discovered that silty sediment with grain size larger than 8 μm does not flocculate in freshwater (0‰ of salinity), which is consistent with our experimental phenomena. Therefore, flocculation was not considered. The hindered settling is an important process in case of high SSC to estimate the ω_s . The larger the SSCs, the smaller the settling velocity of the particle. Therefore, the hindered settling effect is considered by multiplying a coefficient $\Phi_{hs}=(1-0.65c_t/c_{gel})^5$ to ω_s . The c_{gel} is the volume concentration of the immobile sediment bed, $c_{gel}=(D_{50}/d_{sand})c_{gel,s}$, $c_{gel,s}$ is the dry bulk density and c_t is the total volume concentration.

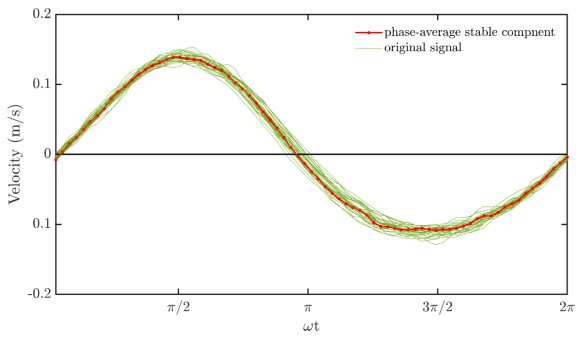

FIGURE 3
The demonstration of phase-average method: decomposition of the velocity into stable components and turbulence components.

3 Results

3.1 Vertical distributions of SSC

Figure 4 shows the vertical profiles of SSC for S1 and S2, respectively. By comparison, the SSC profiles of both S1 and S2 are of the same magnitude as the previous studies under wave-only conditions (Su et al., 2015; Yao et al., 2015), so the rationality and repeatability of our experiments can be proved.

Under paddle wave-only conditions (blue lines in each subplot), larger wave height results in higher SSC of S1. As the wave height increase, the increment of SSC in the middle layers of the water column is more remarkable than in the lower layers, making the SSC profiles more homogeneous in vertical. Compared to S1, the SSC profiles over S2 show the same pattern. However, for the vertical-averaged SSC, c_{t2} are smaller than c_{t1} under the same wave height (Table 2), indicating that fine sediment is easier to suspend in the water column to increase the water SSC.

When the wind is superposed with paddle waves, the SSCs of S1 increase by different degrees, and the SSC distribution patterns of the three cases with different wind speeds are similar. Taking case S1B as an example (i.e., paddle wave height of 10 cm, Figure 4B), the SSC profile is similar to the wave only condition under relatively small wind (2.5m/s), and then the SSCs increase correspondingly with increasing wind speed, especially in the middle layers. When the wind speed is 6m/s, the SSC increment is 41.42% compare to the wave-only condition in the lowest measuring layer while it keeps increasing upward and reaches 275% in the middle layer (z/h=0.37). As the wind grows up to 10m/s, the SSC of each layer enhances

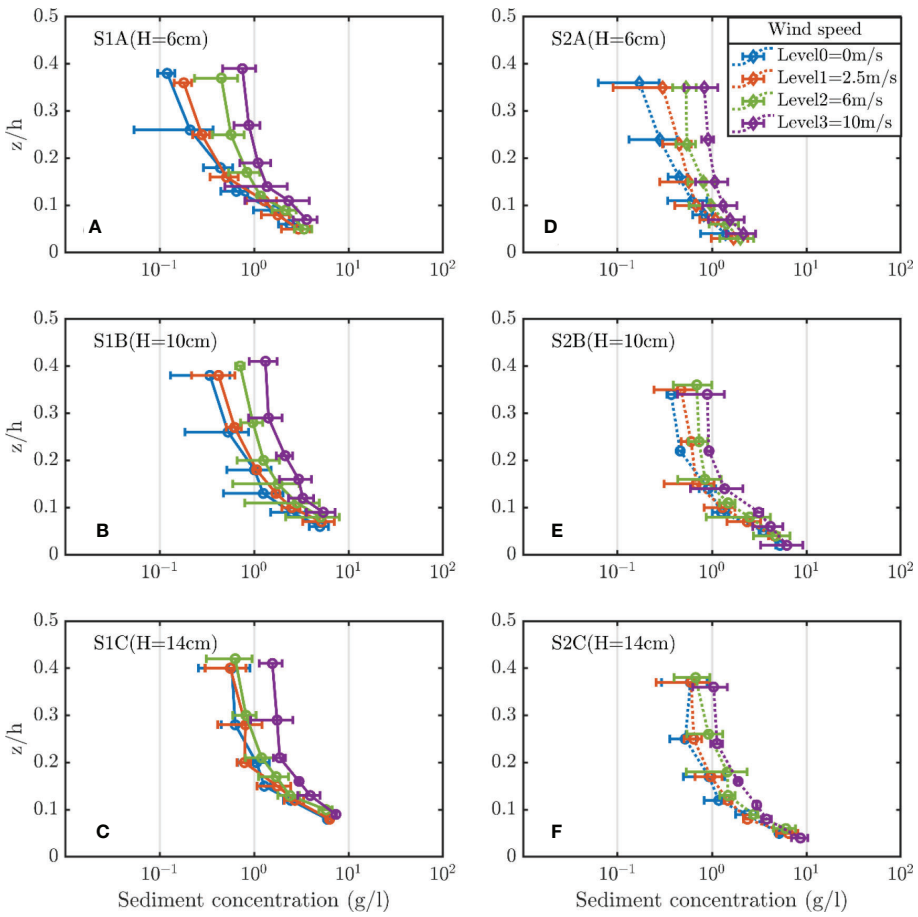

FIGURE 4
Vertical concentration profiles of S1 (solid lines, **A–C**) and S2 (dashed lines, **D–F**). Lines of different colors represent waves combined with the wind of various strengths. The capital letters in the upper left of each graph represent the sediment type and the experimental case. Bars are ensemble standard deviations.

significantly. In the lowest measuring layer, the increment is 50.63% followed by a remarkable increase of over ten times to 525% in the middle layer. One similar phenomenon with the wave-only condition is that the SSC profiles, for all the cases, become homogenizing gradually with the increased wind speed, which is more evident above z/h=0.2. This reveals that under different wind conditions, the SSCs in the middle layers are promoted significantly compared to those in the lowest measuring layers.

The variations of SSC for S2 are generally similar to those of S1 when additional wind is imposed. With increased wind speed, the SSC magnitude of S2 at each elevation increases correspondingly with a more homogeneous profile shape than S1. Besides, the c_{t2} is smaller than the c_{t1} under the same conditions (wave and wind). This is consistent with the phenomenon of wave-only conditions since the S2 is composed of fewer fine grains than S1.

3.2 Vertical distributions of turbulence intensities

The horizontal and vertical turbulence intensities, σ_u and σ_w, at different elevations above the sediment bed were averaged over wave periods and displayed in Figures 5, 6, respectively. We also compared the results of SFE under similar wind and wave conditions. Note that, different from the fixed bed level in the SFE, the mean bed levels in this study are different for each case due to variations in bedforms.

Under paddle wave-only conditions (blue lines in each subplot of Figure 5), compared to the corresponding conditions of SFE (Figures 5G–I), the σ_u profiles over the sediment bed of S1 (Figures 5A–C) are more homogeneous in vertical without evident gradient as the results of SFE. The magnitudes of σ_u over the sediment bed of S1 in each case are smaller than those of SFE, especially in the upper layers (z/h=0.2). The reduction of σ_u in

TABLE 2 The vertical-averaged SSC and bulk Richardson number (Ri_c) of the HCL for S1 and S2 under various experimental conditions, respectively.

Case	U_r (m s^{-1})	S1			S2			Ri_c	
		c_{H1}	c_{u1}	c_{t1}	c_{H2}	c_{u2}	c_{t2}	S1	S2
A0	0	4.47	0.53	2.50	1.45	0.37	0.91	0.21	0.18
A1	2.5	4.44	0.44	2.44	1.65	0.51	1.08	0.18	0.19
		–	–		6.64%	25.12%			
A2	6	5.36	0.82	3.10	1.84	0.58	1.21	0.35	0.20
		16.69%	35.46%		15.89%	34.85%			
A3	10	6.86	1.59	4.23	2.10	1.01	1.56	0.54	0.18
		34.82%	66.15%		25.91%	62.79%			
B0	0	7.47	0.69	4.08	3.83	0.50	2.17	0.39	0.27
B1	2.5	7.53	0.72	4.18	3.93	0.57	2.25	0.39	0.26
		0.76%	15.89%		2.56%	12.48%			
B2	6	8.80	1.11	4.96	4.54	0.76	2.66	0.49	0.27
		15.12%	37.94%		15.61%	34.45%			
B3	10	8.55	1.77	5.17	4.61	1.20	2.91	0.47	0.37
		12.65%	61.20%		16.86%	58.06%			
C0	0	15.27	1.35	8.31	7.16	0.85	4.00	0.58	0.32
C1	2.5	15.94	1.46	8.70	8.16	0.94	4.55	0.66	0.40
		4.17%	7.53%		12.32%	9.8%			
C2	6	15.18	1.54	8.36	8.78	1.20	4.99	0.54	0.45
		–	12.38%		18.50%	29.56%			
C3	10	16.65	2.56	9.61	8.38	1.69	5.04	0.65	0.29
		14.43%	47.36%		14.58%	50.26%			

c_H represents the vertical-averaged SSC inside the HCL while c_u represents the vertical-averaged SSC outside the HCL and $c_t$represents the average of c_H and c_u. The percentages below the corresponding c_H and c_u represent the wind contribution rate (i.e. SSC increase rate relative to paddle wave-only conditions) on SSC increment inside and outside the HCL, respectively.

upper layers is because part of the turbulence energy is consumed by maintaining sediment suspension. Meanwhile, the σ_u is reinforced near the bed to a certain degree due to the development of the wave ripples. Compared to S1, the σ_u profiles of S2 exhibit a similar pattern with a relatively small magnitude (Table 1). This reveals that coarse sediment suspensions consume more energy than fine ones.

When the wind is added, the σ_u of both S1 and S2 increase with the wind speed proportionally (Figure 5). For S1, when the wind speed is 2.5m/s, the σ_u profile of each case is similar to the wave-only condition with slightly larger magnitudes. However, as the wind becomes more substantial (i.e., 6m/s, 10m/s), the profiles of σ_u exhibit vertical gradient shapes, which is consistent with the pattern of SFE. For example, the σ_u are reinforced significantly in case S1C2 (i.e., 6m/s wind) and are nearly twice as large on average as those in S1C1 (i.e., 2.5m/s wind) in each elevation (Table 1 and Figure 5). The increase rate of corresponding vertical-averaged value exceeds 58%. The increment declines with the elevation downward, indicating that the wind-induced energy transfers downward into the water with attenuation. This phenomenon is in line with that of SFE. Besides, it can be found that the value of σ_u is smaller than the corresponding result of SFE under the same wave and wind conditions (Table 1). For S2, compared to S1, there are mainly two differences. First, the σ_u profiles are basically homogeneous along the water depth and show no significant gradient shape in each case, even under stronger winds (6m/s and 10m/s) except S2C2. Second, the σ_u values are not as large as S1, as shown by v-σ_u in Table 1. Furthermore, the σ_u enhancement of S2 is more promoted in lowest measuring layers than in S1.

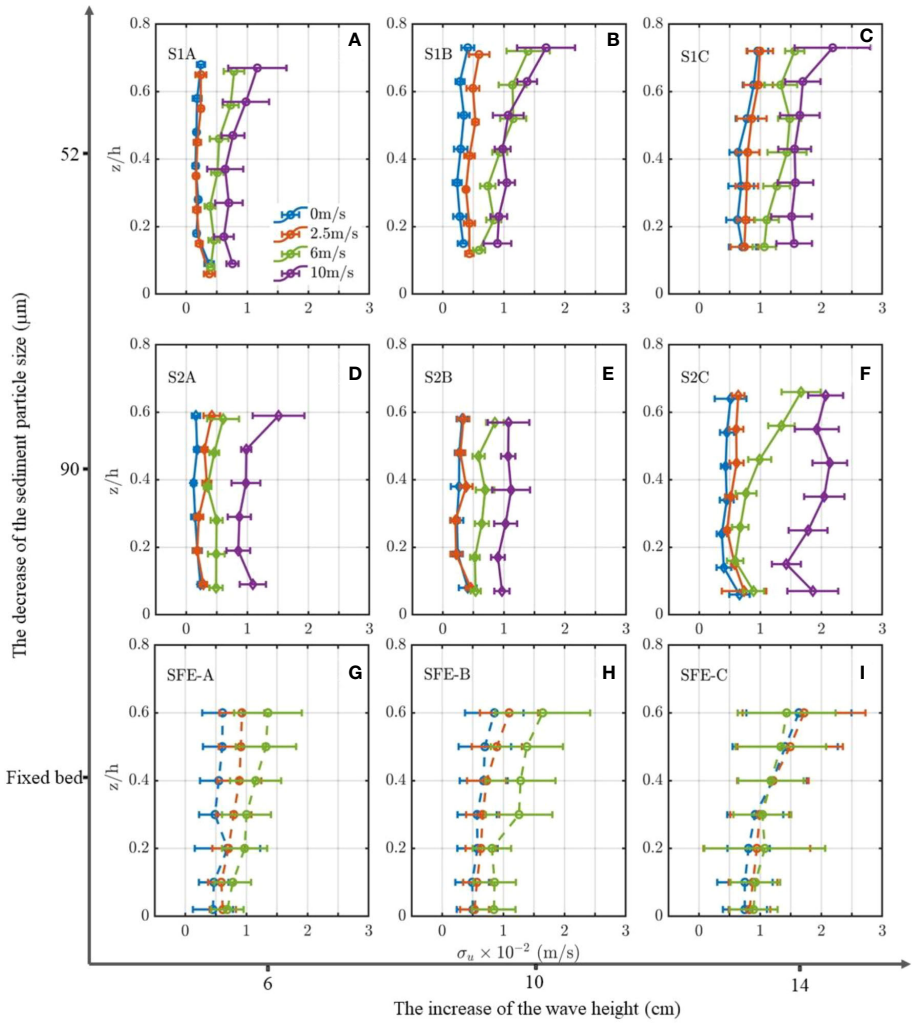

FIGURE 5
Time-averaged σ_u of S1 **(A–C)**, S2**(D–E)** and 2017-SFE **(G–I)**. Lines of different colors represent waves combined with the wind of various strengths. The capital letters in the upper left of each graph represent the sediment type and the experimental case. Bars are ensemble standard deviations.

Regarding vertical turbulence intensities, the σ_w of S1 increases with wave height under paddle wave-only conditions (Figures 6A–C). As the wind is superimposed with the paddle wave, the σ_w increases correspondingly with the wind speed by different degrees, similar to the variation pattern of σ_u. For example, the σ_w, in S1C3 (i.e., 10 m/s wind) at each elevation is twice larger on average than the results of relatively minor wind (S1C0 and S1C1). The corresponding increase rates of vertical averaged values are 138.7% and 131.3%, respectively. Compared to the σ_w of SFE, the σ_w profile of S1 only display a gradient shape under stronger wind (6m/s and 10m/s) and more considerable wave height (10cm and 14cm) in case S1B and S1C. In contrast, the profiles are homogenous in vertical under wave-only and 2.5m/s wind conditions. It is worth noting that the σ_w values of S1A are lower than those of SFE but they overtake the SFE as the wave and wind intensify (case S1B and S1C, Figures 6B, C and Table 1). This is different from that of σ_u, which is always smaller than SFE.

In the cases of S2A and S2B, the σ_w profiles are relatively homogeneous in vertical, whereas noticeable gradient shapes only appear in S2C2 and S2C3 (Figures 6D–F). Overall, the σ_w profiles of S2 are consistent with S1, but the magnitudes are smaller. Meanwhile, the σ_w magnitude in S2A is smaller than that of SFE while it is larger in S2B and S2C. This is consistent with the phenomenon of S1 in general. Moreover, the enhancement of σ_w in the lowest measuring layers due to bed forms of S2 is more promoted than S1.

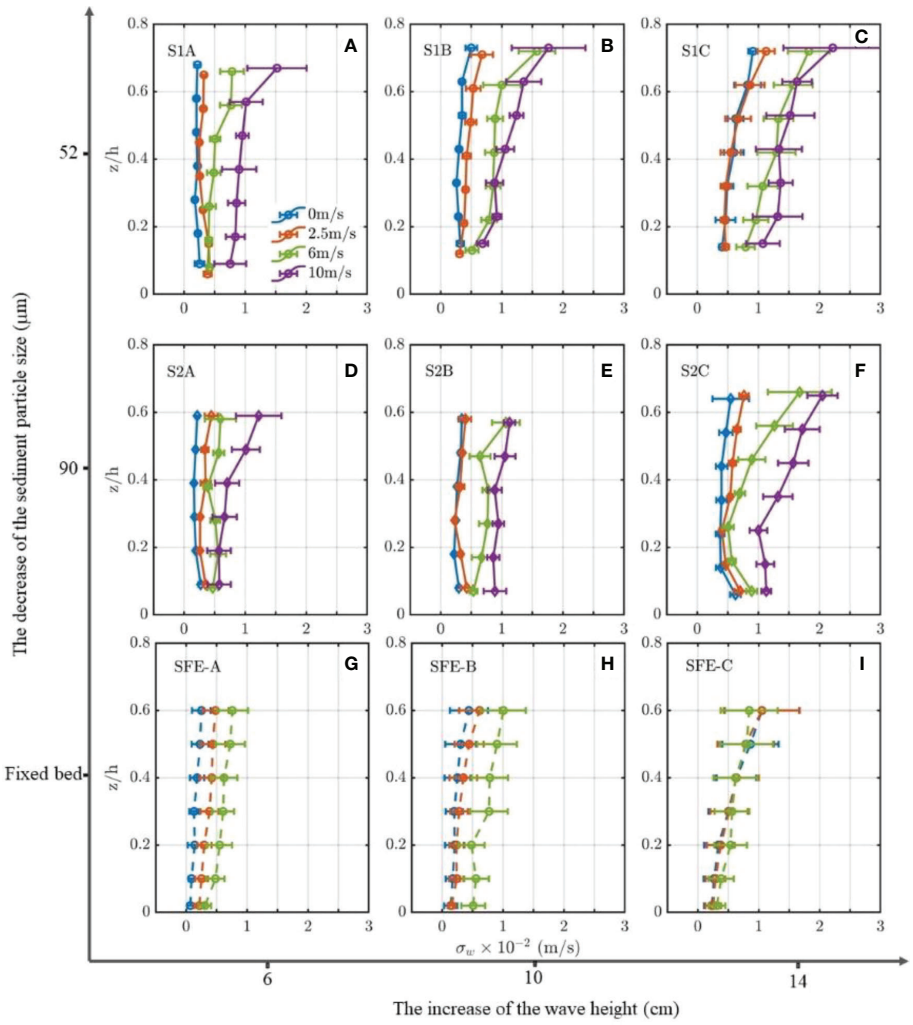

FIGURE 6
Time-averaged σ_w of S1 **(A–C)**, S2**(D, E)** and 2017-SFE **(G–I)**. Lines of different colors represent waves combined with the wind of various strengths. The capital letters in the upper left of each graph represent the sediment type and the experimental case. Bars are ensemble standard deviations.

4 Discussions

4.1 How sediment suspensions respond to different wind conditions

In natural systems, the wind blows across the water surface constantly, propagating energy into the water column and affecting water motions and suspended sediments in various ways. Water waves are the most notorious form of wind-induced movement, and the wave-induced turbulence inside the wave boundary layer is the primary driven source of sediment suspension. Similarly, the vertical profile of SSC exhibits a gradient shape that decreases from the wave boundary layer toward the water surface (Figure 4). Figure 7 shows the relationship between depth-averaged SSCs and bed shear stress under different experimental conditions. Under the same paddle wave conditions, the near bed orbital velocity is similar with different wind speeds (Table 1), and the resulting bed shear stress is also similar. This implies that surface wind blowing can hardly influence bed shear stress. For both sediment S1 and S2, the SSC is increased with bed shear stress. The fine-grained sediment (i.e., sediment S1) leads to larger SSCs than the coarser one (i.e., sediment S2) when the bed shear stress is the same.

Figure 7 indicates that under the same bed shear stress, there is an increased trend of SSC with increased wind speed, implying an enhanced effect of wind on SSCs. In combination with Figures 4–6 and Table 2, the wind can enhance turbulence intensities in addition to wave-supported sediment suspension, leading to an increase of SSCs mainly in the upper water column (i.e., outside wave boundary layers). This implies that under

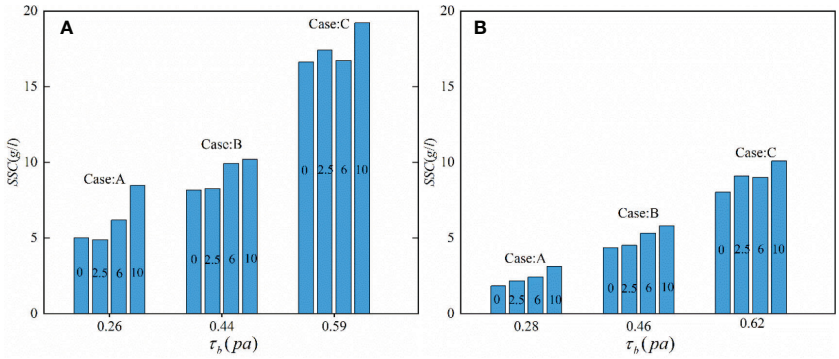

FIGURE 7
The relationship between bed shear stress and SSC for sediment S1 **(A)** and S2 **(B)**. The column represents the SSC, and the number in each column denotes the wind speed (unit: m/s) in the corresponding case.

wind and wave conditions, orbital wave motion controls the suspended sediment dynamics inside the wave boundary layers. In contrast, wind can interfere with sediment mixing processes in terms of wind-induced turbulence outside the wave boundary layers. The results indicate that the stronger the winds, the more homogeneous the SSC profile and the higher the SSC magnitude that can be developed.

To explore to what extent the SSCs respond to the winds, we first define relative wind strength, i.e., the ratio of wind speed to the maximum near-bed velocity, and then investigate the relationship between the increment (δ) of vertical-averaged SSCs and the relative wind strength in Figure 8. A linear curve, fitted with data from different combinations of winds and waves, depicts a positive correlation between the two terms. This further confirms that the wind can enlarge the SSCs but the enhancement depends on the relative strength between the local winds and offshore waves (e.g., swells during rough weather).

Furthermore, we separate the depth-averaged SSC into two parts, inside and outside the HCL, respectively, and calculate the wind contribution rate on the increment of SSC (Table 2). The SSC for both inside and outside the HCL increases proportionally with the increase of wind speed but in different magnitudes. The SSC increase rates inside the HCL are generally below 20%, whereas they can be as large as 66.15% (S1A3) outside the HCL. This indicates that the wind mainly promotes the SSC outside the HCL while the wave-induced turbulence maintains the SSC inside the HCL.

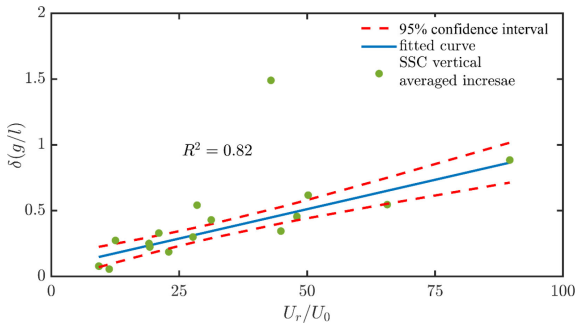

FIGURE 8
The SSC increments of various experimental cases verse the relative wind strength.

4.2 Mechanisms underlying the SSC enhancement by winds

During rough weather, offshore wind-generated waves (e.g., swells) propagate into shallow waters, touch the seabed, and entrain bed sediment into suspension. Wave-induced turbulence is a significant force that maintains sediment suspension balancing with the settling process. Thus, when the local wind is superimposed with offshore waves, the increase of SSC (see Figure 4) can be attributed to either the enhancement of turbulence intensities or the reduction of settling velocity. On the one hand, when the wind is introduced, wind-induced turbulence can be transferred into the water column, coupling with wave-induced turbulence, enhancing both horizontal and vertical turbulence intensities (σ_u and σ_w) (Figures 5, 6). Our previous clean-water experiment (SFE, Table 1) also suggested that the σ_w is more sensitive to the wind than σ_u. On the other hand, finer particles with smaller settling velocities can lead to larger SSC and are more sensitive to wind than coarser ones (Figure 4 and Table 2).

With surface blowing wind, the horizontal intensity (σ_u) would be increased, contributing to sediment suspension variations by influencing the lateral dispersion process. The σ_u of both S1 and S2 is smaller than that of SFE (sediment-free experiment) and only shows a gradient under relatively stronger

winds (i.e., 6m/s and 10m/s). This indicates that a part of the increased horizontal turbulence energy is consumed by maintaining the lateral dispersion of suspended sediments. Thus, under the same condition, coarser sediments S2 tend to consume more energy than the finer sediments S1, as shown by v-σ_u of S1 and S2 (Table 1).

Regarding the vertical intensity (σ_w), the enhancement of σ_w by winds directly alters the vertical diffusion processes of suspended sediments. The larger σ_w, the larger the SSC with a more homogenous profile shape (Figure 6 and Table 1). In contrast to σ_u, the σ_w of both S1 and S2 is larger than that of SFE, indicating a controversial way wind affects sediment diffusion in horizontal and vertical directions. This can be explained by developing the high concentration layer (HCL) over sand-silt mixtures, where the turbulent motion can be significantly constrained (Trowbridge and Kineke, 1994; Kineke et al., 1996; Yao et al., 2015). To characterize the stratification effect inside HCL, the bulk Richardson number (Ri_c) is chosen (Wright et al., 2001):

$$Ri_c = s' c'_{ave} g \delta_{HCL} / (U_\delta / 3)^2, \quad (7)$$

where s'=s−1 is the relative excess density; c'_{ave} is the averaged HCL concentration in volume; g is the gravity acceleration; δ_{HCL} is the HCL thickness and U_δ is the maximum orbital velocity near bed. The Ri_c of steady stratified flow is approximately 0.25 but varies with grain sizes. In this study, the thickness of HCL was defined as twice the thickness of the wave boundary layer according to Yao et al. (2015). The relative water depth of each measuring elevation is different in each experiment case. In some cases, there were only one or two SSC measurement points inside HCL. Therefore, the data extrapolation method was applied toward reference height to ensure the vertically averaged SSC calculation. The Ri_c of HCL (see Table 2) exceeds 0.25 except for A0 and A1 for S1 and A0-A3 for S2, confirming the existence of stable HCLs under the present experimental conditions. Hence, wind-induced turbulence can hardly penetrate HCL due to the stratification effect but can exert more effects on turbulence intensities outside HCL.

Figure 9 depicts a conceptual diagram showing how wind influence SSCs by turbulence intensification outside the HCL. Under wave-only conditions (i.e., offshore swells), a steady HCL can be formed over sand-silt mixtures. When local winds overlay with swells, both σ_u and σ_w are intensified, which is only effective outside HCL. Subsequently, increasing σ_w by wind-induced turbulence can lift more suspended sediment to a higher elevation, increasing vertical suspended sediment flux and resulting in a more homogenous SSC profile. Meanwhile, the enlargement of SSC in the upper water column further increases the burden of lateral diffusion processes, reducing σ_u. Finally, after a period of feedback adjustment, a new steady state can be achieved.

4.3 Estimation of vertical mixing coefficient during rough weather

The vertical mixing coefficient, ϵ_s, is one of the most important parameters that describe the vertical diffusion of suspended sediment and the calculation of SSCs in numerical models. In order to interpret the wind effect on vertical distributions of SSC and the mixing process of suspended silty particles, the ϵ_s have been deduced from the measured SSCs according to Eq. (5). Meanwhile, the calculated ϵ_s are then

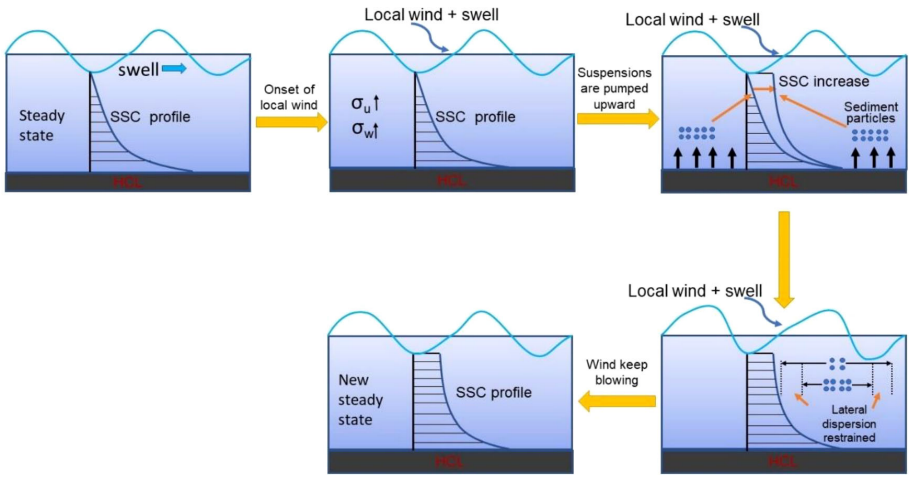

FIGURE 9
The concept diagram on mechanisms of wind effects on SSCs outside the HCL.

compared with results based on the widely applied wave-related mixing coefficients proposed by Van Rijn et al. (1993):

$$\epsilon_{s,w}(z) = \begin{cases} \epsilon_{s,w,bed} = \alpha_b U_\delta \delta_s \quad \text{for } z \le \delta_s \\ \epsilon_{s,w,max} = \frac{0.0035hH}{T} \quad \text{for} z \ge 0.5h \\ \epsilon_{s,w,bed} + \left(\epsilon_{s,w,max} - \epsilon_{s,w,bed}\right) \frac{z-\delta_s}{0.5h-\delta_s} \text{for } \delta_s < z < 0.5h \end{cases} \tag{8}$$

where α_b=0.0018D_* , D_*= $D_{50}[(s-1)]g/\nu^2]^{1/3}$, U_δ is the peak near-bed peak orbital velocity; δ_s is the thickness of the sediment mixing layer, and z is the vertical elevation above the sediment bed.

Figure 10 illustrates comparisons of vertical distributions of ϵ_s from measured SSCs (by Eq.(5) and from Eq. (8). Note that the calculation of the SSC gradient starts from the lowest measurement point, so only five points of the mixing coefficient are displayed. Under wave-only conditions, the ϵ_s of S1, for the three cases, display roughly the same pattern. Below z/h=0.1, the ϵ_s remains relatively stable, with a slight increase above z/h=0.1. As the wind was introduced, the ϵ_s varied correspondingly with the wind speed. In S1B, for example, the ϵ_s increase slightly when the wind speed is 2.5m/s; however, when the wind speed increases to 10m/s, the ϵ_s of z/h=0.1 enhances significantly. Concerning S2, the ϵ_s display a similar

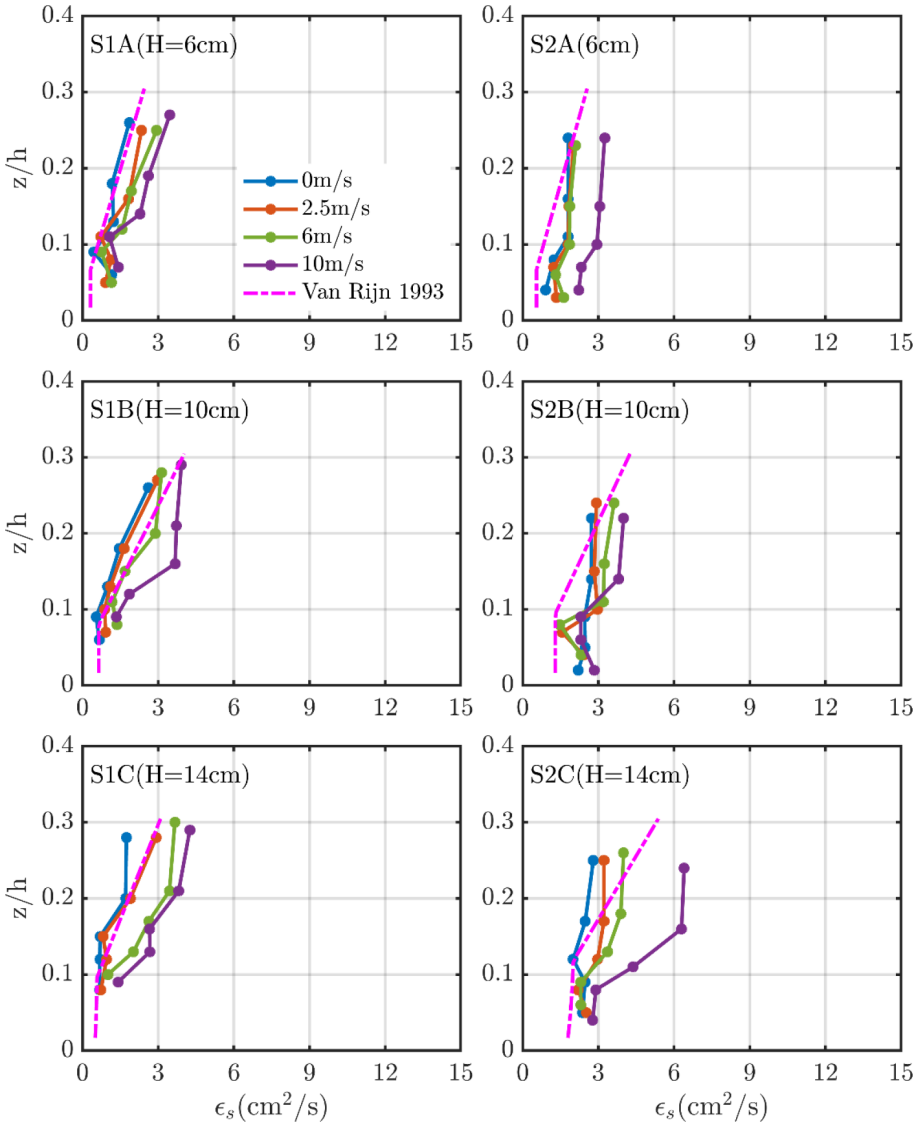

FIGURE 10
The sediment mixing coefficient, ϵ_s of each case, and the pink dotted dash lines are the theoretical modeled results of Van Rijn et al. (1993).

pattern under both wave-only and wave with wind conditions. One difference is that the ϵ_s of S2 is larger than that of S1 under the same dynamic conditions.

The ϵ_s under wave only and small wind conditions (2.5m/s) show better agreement with Van Rijn et al. (1993). However, in relatively stronger wind conditions (6m/s and 10m/s), the model may underestimate the $\epsilon_{s,}$ especially for the elevations above z/h=0.1. Considering van Rijn's model is derived from the fine sand (D_{50} = 200μm) under wave-only conditions, it can be drawn that the model can be applied for wave-only and minor wind conditions in shallow waters, while for rough weather, the mixing coefficients need to be expanded to avoid the underestimation of SSCs. Deriving a quantitative estimation model of the ϵ_s under wind and wave conditions would be a future research direction to improve the performance of numerical modeling.

5 Conclusions

The present study investigated the influence of local wind on sediment suspension over silt-dominated mixtures using a wind-wave flume experiment. Different combinations of paddle waves (representing swells) with wind speeds (representing local wind waves) have been conducted to explore the wind-induced effect on the SSCs and turbulence structures in addition to the wave. The following conclusions can be summarized:

During rough weather, the swell wave is the primary driver maintaining the high concentration layer near the bottom over silt-dominated mixtures, while local wind can promote more suspensions in the water, especially in the upper water column. The stronger the wind, the higher the SSCs develop. Furthermore, the fine sediment S1 is more sensitive to wind than coarse grains.

The vertical turbulence intensity σ_w, which is enhanced in the upper water column than in the lowest measuring layer, is the main reason for the increased SSCs. The wind contribution to SSC increment can be over 65% outside the HCL. By contrast, the wind contribution rates inside the HCL all remain less than 20%, indicating the main driver of the HCL during rough weather is the swell wave-induced turbulence. Meanwhile, the existence of the HCL hampered the further downward transfer of the surface wind-induced turbulence into the HCL.

Further analyses on the vertical mixing coefficient of sediment suspensions also depict an enhancement of mixing processes by local wind, especially in the upper layer. Hence, it is necessary to consider the enhancement of SSCs when predicting sediment suspension during rough weather in fine-grained systems. Future studies may focus on formulating a modified ϵ_s considering wind effects to increase the modeling accuracy of suspended sediment transport in rough weather.

Data availability statement

The raw data supporting the conclusions of this article will be made available by the authors, without undue reservation.

Author contributions

Conceptualization, YC and PY; methodology, PY and JP; formal analysis, JP, MS, and QZ; data curation, PY and CX; writing—original draft preparation; YC, JP, and PY. Writing—review & editing, MS and ZZ; visualization, JP, ZQ, and QZ. All authors have read and agreed to the published version of the manuscript.

Funding

This work was funded jointly by the National Natural Science Foundation of China (Grant No. 51979076, 51709288, 51909038, 51620105005) and the Open Research Fund of State Key Laboratory of Estuarine and Coastal Research (Grant No. SKLEC-KF202006). PY and MS gratefully acknowledge the Jiangsu Provincial Innovative and Entrepreneurial Doctor Program.

Conflict of interest

The authors declare that the research was conducted in the absence of any commercial or financial relationships that could be construed as a potential conflict of interest.

Publisher's note

Supplementary material

The Supplementary Material for this article can be found online at: https://www.frontiersin.org/articles/10.3389/fmars.2022.1036381/full#supplementary-material

References

Aagaard, T., and Hughes, M. G. (2010). Breaker turbulence and sediment suspension in the surf zone. *Mar. Geol.* 271, 250–259. doi: 10.1016/j.margeo.2010.02.019

Alsina, J. M., van der Zanden, J., Cáceres, I., and Ribberink, J. S. (2018). The influence of wave groups and wave-swash interactions on sediment transport and bed evolution in the swash zone. *Coast. Eng.* 140, 23–42. doi: 10.1016/j.coastaleng.2018.06.005

Bailard, J. A. (1981). An energetics total load sediment transport model for a plane sloping beach. *J. Geophys. Res.* 86, 10938. doi: 10.1029/JC086iC11p10938

Bailey, M. C., and Hamilton, D. P. (1997). Wind induced sediment resuspension: A lake-wide model. *Ecol. Model.* 99, 217–228. doi: 10.1016/S0304-3800(97)01955-8

Benilov, A., Kouznetsov, O. A., and Panin, G. N. (1974). On the analysis of wind wave-induced disturbances in the atmospheric turbulent surface layer. *Bound.-Layer Meteorol.* 6, 269–285. doi: 10.1007/BF00232489

Booth, J. G., Miller, R. L., McKee, B. A., and Leathers, R. A. (2000). Wind-induced bottom sediment resuspension in a microtidal coastal environment. *Cont. Shelf Res.* 20, 785–806. doi: 10.1016/S0278-4343(00)00002-9

Cheng, Z., and Mitsuyasu, H. (1992). Laboratory studies on the surface drift current induced by wind and swell. *J. Fluid Mech.* 243, 247. doi: 10.1017/S0022112092002714

Cheung, T. K., and Street, R. L. (1988). The turbulent layer in the water at an air–water interface. *J. Fluid Mech.* 194, 133. doi: 10.1017/S0022112088002927

Cloern, J. E. (1987). Turbidity as a control on phytoplankton biomass and productivity in estuaries. *Cont. Shelf Res.* 7, 1367–1381. doi: 10.1016/0278-4343(87)90042-2

Davies, A. G., and Thorne, P. D. (2016). On the suspension of graded sediment by waves above ripples: Inferences of convective and diffusive processes. *Cont. Shelf Res.* 112, 46–67. doi: 10.1016/j.csr.2015.10.006

Gong, Z., Jin, C., Zhang, C., Zhou, Z., Zhang, Q., and Li, H. (2017). Temporal and spatial morphological variations along a cross-shore intertidal profile, jiangsu, China. *Cont. Shelf Res.* 144, 1–9. doi: 10.1016/j.csr.2017.06.009

Green, M. O., and Coco, G. (2014). Review of wave-driven sediment resuspension and transport in estuaries. *Rev. Geophys.* 52, 77–117. doi: 10.1002/2013RG000437

Hassan, W. N., and Ribberink, J. S. (2005). Transport processes of uniform and mixed sands in oscillatory sheet flow. *Coast. Eng.* 52, 745–770. doi: 10.1016/j.coastaleng.2005.06.002

Hooshmand, A., Horner-Devine, A. R., and Lamb, M. P. (2015). Structure of turbulence and sediment stratification in wave-supported mud layers. *J. Geophys. Res. Oceans* 120, 2430–2448. doi: 10.1002/2014JC010231

Hu, Z., Yao, P., Wal van der, D., and Bouma, T. J. (2017). Patterns and drivers of daily bed-level dynamics on two tidal flats with contrasting wave exposure. *Sci. Rep.* 7, 7088. doi: 10.1038/s41598-017-07515-y

Jacobs, W., Le Hir, P., Van Kesteren, W., and Cann, P. (2011). "Erosion threshold of sand–mud mixtures," in *Cont. Shelf Res., Proceedings of the 9th International Conference on Nearshore and Estuarine Cohesive Sediment Transport Processes*, Netherlands: Elsevier. Vol. 31. S14–S25. doi: 10.1016/j.csr.2010.05.012

Kassem, H., Thompson, C. E. L., Amos, C. L., and Townend, I. H. (2015). Wave-induced coherent turbulence structures and sediment resuspension in the nearshore of a prototype-scale sandy barrier beach. *Cont. Shelf Res.* 109, 78–94. doi: 10.1016/j.csr.2015.09.007

Kineke, G. C., Sternberg, R. W., Trowbridge, J. H., and Geyer, W. R. (1996). Fluid-mud processes on the Amazon continental shelf. *Cont. Shelf Res.* 16, 667–696. doi: 10.1016/0278-4343(95)00050-X

Kobayashi, N., Payo, A., and Schmied, L. (2008). Cross-shore suspended sand and bed load transport on beaches. *J. Geophys. Res. Oceans* 113, C07001. doi: 10.1029/2007JC004203

Lamb, M. P. (2004). Turbulent structure of high-density suspensions formed under waves. *J. Geophys. Res.* 109, C12026. doi: 10.1029/2004JC002355

Liu, J. H., Yang, S. L., Zhu, Q., and Zhang, J. (2014). Controls on suspended sediment concentration profiles in the shallow and turbid Yangtze estuary. *Cont. Shelf Res.* 90, 96–108. doi: 10.1016/j.csr.2014.01.021

Maa, P.-Y., and Mehta, A. J. (1987). Mud erosion by waves: A laoratory study. *Cont. Shelf Res.* 7, 1269–1284. doi: 10.1016/0198-0254(88)92531-9

Mansard, E. P. D., and Funke, E. R. (1980). "The measurement of incident and reflected spectra using a least squares method," *Coastal Engineering*. 1980 United States: ASCE 154–172.

Mariotti, G., and Fagherazzi, S. (2013). Wind waves on a mudflat: The influence of fetch and depth on bed shear stresses. *Cont. Shelf Res.* 60, S99–S110. doi: 10.1016/j.csr.2012.03.001

Mitchener, H., and Torfs, H. (1996). Erosion of mud/sand mixtures. *Coast. Eng.* 29, 1–25. doi: 10.1016/S0378-3839(96)00002-6

Mitsuyasu, H., and Yoshida, Y. (2005). Air-Sea interactions under the existence of opposing swell. *J. Oceanogr.* 61, 141–154. doi: 10.1007/s10872-005-0027-1

Ogston, A. S., and Sternberg, R. W. (2002). Effect of wave breaking on sediment eddy diffusivity, suspended-sediment and longshore sediment flux profiles in the surf zone. *Cont. Shelf Res.* 22, 633–655. doi: 10.1016/S0278-4343(01)00033-4

O'Hara Murray, R. B., Hodgson, D. M., and Thorne, P. D. (2012). "Wave groups and sediment resuspension processes over evolving sandy bedforms," in *Cont. shelf res* Netherlands: Elsevier, vol. 46. , 16–30. The application of acoustics to sediment transport processes. doi: 10.1016/j.csr.2012.02.011

Olfateh, M., Ware, P., Callaghan, D. P., Nielsen, P., and Baldock, T. E. (2017). Momentum transfer under laboratory wind waves. *Coast. Eng.* 121, 255–264. doi: 10.1016/j.coastaleng.2016.09.001

Pang, W., Dai, Z., Ma, B., Wang, J., Huang, H., and Li, S. (2020). Linkage between turbulent kinetic energy, waves and suspended sediment concentrations in the nearshore zone. *Mar. Geol.* 425, 106190. doi: 10.1016/j.margeo.2020.106190

Pu, J., Chen, Y., Su, M., Mei, J., Yang, X., Yu, Z., et al. (2022). Residual sediment transport in the fine-grained jiangsu coast under changing climate: The role of wind-driven currents. *Water* 14, 3113. doi: 10.3390/w14193113

Qiao, F., Yuan, Y., Deng, J., Dai, D., and Song, Z. (2016). Wave–turbulence interaction-induced vertical mixing and its effects in ocean and climate models. *Philos. Trans. R. Soc Math. Phys. Eng. Sci.* 374, 20150201. doi: 10.1098/rsta.2015.0201

Sanford, L. P. (2008). Modeling a dynamically varying mixed sediment bed with erosion, deposition, bioturbation, consolidation, and armoring. *Comput. Geosci.* 34, 1263–1283. doi: 10.1016/j.cageo.2008.02.011. Predictive Modeling in Sediment Transport and Stratigraphy.

Soulsby, R. L., and Humphery, J. D. (1990). Field Observations of Wave-Current Interaction at the Sea Bed. In: A. Tørum and O. T. Gudmestad (eds) *Water Wave Kinematics. NATO ASI Series*, vol 178. Dordrecht: Springer. doi: 10.1007/978-94-009-0531-3_25

Su, M., Yao, P., Wang, Z. B., Chen, Y. P., Zhang, C. K., and Stive, M. J. F. (2015). Laboratory studies on the response of fine sediment to wind. Proceedings of 36th IAHR World Congress (the Hague, The Netherlands: Taylor & Francis), 1–9.

Su, M., Yao, P., Wang, Z., Zhang, C., Chen, Y., and Stive, M. J. F. (2016). Conversion of electro-optical signals to sediment concentration in a silt–sand suspension environment. *Coast. Eng.* 114, 284–294. doi: 10.1016/j.coastaleng.2016.04.014

Sun, H. Q., Wang, Y. X., and Peng, J. P. (2002). Hilbert Transform applied to separation of waves. *China Ocean Eng.* 16, 239–248.

Tao, Z. J., Chu, A., Chen, Y. P., Lu, S. Q., and Wang, B. (2020). Wind effect on the saltwater intrusion in the Yangtze estuary. *J. Coast. Res.* 105 (SI), 42–46. doi: 10.2112/JCR-SI105-009.1

te Slaa, S., He, Q., van Maren, D. S., and Winterwerp, J. C. (2013). Sedimentation processes in silt-rich sediment systems. *Ocean Dynamics* 63, 399–421. doi: 10.1007/s10236-013-0600-x

te Slaa, S., van Maren, D., He, Q., and Winterwerp, J. (2015). Hindered settling of silt. *J. Hydraul. Eng.* 141 (9), 04015020. doi: 10.1061/(ASCE)HY.1943-7900.0001038

Thais, L., and Magnaudet, J. (1996). Turbulent structure beneath surface gravity waves sheared by the wind. *J. Fluid Mech.* 328, 313–344. doi: 10.1017/S0022112096008749

Thorne, P. D., Williams, J. J., and Davies, A. G. (2002). Suspended sediments under waves measured in a large-scale flume facility. *J. Geophys. Res.* 107, 3178. doi: 10.1029/2001JC000988

Trowbridge, J. H., and Kineke, G. C. (1994). Structure and dynamics of fluid muds on the Amazon continental shelf. *J. Geophys. Res.* 99, 865. doi: 10.1029/93JC02860

van Ledden, M., van Kesteren, W. G. M., and Winterwerp, J. C. (2004). A conceptual framework for the erosion behaviour of sand–mud mixtures. *Continental Shelf Res.* 24, 1–11. doi: 10.1016/j.csr.2003.09.002

van Ledden, M., Wang, Z. B., Winterwerp, H., and de Vriend, H. (2006). Modelling sand–mud morphodynamics in the friesche zeegat. *Ocean Dyn.* 56, 248–265. doi: 10.1007/s10236-005-0055-9

van Rijn, (1989). Handbook sediment transport by currents and waves (*2nd* ed.). *Delft Hydraulics Laboratory*.

van Rijn, L. C. (2007). Unified view of sediment transport by currents and waves. *II: Suspended Transport. J. Hydraul. Eng.* 133, 668–689. doi: 10.1061/(ASCE)0733-9429(2007)133:6(668

van Rijn, L. C., and Kroon, A. (1992). "Sediment transport by currents and waves, in: Coastal engineering 1992," in *Presented at the 23rd International Conference on Coastal Engineering, American Society of Civil Engineers*. United States, ASCE. 2613–2628. doi: 10.1061/9780872629332.199

van Rijn, L. C., and Louisse, C. J. (1987). "The effect of waves on cohesive bed surface. *Proceedings on Coastal and Port Engineering*; Netherlands, A.A. Balkema.

van Rijn, L. C., Nieuwjaar, M. W. C., van der Kaay, T., Nap, E., and van Kampen, A. (1993). Transport of fine sands by currents and waves. *J. Waterw. Port Coast. Ocean Eng.* 119, 123–143. doi: 10.1061/(ASCE)0733-950X(1993)119:2(123

Waeles, B., Hir, P. L., and Lesueur, P. (2008). "Chapter 32 a 3D morphodynamic process-based modelling of a mixed sand/mud coastal environment: The seine estuary, France," in *Proceedings in marine science, sediment and ecohydraulics*. Eds. T. Kusuda, H. Yamanishi, J. Spearman and J. Z. Gailani (Netherlands: Elsevier), 477–498. doi: 10.1016/S1568-2692(08)80034-4

Wright, L. D., Friedrichs, C. T., Kim, S. C., and Scully, M. E. (2001). Effects of ambient currents and waves on gravity-driven sediment transport on continental shelves. *Mar. Geol.* 175, 25–45. doi: 10.1016/S0025-3227(01)00140-2

Wu, D., and Hua, Z. (2014). The effect of vegetation on sediment resuspension and phosphorus release under hydrodynamic disturbance in shallow lakes. *Ecol. Eng.* 69, 55–62. doi: 10.1016/j.ecoleng.2014.03.059

Xu, B., Gong, Z., Zhang, Q., Zhang, C., and Zhao, K. (2018). Non-equilibrium suspended sediment transport on the intertidal flats of jiangsu coast, China. s*J. Coast. Res.* 85, 251–255. doi: 10.2112/SI85-051.1

Xu, C., Odum, B., Chen, Y., and Yao, P. (2022). Evaluation of the role of silt content on the flocculation behavior of clay-silt mixtures. *Water Resour. Res.* 58, e2021WR030964. doi: 10.1029/2021WR030964

Yao, P., Sun, W., Guo, Q., and Su, M. (2022a). Experimental study on the effect of sediment composition and water salinity on settling processes of quartz silt in still water. *J. Sediment Res.* 47 (5), 15–22.

Yao, P., Su, M., Wang, Z., van Rijn, L. C., Stive, M. J. F., Xu, C., et al. (2022b). Erosion behavior of sand-silt mixtures: Revisiting the erosion threshold. *Water Resour. Res.* 58, e2021WR031788. doi: 10.1029/2021WR031788

Yao, P., Su, M., Wang, Z., van Rijn, L. C., Zhang, C., Chen, Y., et al. (2015). Experiment inspired numerical modeling of sediment concentration over sand–silt mixtures. *Coast. Eng.* 105, 75–89. doi: 10.1016/j.coastaleng.2015.07.008

Zhao, C. J. (2003). *Study on Power Sand Movement Laws in Coastal Dynamic Condition. PhD Thesis*, Tianjin University, China. (in Chinese with English (abstract)

Zhu, Q., van Prooijen, B. C., Wang, Z. B., Ma, Y. X., and Yang, S. L. (2016). Bed shear stress estimation on an open intertidal flat using *in situ* measurements. *Estuar. Coast. Shelf Sci.* 182, 190–201. doi: 10.1016/j.ecss.2016.08.028

Zuo, L., Roelvink, D., Lu, Y., and Dong, G. (2021). Process-based suspended sediment carrying capacity of silt-sand sediment in wave conditions. *Int. J. Sediment Res.* 37 (2), 229–237. doi: 10.1016/j.ijsrc.2021.09.007

Zuo, L., Roelvink, D., Lu, Y., and Li, S. (2017). On incipient motion of silt-sand under combined action of waves and currents. *Appl. Ocean Res.* 69, 116–125. doi: 10.1016/j.apor.2017.10.005

frontiers | Frontiers in Marine Science

TYPE Original Research
PUBLISHED 11 April 2023
DOI 10.3389/fmars.2023.1129643

OPEN ACCESS

EDITED BY
Ton Van Den Bremer,
Delft University of Technology,
Netherlands

REVIEWED BY
Kannabiran Seshasayanan,
Indian Institute of Technology Kharagpur,
India
Christopher Higgins,
Commissariat à l'Energie Atomique et aux
Energies Alternatives (CEA), France

*CORRESPONDENCE
Kai Håkon Christensen
kaihc@met.no

†These authors have contributed equally to
this work

SPECIALTY SECTION
This article was submitted to
Physical Oceanography,
a section of the journal
Frontiers in Marine Science

RECEIVED 22 December 2022
ACCEPTED 13 March 2023
PUBLISHED 11 April 2023

CITATION
Christensen KH and Weber JEH (2023)
Application of a Robin boundary condition
to surface waves.
Front. Mar. Sci. 10:1129643.
doi: 10.3389/fmars.2023.1129643

Application of a Robin boundary condition to surface waves

Kai Håkon Christensen[1,2*†] and Jan Erik Hobæk Weber[2†]

[1]Research and Development Department, Norwegian Meteorological Institute, Oslo, Norway,
[2]Department of Geosciences, University of Oslo, Oslo, Norway

Surface effects on deep-water gravity waves are investigated theoretically by the application of a Robin boundary condition with a complex Robin parameter, $R = R_r + iR_i$. The Robin condition combines the shear stress and the horizontal velocity at the ocean surface. We show that this condition describes wave damping related to surface phenomena like elastic films or thin viscous fluid layers. It may also model wave generation by oscillating surface stresses depending on the signs and magnitudes of R_r and R_i.

KEYWORDS

Robin condition, surface gravity waves, elastic film, viscous surface layer, wave growth, wave damping

1 Introduction

We study surface gravity waves in a homogeneous ocean where the depth is very much larger than the wavelength. These waves are affected by the physical conditions at the sea surface, most notably by the presence of thin flexible covers like biogenic films, which may cover large areas of the ocean surface (Gade et al., 2006). In addition to these natural films, we find pollutant slicks from petroleum spills or municipal effluents, which change the surface conditions. In cold regions, the surface cover is usually related to the presence of ice, for example, grease ice (Martin and Kauffman, 1981; Sutherland et al., 2019), or densely packed ice rubble in the marginal ice zone (Squire, 1984). Another example is the seasonal accumulation of *Sargassum* mats in the Tropical Atlantic (Marsh et al., 2022).

It is practically impossible to formulate a unified mathematical theory for explaining the effect on surface waves of floating material like oil, grease ice, or vegetation. We therefore intend to model this interaction by introducing a freely varying parameter R, which can be adapted to the problem in question. This parameter appears in a very general condition at the ocean surface. The condition is called a Robin condition (Gustafson, 1998; Akin, 2005) and R is the Robin parameter. Traditionally, the Robin condition is a relation between a quantity T (temperature, velocity, etc.) and its derivative $\partial T/\partial x_n$, where x_n is directed normal to the boundary. The homogeneous Robin condition can be written $\partial T/\partial x_n + RT = 0$ at the boundary (sometimes $\hat{R}\,\partial T/\partial x_n + T = 0$ is used). In this way, the Robin condition becomes a weighted combination of Dirichlet and Neumann boundary conditions. It is common in many branches of physics; see, for example, Hahn and Ozisk (2012) for applications to heat conduction, Tyvand and Nøland (2019) for convection in a porous medium, and Weber and Børve (2021) in the case of continental shelf waves with a

permeable coastline. The relevance for oceanographic purposes is the role of the fluctuating tangential stress at the surface, which is typically small compared to the fluctuating normal stress (form stress) for uncontaminated surfaces, but can be large when the surface is covered by sea slicks, oil spills, sea ice, and other materials (e.g., Dorrestein, 1951). The framework presented here is mostly relevant for waves in deep water since the bottom friction and wave radiation stresses will typically dominate in shallow water. We will therefore only discuss waves for which $kH \gg 1$, where k is the wave number and H is the local water depth. We will also ignore rotational effects; hence, we assume that $\omega \gg f$, where ω is the angular frequency of the waves and f is the Coriolis parameter.

In Figure 1, we have depicted a general configuration relevant to the discussion here. The x-axis is horizontal and placed along the undisturbed sea surface, while the z-axis is positive upwards. The x-direction is, without loss of generality, in the direction of wave propagation. In the presence of waves, the sea surface is given by $z = \eta(x, y, t)$.

We shall here use the Robin formalism to describe the tangential conditions at the surface. Thus, we write

$$\partial u/\partial z + \partial w/\partial x + Ru = 0, \quad z = \eta(x, y, t), \tag{1}$$

where u and w are the horizontal and vertical velocity components. In Equation 1, R is generally complex, i.e.,

$$R = R_r + iR_i. \tag{2}$$

We note from Equation 1 that when $R = 0$, the viscous shear stress at the surface vanishes, defining a free surface. At the other extreme, when $R \to \infty$, the horizontal motion is zero at the surface, which models a flexible, but horizontally inextensible top layer (Lamb, 1932). The application of Equation 1 as a general model for the physical conditions at the surface appears to be novel. We will relate the Robin parameter to the rate of growth and decay in the waves, using known examples for elastic monolayers and thin layers of viscous fluids to aid the physical interpretation of our results.

The rest of this paper is organized as follows: In Section 2, we calculate the wave attenuation/growth by applying the Robin condition, and in Section 3, we discuss the solution when the Robin parameter is purely real. The case of a complex Robin parameter is considered in Section 4. Energy considerations due to dilational waves excited in the surface layer is discussed in Section 5. Finally, Section 6 contains some concluding remarks.

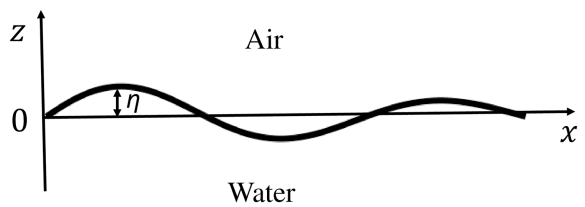

FIGURE 1
A diagram of spatially damped surface waves. The surface can be free or covered by a flexible layer, depending on the problem in question.

2 Mathematical analysis

We here consider two-dimensional wave motion in a viscous ocean. For a fluid with viscosity ν, the two-dimensional velocity field can be separated into two parts: one potential part φ and one vorticity part ψ; see Lamb (1932), such that

$$u = -\partial\varphi/\partial x - \partial\psi/\partial z, \tag{3}$$

$$w = -\partial\varphi/\partial z + \partial\psi/\partial x. \tag{4}$$

Inserting into the governing equations, we then obtain for the linear part of the wave field

$$\partial^2\varphi/\partial x^2 + \partial^2\varphi/\partial z^2 = 0, \tag{5}$$

$$\partial\psi/\partial t - \nu(\partial^2\psi/\partial x^2 + \partial^2\psi/\partial z^2) = 0, \tag{6}$$

$$p/\rho = \partial\varphi/\partial t - gz. \tag{7}$$

Assuming that $\varphi, \psi \to 0$, $z \to -\infty$, the normalized linear solutions can be written

$$\varphi = \exp(\kappa z)\exp i(\kappa x - nt), \tag{8}$$

$$\psi = C\exp(mz)\exp i(\kappa x - nt), \tag{9}$$

where C is a constant. In Equations 8 and 9, the complex wave number and frequency are defined by

$$\kappa = k + i\alpha, \tag{10}$$

$$n = \omega - i\beta. \tag{11}$$

Here α, β are the real (and small) spatial and temporal damping rates. From Equation 6, we obtain that $m^2 = \kappa^2 - in/\nu$. If we now assume that the wavelength is much larger than the thickness of the oscillatory viscous boundary layer, and that the wave growth/damping is slow compared to the wave period, we have $|m| \gg |\kappa|$ and $|\omega \gg |\beta|$. Then, we have to leading order that

$$m = (1 - i)\gamma, \tag{12}$$

where γ is defined by

$$\gamma = \omega^{1/2}/(2\nu)^{1/2}. \tag{13}$$

Here, the quantity γ^{-1} represents the thin viscous boundary-layer thickness at the surface. To obtain Equation 12, we thus assume that $k/\gamma \ll 1$. From Equation 1, we find that

$$C = -i\kappa(2\kappa + R)/(m^2 + mR + \kappa^2). \tag{14}$$

Finally, assuming no fluctuating normal stress at the water surface, the dynamic boundary condition in the z-direction becomes

$$p/\rho = 2\nu\partial w/\partial z, \quad z = \eta. \tag{15}$$

It is worth noting at this point that capillary waves can be included in the analysis by adding the normal stress due to the equilibrium value of the surface tension in Equation 15; see, for

example, Lucassen (1968). The main conclusions in the present study will not change, however, and we ignore capillary waves in our examples here since their inclusion complicates the mathematical expressions without contributing to the physical interpretation of our results. From Equation 15, we find that

$$\eta = (1/g)[(-in + 2\nu\kappa^2)\varphi - 2i\kappa m\psi],\ z = 0 \tag{16}$$

Inserting from Equations 8 and 9 into Equation 16, we obtain the dispersion relation for this problem:

$$n^2 + 2i\nu\kappa^2 n - g\kappa + iM = 0, \tag{17}$$

where

$$M = -\kappa^2(ig + 2\nu mn)(2\kappa + R)/(m^2 + mR + \kappa^2). \tag{18}$$

Utilizing Equations 10–12, we obtain from the real part of Equation 17 to lowest order the obvious result $\omega^2 = gk$. The imaginary part yields to lowest order that

$$\beta + c_g\alpha = \omega k^2/(2\gamma^2) + \Re(M)/(2\omega), \tag{19}$$

where now $c_g = \omega/(2k)$ is the usual deep-water wave group velocity. Here, $\Re$ denotes the real part of a complex quantity. We define a nondimensional Robin parameter by

$$A = R_r/\gamma,\ B = R_i/\gamma \tag{20}$$

and we scale β in Equation 19 by $\beta_{inex} = \omega k/(4\gamma)$, which is the temporal damping coefficient for an inextensible surface film (Lamb, 1932). Furthermore, we define $\hat{\beta} = \beta/\beta_{inex}$ and the nondimensional spatial damping rate by $\hat{\alpha} = 4\gamma\alpha/k^2$. Using that $k/\gamma \ll 1$, $\beta/\omega \ll 1$, and $\alpha/k \ll 1$, we obtain from Equation 19 that

$$\hat{\beta} + \frac{1}{2}\hat{\alpha} = (2k/\gamma)P + Q, \tag{21}$$

where

$$P = 1 + 2/[A^2 + B^2 + 2A - 2B + 2], \tag{22}$$

$$Q = (A^2 + B^2 + 2A)/[A^2 + B^2 + 2A - 2B + 2]. \tag{23}$$

In Equations 22 and 23, $A, B \in (-\infty, \infty)$, and it is easily seen that both P and Q are of order unity. When $A = B = 0$, we have $P = 2$ and $Q = 0$. Then Equation 21, in dimensional form, reduces to $\beta + c_g\alpha = \omega k^2/\gamma^2$, as first obtained in Jenkins (1986) for a free surface. For larger values of A, B, we find that $(2k/\gamma)P$ becomes negligible in Equation 20. A general form of Equation 19 for damped waves has been derived in Weber (2022), relating the right-hand side to the dissipation in the wave motion.

3 Real Robin parameter

It is natural to start our discussion for the case when R is purely real, i.e., when $B = 0$ in Equations 22 and 23. In Figure 2, we have plotted the attenuation rate Q vs. $A = R_r/\gamma$ in this case. We will assume that the waves are already present; hence, we ignore the generation mechanism and focus on the transient development of the existing wave field. In our analysis here, it is the fluctuating part of the tangential surface stress that is of interest, and hence, we will neglect the slowly varying wind stress that contributes to the upper ocean Ekman response, which is a second-order effect in the theoretical framework we apply here (e.g., Weber, 1983).

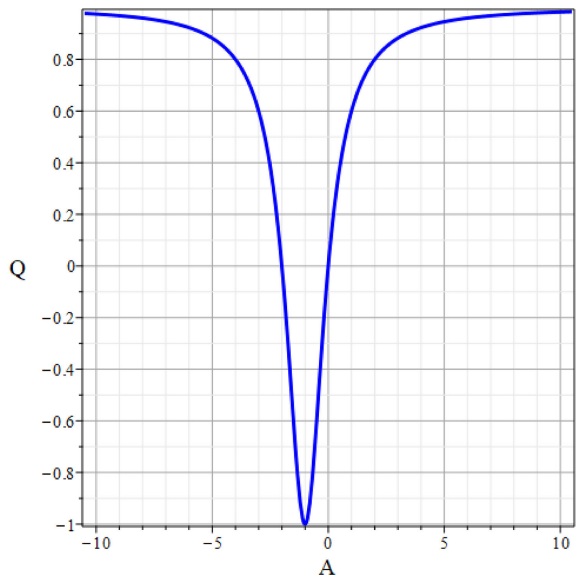

FIGURE 2
Nondimensional attenuation rate Q from (22) for deep-water waves as a function of the nondimensional real Robin parameter $A = R_r/\gamma$.

We note from Figure 2 that the depicted line tends to unity as A becomes infinitely large. Physically, this means that the horizontal velocity becomes zero at the contact with the surface cover, which is often referred to as the inextensible layer limit. Overall, real R is related to wave damping ($Q > 0$). However, it is interesting to note that $Q < 0$ (wave growth) occurs when $-2 \le A \le 0$. This may be explained in terms of the wave energy balance. From Equation 1, we may write at the surface that

$$\rho\nu(\partial u/\partial z + \partial w/\partial x) = \tau = -\rho\nu Ru, \tag{24}$$

where τ is the horizontal shear stress at the surface. Hence, by multiplying with the real u and average over the wave cycle (denoted by an over-bar), we find for the work per unit time of the shear stress on the fluid that

$$\overline{\tau u} = -\rho\nu R\overline{u^2}, \qquad z = 0. \tag{25}$$

We note that the work is proportional to the square of the horizontal velocity component and independent of the vertical velocity. This is a general result that holds for any value of the Robin parameter. From Equation 25, we realize that to have a positive energy input, we must have $R < 0$. Furthermore, to have wave growth, this input must be larger than the viscous dissipation D in the fluid. Here,

$$D = \rho\nu \int_{-\infty}^{0} (\overline{\nabla u \cdot \nabla u} + \overline{\nabla w \cdot \nabla w})dz \tag{26}$$

Due to the strong gradients near the surface, $\overline{(\partial u/\partial z)^2}$ will dominate in Equation 26. We derive real velocities from Equations 2, 3, 8, 9, and 14, and use that $k/\gamma \ll 1$. In Figure 3, we have plotted the dimensionless quantities $f_1 = 2\overline{\tau u}/(\rho\nu k^2\gamma)$ and $f_2 = 2D/(\rho\nu k^2\gamma)$ as functions of A.

We note that in a small window, $-2 \le A \le 0$, the work by the surface stress is larger than the dissipation, so here we have wave growth. The maximum growth occurs for $A = -1$. At $A = -2$, the two effects balance, so here the growth rate is zero. These results confirm the findings for the attenuation rates depicted in Figure 2.

Jenkins and Jacobs (1997) studied the wave damping by a thin layer of viscous fluid on top of an infinitely deep fluid of a different viscosity. For a thin, very viscous film of thickness d, they showed that the dynamic boundary condition in the horizontal direction between the two immiscible fluids could be written as

$$\partial u/\partial z + \partial w/\partial x + (4dk^2\mu_s/\mu)u = 0, \quad z = 0 \tag{27}$$

where μ_s and μ are the dynamic viscosities of the thin upper surface layer and the infinitely deep bottom layer, respectively. Now, by comparison with Equation 1, we see that in this case

$$R_r = 4dk^2\mu_s/\mu, \tag{28}$$

$$R_i = 0. \tag{29}$$

Since R is purely real, the damping in this case will follow the curve for $A > 0$ in Figure 2. Here, we ignore any internal motion in the film itself since the analysis is only valid for thin films, with monomolecular films as the limit.

4 Damping for a complex Robin parameter

We now study the case $R_r = \gamma A \ge 0$, $R_i = \gamma B \ge 0$. In Figure 4, we have plotted the attenuation rate Q from Equation 23 as a function of B for various values of A.

One classic (and striking) result in Figure 4 is that the maximum nondimensional attenuation rate becomes twice as large as inextensible limit when $A = 0$ (blue line), i.e., when the Robin parameter is purely imaginary and positive. This is related to the excitation of longitudinal elastic, or dilational, waves at the surface (i.e., Equation 9). Dilational waves in thin surface films efficiently dampen short waves—an intriguing phenomenon that has been the subject of study since antiquity (see, e.g., the historical review by Scott, 1977). From Miles (1967), generalizing an earlier result by Dorrestein (1951), we can write in our notation for an insoluble visco-elastic monolayer at the surface:

$$\partial u/\partial z + \partial w/\partial x + [(\zeta_1 + \zeta_2)k^2/(\rho\nu) + iE_\star k^2/(\nu\omega)]u = 0, \quad z = 0, \tag{30}$$

where $E_\star$ is the surface elasticity per unit density, and ζ_1 and ζ_2 are the dilatational and shear viscosities of the film; see also Miles (1991). Comparing with Equation 1, we note that here

$$R_r = (\zeta_1 + \zeta_2)k^2/(\rho\nu), \tag{31}$$

$$R_i = E_\star k^2/(\nu\omega). \tag{32}$$

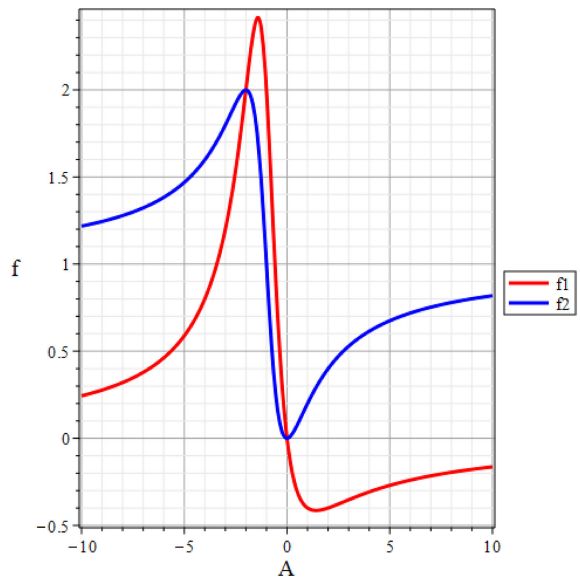

FIGURE 3
Work by the dimensionless surface stress (f_1) and the dimensionless dissipation (f_2) as functions of the nondimensional real Robin parameter $A = R_r/\gamma$.

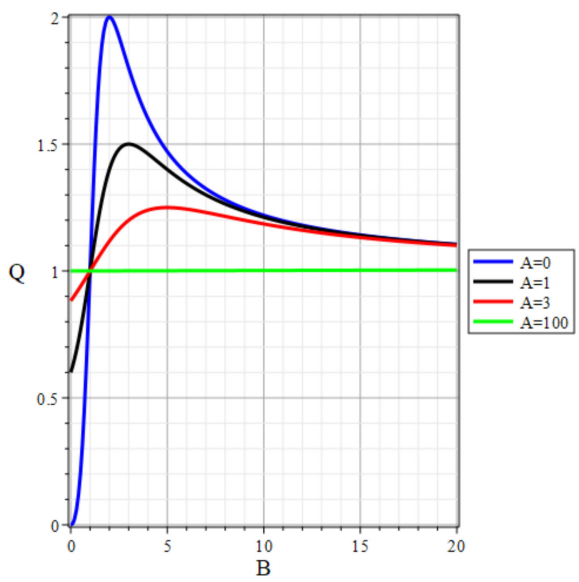

FIGURE 4
Attenuation rate Q as a function of nondimensional imaginary Robin parameter B for various values of nondimensional real Robin parameter A.

We thus see that the Robin boundary condition (Equation 1), with $R_r, R_i > 0$, is related to the viscoelastic properties of the surface cover in that the real part of the Robin parameter represents the viscous effects (as we already have explored), while the imaginary part captures the elastic properties of the cover. This means that R_i, and hence B, must be positive since a negative value of the elasticity is unphysical. Miles (1991) was the first to point out that the coefficient in Equation 24 was a complex quantity.

In the film problem, we take that the surface viscosities are negligibly small (Dorrestein, 1951; Lucassen, 1968). Hence, the Robin parameter is purely imaginary. From Equation 23 we then have that

$$Q = B^2/(B^2 - 2B + 2). \tag{33}$$

The maximum value is $Q = 2$ when $B = 2$, as seen in Figure 4. Introducing the dimensionless parameter $\delta = \gamma k^2 E_\star/\omega^2$ (Dorrestein, 1951), we have from Equation 32 that $B \equiv R_i/\gamma = 2\delta$. Hence, we obtain from Equation 21 for pure temporal damping, when $2k/\gamma$ is small, that $\hat{\beta}_{max} = Q_{max} = 2$ for $\delta = 1$, which is Dorrestein's classic result.

Since the wave modes are coupled, Equation 21 yields the damping rate for both the dilational and surface waves.

Jenkins and Jacobs (1997) compare Equations 30 and 27 and conclude that Equation 30 has exactly the same properties as Equation 27 regarding wave damping if we replace $(\zeta_1 + \zeta_2)k^2/(\rho\nu) + iE_\star k^2/(\nu\omega)$ in the film case by $4dk^2\mu_s/\mu$. However, as shown here, this is not true since the elastic film case has a dominant imaginary Robin part yielding increased damping (Figure 4, blue line), whereas in the viscous layer case, the Robin parameter is real.

5 The energetics of dilational wave damping

As mentioned, the increased maximum damping for a certain R_i as seen in Figure 4, is related to the existence of dilational waves (Lucassen, 1968; Weber and Christensen, 2003). Free dilational waves are critically damped through viscous dissipation in the oscillatory boundary layer. For this reason, the linear dispersion relation differs depending on whether the dilational waves are (i) damped in time, (ii) damped in space, or (iii) sustained by an undulating stress at the surface, i.e., forced waves (Weber and Christensen, 2003). Surface waves provide just such a mechanism for sustaining the dilational waves, and the dilational wave frequency relevant here is given by the dispersion relation for forced waves:

$$\omega_D = [k^4 E_\star^2/(2\nu)]^{1/3}. \tag{34}$$

In the present problem, where maximum damping occurs for $B = R_i/\gamma = 2$, we find from Equation 34), by using Equations 13 and 32, that

$$\omega_D = \omega. \tag{35}$$

Hence, as pointed out in Christensen (2005), maximum damping occurs when the natural frequency of the forced dilational waves exactly coincides with the natural frequency of the surface waves. Physically, the dilational waves, which would, in the absence of surface waves, be nearly critically damped, act as a sink of energy for short gravity waves. This phenomenon is sometimes referred to as "negative resonance". Similar behaviors appear in more complex setups, for example, the case of finite layer thickness with two elastic interfaces, for which two damping maxima are possible (Ermakov and Khazanov, 2022).

We can gain more insight into the role of dilational waves as an energy sink if we split the horizontal velocity components into two parts $u = \tilde{u} + \hat{u}$, representing the surface wave (Equation 8) and the dilational wave (Equation 9), respectively. The presence of the dilational wave makes the amplitude of the total horizontal velocity u dependent on the elasticity parameter. Maximum damping is associated with a maximum in the horizontal velocity u, and hence a maximum in the work per unit time done by the surface stress (Equation 25). The dissipation is primarily due to the strongly sheared dilational wave motion:

$$\begin{aligned} D \approx \hat{D} &= \rho\nu \int_{-\infty}^{0} \overline{(\partial\hat{u}/\partial z)^2}\, dz \\ &= \rho\nu \int_{-\infty}^{0} \overline{[\partial/\partial z[\hat{u}(\partial\hat{u}/\partial z)] - \hat{u}(\partial^2\hat{u}/\partial z^2)]}\, dz\,. \end{aligned} \tag{36}$$

The surface stress is well approximated by $\tau = \rho\nu\,\partial\hat{u}/\partial z (z = 0)$. We now define the work per unit time on the oscillatory boundary layer:

$$\hat{W} = \overline{\tau\hat{u}} = \rho\nu\overline{\hat{u}(\partial\hat{u}/\partial z)}, \qquad z = 0. \tag{37}$$

The second term on the right-hand side of Equation 36 is zero because of $\hat{u}$ and $\partial^2\hat{u}/\partial z^2$ always being 90° out of phase, cf. Equations 9 and 13. From Equations 36 and 37, we find that $\hat{W} = \hat{D}$ as we would expect for dilational waves (Weber and Christensen, 2003), which means that although the dilational waves are continuously excited by the surface waves, being coupled through the surface condition (Equation 1), they are continuously being dissipated in the oscillatory boundary layer at the same rate.

6 Concluding remarks

To model the various effects that may change the physics of the ocean surface, and hence affect growth and decay of surface waves, we have related the shear stress at the water surface and the horizontal velocity using a Robin condition with a complex Robin parameter. Using known results for viscous fluid layers and elastic monolayers, we show how the real part of the Robin parameter is related to viscous or frictional surface effects, while the imaginary part is associated with surface elasticity. In many situations of practical interest, for instance for ice covered waters, large floating mats of seaweeds, or more complex sea slicks with anisotropic horizontal distributions of surfactant, the dynamical conditions at the surface quickly become very complex, and we need to resort to simplified parameterizations of average behavior, particularly on the horizontal scales of numerical wave prediction models. Since it is practically impossible to formulate a unified mathematical theory

explaining the effect of surface constituents on surface waves, or even to formulate constitutive relations, we may resort to modeling the interaction between the surface waves and the floating materials by applying the Robin condition and adapting the Robin parameter to the problem in question. Even if a quantitative estimation of the Robin parameter is not possible, a discussion of the problem for limiting values of R may still improve our understanding of the basic physics involved.

Data availability statement

The original contributions presented in the study are included in the article/supplementary material. Further inquiries can be directed to the corresponding author.

Author contributions

JW contributed the original idea behind this study. JW and KC contributed equally to the mathematical analysis and writing. Both authors contributed to the article and approved the submitted version.

Funding

Financial support from the Research Council of Norway through the grants 280625 (Dynamics of floating ice) and 314449 (ACTION) is gratefully acknowledged.

Conflict of interest

The authors declare that the research was conducted in the absence of any commercial or financial relationships that could be construed as a potential conflict of interest.

Publisher's note

All claims expressed in this article are solely those of the authors and do not necessarily represent those of their affiliated organizations, or those of the publisher, the editors and the reviewers. Any product that may be evaluated in this article, or claim that may be made by its manufacturer, is not guaranteed or endorsed by the publisher.

References

Akin, J. E. (2005). Finite element analysis with error estimators: An introduction to the FEM and adaptive error analysis for engineering students. *Elsevier Butterworth-Heinemann*. doi: 10.1016/B978-0-7506-6722-7.X5030-9

Christensen, K. H. (2005). Transient and steady drift currents in waves damped by surfactants. *Phys.Fluids* 17, 9. doi: 10.1063/1.1872112

Dorrestein, R. (1951). General linearized theory of the effect of surface films on water ripples. *Proc. K. Ned. Akad. Wet. Ser. B: Palaeontol. Geol. Phys. Chem. Anthropol. B* 54, 260; 54, 350.

Ermakov, S. A., and Khazanov, G. E. (2022). Resonance damping of gravity-capillary waves on water covered with a visco-elastic film of finite thickness. a reappraisal. *Phys. Fluids* 34, 092107. doi: 10.1063/5.0103110

Gade, M., Hühnerfuss, H., and Korenowski, G. (2006). *Marine surface films: Chemical characteristics, influence on air-Sea interactions and remote sensing* (New York: Springer, Berlin Heidelberg).

Gustafson, K. (1998). Domain decomposition, operator trigonometry, robin condition. *Contemp. Math.* 218, 432–437. doi: 10.1090/conm/218/3039

Hahn, D. W., and Ozisk, M. N. (2012). *Heat conduction. 3rd edition* (New York: Wiley).

Jenkins, A. D. (1986). A theory for steady and variable wind- and wave-induced currents. *J. Phys. Oceanogr.* 16, 1370–1377. doi: 10.1175/1520-0485(1986)016<1370:ATFSAV>2.0.CO;2

Jenkins, A. D., and Jacobs, S. J. (1997). "Wave damping by a thin layer of viscous fluid". *Phys. Fluids* 9, 1256–1264. doi: 10.1063/1.869240

Lamb, H. (1932). *Hydrodynamics. 6th ed* (Cambridge, UK: Cambridge University Press).

Lucassen, J. (1968). Longitudinal capillary waves, part 1-theory. *Trans. Faraday Soc* 64, 2221–2229. doi: 10.1039/TF9686402221

Marsh, R., Oxenford, H. A., Cox, S. A., Johnson, D. R., and Bellamy, J. (2022). Forecasting seasonal sargassum events across the tropical Atlantic: overview and challenges. *Front. Mar. Sci.* 9. doi: 10.3389/fmars.2022.914501

Martin, S., and Kauffman, P. (1981). A field and laboratory study of wave damping by grease ice. *J. Glaciol.* 27, 283–313. doi: 10.1017/S0022143000015392

Miles, J. W. (1967). Surface-wave damping in closed basins. *Proc. R. Soc A* 297, 459–475. doi: 10.1098/rspa.1967.0081

Miles, J. W. (1991). A note on surface films and surface waves. *Wave Motion* 13, 303–306. doi: 10.1016/0165-2125(91)90066-W

Scott, J. C. (1977). The historical development of theories of wave-calming using oil. *Hist. Technol.* 3, 163–186. doi: 10.5040/9781350017429.0011

Squire, V. A. (1984). Sea Ice. *Sci. Prog. Oxf.* 69, 19–43.

Sutherland, G., Rabault, J., and Christensen and A. Jensen, K. H. (2019). A two layer model for wave dissipation in sea ice. *Appl. Ocean Res.* 88, 111–118. doi: 10.1016/j.apor.2019.03.023

Tyvand, P., and Nøland, J. K. (2019). Onset of convection in a triangular porous prism with robin-type thermal wall condition. *Transp. Porous Med.* 130, 751–767. doi: 10.1007/s11242-019-01337-4

Weber, J. E. (1983). Steady wind-and wave-induced currents in the open ocean. *J. Phys. Oceanogr.* 13, 524–530. doi: 10.1175/1520-0485(1983)013<0524:SWAWIC>2.0.CO;2

Weber, J. E. H. (2022). A note on the temporal and spatial attenuation of ocean waves. *Ocean Model.* 175, 102027. doi: 10.1016/j.ocemod.2022.102027

Weber, J. E. H., and Børve, E. (2021). Diurnal continental shelf waves with a permeable coastal boundary: Application to the shelf northwest of Norway. *Eur. J. Mech./B Fluids* 86, 64–71. doi: 10.1016/j.euromechflu.2021.05.003

Weber, J. E., and Christensen, K. H. (2003). Mean drift induced by free and forced dilational waves. *Phys. Fluids* 15, 3703–3709. doi: 10.1063/1.1621867

frontiers | Frontiers in Marine Science

TYPE Original Research
PUBLISHED 11 April 2023
DOI 10.3389/fmars.2023.1115986

OPEN ACCESS

EDITED BY
Nick Pizzo,
University of California, San Diego,
United States

REVIEWED BY
Gregory Wagner,
Massachusetts Institute of Technology,
United States
Henrik Kalisch,
University of Bergen, Norway

*CORRESPONDENCE
Johannes Röhrs
johannes.rohrs@met.no

SPECIALTY SECTION
This article was submitted to
Physical Oceanography,
a section of the journal
Frontiers in Marine Science

RECEIVED 04 December 2022
ACCEPTED 22 March 2023
PUBLISHED 11 April 2023

CITATION
Röhrs J, Halsne T, Sutherland G,
Dagestad K-F, Hole LR, Broström G and
Christensen KH (2023) Current shear and
turbulence during a near-inertial wave.
Front. Mar. Sci. 10:1115986.
doi: 10.3389/fmars.2023.1115986

Current shear and turbulence during a near-inertial wave

Johannes Röhrs[1*], Trygve Halsne[1,2], Graig Sutherland[3], Knut-Frode Dagestad[1], Lars Robert Hole[1], Göran Broström[4] and Kai H. Christensen[1,5]

[1]Norwegian Meteorological Institute, Oslo, Norway, [2]Geophysical Institute, University of Bergen, Bergen, Norway, [3]Environmental Numerical Prediction Research, Environment and Climate Change Canada, Dorval, QC, Canada, [4]Department of Marine Sciences, University of Gothenburg, Gothenburg, Sweden, [5]Institute for Geoscience, University of Oslo, Oslo, Norway

Surface currents and turbulent mixing were observed during a near-inertial wave (NIW) using an accousting doppler current profiler (ADCP) and satellite-tracked drifters. Drifter trajectories sampled at three depth levels show characteristics of an Ekman solution superposed with the NIW. Velocity and dissipation estimates from the ADCP reveal strong shear with a distinct constant flux layer in between the roughness length and a critical depth at 4m. Below, a shear free slab layer performing an inertial oscillation is observed. Dissipation, as estimated from the vertical beam of the ADCP, peaks in the wave-enhanced friction layer when the current opposes the wind and wave direction. Below the constant flux layer, maximum turbulence is observed when the NIW is in a phase that is in opposite direction to the time-averaged current. During this phase, currents at various depths rapidly realign in the entire boundary layer.

KEYWORDS

near-inertial wave, surface current, turbulence, dissipation, ADCP, drifter trajectory

1 Introduction

Intense turbulent mixing characterizes the ocean surface boundary layer during wind events. The level of turbulent kinetic energy (TKE) near the surface determines momentum, energy, and tracer fluxes at the air-ocean interface (e.g. D'Asaro, 2014). As a consequence, turbulent mixing also determines how surface currents respond to wind forcing, and the vertical current profile provides a transition between the wind stress and currents at depth (Rascle et al., 2006). Whenever the wind forcing is time dependent, the ocean surface boundary layer (OSBL) responds with near-inertial waves (NIW's) during a transition to a new steady state (Alford, 2003). NIW's have frequencies slightly higher than pure inertial oscillations and contribute prominently to the internal wave spectrum (Alford et al., 2016).

NIW's are often seen as anticyclonic loops (Northern hempisphere) in drifter trajectories (Röhrs and Christensen, 2015). Changes in wind and wave forcing are often faster than the inertial period - therefore much of the upper ocean is in a state of NIW's (D'Asaro, 1985). At times, the NIW energy has a comparable magnitude to the energy in

the balanced background flow, e.g. geostrophic and wind-driven Ekman currents. Energy transfer between these reservoirs is an active field of research, and the NIW's can both feed into and drain energy from steady-state flows (Thomas and Daniel, 2020). At the same time, energy from NIWs may cascade into turbulent dissipation and thereby change dynamical balances in the mixed layer (Asselin and Young, 2020).

Turbulence in the OSBL has been studied for decades and today we have detailed understanding of how turbulent mixing and current velocities interact in a near-steady state. Prognostic numerical models can also predict turbulence and currents in non-steady states (Umlauf and Burchard, 2003), however a mechanistic description of near surface turbulence and currents in non-steady states is not widely established. Evaluation of both observations and models is required, as some of the basics in the common models, e.g. the eddy viscosity concept, are currently being revisited in light of hypothesis of counter-gradient turbulent fluxes (Milani et al., 2021).

A classic view of the OSBL is that of a *constant-flux layer*, such as in Monin-Obhukov similarity theory, where the momentum flux is assumed constant throughout the boundary layer. This assumption leads to a logarithmic ocean current profile $u(z)$, the often called *law of the wall* (LOW),

$$u(z) = \frac{u_\star}{\kappa} \log\left(\frac{z}{z_0}\right) \tag{1}$$

where $\kappa = 0.4$ is the von Kármán constant, z_0 is the roughness length and $u_\star$ is the friction velocity which is related to the surface stress τ and the density ρ by $\tau = \rho u_\star^2$. Furthermore, for a constant flux layer, the eddy viscosity will be

$$\nu_e = u_\star \kappa z \tag{2}$$

for depths greater than z_0. Technically, ν_e is not defined for depths less than z_0, but it is not uncommon to add a constant (Craig and Banner, 1994). Typically in the ocean, turbulent dynamics are described in terms of the dissipation rate of turbulent kinetic energy (TKE), ϵ, which for the constant flux layer is given by

$$\epsilon = \frac{u_\star^3}{\kappa z} \tag{3}$$

assuming a steady state and ignoring buoyancy effects (e.g. Sutherland et al., 2013).

Breaking surface gravity waves at the sea surface are known to interrupt the balance in the constant flux layer by inducing additional TKE near the surface (Craig and Banner, 1994; Sutherland et al., 2013). The decay of dissipation with depth becomes more rapid than in Eq. 3, such that $\epsilon \propto z^{-2}$ (Terray et al., 1996; Esters et al., 2018). Other studies find even stronger decay as $\epsilon \propto z^{-\lambda}$ with $-1 > \lambda > -3$ (Anis and Moum, 1995; Gemmrich, 2012). Sutherland and Melville (2015) present detailed observations of dissipation near the surface, finding that surface wave dissipation F_{ds} provides a good fit for scaling TKE dissipation in the wave-enhanced friction layer.

Dissipation has been observed to be constant in the friction layer above z_0 (Sutherland and Melville, 2015). Hence the $\epsilon \propto z^{-\lambda}$ decay starts below z_0. The transition between these vertical regimes motivates to depict the OSBL as comprising three vertical components (Röhrs et al., 2023): a near-surface friction layer where wave breaking disrupts the air-sea interface, a constant flux layer where the vertical momentum flux is approximately constant and dynamics are described by the Monin-Obhukov similarity theory, and an Ekman layer where the dynamics are dominated by τ and the Earth's rotation.

The description of turbulent mixing by Eqs. 1 and 3 assume a steady state. Often this is not the case, with currents and turbulence constantly adapting to changing winds and waves. Lewis and Belcher (2004) formulate a time-dependent solution for the current profile and ν_e, whereas NIW is part of the solution before a steady state is reached. In this study we also examine the coupling between the constant flux layer and a NIW - based on observations of currents profiles and TKE dissipation.

Common observations of ocean turbulence have relied on estimating dissipation rates using a shear-probe for the microstructure of vertical velocities (Osborn, 1980). However, retrieving dissipation rates within a few meters close to the wavy surface has proven difficult even when an upward profiling shear probe is used (e.g. Ward et al., 2014). Recent advances in Acoustic Doppler Current Profilers (ADCP) - sampling vertical velocities using a vertical beam at high frequency – allow to observe the TKE profile directly along the line of sight of the vertical beam (Guerra and Thomson, 2017; Zippel et al., 2020), however, with lower resolution than with shear probes. Herein we apply an upward looking ADCP to estimate dissipation near the surface continuously throughout a NIW cycle. The ADCP also allows to record horizontal currents simultaneously with the turbulence measurements.

In the analysis we show that velocity and dissipation reveal strong shear and a distinct constant flux layer. Below this layer, a shear free slab layer is observed. Dissipation peaks in the wave-enhanced friction layer when the current opposes the wind and wave direction. Maximum turbulence below the constant flux layer is observed when the NIW is in a phase that is in opposite direction to the time-averaged current.

This paper is structured as follows. Section 2 provides an overview of the field experiment and the type of measurements involved. In section 3 we present our data and document how the observations are processed to yield Eulerian and Lagrangian currents as well as TKE dissipation rates. In section 6 we present the vertical and temporal evolution of currents, shear and dissipation. Finally we depict the difference between vertical layers and discuss the evolution of time-dependent TKE dissipation in the presence of a NIW.

2 Data and methods

2.1 Field campaign

This research was conducted in the North Sea in June 2019 as part of the annual oil-on-water exercise arranged by the Norwegian Clean Seas Association for Operating Companies and the Norwegian Coastal Administration. A general overview of the

2019 experiment can be found in?. The main purpose of the oil-on-water exercises is to study the behavior of various types of oil on the ocean surface in realistic offshore conditions, and to test different equipment for collection and burning. As part of the 2019 exercise described in Brekke et al. (2021), two oils were left to drift freely, allowing their undisturbed drift and behavior to be studied with both remote sensing and *in situ* measurements of oil thickness.

The *Offshore Sensing SailBuoy* was deployed from the ship on 11 June at 5:54 and retrieved on 13 June at 17:39. The SailBuoy was equipped with an *AirMar weather station 200 WX* and provided wind speed, wind direction and air temperature measurements at about 0.5 m above the sea surface. The measurements compared well with the ship mast measurements when corrected for altitude using a power law correction for the atmospheric boundary layer.

Three types of ocean surface drifters were deployed covering three distinct depths (Brekke et al., 2021). The path for one of each drifter type during the experiment duration is shown in Figure 1A. An animation in the electronic supplement shows all trajectories for a period of 3 days. Two buoys with drogues centered at 15 m depth (Surface Velocity Program, SVP) showed inertial oscillations, with a period of about 13.8 hours, superimposed on a general westward drift. Two drifters with drogues centered at 60 cm depth (CODE type) showed the same inertial oscillations, but with an overall drifter velocities closer to the wind direction (south-westwards), whereas a surface drifter at the air-sea interface (iSphere) showed the same inertial oscillations superimposed with the wind direction.

A *Nortek Signature 500* 5-beam ADCP was deployed on a moored rig at 59.85 N 2.4 E from June 12 04:00 - June 13 07:00 2019. The ADCP was situated ≈ 13 m below the sea surface in an upward looking position. Maximum pitch and roll of the instrument was kept within 2°. The exact depth of the sensor varied between 13.5 m and 15 m depending on the phase of the tide. The mean water depth at the mooring location is 60 m.

The ADCP was configured to sample average horizontal currents from the slanted beams in 0.5 m vertical bins on 10 minute intervals. High frequency samples of the velocity from the vertical beam were recorded at 1 Hz in 0.5 m vertical bins, these will provide estimates of turbulent kinetic energy. In addition, a pre-set program to observe wave conditions was used to obtain surface gravity wave spectra and wave dissipation as described in Appendix A.

2.2 Meteorological measurements

Relatively strong winds characterize the time period leading up to the experiment, with winds reaching up to 11 m/s during the day before the ADCP deployment (Figure 2). This implies a well-mixed boundary layer at the onset of the experiment, with ocean forecast models indicating neutral stratification in the upper 30 m of the ocean at the experiment site (not shown).

Wind direction throughout this experiment was relatively constant from NNE with strength increasing from around 6 m/s to 14 m/s during the 26 hours observed (Figures 3A, B). Wave direction is roughly aligned with the wind, yielding significant wave height in the range of 2-3 m, shown in Appendix A.

2.3 Ocean currents

Ocean currents can be inferred from surface drifters as well as ADCP measurements. Trajectories from surface drifters (Figure 1A) and progressive vector diagrams from ADCP measurements (Figure 1B) show a similar structure. Both show a strong inertial signal – "loops" in the trajectories – in addition to a strong downwind shear in the upper 4 m. The inertial period at this latitude is 13.8 hours.

Current velocities are in a downwind phase at roughly 0 h and 13 h and in an upwind phase at about 6h and 19h (Figure 3C), hence the observed motion is well within the near-inertial frequency

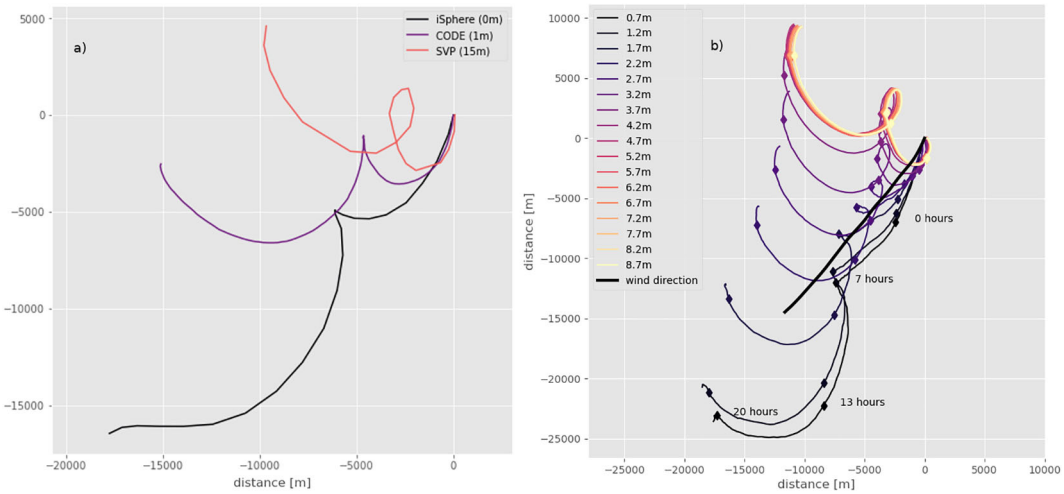

FIGURE 1
(A) Trajectories from GPS-tracked drifters at three different depths. **(B)** Progessive vector diagram of ADCP current velocities at various depths during the same time period as in **(A)**.

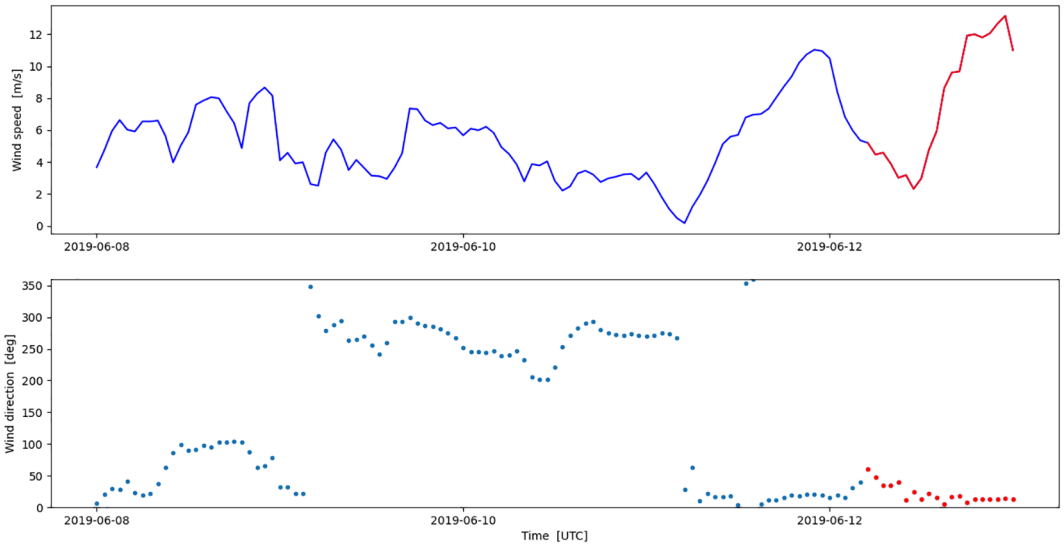

FIGURE 2
Wind speed and direction the last 7 days before the campaign period, provided by the regional weather prediction model *Arome* MEPS (Müller et al., 2017). The experiment period 12 June 04:00 UTC to ¨ 13 June 00:00 UTC is marked with red color.

band. Vertical shear is seen in the along-wind component of current velocities, while the cross-wind component exhibits very little vertical shear. Due to this shear, the surface current exhibits a downwind component throughout the NIW cycle. Transition between surface and lower level occurs between 1.2 to 3.7 m depth. From 4.2 m and below we see little variation with depth, indicating a slab layer motion performing the NIW. Averaged over a full inertial period, the vertically integrated mean current is about 90° to the right of the wind, i.e. consistent with a steady-state Ekman balance.

2.4 Turbulence measurements

Turbulence below the ocean surface is evaluated from data of the vertical ADCP beam, following the same general methodology as in Guerra and Thomson (2017), but with an additional processing step in which we reduce the signal of surface gravity waves.

For each depth in 0.5 m bins, variance spectra are calculated from the vertical velocity component w at 1 Hz. This is done for 0.5 hour segments with the method of Welch, using windows of 1200 samples with 50% overlap. We obtain energy spectra P_{ww} for the total vertical velocity that includes the orbital motion of surface gravity waves.

The ADCP is equipped with a pressure sensor sampling at 1 Hz, and this is used in a multi-step process to remove the wave orbital motion from the vertical velocity spectrum. First, the variance spectrum is calculated in the same manner as the vertical velocity spectrum, and is converted to a surface energy spectrum P_{aa}

$$P_{aa}(\omega) = P_{pp}(\omega)[\rho g \Gamma(\omega, z)]^{-2} \tag{4}$$

where P_{pp} is the pressure spectrum recorded at depth z, g is the acceleration due to gravity and $\Gamma(\omega, z)$ is the function that transforms the pressure due to wave motion recorded at depth z to the wave amplitude at the surface for each angular frequency ω,

$$\Gamma(\omega, z) = \frac{cosh\ \ k(\omega)(z + D)}{cosh\ \ k(\omega)D}, \tag{5}$$

where D is the water depth and $k(\omega)$is the wave number as calculated from the nonlinear dispersion relation for finite depth

$$\omega^2 = gk \tanh\ kD\,. \tag{6}$$

Second, from P_{aa} calculated in (4), an idealized wave spectrum is fit to the data to limit high frequency noise in the observations. Taking the peak frequency ω_p of P_{aa}, the Pierson-Moskowitz spectrum for the wind sea is calculated as

$$P_{aa}^{PM}(\omega) = \alpha g^2 \omega^{-5} e^{-\beta(\frac{\omega_p}{\omega})^4}, \tag{7}$$

using the coefficients $\alpha = 8.1e-3$ and $\beta = 0.74$ [35].

Next, the wave amplitude variance spectrum is again transferred to a vertical velocity variance spectrum for the wave motion as function of depth z:

$$P_{ww}^{wave}(\omega, z) = P_{aa}^{PM}(\omega)[\omega \Gamma(\omega, z)]^2 \tag{8}$$

Finally, the estimated wave spectra are subtracted from the total vertical velocity spectra to provide energy spectra for only the turbulent velocity component P

$$P(\omega, z) = P_{ww}(\omega, z) - P_{ww}^{wave}(\omega, z)\,. \tag{9}$$

An example of the resulting spectra for P and P_{ww} are shown in Figure 4, over a range of depths and averaged over the experiment duration. The energy spectra are shown in terms of frequency f where this is related to the angular frequency by $\omega = 2\pi f$. In

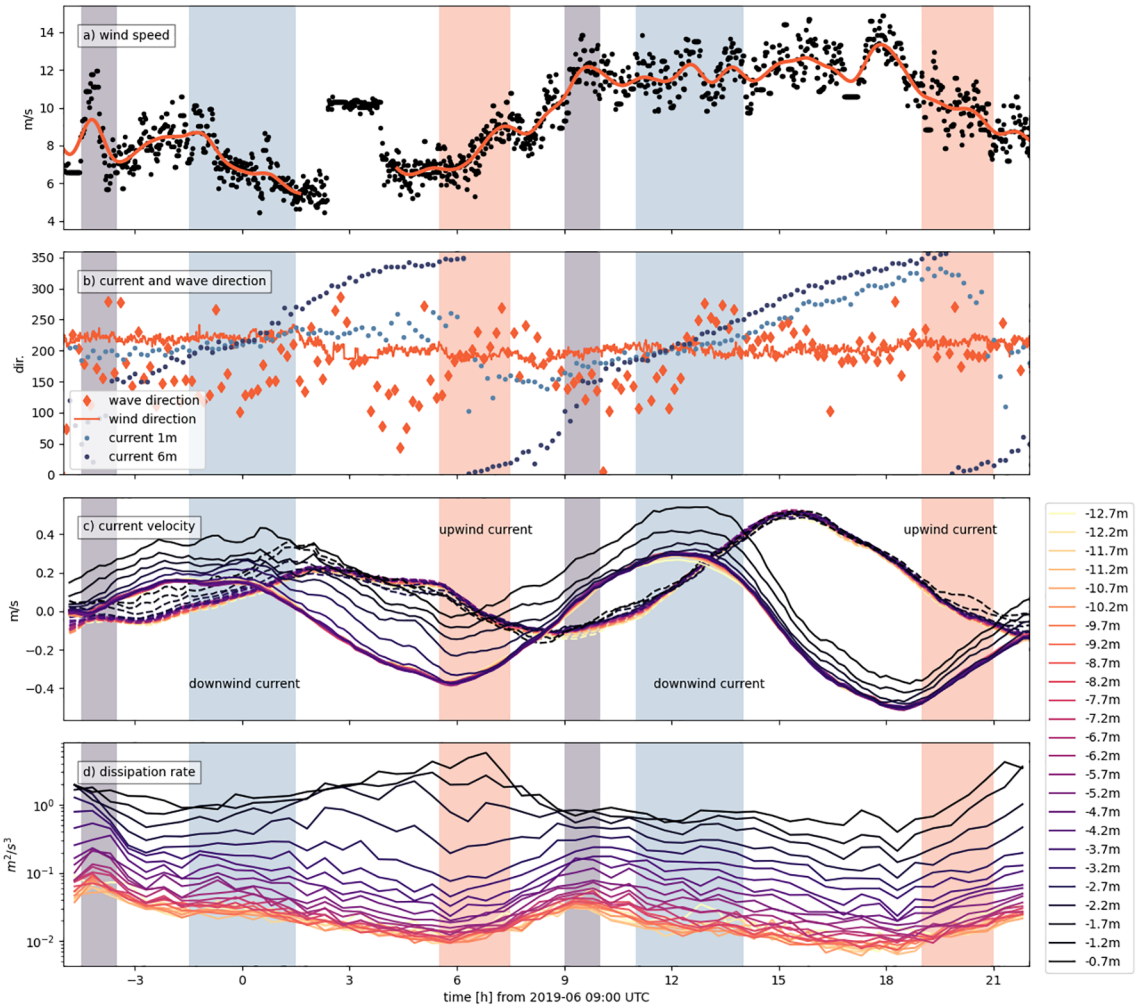

FIGURE 3
Time series of **(A)** wind speed from ship mast (dots) and low-pass filtered (line) **(B)** current, wave and wind directions, **(C)** current velocity in along-wind (solid lines) and cross-wind (dashed lines) components as function of depth, and **(D)** turbulent kinetic dissipation as function of depth. The shaded areas indicate downwind current phase (blue), upwind current phase (red) and 3 hours after upwind phase (grey).

practice, P is not entirely free of the surface gravity waves, but the steps above reduced the wave signal particularly for the energy spectra close to the surface.

A frequency range from $f_{min} = 0.2 \quad Hz$ to $f_{max} = 0.4 \quad Hz$ in the velocity spectra P in Figure 4 is identified that fulfills the property of the turbulent inertial sub-range where $P \propto f^{5/3}$ (Sreenivasan, 1995). We use the same method as [12] to calculate the dissipation rate of TKE, ϵ, from the equation

$$\epsilon = \frac{\overline{P(f) f^{5/3} \int_{f_{min}}^{f_{max}}}^{3/2}}{\alpha_\epsilon^{2/3} (\bar{u}/2\pi)} \tag{10}$$

where $\alpha_\epsilon = 0.69$ is used (Sreenivasan, 1995).

The turbulent dissipation rates are computed at 30 minute intervals at each 0.5 m depth bin. These are presented as time series in Figure 3D. The data shows that dissipation near the surface is associated with the upwind phase of the NIW. Below 3 m depth however, maximum dissipation occurs 3 hours after the surface maximum.

3 Results

3.1 Time averaged current and inertial oscillation

On average – evaluating trajectories in Figure 1 after a full inertial period – we observe downwind current velocities at the surface and a current approx. 90° to the right of the wind for the OSBL current in the Ekman layer. This is coherent with classic Ekman theory, however not with analytical solutions that require constant eddy viscosity (i.e. surface velocities at 45° to the wind). The exact direction of the interfacial surface current depends on the eddy diffusivity profile, and common solutions (e.g. Eq. 1) do not include a wave-enhanced friction layer above z_0. Looking at current directions at the roughness length $z_0 = 0.6H_s$ (Terray et al., 1996) at approx. 1.7-2.2 m in Figure 1B, we come very close to the 45° solution for classic Ekman current. The current direction at z_0 indicates the start of a constant-flux layer.

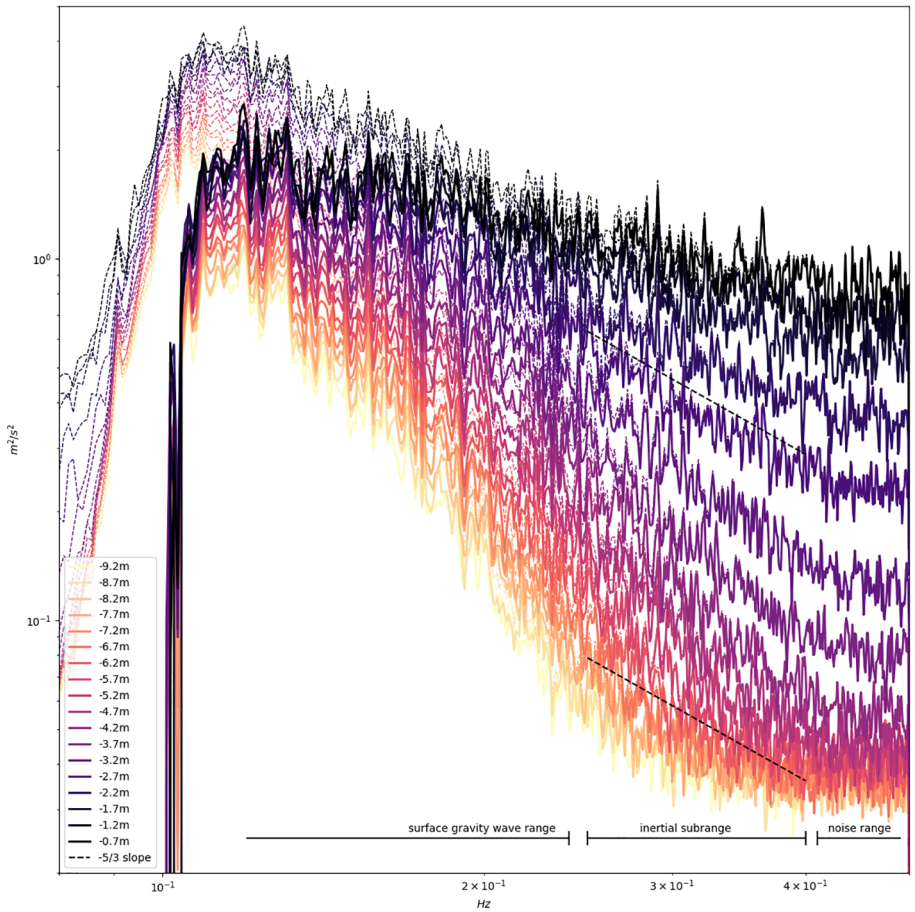

FIGURE 4
Variance spectra of vertical velocities obtained from ADCP measurements sampling at 1 Hz, for various depths below the ocean surface. The dashed lines show energy spectra obtained directly from ADCP currents. Solid lines show energy spectra where the surface gravity wave spectra is subtracted as inferred from the pressure signal at the ADCP sensor.

The direct wind-driven current at 0.7 m depth consists of a downwind current of about 0.3 m/s, superposed with the inertial current imposed by the Ekman layer. This average velocity is obtained from the total distance over two inertial periods in Fig. reffig:progvectorb. Hence the direct-wind driven current is 3% of the wind speed, consistent with the general rule of thumb for wind drift that can be reasoned by the square root of the density ratio between air and water (Wagner et al., 2022) and empirical results from spectral admittance between wind and surface currents (Röhrs and Christensen, 2015).

3.2 Vertical shear

A remarkable insight of the trajectory array in Figure 1B is that the transition between the direct wind-driven current at 0.7 m depth and the shear-free oscillating surface boundary layer current of the Ekman layer occurs over a very confined interval. At 4.2 m, this transition is completed and all deeper trajectories in Figure 1B follow a nearly identical path.

To identify dynamical regimes in these distinct layers, we evaluate a series of profiles at various time steps (Figure 5). All profiles exhibit a logarithmic velocity range $z_0 < z < z_f$, corresponding to a constant-flux layer (Eq. 1). We mark z_f as the lower range of this layer, which is at $\approx$ 4 m. Below z_f the velocity shear is negligible and the OSBL has characteristics consistent with a slab layer model (D'Asaro, 1985).

A constant flux layer is also identifiable in estimated TKE dissipation profiles, shown in Figure 6. The LOW dissipation (Eq. 3) and wave-enhanced dissipation [from Eq. 10 in (Sutherland and Melville, 2015)] are shown in black. The transition between constant ϵ near the surface (friction layer) and the power law decay of ϵ occurs at the depth $z_0 = 0.6H_s$, which is the same as for the velocity profiles. The decay of ϵ is well described by Eq.3 for the lower part of the constant-flux layer where $\epsilon \propto z^{-1}$. Closer to z_0, we see some wave-enhancement such that $\epsilon \approx z^{\lambda}$ with $-1 > \lambda > -3$.

We identified three unique dynamic regimes: i) a wave-enhanced friction layer with constant dissipation and nearly constant current, ii) a near constant-flux layer below z_0, with logarithmic current profile and $\epsilon \propto z^{-n}$, and iii) an inertial Ekman layer with slab-like motion performing a NIW with no vertical shear below a depth $z_f \approx 4$ m. The data reveal a clear distinction between these layers in terms of velocity shear and dissipation.

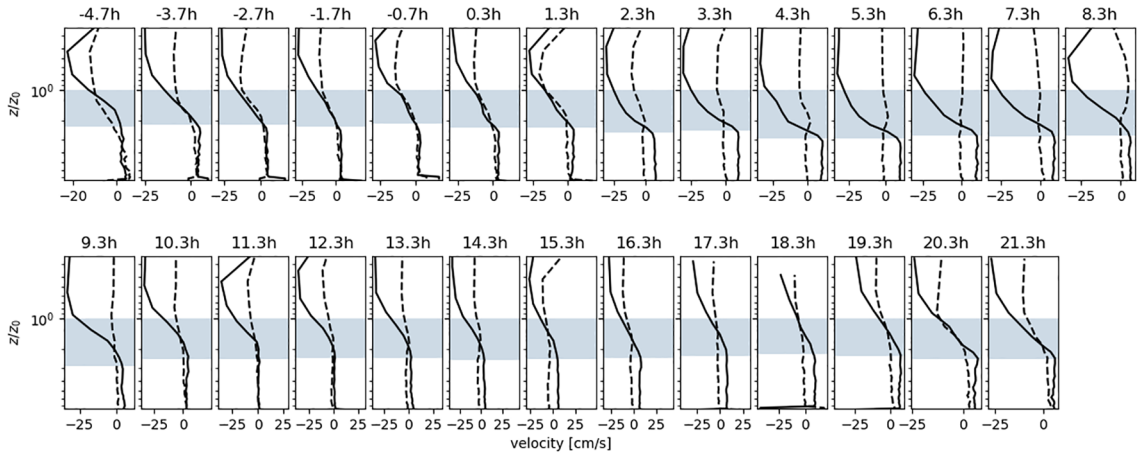

FIGURE 5
Velocity profiles on hourly intervals for eastern (dashed) and northern (solid lines) components. Shading marks the interval between z0 and zf, interpreted as constant-flux layer.

3.3 TKE from wave breaking

Surface gravity waves and the dissipation through white capping have signification implications for the OSBL (D'Asaro, 2014). Breaking waves induce TKE in the uppermost part of the OSBL, possibly explaining the observed pulses in TKE dissipation.

In Appendix A Figure A.1 we establish that the wave field during the experiment is considerably modified by the NIW,

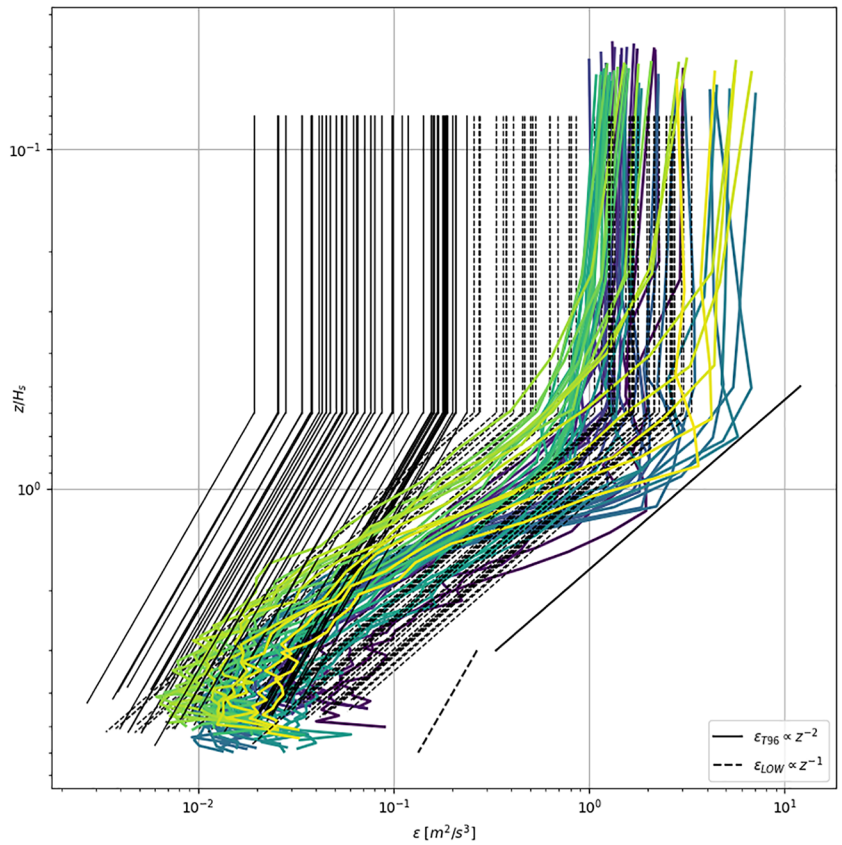

FIGURE 6
Vertical profiles of turbulent kinetic energy dissipation as obtained from vertical velocity observations. Dissipation ϵ_{LOW} as derived from wind speed and Eq. 3 is shown in black solid lines, starting at z_0 = 0.6Hs. Dashed lines use wave dissipation measurements F_{ds} (appendix A) and Eq. 10 in Sutherland and Melville (2015) to estimate ϵ as in Terray et al. (1996) for a wave-enhanced turbulence.

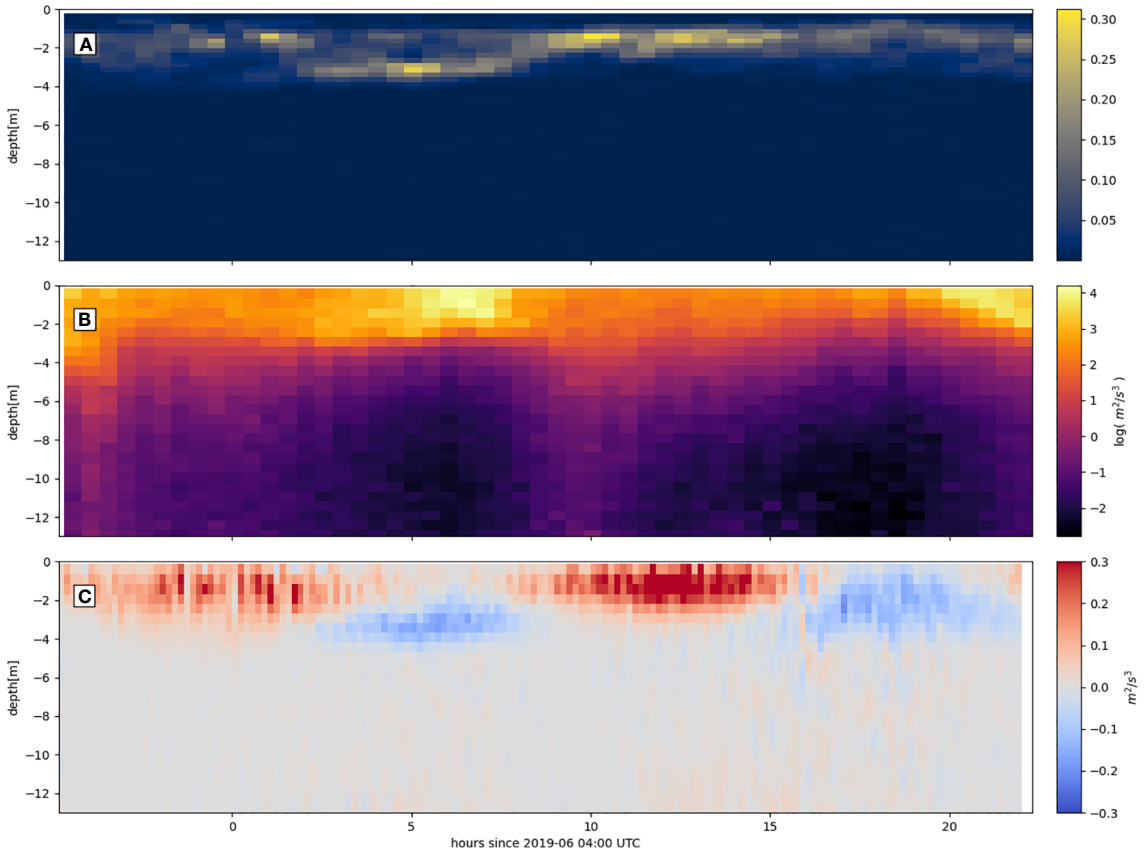

FIGURE 7

(A) Hov-Möller diagram of total vertical shear of horizontal current $\frac{\partial u_x}{\partial z}^2 + \frac{\partial u_y}{\partial z}^2$. **(B)** TKE dissipation rate based on same data is displayed in Figure 3D, referred to depth below surface. **(C)** Work exerted by shear stress on current below scaled as $W \times \rho$, as defined in Eq. 13.

causing steepening of waves during the upwind phase of the NIW. Hence we expect that increased surface wave dissipation causes pulses of TKE when the current opposes the wave propagation direction, provided that the NIW is strong enough to exceed a critical wave steepness. During the second cycle of opposing currents at t=18 h, the effective current alters the wave field enough to cause steepening of the shorter waves and associated wave breaking. In fact, we see peaks in TKE dissipation near the surface (Figure 3D), but only up to a depth $\approx z_0$.

The NIW may extract energy from the wave field at intervals of the inertial period. However, the increased TKE dissipation above z_0 does not extend into the constant flux layer. Below z_0, TKE dissipation peaks at a later time (t=-4h,9h,22h) that is not associated to changes in the surface wave field.

3.4 Vertical momentum transfer and time-dependent dissipation

Pulses of TKE dissipation above z_0 coincides with the upwind phase of the NIW as a consequence of increased relative wind stress and surface wave breaking. The TKE maxima below z_0 occur after the surface pulses, but not as a downward propagation of the surface signal. Instead, new peaks develop 3 hours after the surface peak. Figures 7A, B shows the total vertical shear and TKE dissipation as function of time and depth. With little shear below a depth of $z_f \approx 4$ m, we conclude that dissipation at depth is not primarily driven by shear production.

Assuming horizontally homogeneous flow and no stratification, the momentum equation is given by

$$\frac{\partial}{\partial t} u + 2\Omega \times u = -\frac{1}{\rho}\frac{\partial}{\partial z}\tau \tag{11}$$

where u is the velocity vector, τ is the stress vector, and Ω is the Earth's rotation vector. Taking the dot product of Eq. 11 with u yields an equation for the total kinetic energy:

$$\frac{1}{2}\frac{\partial}{\partial t}(u^2) = -\frac{1}{\rho}\frac{\partial}{\partial z}(\tau \cdot u) + \frac{1}{\rho}\tau\frac{\partial u}{\partial z}. \tag{12}$$

The terms on the right hand side represent a transport of energy and dissipation of energy, respectively. Vertical integration of Eq. 12 between depth intervals yields the total energy content in finite layers, and the first term on the right-hand-side becomes the work that is exerted by the stress τ on the velocity of the layer below:

$$W(z) = \frac{1}{\rho}\tau \cdot u, \tag{13}$$

which is evaluated at observed depths intervals shown in Figure 7C. The work of the vertical shear stress on the current of the constant flux layer is strongest positive during the downwind phase of the NIW, accelerating surface currents. During the upwind phase, the current in the constant-flux layer is decelerated. Maximum dissipation in the Ekman layer coincides with the transition from deceleration to acceleration of the current at -4h, 9h, and 22h. In these moments, current at all depths rapidly realigns in direction, as seen by the current direction at 6m depth changing quickly at $t = 9h$ (Figure 3B).

As evident from the drifter trajectories (Figure 1) and current directions (Figure 3B), particles spend considerably less time in the motion against the mean current and the strong mixing accomplishes a quick transition through this part of the NIW. It is not clear what causes this additional mixing, having excluded both shear production and surface wave dissipation. Possible reasons could be breaking of internal wave energy at the base of the mixed layer or horizontal advection of TKE, but our measurements do not provide information on these processes.

The timing of dissipation at depth in Figure 7B supports the steady state mean current by decelerating inertial currents when they are opposite to the steady state solution. The presented measurements represent the case when the mean current is directed to the right of the wind, i.e. is near a steady state balance. In the opposite case, provided that mixing at depth remains strongest when the NIW is in a phase with instantaneous currents opposite to the time-mean current, the result would be downward mixing of to-the-right-of-the-wind momentum and hence working *towards* the steady state.

4 Summary and discussion

We demonstrate the feasibility and limitations for TKE observations near the surface using a 5-beam ADCP. The observed TKE spectra exhibit strong signatures from surface gravity waves (Figure 4), and from the data it is obvious that the processing step by Eq. (9) does not succeed to remove the entire contribution from waves at low frequencies near 0.1 Hz. Due to the low sampling ratio (1 Hz) compared to turbulence observations from shear probes we also see a high noise level for frequencies above 0.4 Hz, reaching down to 0.3 Hz for depths below 4m.

The TKE dissipation signal is very strong near the surface, allowing us to estimate dissipation from 1 Hz samples in the presence of waves. This works sufficiently well near the surface in the range between 0.25 - 0.4 Hz, however below 6 m depth we suspect that noise and waves cause an overestimation of ϵ.

Despite the uncertainties of the turbulence measurements, we see a time variation at any level that is coherent with the phase of the NIW (Figure 3E). We also see a clear depth dependence throughout time that corresponds to a constant flux level with some wave enhancement (Figure 6).

The existence of a clear wave-enhanced friction layer above the constant-flux layer, as expressed by constant ϵ above z_0 in Figure 6 and in previous studies (Terray et al., 1996; Sutherland and Melville, 2015), strongly supports the concept of a roughness length z_0 that separates a friction layer from a constant-flux layer. Momentum injections from breaking waves, interruption of the air-sea interface and bubble entrainment maintain the excess momentum and energy above z_0, forcing current velocities to go straight downwind as seen in currents and drifter velocities of the uppermost observations (Figure 1).

The $\epsilon \propto z^{-2}$ dependency in the upper part of the constant flux layer (Figure 6) is indicative of wave breaking at the surface (Craig and Banner, 1994). Further below, energy from breaking waves ceases, and shear production becomes the only source of turbulence. Hence the $\epsilon \propto z^{-1}$ dissipation regime is first realized at sufficient distance from the surface. The vertical integral of the total Ekman layer being fixed at 90° or slightly more accounting for wave-current interaction (Lewis and Belcher, 2004), the overall shear in the boundary layer is fixed. With stronger shear near the surface, shear in the lower parts of the mixed layer must be lower. This could confine the lower base of the constant flux layer to a finite depth, $z_f \approx 4$ m in our case.

Stratification is not a plausible cause for the distinction of the observed layers. At wind speeds of 10 m/s and wave heights above 2 m, a pycnocline at 4 m or shallower is not sustainable given the wind history before and during the experiment. Other studies have reported such strong shear within the upper meters during high winds and in the absence of stratification (e.g. Laxague et al., 2018; Morey et al., 2018).

The presented velocity and TKE observations from the ADCP and surface drifters reveal a distinct separation of a wave-enhanced friction layer, a near constant flux layer with strong shear below the roughness length, and an inertial layer performing slab-like oscillations. Drifter trajectories perform loops in the NIW, whereby increased mixing at depth accomplishes a rapid transition through the phase of the NIW that opposes the steady-state current.

Data availability statement

The datasets presented in this study can be found in online repositories. The names of the repository/repositories and accession number(s) can be found below: https://doi.org/10.5281/zenodo.7390613, https://doi.org/10.5281/zenodo.7391898.

Author contributions

JR: Study concept, ADCP deployment, initial manuscript and editing. TH: Analysis of wave measurements, initial manuscript and editing. GS: Drifter deployment, initial manuscript and editing. K-FD: Drifter deployment, analysis of drifter data, analysis of wind data, initial manuscript and editing. LH: Drifter deployment, analysis of wind data. GB: ADCP deployment. KC:

Study concept, initial manuscript. All authors contributed to the article and approved the submitted version.

Funding

This study is financed by the Research Council of Norway, grant 237906 (CIRFA) and grant 300329 (EcoPulse).

Acknowledgments

We gratefully acknowledge the crew of R/V Helmer Hansen and the Norwegian Clean Seas Association for Operating Companies (NOFO) for enabling the measurement campaign in the North Sea. We would like to thank the reviewers for providing substantial comments improving this work.

Conflict of interest

The authors declare that the research was conducted in the absence of any commercial or financial relationships that could be construed as a potential conflict of interest.

The reviewer HK declared a shared affiliation with the author TH to the handling editor at the time of the review.

Publisher's note

All claims expressed in this article are solely those of the authors and do not necessarily represent those of their affiliated organizations, or those of the publisher, the editors and the reviewers. Any product that may be evaluated in this article, or claim that may be made by its manufacturer, is not guaranteed or endorsed by the publisher.

Supplementary material

The Supplementary Material for this article can be found online at: https://www.frontiersin.org/articles/10.3389/fmars.2023.1115986/full#supplementary-material

SUPPLEMENTARY VIDEO FILE

Animated drifter paths for all 3 drifter pairs, whereas each pair is deployed simultaneously. The motion of the drifters highlights the slab-type motion of the OSBL.

References

Alford, M. H. (2003). Redistribution of energy available for ocean mixing by long-range propagation of internal waves. *Nature* 423, 159–162. doi: 10.1038/nature01628

Alford, M. H., MacKinnon, J. A., Simmons, H. L., and Nash, J. D. (2016). Near-inertial internal gravity waves in the ocean. *Annu. Rev. Mar. Sci.* 8, 95–123. doi: 10.1146/annurev-marine-010814-015746

Anis, A., and Moum, J. N. (1995). Surface wave–turbulence interactions. scaling epsilon near the Sea surface. *J. Phys. Oceanogr.* 25, 2025–2045. doi: 10.1175/1520-0485(1995)025<2025:SWISNT>2.0.CO;2

Asselin, O., and Young, W. R. (2020). Penetration of wind-generated near-inertial waves into a turbulent ocean. *J. Phys. Oceanogr.* 50, 1699–1716. doi: 10.1175/JPO-D-19-0319.1

Brekke, C., Espeseth, M. M., Dagestad, K.-F., Röhrs, J., Hole, L. R., and Reigber, A. (2021). Integrated analysis of multisensor datasets and oil drift simulations–a free-floating oil experiment in the open ocean. *J. Geophys. Res.: Oceans* 126, e2020JC016499. doi: 10.1029/2020JC016499

Bretherton, F. P., Garrett, C. J. R., and Lighthill, M. J. (1968). Wavetrains in inhomogeneous moving media. proceedings of the royal society of london. series a. *Math. Phys. Sci.* 302, 529–554. doi: 10.1098/rspa.1968.0034

Craig, P. D., and Banner, M. L. (1994). Modeling wave-enhanced turbulence in the ocean surface layer. *J. Phys. Oceanogr.* 24, 2546–2559. doi: 10.1175/1520-0485(1994)024<2546:MWETIT>2.0.CO;2

D'Asaro, E. A. (1985). The energy flux from the wind to near-inertial motions in the surface mixed layer. *J. Phys. Oceanogr.* 15, 1043–1059. doi: 10.1175/1520-0485(1985)015<1043:TEFFTW>2.0.CO;2

D'Asaro, E. A. (2014). Turbulence in the upper-ocean mixed layer. *Annu. Rev. Mar. Sci.* 6, 101–115. doi: 10.1146/annurev-marine-010213-135138

Esters, L., Breivik, O., Landwehr, S., ten Doeschate, A., Sutherland, G., Christensen, K. H., et al. (2018). Turbulence scaling comparisons in the ocean surface boundary layer. *J. Geophys. Res.: Oceans* 123, 2172–2191. doi: 10.1002/2017JC013525

Gemmrich, J. (2012). Bubble-induced turbulence suppression in langmuir circulation. *Geophys. Res. Lett.* 39, L10604. doi: 10.1029/2012GL051691

Guerra, M., and Thomson, J. (2017). Turbulence measurements from five-beam acoustic Doppler current profilers. *J. Atmospheric Oceanic Technol.* 34, 1267–1284. doi: 10.1175/JTECH-D-16-0148.1

Laxague, N., Özgökmen Tamay, M., Haus Brian, K., Guillaume, N., Shcherbina, A., Sutherland, P., et al. (2018). Observations of near surface current shear help describe oceanic oil and plastic transport. *Geophys. Res. Lett.* 45, 245–249. doi: 10.1002/2017GL075891

Lewis, D., and Belcher, S. (2004). Time-dependent, coupled, ekman boundary layer solutions incorporating stokes drift. *Dynam. Atmos. Oceans* 37, 313–351. doi: 10.1016/j.dynatmoce.2003.11.001

Milani, P. M., Ling, J., and Eaton, J. K. (2021). Turbulent scalar flux in inclined jets in crossflow: counter gradient transport and deep learning modelling. *J. Fluid Mechanics* 906, A27. doi: 10.1017/jfm.2020.820

Morey, S. L., Wienders, N., Dukhovskoy, D. S., and Bourassa, M. A. (2018). Measurement characteristics of near-surface currents from ultra-thin drifters, drogued drifters, and HF radar. *Remote Sens.-Basel* 10, 1633. doi: 10.3390/rs10101633

Müller, M., Homleid, M., Ivarsson, K.-I., Koltzow, M. A. O., Lindskog, M., Midtbø, K. H., et al. (2017). AROME-MetCoOp: A Nordic convective-scale operational weather prediction model. *Weather Forecasting* 32, 609–627. doi: 10.1175/WAF-D-16-0099.1

Osborn, T. R. (1980). Estimates of the local rate of vertical diffusion from dissipation measurements. *J. Phys. Oceanogr.* 10, 83–89. doi: 10.1175/1520-0485(1980)010<0083:EOTLRO>2.0.CO;2

Rapizo, H., Babanin, A. V., Provis, D., and Rogers, W. E. (2017). Current-induced dissipation in spectral wave models. *J. Geophys. Res.: Oceans* 122, 2205–2225. doi: 10.1002/2016JC012367

Rascle, N., Ardhuin, F., and Terray, E. A. (2006). Drift and mixing under the ocean surface: A coherent one-dimensional description with application to unstratified conditions. *J. Geophys. Res.: Oceans* 111, C03016. doi: 10.1029/2005JC003004

Rogers, W. E., Babanin, A. V., and Wang, D. W. (2012). Observation-consistent input and whitecapping dissipation in a model for wind-generated surface waves: Description and simple calculations. *J. Atmospheric Oceanic Technol.* 29, 1329–1346. doi: 10.1175/JTECH-D-11-00092.1

Röhrs, J., and Christensen, K. H. (2015). Drift in the uppermost part of the ocean. *Geophy. Res. Lett.* 42, 1–8. doi: 10.1002/2015GL066733

Röhrs, J., Sutherland, G., Jeans, G., Bedington, M., Sperrevik, A. K., Dagestad, K.-F., et al. (2023). Surface currents in operational oceanography: Key applications, mechanisms, and methods. *J. Operational Oceanogr.* 16, 60–88. doi: 10.1080/1755876X.2021.1903221

Sreenivasan, K. R. (1995). On the universality of the kolmogorov constant. *Phys. Fluids* 7, 2778–2784. doi: 10.1063/1.868656

Stewart, R. H., and Joy, J. W. (1974). HF Radio measurements of surface currents. *Deep Sea Res.* 21, 1039–1049. doi: 10.1016/0011-7471(74)90066-7

Strand, K. O., Breivik, O., Pedersen, G., Vikebø, F. B., Sundby, S., and Christensen, K. H. (2020). Long-term statistics of observed bubble depth versus modeled wave dissipation. *J. Geophys. Res.: Oceans* 125, e2019JC015906. doi: 10.1029/2019JC015906

Sutherland, P., and Melville, W. K. (2015). Field measurements of surface and near-surface turbulence in the presence of breaking waves. *J. Phys. Oceanogr.* 45, 943–965. doi: 10.1175/JPO-D-14-0133.1

Sutherland, G., Ward, B., and Christensen, K. H. (2013). Wave-turbulence scaling in the ocean mixed layer. *Ocean Sci.* 9, 597–608. doi: 10.5194/os-9-597-2013

Terray, E. A., Donelan, M. A., Agrawal, Y. C., Drennan, W. M., Kahma, K. K., Williams, A. J., et al. (1996). Estimates of kinetic energy dissipation under breaking waves. *J. Phys. Oceanogr.* 26, 792–807. doi: 10.1175/1520-0485(1996)026<0792:EOKEDU>2.0.CO;2

Thomas, J., and Daniel, D. (2020). Turbulent exchanges between near-inertial waves and balanced flows. *J. Fluid Mechanics* 902, 1. doi: 10.1017/jfm.2020.510

Umlauf, L., and Burchard, H. (2003). A generic length-scale equation for geophysical turbulence models. *J. Mar. Res.* 61, 235–265. doi: 10.1357/002224003322005087

Wagner, T. J. W., Eisenman, I., Ceroli, A. M., and Constantinou, N. C. (2022). How winds and ocean currents influence the drift of floating objects. *J. Phys. Oceanogr.* 52, 907–916. doi: 10.1175/JPO-D-20-0275.1

Ward, B., Fristedt, T., Callaghan, A. H., Sutherland, G., Sanchez, X., Vialard, J., et al. (2014). The air–Sea interaction profiler (ASIP): An autonomous upwardly rising profiler for microstructure measurements in the upper ocean. *J. Atmospheric Oceanic Technol.* 31, 2246–2267. doi: 10.1175/JTECH-D-14-00010.1

Westhuysen, A. (2012). Spectral modeling of wave dissipation on negative current gradients. *Coast. Eng.* 68, 17–30. doi: 10.1016/j.coastaleng.2012.05.001

Zippel, S. F., Maksym, T., Scully, M., Sutherland, P., and Dumont, D. (2020). Measurements of enhanced near-surface turbulence under windrows. *J. Phys. Oceanogr.* 50, 197–215. doi: 10.1175/JPO-D-18-0265.1

Appendix A: surface gravity waves and wave dissipation

Information about the wave field was collected in the burst mode ADCP measurements, and the wave variance spectrum and integrated spectral parameters were computed using Nortek's OceanContour (v. 2.1.2) software. This section documents how surface gravity wave dissipation F_{ds} is obtained from these measurements, and how F_{ds} is influenced by ambient surface currents of the NIW.

The wave field evolves according to the wave action balance equation

$$\frac{\partial}{\partial t}\left(\frac{E}{\sigma}\right) + \nabla \cdot \left[(u + c_g)\frac{E}{\sigma}\right] = \frac{S}{\sigma}, \tag{14}$$

where the wave action density (E/σ) is the ratio of the wave variance density and σ, and $c_g = \partial\sigma/\partial k\frac{\mathbf{k}}{k}$ is the group velocity vector. In contrast to wave variance density, the wave action density E/σ is conserved in the presence of currents (Bretherton et al., 1968). The source terms in S represents the generation (S_{in}), non-linear wave-wave interaction (S_{nl}), and dissipation (S_{ds}) of waves in an active field, such that

$$S = S_{in} + S_{nl} + S_{ds}\,. \tag{15}$$

In spectral wave models, the source terms are parameterized according to the underlying physical mechanisms and its impact on the variance spectrum. Some studies suggest that typical S_{ds} parametrizations are not capable of representing the influence of currents (e.g. Westhuysen, 2012). Rapizo et al. (2017) suggested to add a term to one of the standard parametrizations in order to account for wave field modulations due to ambient currents. More specifically, the term considers the degree of alignment between the current the wave propagation direction. The wave dissipation term reads

$$S_{ds,r} = (1 + a_3 \times \max[-\frac{u_{wdir}k}{\omega}, 0]\frac{E}{E_T})[T_1 + T_2], \tag{16}$$

where a_3 is a calibration coefficient for the energy loss due to currents and u_{wdir} is the current speed in the wave propagation direction, which is positive for aligned waves and currents. For evaluating u_{wdir}, the "effective current" should be evaluated, which takes into account the depth of influence of the various wave components (Stewart and Joy, 1974). The maximum operator limits the formulation to apply for opposing waves and currents only. E_T represent a threshold spectral density by which waves break, and the ratio will increase the dissipation for frequencies above this level. The two terms T_1 and T_2 represent the maybe most common physical parametrizations, representing a threshold behavior of wave breaking and a cumulative effect by which short wave dissipation is induced by breaking of the longer components, respectively (Rogers et al., 2012). We used $a_3 = 5$ and additional calibration coefficients for T_1 and T_2 as proposed in (Rapizo et al., 2017). The wave dissipation F_{ds} can be derived by integrating the 1D variance spectrum (Strand et al., 2020)

$$F_{ds} = -\rho g \int_{f_0}^{f_n} S_{ds,r}\,df\,. \tag{17}$$

At the beginning of the measurement period, the sea state is considered fully developed and thus estimated using a Pierson-Moskowitz spectrum (Figure A.1). The impact of u_{wdir} on the fully developed spectrum in time, only considering the effect by opposing waves and currents and ignoring wave breaking, is shown in (Figure A.1). Here, the relative growth in wave energy E/E_0 (subscript denotes initial reference value) follows the phase of the current, as waves become steeper during opposing currents (between 6–9h and 18–22h). The wave dissipation computed from Eqs. (16), (17) is shown in Figure A.1. The parameterized wave dissipation follows the significant wave height H_s (Figure A.1), and obtain a peak during the second NIW where $S_{ds,r}$ from Eq. (16) exceeds the classical parametrization (i.e. $S_{ds} = T_1 + T_2$ from Eq. 16).

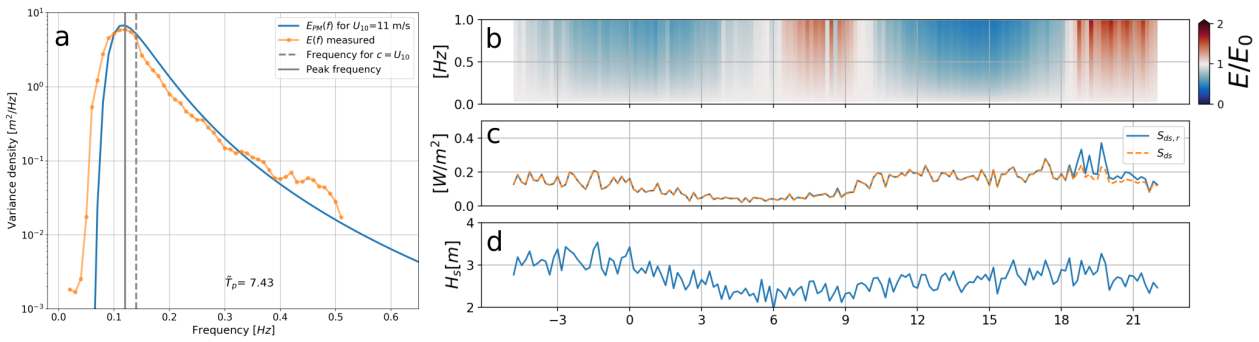

FIGURE A. 1
The impact of ambient currents on the wave field. **(A)** show the measured wave variance density spectrum at the beginning of the time series together with a computed Pierson-Moskowitz spectrum. **(B)** show the time evolution of the initial Pierson-Moskowitz spectrum in **(A)** when exposed to the effective current in the wave propagation direction uwdir. **(C)** show TKE flux computed from the measured 1D variance spectrum according to Eq. (17) for Sds,r [Eq. (16)] and without the contribution from the ambient current [Fds, i.e. a3 = 0 in Eq. (16)]. **(D)** Time series of the measured significant wave height Hs.

frontiers | Frontiers in Marine Science

TYPE Original Research
PUBLISHED 09 May 2023
DOI 10.3389/fmars.2023.1181347

OPEN ACCESS

EDITED BY
Zeng Zhou,
Hohai University, China

REVIEWED BY
Junbiao Tu,
Tongji University, China
Yunhai Li,
Ministry of Natural Resources, China

*CORRESPONDENCE
Jianrong Zhu
jrzhu@sklec.ecnu.edu.cn

RECEIVED 07 March 2023
ACCEPTED 17 April 2023
PUBLISHED 09 May 2023

CITATION
Cheng X, Zhu J and Chen S (2023) Dynamic response of water flow and sediment transport off the Yellow River mouth to tides and waves in winter. *Front. Mar. Sci.* 10:1181347. doi: 10.3389/fmars.2023.1181347

Dynamic response of water flow and sediment transport off the Yellow River mouth to tides and waves in winter

Xinyue Cheng[1,2,3], Jianrong Zhu[2]* and Shenliang Chen[2]

[1]Shanghai National Engineering Research Center of Urban Water Resources Co., Ltd., Shanghai, China, [2]State Key Laboratory of Estuarine and Coastal Research, East China Normal University, Shanghai, China, [3]College of Environmental Science and Engineering, Tongji University, Shanghai, China

Freshwater and sediments are transported from the Yellow River mouth downstream along the coast into Laizhou Bay under the northeasterly wind in winter. Numerical experiments indicate that sediment transport shows the tendency of convergence in the river mouth, divergence in the downstream area, and convergence in the north of Laizhou Bay. Tides and waves are the two main forcings affecting the transport of water and sediments off river mouths. For the high-turbidity Yellow River mouth and the adjacent sea, tidal forcing enhances the subtidal downstream transport of water and sediments off the river mouth into Laizhou Bay, whereas wave forcing has little effect on the advection of water and sediments. Sediment resuspension is controlled by the bottom shear stress induced by tides and waves. The tide-induced bottom shear stress is higher in the north of Laizhou Bay and south of Bohai Bay due to the stronger bottom tidal current. The wave-induced bottom shear stress plays a more important role in sediment resuspension, which is higher in the nearshore region along the Yellow River Delta away from the coast to some extent on account of the maximum near-bottom wave orbital velocity. Tidal mixing strengthens the upward diffusion of the bottom suspended sediments. Without tidal forcing, there is an interesting phenomenon along the Yellow River Delta. In the nearshore region, the decreased bottom shear stress suspends less sediment above the bed. However, in the offshore region, the enhanced stratification hinders the upward diffusion of the bottom sediment due to the lack of tidal mixing, resulting in higher suspended sediment concentration (SSC) in the bottom layer.

KEYWORDS

water and sediment transport, suspended sediment, bottom shear stress, tide, wave

1 Introduction

The Bohai Sea is a shallow semi-enclosed marginal sea in the West Pacific and the only inner sea in China (Figure 1). It receives about 1.5×10^{10} m^3 freshwater and 6.9×10^8 t sediment annually from the Yellow River (Cheng et al., 2021a), the second largest river in China, which is famous for its high sediment concentration. The water and sediment discharge of the Yellow River varies seasonally. Due to the frequent rainfall during the flood season (from July to October), the discharge is higher in the flood season and lower in the dry season (Wang et al., 2007; Yu et al., 2013). Approximately 30%–40% of sediments from the Yellow River are trapped in the river mouth, forming the Yellow River Delta (Li et al., 1998a), which is well known for its rapid erosion–deposition variations (Cui and Li, 2011). The Yellow River Delta and the adjacent sea are of great socioeconomic importance and are rich in biological resources, which are highly influenced by the water and sediment transport of the Yellow River (Kong et al., 2015).

The transport of water and sediments off the river mouth is influenced by river discharge, tide, wave, topography, temperature, and salinity, among others (Fettweis et al., 1998). Of these factors, data showed that wave and tidal currents are the two dominant ones affecting the transport of water and sediment, further influencing the suspended sediment concentration (SSC) in the river mouth (Chen, 2001). Wolanski et al. (1995) studied the sediment transport in the Fly River estuary and found that at least three-quarters of the sediment from the river settled in the estuary. Numerical results showed that the turbidity maximum was caused by the simultaneous influence of the baroclinic circulation and the tidal pumping, resulting in the turbidity maximum in the Fly River estuary existing only at spring tides. The vertical stratification caused by the residual baroclinic circulation driven by the along-channel density gradient plays an important role in trapping sediment in the turbidity maximum. As a result, the turbidity maximum is often located at the upstream limit of the salt intrusion (Lin and Kuo, 2001). The turbidity maximum is often accompanied by a bottom pool of easily erodible sediments, formed by further convergent sediment transport beyond the sediment capacity of the water column, which is highly variable in time and in return acts as a restoring force for the turbidity maximum location (Burchard et al., 2018).

The sediment transport shows flood and ebb variability. The eddy viscosity is higher during flood tide and lower during ebb tide in a partially mixed estuarine channel. This strong tidal asymmetry in turbulent mixing due to tidal straining induces more sediments resuspended during flood tide. As a result, there is an up-estuary pumping of sediments despite a net down-estuary advective flux (Simpson et al., 1990; Geyer, 1993; Scully and Friedrichs, 2003; Scully and Friedrichs, 2007). For fine cohesive sediments, the stronger turbulent mixing during flood tide plays a role in the breakup of aggregated flocs, resulting in the change of settling velocity (van Leussen, 1988; Traykovski et al., 2004).

There exists a shear front zone off the Yellow River mouth where sediment is accumulated as a result of the low velocity between flood and ebb (Li et al., 2001). Most of the river-laden sediments deposit inside the shear front with a high accumulation rate, while erosion is dominant outside the shear front due to the lack of sediment supply (Wang et al., 2007). Qin and Li (1983) found that about 80% of the sediments are deposited in the region less than 30 km away from the Yellow River mouth. Only less than 2% of the sediments can be transported to the Yellow Sea through the Bohai Strait (Martin et al., 1993).

Surface waves are assumed to be the major cause of sediment resuspension due to their influence on the bottom shear stress in shallow waters, especially during significant wind events (Luettich et al., 1990). Wave-induced sediment resuspension is three to five times higher than tide-induced resuspension in Upper Chesapeake Bay (Sanford, 1994). The SSC in the bottom layer increases with both wave height and wave bottom orbital velocity (Liu and Cai, 2019). Sediments are resuspended mostly during the flood tides that follow wave events during low water in the shallow waters of South San Francisco Bay. However, the strong sediment transport is a result of the non-linear interaction of wind waves and tidal currents (Brand et al., 2010).

The tidal regime off the Yellow River mouth is irregular semidiurnal tides, and the average tidal range is 0.6–1.0 m (Pang and Si, 1979). There is an amphidromic point of an M_2 tidal constituent near Dongying station, north of the current Yellow River mouth. The tidal currents are rectilinear along the Yellow River Delta and rotary in the central Bohai Sea (Li et al., 1998b; Fan and Huang, 2005). The flood current usually flows SSE, while the ebb current directs NNW around the Yellow River mouth (Fan et al., 2006). The prevailing wind in the Bohai Sea is the northerly wind with a speed of 5–10 m/s in winter and southerly wind with a lower speed of 1–3 m/s in summer influenced by the East Asian Monsoon (Bian et al., 2013). As a result, waves are stronger in winter and weaker in summer. The significant wave height and wave period are higher in the central Bohai Sea and decrease shoreward (Lv et al., 2014).

Previous studies have done a lot of work explaining the dynamics of water and sediment transport in river mouths. However, the dynamic mechanism of water and sediment transport in the Yellow River mouth and adjacent seas is little known, especially the responses to tides and waves. This paper explores the influence of tides and waves on the transport of water and sediment in the Yellow River mouth and the adjacent sea in winter using a 3D high-resolution numerical model. The detailed model description and validation are presented in *Section 2*. The results of the numerical experiments and the dynamics of water and sediment transport are analyzed in *Section 3*. The responses of water and sediment transport to tide and wave are discussed in *Section 4*. Finally, the conclusions are presented in *Section 5*.

2 Materials and methods

2.1 Numerical model

2.1.1 Hydrodynamic model

The 3D hydrodynamic numerical model was based on the ECOM-si (estuarine, coastal and ocean model, semi-implicit)

(Blumberg, 1994), which was developed from the Princeton ocean model (POM) (Blumberg and Mellor, 1987) and later improved by Zhu (2003) and Chen et al. (2004). The model adopted the "Arakawa C" grid difference scheme (Arakawa and Lamb, 1977) and the non-orthogonal curvilinear grids in the horizontal direction. In the vertical direction, the model used the σ coordinate system. The vertical eddy viscosity and diffusivity coefficients were calculated using the modified Mellor and Yamada level 2.5 turbulence closure scheme (Mellor and Yamada, 1974; Mellor and Yamada, 1982). The horizontal mixing processes were computed using the parameterization of Smagorinsky's scheme (Smagorinsky, 1963). The transport equations were solved by third-order spatial interpolation at a moderate temporal resolution coupled with a total variation diminishing (TVD) limiter (HSIMT-TVD) advection scheme to prevent numerical oscillations and reduce numerical dissipation (Wu and Zhu, 2010).

The model domain covered the entire Bohai Sea and part of the north Yellow Sea (Figure 1B). The model grid consisted of 381 × 335 cells in the horizontal dimension. To increase the accuracy and stability of the simulation, the mesh was refined near the Yellow River mouth, with a resolution of 0.3–1 km compared with 2–4 km in the outer sea. The vertical direction was divided by 10 σ layers. The model time step was variable based on the Courant, Friedrichs, and Lewyt (CFL) criterion instead of using a constant value. A wet/dry scheme describing the intertidal flat with a critical depth of 0.2 m was included in the model. The upstream river boundary was set at Lijin hydrological station, and *in situ* water and sediment discharge was set as the boundary condition. The open-sea boundary in the north Yellow Sea was driven by 16 astronomical tidal constituents—M_2, S_2, N_2, K_2, K_1, O_1, P_1, Q_1, MU_2, NU_2, T_2, L_2, $2N_2$, J_1, M_1, and OO_1—which were derived from the NaoTide dataset (http://www.miz.nao.ac.jp/). The sea surface wind field was from the European Center for Medium-Range Weather Forecast (ECMWF) reanalysis dataset with a spatial resolution of 0.125 × 0.125 and a temporal resolution of 6 h. The wave boundary conditions were calculated using the simulating waves nearshore (SWAN) model.

2.1.2 Sediment module

The sediment transport equation in the horizontal non-orthogonal curvilinear and vertical σ coordinate system can be written as:

$$\frac{\partial DJC_{sed}}{\partial t} + \frac{\partial DJ\hat{U}C_{sed}}{\partial \xi} + \frac{\partial DJ\hat{V}C_{sed}}{\partial \eta} + \frac{\partial J(\omega-\omega_{sed})C_{sed}}{\partial \sigma} = \frac{1}{D}\frac{\partial}{\partial \sigma}\left(K_h \frac{\partial JC_{sed}}{\partial \sigma}\right) + DJF_{sed} \quad (1)$$

where C_{sed} is the SSC. ω_{sed} is the sediment settling velocity, which was calculated as follows (Mehta and McAnally, 2008):

$$\omega_{sed} = \begin{cases} \omega_0 & C_{sed} \le C_{sed0} \\ \frac{m_1 C_{sed}^{n_1}}{(C_{sed}^2 + m_2^2)^{n_2}} & C_{sed} > C_{sed0} \end{cases} \quad (2)$$

where C_{sed0} is the critical sediment concentration for flocculation. According to Huang et al. (1980), C_{sed0} = 0.2 kg m^{-3}. The empirical coefficients m_1, n_1, m_2, and n_2 were set as 0.012, 2.2, 1.7, and 2.8, respectively. ω_0 is the free settling velocity.

The SSC initial condition was set as a homogeneous constant value. Ignoring the surface sediment flux, the sea surface boundary was calculated as:

$$(\omega_{sed}C_{sed} + \frac{K_v}{D}\frac{\partial C_{sed}}{\partial \sigma})|_{\sigma=0} = 0 \quad (3)$$

The sea bottom boundary was calculated as:

$$(\omega_{sed}C_{sed} + \frac{K_v}{D}\frac{\partial C_{sed}}{\partial \sigma})|_{\sigma=-1} = q_{dep} - q_{ero} \quad (4)$$

where q_{dep} and q_{ero} are the bottom sediment flux due to deposition and erosion, respectively, which can be calculated as follows (Cao and Wang, 1994):

$$q_{dep} = \begin{cases} 0, & \tau_b > \tau_d \\ \alpha' \omega_{sed} C_{sed}(1 - \frac{\tau_b}{\tau_d}), & \tau_b \le \tau_d \end{cases} \quad (5)$$

$$q_{ero} = \begin{cases} 0, & \tau_b < \tau_e \\ M(\frac{\tau_b}{\tau_e} - 1), & \tau_b \ge \tau_e \end{cases} \quad (6)$$

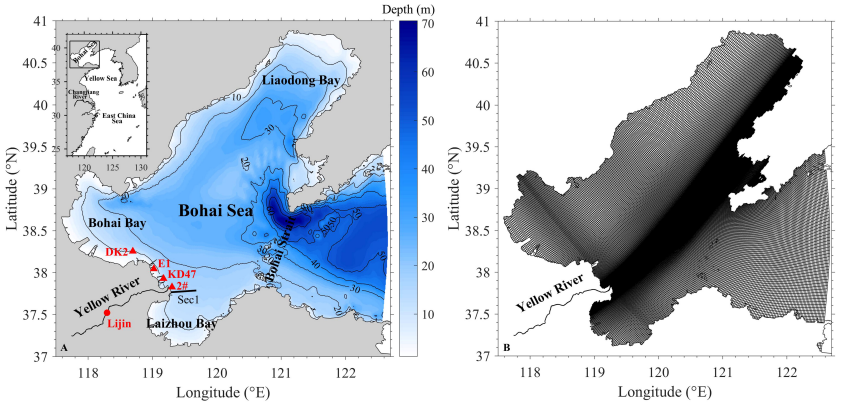

FIGURE 1
Topography of the Bohai Sea **(A)** (The black contours are the water depth (in meters), the red solid circle denotes the location of the Lijin hydrological station, and the red triangles signify the locations of the anchored ship measurement sites). The mesh of the domain **(B)**.

where τ_b is the simulated bottom shear stress; τ_e and τ_d are the critical shear stresses for erosion and deposition, respectively; a' is the deposition coefficient, which was generally set as 0.67–0.84; and M is the erosion coefficient, which generally ranged from 1×10^{-5} to 4×10^{-3} kg m^{-2} s^{-1}.

The bottom shear stress under the influence of wave–current interaction was expressed as (Liang et al., 2008):

$$\begin{aligned}\tau_b &= |\tau_{wm} + \tau_c| \\ &= \sqrt{\tau_{wm} + \tau_c|\cos \Phi_{wc}|^2 + \tau_c \sin \Phi_{wc}^2} \\ &= \tau_{wm}\sqrt{1 + 2\frac{\tau_c}{\tau_{wm}}|\cos \Phi_{wc}| + (\frac{\tau_c}{\tau_{wm}})^2}\end{aligned} \quad (7)$$

where τ_{wm} is the maximum wave bed shear stress, τ_c is the current shear stress, and Φ_{wc} is the angle between wave propagation and the current.

The algorithm for wave bed shear stress was:

$$\tau_{wm} = \frac{1}{2}\rho f_{cw} u_{bm}^2 \quad (8)$$

where p is the water density; f_{cw} is the wave fiction factor, which can be evaluated with the empirical relations according to Signell et al. (1990); and u_{bm} is the maximum near-bottom wave orbital velocity, which can be calculated as:

$$u_{bm} = \frac{0.5H\omega}{\sin hkh} \quad (9)$$

where k is the wave number; h is the water depth; $H = H_{rms} = H_s/\sqrt{2}$; $\omega = 2\pi/T$; H_s is the significant wave height; and T is the significant wave period.

The current shear stress τ_c is related to the bottom current velocity u_c:

$$\tau_c = \rho C_D u_c^2 \quad (10)$$

where C_D is the bottom drag coefficient under the influence of wave–current interaction, which was solved using an iterative procedure. Additional details about the calculation procedure can be found in Liang et al. (2008).

Critical shear stress is an important parameter for calculation of the bottom sediment flux. The equation by Dou (1999) considered the influence of sediment diameter and water depth on the sediment viscosity, which is suitable for areas with significant water depth variance. In this study, we first collected the distribution of the median particle diameter, D_{50}, and the water content, W, of the surface bed sediment in the Bohai Sea from the literature, book, and atlas (Wang, 2003; Shi, 2008; Marine Atlas of Offshore China—Marine Sediment, 2017). Subsequently, the critical shear stress for erosion, τ_e, was calculated using the equation by Dou (1999).

$$\tau_e = k^2\rho_w\left(\frac{d'}{d^*}\right)^{1/3}\left(3.6\frac{\rho_s - \rho_w}{\rho_w}gD_{50} + \left(\frac{\gamma_0}{\gamma_0^*}\right)^{5/2}\left(\frac{\epsilon_0 + gh\delta(\delta/D_{50})^{1/2}}{D_{50}}\right)\right) \quad (11)$$

In general, the parameter k was set as 0.128. The water density p_w = 1,025 kg/m^3 and the sediment density p_s = 2,650 kg/m^3. ϵ_0 is the viscosity parameter, which was usually set as 1.75, while δ is the thickness of pellicular water, which was measured as 2.31×10^{-5} cm in the laboratory. The height of roughness was d' = 0.5mm. d^* = 10mm. γ_0 is the sediment dry density, whereas γ_0^* is the stable dry density, the ratio of which represents the compaction rate of bed sediments. The value of γ_0^* referred to Han (1997). The sediment dry density was calculated as:

$$\gamma_0 = \frac{\rho_w}{W + \frac{\rho_w}{\rho_s}} \quad (12)$$

The components of bed sediments are variable in the Yellow River mouth and the adjacent sea, including grit, fine sand, silt, and clay, among others. The sediment diameter varies between 0.005 and 0.08 mm (Sun, 2013). The water content of the bed sediment is lower (50%–60%) in the north side of the current Yellow River mouth and higher (approximately 80%) in the south side. The critical shear stress for erosion along the Yellow River Delta is lower than 0.5 N/m^2, while that in the northeast side of the current Yellow River mouth is approximately 0.8 N/m^2 (Supplementary Figure S1). The critical shear stress in some areas north of Laizhou Bay is higher because these areas are dominated by fine cohesive sediment. The critical shear stress for deposition, τ_d, was calculated as (Cao and Wang, 1994):

$$\tau_d = \frac{4}{9}\tau_e \quad (13)$$

Based on the calculated critical shear stress for erosion and deposition, the model was calibrated and validated using measured and remote sensing retrieval SSC data to obtain a better distribution of critical shear stress suitable for the current Yellow River mouth and adjacent sea.

2.2 Model validation

The model has been well calibrated and verified numerous times for elevation, current velocity, and salinity in previous studies (Cheng et al., 2021a; Cheng et al., 2021b). This study further validated the model with current, salinity, SSC, and wave for the SWAN model. The following three skill assessments were used to quantify the validations: correlation coefficient (CC), root mean square error (RMSE), and skill score (SS) (Murphy, 1988; Ralston et al., 2010).

$$CC = \frac{\sum_{i=1}^{N}(X_{mod} - \bar{X}_{mod})(X_{obs} - \bar{X}_{obs})}{(\sum_{i=1}^{N}(X_{mod} - \bar{X}_{mod})^2\sum_{i=1}^{N}(X_{obs} - \bar{X}_{obs})^2)^{1/2}} \quad (14)$$

$$RMSE = (\sum_{i=1}^{N}\frac{(X_{mod} - X_{obs})^2}{N})^{1/2} \quad (15)$$

$$SS = 1 - \frac{\sum_{i=1}^{N}(X_{mod} - X_{obs})^2}{\sum_{i=1}^{N}(X_{obs} - \bar{X}_{obs})^2} \quad (16)$$

where X is the variable of interest and $\bar{X}$ is the time-averaged value. The agreement between the modeled and the observed results was assessed as follows: SS > 0.65, excellent; SS = 0.65–0.5, very good; SS = 0.5–0.2, good; and SS< 0.2, poor (Maréchal, 2004; Liu et al., 2009).

2.2.1 Current, salinity, and SSC

We used the *in situ* water velocity, salinity, and SSC data at the anchored ship stations (labeled in Figure 1) to validate the model. Site DK2 was measured from August 29 to 30, 2018; site E1 was measured from October 11 to 12, 2009; and site 2# was measured from August 6 to 7, 2017. The mean water depths at sites DK2, E1, and 2# were 9.3, 6.91, and 5.7 m, respectively.

The comparisons between the observed data and the simulated results are shown in Figure 2. At the measured site DK2, the current was rectilinear, the flood current velocity was almost the same as the ebb current velocity, and the bottom velocity was smaller than the surface velocity due to bottom friction. The salinity was approximately 30.5 at the surface layer (the first σ layer) and was 30.5 at the bottom layer (the last σ layer), with almost little temporal variation. The SSC varied with tide, with maximum values of 0.15 and 0.2 kg/m^3 at the surface and bottom, respectively. At the measured site E1, the water velocity was smaller than that of DK2 and 2# due to the artificial dams nearby. The maximum surface water velocity was only 0.6 m/s. The surface salinity was approximately 27.5 and the bottom salinity approximately 28, with a little temporal variation. The maximum SSCs were 0.12 and 0.17 kg/m^3 at the surface and bottom layers, respectively, with a downtrend. At the measured site 2#, the maximum water velocities were 0.9 and 0.6 m/s at the surface and bottom layers, respectively.

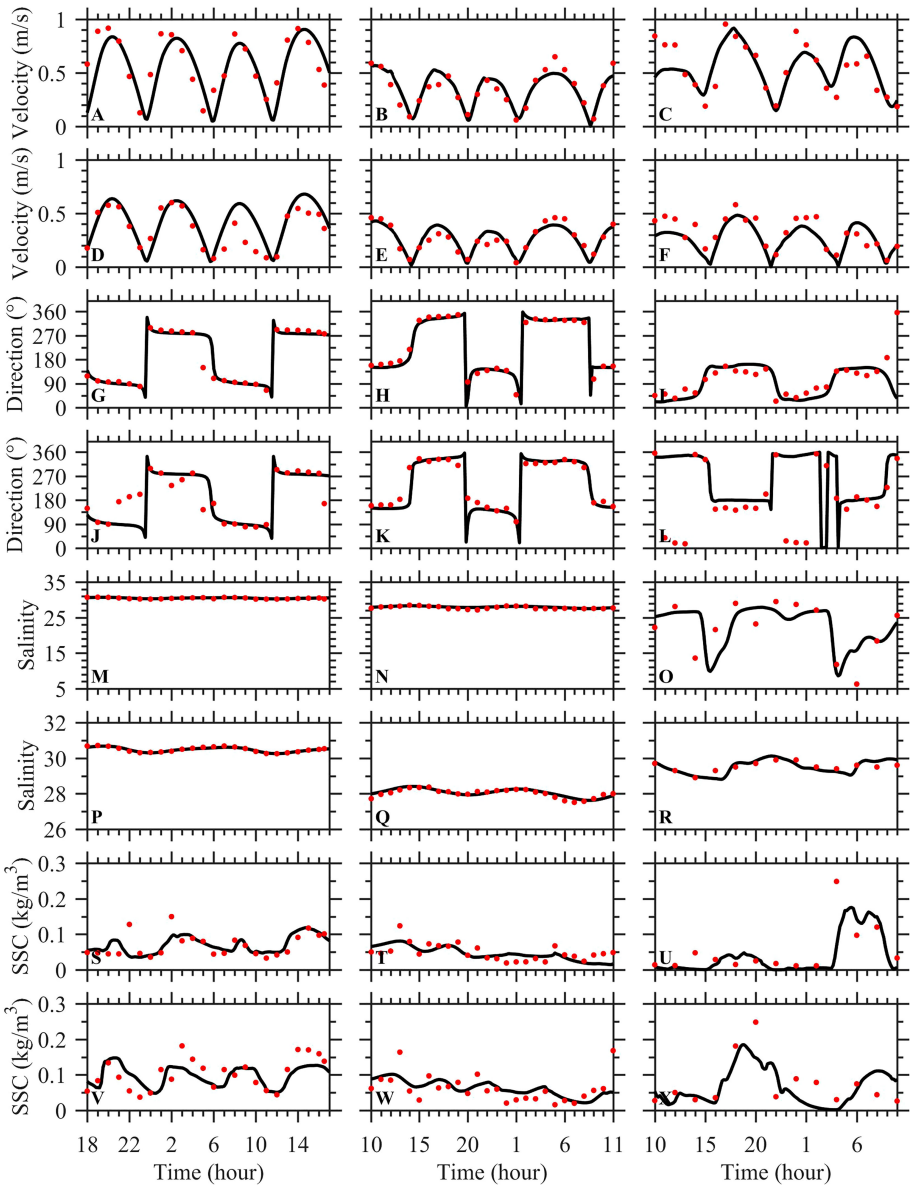

FIGURE 2
Comparisons between the observed data (*red dots*) and the simulated results (*black line*). The *left column* represents site DK2, the *middle column* represents site E1, and the *right column* represents site 2#. **(A–C)** Surface velocity. **(D–F)** Bottom velocity. **(G–I)** Surface direction. **(J–L)** Bottom direction. **(M–O)** Surface salinity. **(P–R)** Bottom salinity. **(S–U)** Surface suspended sediment concentration (SSC). **(V–X)** Bottom SSC.

The salinity had a semidiurnal variation, with a minimum 5.1 and a maximum of 29.5 at the surface layer. The maximum SSCs were 0.25 and 0.26 kg/m^3 at the surface and bottom layers, respectively.

The CC, RMSE, and SS for comparison of the modeled and the observed water velocity and salinity at the measured sites are shown in Supplementary Table S1. For water velocity, the mean CC, RMSE, and SS were 0.79, 0.14 m/s, and 0.57 for the surface water velocity; 0.84, 0.09 m/s, and 0.61 for the bottom water velocity; and 0.82, 0.12 m/s, and 0.59 for the vertically averaged water velocity, respectively. For salinity, the mean CC, RMSE, and SS were 0.76, 2.04, and 0.45 for the surface salinity; 0.88, 0.13, and 0.64 for the bottom salinity; and 0.82, 1.09, and 0.55 for the vertically averaged salinity, respectively. For SSC, the mean of these values were 0.61, 0.04 kg/m^3, and 0.31 for the surface SSC; 0.62, 0.04 kg/m^3, and 0.35 for the bottom SSC; and 0.62, 0.04 kg/m^3, and 0.33 for the vertically averaged SSC, respectively. In general, the model reproduced the processes of water current, salinity, and SSC well and can be used to study the hydrodynamics and sediment transport in the Bohai Sea.

2.2.2 Remote sensing retrieval and validation

The sea surface SSC was validated using remote sensing retrieval in winter and summer of Landsat 8 OLI (Operational Land Imager) imagery, which was downloaded from USGS (http://glovis.usgs.gov/). The remote sensing image was captured in March and August 2018 (Figure 3). Studies have shown that the spectral reflectance range of 700–900 nm in the image is more sensitive to the variation of sea surface SSC (Doxaran et al., 2002). The green or blue band combined with the near-infrared band is more suitable for the retrieval of high-turbidity water near the Yellow River mouth (Long and Pavelsky, 2013). Therefore, the SSC retrieval formula of Zhan et al. (2017) was adopted, which was given by:

$$\mathrm{SSC} = 1622.6X^3 - 3518.7X^2 + 3180.8X - 544.7 \qquad (17)$$

where the unit of SSC was milligrams per liter. $X = R_{rs}(820)/R_{rs}(490)$, where $R_{rs}(820)$ and $R_{rs}(490)$ are the sea surface spectral reflectance at 820 and 490 nm, respectively.

The remote sensing retrieval and validation of the sea surface SSC is shown in Figure 4. The sea surface SSC was higher in winter and lower in summer. In winter, the sea surface SSC was higher near the Yellow River mouth, north of Laizhou Bay, and south of Bohai Bay. The retrieval SSC corresponded to that of the remote image. In summer, the sea surface SSC was higher in the Yellow River mouth and north of Laizhou Bay, with the highest value lower than 1 kg/m^3. The simulated sea surface SSC was close to the retrieval result. The simulated high-SSC areas corresponded to the retrieval, but the magnitude of SSC was a little higher than the retrieval SSC. In general, the remote sensing retrieval and model validation results were good. Therefore, the model can be used to study the variations in SSC in the Yellow River mouth and adjacent sea.

2.2.3 Wave

The wave parameters were simulated by the SWAN model. The SWAN model was driven by the wind field 10 m off the ground downloaded from the ECMWF. The outputs of the SWAN model were significant wave height, wave period, wave direction, wave length, etc. The model was validated using the measured significant wave height and the period November 9–22, 2012 in site KD47 (labeled in Figure 1) (data from Wang, 2014). As shown in Supplementary Figure S2, the variation of the simulated significant wave height and period corresponded to the measured data. However, the simulated crest of significant wave height was lower than the measured data, which might be the result of the low time resolution of the wind data. In general, the SWAN model simulated the wave parameters well. Therefore, it is able to provide the wave boundary condition in the ECOM-si model.

2.3 Numerical experiment settings

Three numerical experiments were set to study the transport of water and sediment off the Yellow River mouth in winter and the responses to tide and wave (Supplementary Table S2). Exp 0 is the control experiment, which considered the river discharge, tide, and

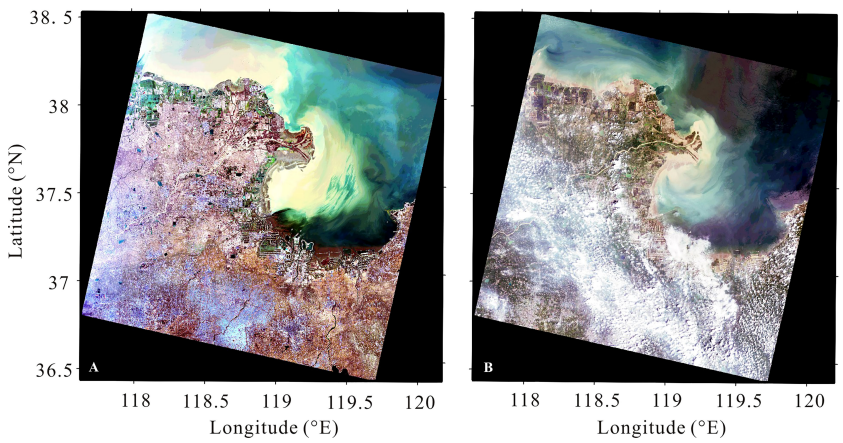

FIGURE 3
Remote sensing images of Landsat 8 OLI (Operational Land Imager) in the sea near the Yellow River mouth in March **(A)** and August **(B)** 2018.

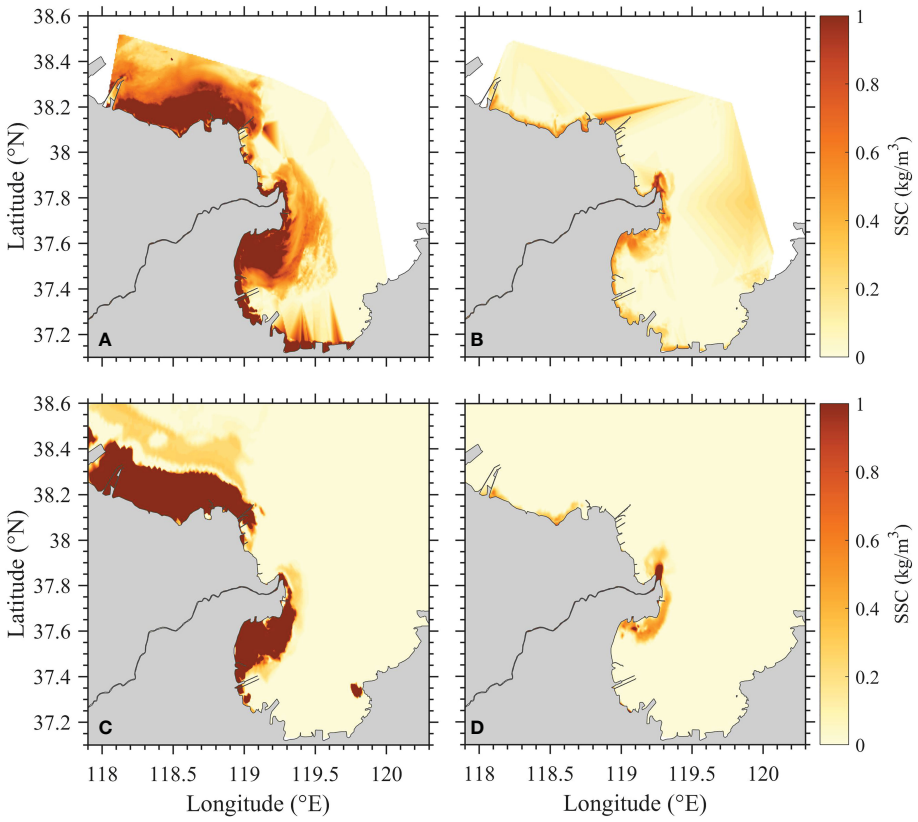

FIGURE 4
Comparisons between the remote sensing retrievals of the sea surface suspended sediment concentration (SSC) from Landsat 8 images **(A, B)** and the model results **(C, D)** in March **(A, C)** and August **(B, D)** 2018.

wave, among others. Exp 1 excluded the influence of tide in order to study its effect on the transport of water and sediment. Exp 2 excluded the influence of wave in order to study its effect by comparing with Exp 0. The model ran from January to December, and the subtidal results during spring tide in December were analyzed. The river discharge is the monthly mean data recorded in Lijin hydrological station. The wind data were from the ECMWF with a time resolution of 6 h. The wave boundary condition was the simulated result of the SWAN model. The residual sediment flux was used to represent the sediment transport in the shallow sea with tidal rise and fall. This flux was calculated as follows:

$$\overrightarrow{F_C} = \frac{1}{T}\int_0^T \int_{h_1}^{h_2} \vec{V} \cdot C_{sed} dz dt \tag{18}$$

where T is the averaged time of six tidal periods, which was approximately 3 days; h_2 and h_1 are the top and bottom depths of the water layer, respectively; C_{sed} is the SSC; and $\vec{V}$ is the horizontal velocity.

The convergence and divergence of sediment transport (condiv) was used to reflect the sediment transport condition. The formula was given by:

$$\text{condiv} = \frac{\partial uC_{sed}}{\partial x} + \frac{\partial vC_{sed}}{\partial y} \tag{19}$$

where x and y denote the east and north directions, respectively. u and v represent the velocity in the east and north directions, respectively. The variation of SSC in the water column induced by horizontal sediment transport was calculated by integrating the horizontal sediment transport term vertically. Convergence of sediment transport means that the SSC increased locally, while divergence indicates that the SSC decreased locally.

3 Results

The prevailing wind above the Bohai Sea was northeasterly during spring tide in December 2012, with values of 5–7 m/s. The northeasterly wind induced a northwestward Ekman transport. As a result, the residual water fluxes in the Bohai Sea in the surface layer were mostly westward/northwestward (Figure 5A). The freshwater off the Yellow River flowed downstream (the direction in which a Kelvin wave propagates) into Laizhou Bay, resulting in the lowest salinity value of approximately 25 in Laizhou Bay. The residual water fluxes in Laizhou Bay were lower than 0.01 m^3/s due to the weak salinity gradient. The salinity gradient was higher to the east of Laizhou Bay, which was due to the stronger residual water flux from the coast to the northwest induced by the Ekman transport. The salinity distribution in the bottom layer was close to that in the surface layer as a result of the strong vertical mixing in winter (Figure 5B).

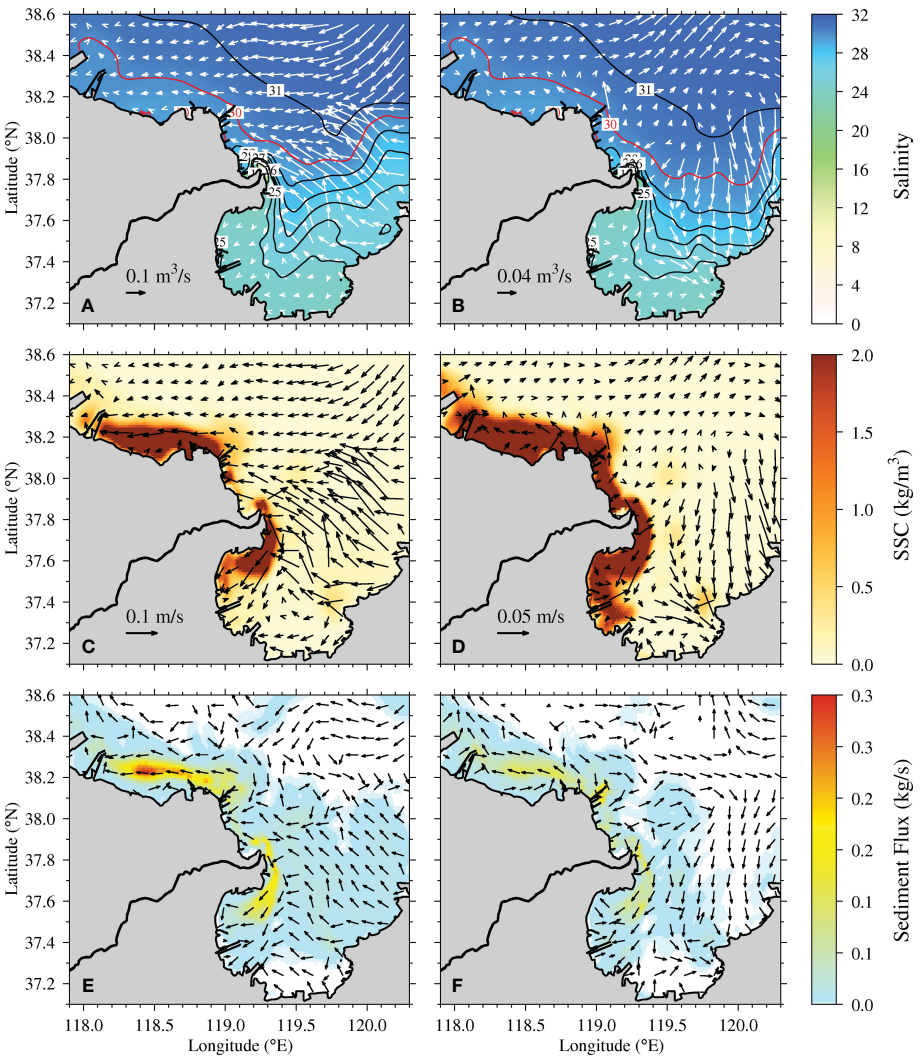

FIGURE 5
Distributions of residual unit width water flux and salinity **(A, B)**, residual water velocity and suspended sediment concentration (SSC) **(C, D)**, and residual unit width sediment flux **(E, F)** at the surface (*left panel*) and bottom (*right panel*) layers during spring tide in December 2012 in Exp 0. *Arrows* only signify direction, while *color* signifies the value of residual sediment flux in **(E)** and **(F)**.

The bottom salinity to the east of Laizhou Bay was higher than the surface layer salinity, where the bottom residual water fluxes were southward across the salinity gradient induced by the baroclinic gradient force, with values of 0.04–0.1 m^3/s. The bottom residual water fluxes in the central area of Bohai Sea were northeastward due to the compensational transport for water conservation, with values lower than 0.04 m^3/s. However, the water transport in the south of Bohai Bay and the head of Laizhou Bay was weak due to the homogeneous salinity distribution.

The strong wind in winter induced a strong wave effect along the coast. As a result, the bottom shear stress induced by wave was higher in the shallow water along the coast of the Yellow River Delta (Figure 6). The bottom shear stress induced by tide was higher in the north of Laizhou Bay and south of Bohai Bay due to the larger water velocities. The total bottom shear stress was strong along the coast of the Yellow River Delta, with maximum values in the north of Laizhou Bay and south of Bohai Bay (approximately 1 N/m^2 compared with the critical shear stress for erosion lower than 0.5 N/m^2 along the coast, as shown in Supplementary Figure S1). The total bottom shear stress suspended the bed sediment to the upper layer. As a result, the bottom SSC was higher than 2 kg/m^3 along the coast of the Yellow River Delta, whereas the surface SSC was higher in the north of Laizhou Bay and south of Bohai Bay, which corresponded to the bottom shear stress induced by tide. The directions of the residual water velocities were similar to those of the residual water fluxes (Figures 5C, D). The water from the Yellow River flowed downstream along the coast, carrying the river sediment into Laizhou Bay. The residual water velocities were 0.05–0.15 m/s, while the residual sediment fluxes were 0.15–0.2 kg/s in the surface layer downstream of the Yellow River mouth (Figure 5E). In the bottom layer, the residual water velocities and sediment fluxes were in the same direction as those in the surface layer, but were weaker than those in the surface. Therefore, the sediment sources of this area were the Yellow River and local bottom sediment resuspension. In the north side of the Yellow River mouth, the surface residual water velocities and sediment fluxes were upstream, but were a lot

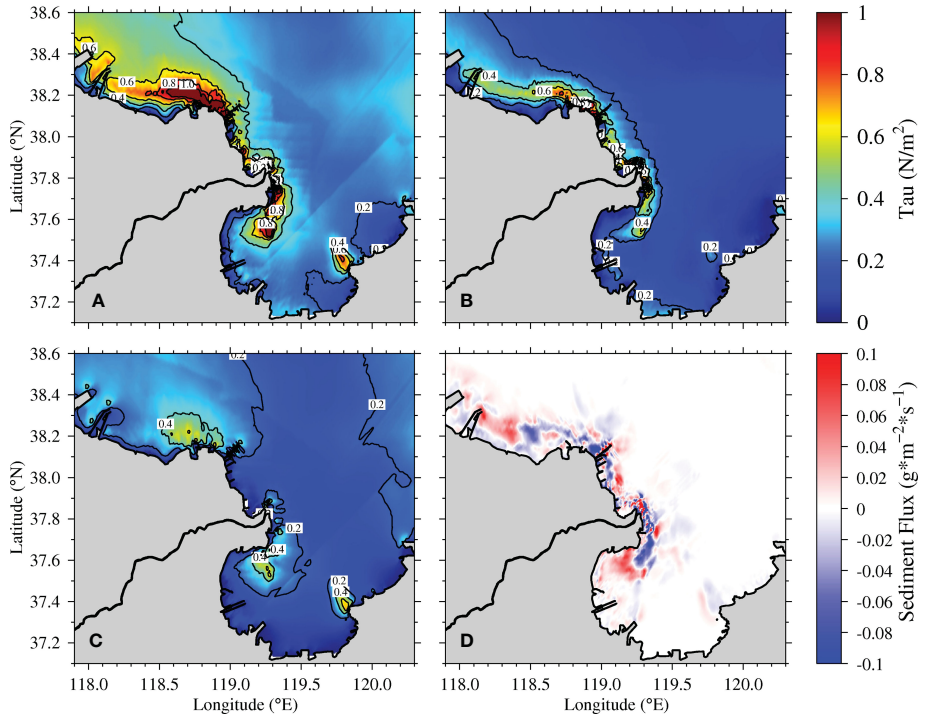

FIGURE 6
Distributions of the total bottom shear stress **(A)**, bottom shear stress induced by wave **(B)**, bottom shear stress induced by tide **(C)**, and sediment convergence and divergence **(D)** during spring tide in December 2012 in Exp 0. *Positive value* and *red color* indicate convergence, while *negative value* and *blue color* indicate divergence in **(D)**.

weaker than those south of the river mouth. Thereby, the surface SSC in the north side of the river mouth was lower than 0.5 kg/m^3. In the south of Bohai Bay, the water and sediment transport was westward. The residual water velocities ranged 0.02–0.05 m/s, while the residual sediment fluxes were 0.05–0.3 kg/s. The SSC south of Bohai Bay was higher at the bottom and lower at the surface. However, sediment transport was stronger at the surface and weaker at the bottom. The strong bottom shear stress in the south of Bohai Bay and the far distance from the river mouth suggest that the high SSC was mainly caused by local bottom sediment resuspension.

The sediment transport converged in the Yellow River mouth, with sediment fluxes of approximately 0.1 g m^{-2} s^{-1} as a result of river sediment deposition (Figure 6D). There was a divergence area east of the convergence area, indicating that part of the sediments was transported landward to the river mouth. The sediment transport was divergence downstream of the river mouth, with sediment fluxes of approximately 0.08 g m^{-2} s^{-1}, whereas in the adjacent north of Laizhou Bay, the sediment transport converged with fluxes of 0–0.06 g m^{-2} s^{-1}. It is presumable that the sediments from the Yellow River were transported downstream along the coast and mainly deposited in the north of Laizhou Bay. To the upstream of the Yellow River mouth, the sediment transport was divergence nearshore and convergence offshore, indicating that sediments were transported from the coast to the sea. In the south of Bohai Bay, the sediment transport was divergence at the east side and convergence at the west side. The residual sediment fluxes were approximately 0.04–0.06 g m^{-2} s^{-1}. The sediment transport in the south of Bohai Bay was westward, which corresponded to the diagram of the residual sediment flux (Figures 5E, F).

Sec 1 is located at the south side of the Yellow River mouth (labeled in Figure 1). The residual water currents along Sec 1 were mainly landward in the surface layer driven by the westward Ekman transport induced by the northeasterly wind. The surface residual water velocities along Sec 1 were approximately 1–8 cm/s. In the bottom layer, the along-section residual water currents were also landward due to the baroclinic gradient force. However, the velocities were much smaller than those in the surface layer, with values lower than 1 m/s. The strong landward surface currents induced an upwelling at about 28 km away from the coast and a downwelling at 10 km away from the coast, which was suggested to be the result of the convergence and divergence of the Ekman transport in the bottom boundary layer during the trapping of the river plume front (Chapman and Lentz, 1994; Wu and Wu, 2018; Cheng et al., 2021a). As for the cross-section currents, the residual water flowed downstream within 8 km away from the coast, with velocities larger than 6 cm/s. At the seaward side of Sec 1, the residual water flowed upstream in the surface layer due to the Ekman transport and downstream in the bottom layer as compensational flow across the section. The maximum cross-section water velocities were higher than 6 cm/s at the surface and lower than 4 cm/s at the bottom.

The strong wind wave in winter induced strong vertical mixing in the shallow water. As a result, the salinity was well mixed at the nearshore side of Sec 1 (Figure 7). Within 4 km away from the coast, the salinity in the surface layer was approximately 23 as a result of

10.3389/fmars.2023.1181347

the freshwater flowing downstream across Sec 1. At the seaward side of the section, the salinity was stratified in the water column due to the downstream transport of saline water in the bottom layer induced by the baroclinic gradient force, with surface salinity lower than 29 and bottom salinity close to 30. The SSC profile indicated that the high-SSC area is located 10 km away from the coast. The SSC in the water column was stratified within 5 km and mixed over 5 km away from the coast. The maximum SSC along Sec 1 was approximately 5 kg/m^3 in the near-bed layer at about 1–3 km away from the coast, decreasing upward to approximately 3–4 kg/m^3 in the surface layer. It was predictable that the nearshore high SSC was mainly derived from bottom sediment resuspension rather than along-shelf sediment transport.

The water flux and salinity flux across Sec 1 showed similar temporal variations (Figures 8A, B). The water and salt transport was mainly downstream in December 2012, especially during the early part of the month. During spring tide, the total water and salt fluxes across Sec 1 were firstly upstream, which then turned downstream, then once again diverting upstream. The maximum water flux was approximately 0.8 × 10^4 m^3/s, while the maximum salt flux was approximately 200 kg/s, both in the downstream direction. However, the sediment flux across Sec 1 was mainly in the downstream direction in December because the sediment from the Yellow River was transported downstream across the section. During spring tide, sediments were transported downstream across Sec 1 with fluxes of approximately 0–1 × 10^4 kg/s.

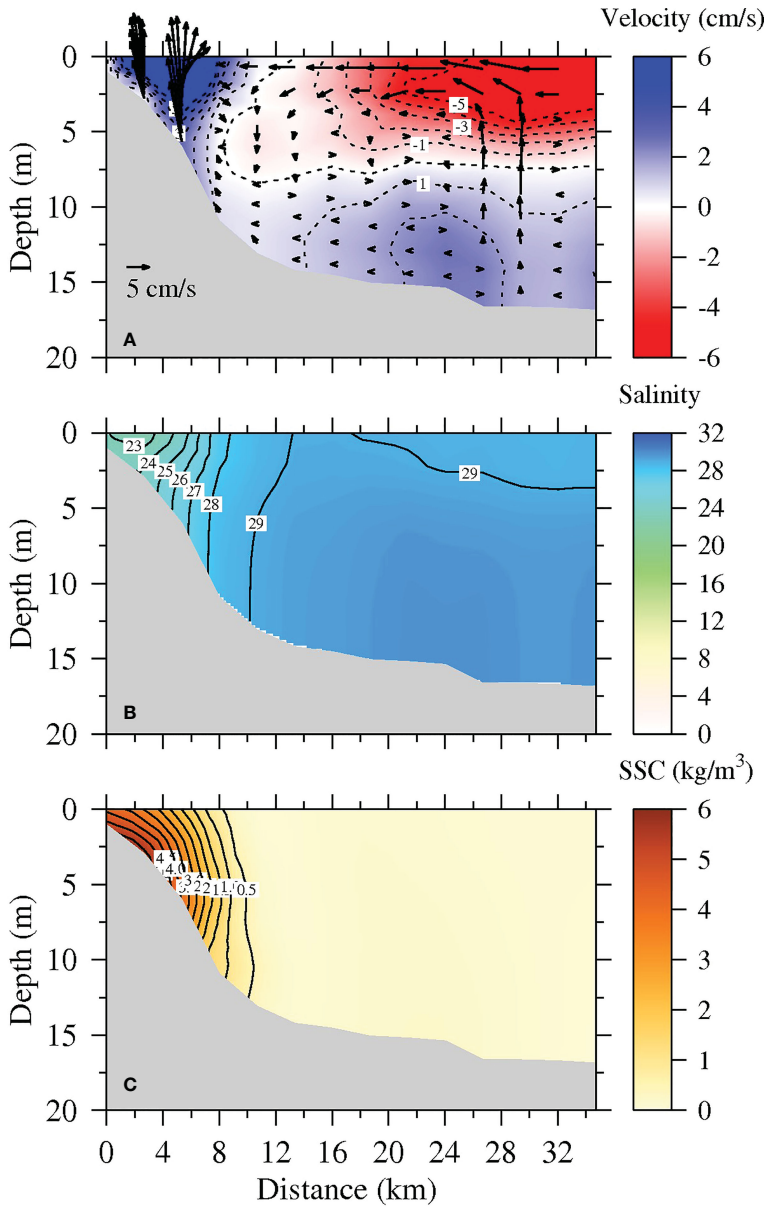

FIGURE 7
Vertical profile distributions of residual velocity **(A)**, salinity **(B)**, and suspended sediment concentration (SSC) **(C)** along Sec 1 in Exp 0 during spring tide in December 2012. *Arrows* in **(A)** denote current vectors along the section, while the *contours* signify current velocities perpendicular to the section (*positive values* indicate downstream current).

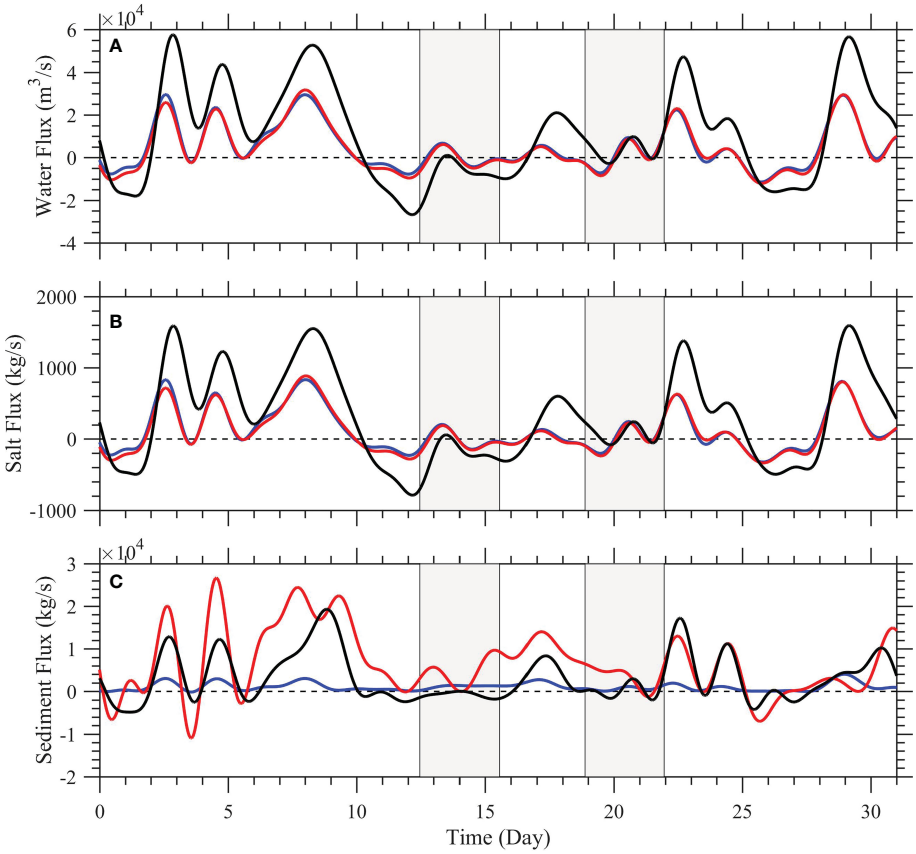

FIGURE 8
Temporal variations in water flux **(A)**, salt flux **(B)**, and sediment flux **(C)** across Sec 1 in December 2012 in Exp 0 (*red line*), Exp 1 (*black line*), and Exp 2 (*blue line*). *Positive values* indicate downstream transport, the *left shadow* indicates the duration of spring tide, and the *right shadow* indicates the duration of neap tide.

4 Discussion

4.1 The effect of tides on the transport of water flow and sediments

Exp 1 excluded tide as a driving force, and the results were compared with those of Exp 0. Without tidal forcing, the surface water currents were mainly driven by the northwestward Ekman transport induced by the northeasterly wind in winter. The residual water fluxes were larger in the central area of Bohai Sea, with values of 0.2–0.3 m^3/s, but were smaller in Laizhou Bay with values lower than 0.1 m^3/s due to the special shoreline and topography. The low-salinity water was transported upstream to some extent. However, the majority of the low-salinity water penetrated downstream along the coast due to the geostrophic adjustment. In the bottom layer, the residual water fluxes were mainly downgradient of salinity induced by the baroclinic pressure gradient. The salinity was higher than that in the surface layer, and low-salinity water was mostly transported downstream rather than upstream. The differences between Exp 0 and Exp 1 indicated the effect of tide. Tide induced downstream residual water fluxes along the coast of the Yellow River Delta in the surface layer, but northward water fluxes in the central area of Bohai Sea in the bottom layer. The salinity differences between Exp 0 and Exp 1 were positive in the surface layer near the Yellow River mouth, especially in the north side, with values of 0–3, higher in the river mouth and decreasing offshore. This was induced by the combined effect of vertical mixing and more freshwater transported downstream due to tidal forcing. As a result, the salinity differences were negative in Laizhou Bay and extended northeast along the coast in both surface and bottom layers due to the shallow depth in Laizhou Bay (Figure 9).

Without tidal forcing, the SSC decreased a lot in the surface layer, especially in the south of Bohai Bay and downstream of the Yellow River mouth (Figure 9G). The maximum SSC in the surface layer was approximately 1.5 kg/m^3 in the river mouth. In other areas along the Yellow River Delta with suspended sediments in the surface layer, the SSCs were approximately 0–1 kg/m^3. The bottom shear stress induced by wave remained unchanged, whereas the bottom shear stress induced by tide decreased approximately 0–0.5 N/m^2 in the south side of the Yellow River mouth, the east head of Laizhou Bay, and the south of Bohai Bay (Figure 10). The bottom shear stress induced by tide was lower than 0.2 N/m^2. As a result, the total bottom shear stress was 0–1 N/m^2 along the Yellow River Delta, mainly induced by wave. The lower bottom shear stress resuspended less sediment above the bed. In the bottom layer, the SSCs were higher than 2 kg/m^3 along the Yellow River Delta. There

was an interesting phenomenon along the Yellow River Delta. Compared with Exp 0, the bottom SSCs decreased in the nearshore region, but increased in the offshore region. This was because stratification hindered the upward diffusion of the bottom suspended sediment due to the lack of tidal mixing. As a result, most of the sediments can only be advected in the horizontal direction. Due to the less decreased bottom shear stress in the north of the Yellow River mouth, nearly the same amount of sediments was resuspended compared with Exp 0. Therefore, the increase in the bottom SSC was more significant. On the other hand, the bottom shear stress decreased a lot in the south of the river mouth, resulting in a large-scale SSC decrease and a localized SSC increase in the bottom layer. The sediments in the surface layer were transported upstream with fluxes of 0.05–0.1 kg/s and downstream with fluxes lower than 0.05 kg/s from the Yellow River mouth. The surface sediment fluxes in the south of Bohai Bay were westward,

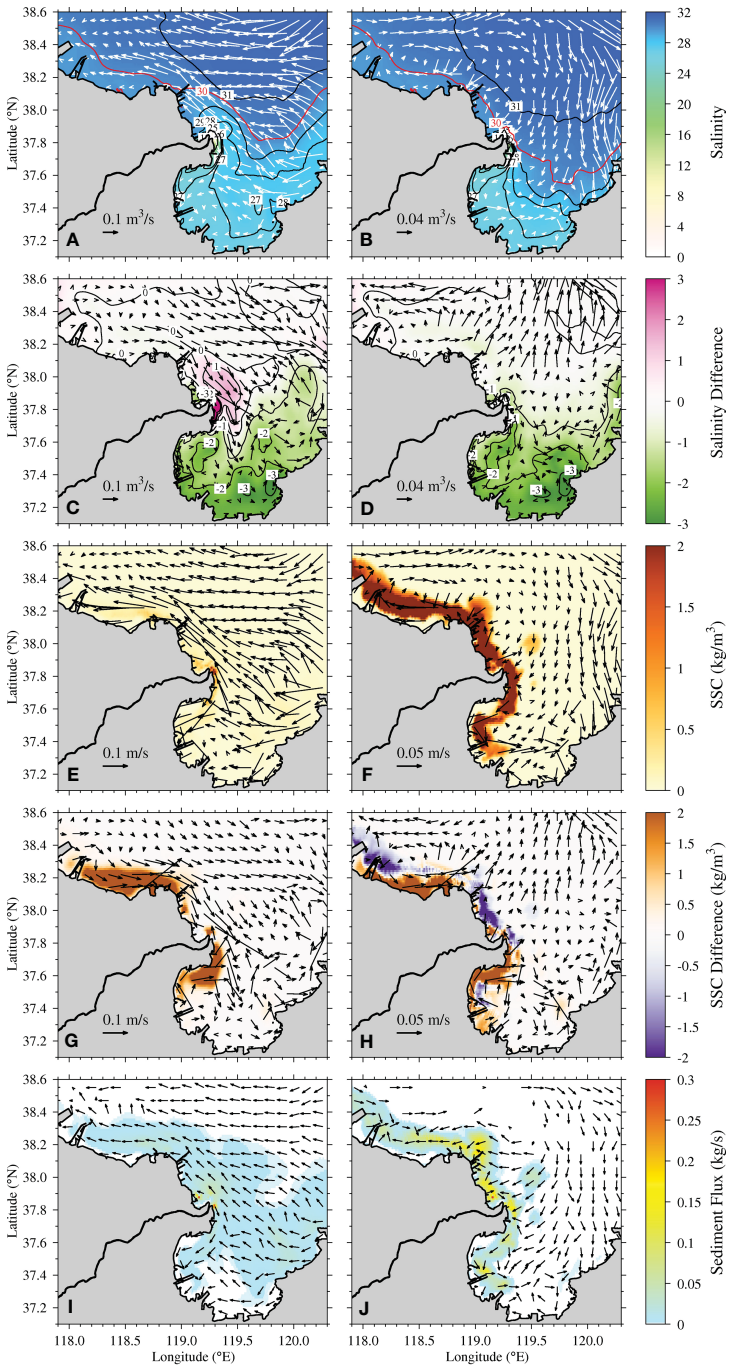

FIGURE 9
Distributions of residual unit width water flux and salinity **(A, B)**, residual water velocity and suspended sediment concentration (SSC) **(E, F)**, and residual unit width sediment flux **(I, J)** in Exp 1 and differences in residual unit width water flux and salinity **(C, D)** and residual water velocity and SSC **(G, H)** of Exp 0 (control run) – Exp 1 (without tide) at the surface (*left panel*) and bottom (*right panel*) layers during spring tide in December 2012. *Arrows* only signify direction, while *color* signifies the value of residual sediment flux in **(I)** and **(J)**.

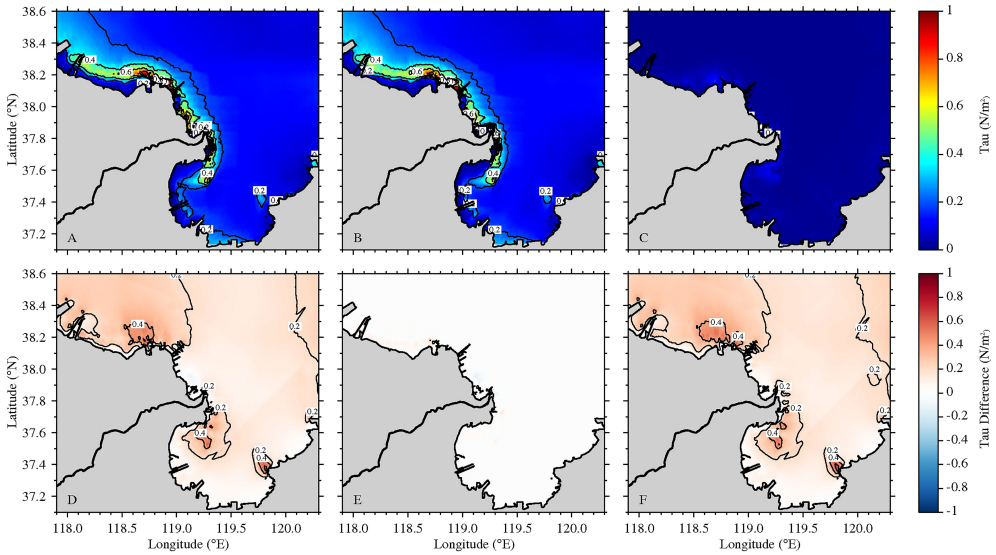

FIGURE 10
Distributions of total bottom shear stress **(A)**, bottom shear stress induced by wave **(B)**, and bottom shear stress induced by tide **(C)** in Exp 1 and differences in total bottom shear stress **(D)**, bottom shear stress induced by wave **(E)**, and bottom shear stress induced by tide **(F)** of Exp 0 (control run) – Exp 1 (without tide) during spring tide in December 2012.

with fluxes of 0–0.05 kg/s. In the bottom layer, the sediments were transported onshore in the north side of the Yellow River mouth, downstream in the northwest of Laizhou Bay, and westward in the south of Bohai Bay. More sediments were transported upstream without than with tidal forcing.

The residual water from the Yellow River mouth flowed downstream across Sec 1 in the upper layer within 7 km away from the coast, with velocities of approximately 0–8 m/s (Figure 11). Over 7 km, the residual water was transported upstream in the upper layer and downstream in the lower layer. The surface along-section currents were shoreward, with velocities of 5–8 m/s driven by the northwestward Ekman transport induced by the northeasterly wind. The bottom currents flowed onshore along Sec 1 driven by the baroclinic gradient force. The low-salinity water was transported downstream to Sec 1, forming a salinity variance of 17–31. The water column was well mixed in the surface layer due to the wave mixing and was stratified in the middle and bottom layers due to the lack of tidal mixing. The differences between Exp 0 and Exp 1 indicated the effect of tide. Tidal forcing induced more residual water transported downstream across Sec 1 within 28 km away from the coast. As a result, the salinity of Exp 0 in most areas along Sec 1, especially in the bottom layer, was lower than that of Exp 1. However, in the upper layer, the salinity of Exp 0 with tidal forcing was higher than that of Exp 1 without tidal forcing. This was caused by the mixing of bottom saline water with surface freshwater induced by tidal mixing. The salinity differences between Exp 0 and Exp 1 were approximately 0–4 in the upper layer within 26 km and from −2 to 0 in the bottom layer along Sec 1.

The SSCs along Sec 1 were approximately 0–3 kg/m^3 within 10 km away from the coast, with higher values in the bottom and declining upward. Due to the decrease of the bottom shear stress induced by tide, the SSCs of Exp 1 were reduced approximately 0–2.5 kg/m^3 compared with those of Exp 0. The reduction of SSC was highest in the middle layer at about 3 km away from the coast as a result of the lack of tidal mixing and the tide-induced sediment resuspension.

4.2 The effect of waves on the transport of water flow and sediments

Exp 2 considered the effect of tide and excluded wave forcing. The residual water velocities and fluxes were similar to those of Exp 0. Except for the central area of Bohai Sea, where wave induced a northwestward transport in the surface layer, carrying more low-salinity water from the coast to the sea. As a result, the salinity of Exp 0 was approximately 0–1 lower than that of Exp 2. The salinity differences between Exp 0 and Exp 2 were higher than 3 near the Yellow River mouth in the whole water column due to the mixing of surface freshwater with the bottom saline water induced by wave. As a result, more freshwater extended upstream and downstream, resulting in the lower salinity in the northwest side of the Yellow River mouth and in the center and northeast of Laizhou Bay (Figure 12).

Without wave forcing, the bottom shear stress induced by wave was zero (Figure 13). The reduction of the bottom shear stress was approximately 0–1 N/m^2 along the Yellow River Delta. The maximum total bottom shear stress was approximately 0.2 N/m^2 near the Yellow River mouth and on the downstream side, while it was approximately 0.4 N/m^2 in the south of Bohai Bay. The bottom shear stress induced by tide also decreased approximately 0–0.2 in the south of Bohai Bay, from the Yellow River mouth downstream to the north of Laizhou Bay, and in the east head of Laizhou Bay as a result of the change of the bottom water current. The weaker bottom shear stress resuspended less sediment above the bed. The

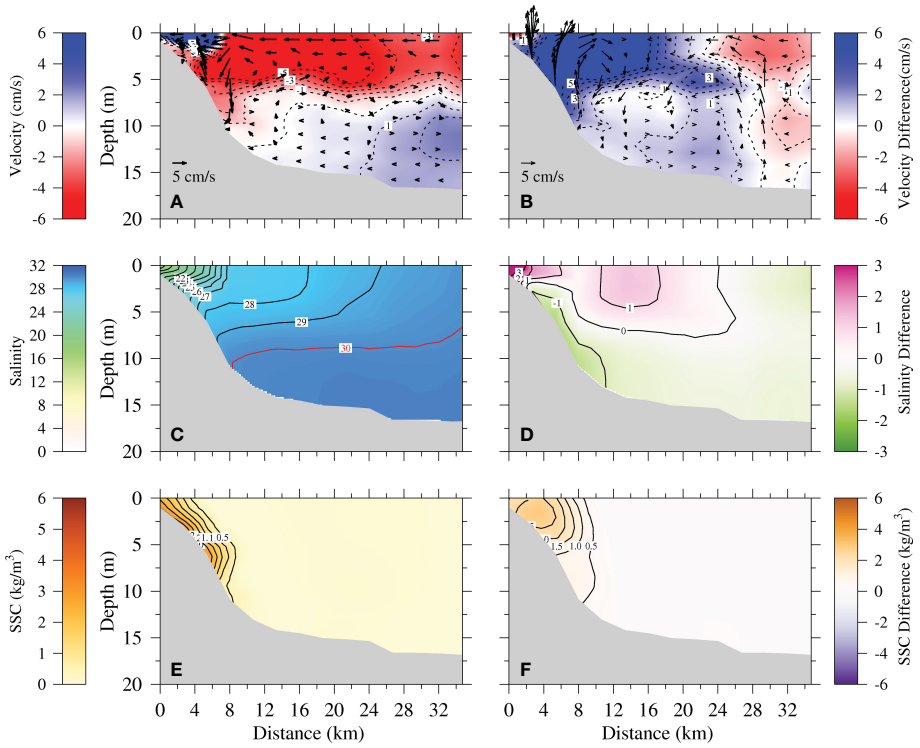

FIGURE 11
Vertical profile distributions of residual velocity **(A)**, salinity **(C)**, and suspended sediment concentration (SSC) **(E)** in Exp 1 and differences in the residual velocity **(B)**, salinity **(D)**, and SSC **(F)** in Exp 0 (control run) – Exp 1 (without tide) along Sec 1 during spring tide in December 2012. *Arrows* in **(A, B)** signify current vectors along the section, while the *contours* signify the current velocities perpendicular to the section (*positive values* indicate downstream current).

bottom SSCs decreased more than 2 kg/m^3 along the Yellow River Delta, while the surface SSCs decreased approximately 2 kg/m^3 from the Yellow River mouth downstream to the north of Laizhou Bay and in the south of Bohai Bay (Figures 12G, H). As a result, the suspended sediments were mostly in the south of Bohai Bay and from the Yellow River mouth downstream to the north of Laizhou Bay, with values of 0–1.5 kg/m^3. The surface SSC was slightly lower than the bottom SSC due to the tidal mixing enhancing the upward diffusion of the bottom suspended sediments. The reduction of the bottom shear stress in Exp 2 was several orders higher than that in Exp 1, indicating that the influence of waves in winter was stronger than that of tides.

The SSCs were low, resulting in the weak sediment transport along the Yellow River Delta. The sediments from the Yellow River mouth were transported downstream into Laizhou Bay, with the largest fluxes of 0.05 and 0.02 kg/s in the surface and bottom layers, respectively. In the south of Bohai Bay, the sediment fluxes were westward, with the largest values of 0.06 and 0.03 kg/s in the surface and bottom layers, respectively. Unlike Exp 1, the sediment fluxes in the surface layer were larger than those in the bottom layer because the surface SSCs were similar to the bottom SSCs and the surface water transport was stronger than the bottom layer.

Without tidal forcing, the sediment transport of Exp 1 was weaker than that of Exp 0, which included tidal forcing. The sediment transport converged in the Yellow River mouth due to the river sediment deposition. Part of the river sediments was transported downstream and settled north of Laizhou Bay, forming a divergence area in the south side of the river mouth and a convergence area in Laizhou Bay (Figure 14A). The downstream sediment transport weakened and the upstream sediment transport strengthened without tidal forcing compared with Exp 0. Therefore, the sediment converged in the north side of the river mouth with fluxes of 0.1 g m^{-2} s^{-1}. In the south of Bohai Bay, the coastal sediments were transported seaward and the marine sediments transported landward. As a result, the sediment transport showed a divergence–convergence–divergence pattern, with fluxes of 0–0.05 g m^{-2} s^{-1} from the coast to the sea. When tidal forcing was considered and wave forcing was excluded, the bottom shear stress decreased a lot and less sediment was suspended. As a result, the sediment transport weakened, except for the river sediment deposition in the Yellow River mouth (Figure 14B). In other areas along the Yellow River Delta, the sediment fluxes were lower than 0.06 g m^{-2} s^{-1}.

The wave induced a downstream transport of surface water within 5 km away from the coast and an upstream transport between 5 and 10 km across Sec 1 (Figure 15). Without wave forcing, the water column was well mixed in the near-shore region and stratified in the offshore area. The salinity within 8 km away from the coast was lower than that in Exp 0 with wave forcing, meaning that the surface freshwater was mixed with the bottom saline water due to the wave mixing. The water column of Sec 1 in Exp 2 was vertically more mixed than that in Exp 1, indicating that

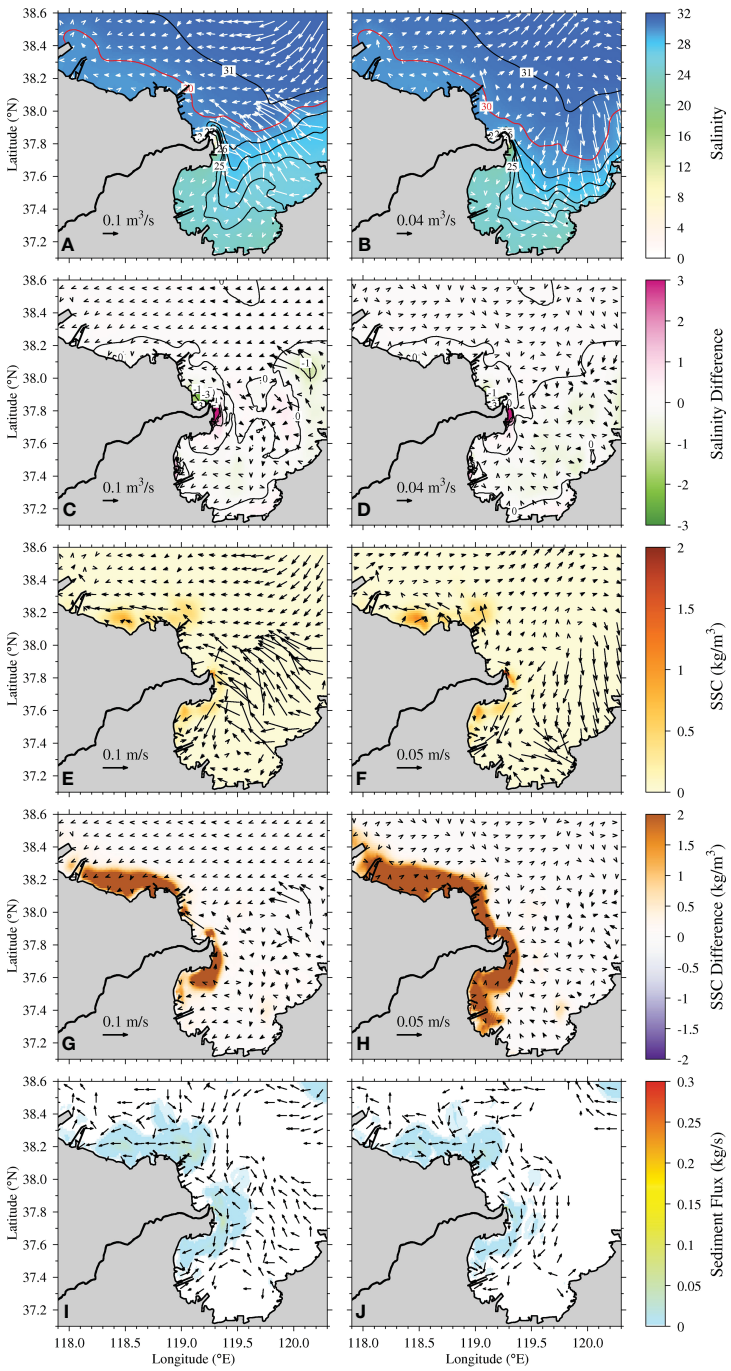

FIGURE 12
Distributions of residual unit width water flux and salinity **(A, B)**, residual water velocity and suspended sediment concentration (SSC) **(E, F)**, and residual unit width sediment flux **(I, J)** in Exp 2 and differences in residual unit width water flux and salinity **(C, D)** and residual water velocity and SSC **(G, H)** of Exp 0 (control run) – Exp 2 (without wave) at the surface (*left panel*) and bottom (*right panel*) layers during spring tide in December 2012. *Arrows* only signify direction, while *color* signifies the value of residual sediment flux in **(I)** and **(J)**.

tidal mixing was stronger than wave mixing (Figure 15C). Due to the weak bottom shear stress in the absence of wave forcing, the SSCs in Sec 1 decreased approximately 5 kg/m^3 in the nearshore bottom. In the bottom layer, the maximum residual SSC in Sec 1 was higher than 0.5 kg/m^3 and lower than 1 kg/m^3 between 2 and 7 km away from the coast (Figure 15E).

The water, salt, and sediment fluxes across Sec 1 in Exp 0, Exp 1, and Exp 2 were mainly in the downstream direction, especially in the beginning and at the end of December 2012 (Figure 8). The water and salt transport patterns with and without wave were similar. However, tidal forcing played an important role in changing the water and salt fluxes. In Exp 1, the water and salt fluxes across Sec 1 increased due to the stratification in the water column without tidal mixing. During spring tide, the net water fluxes in the upstream direction increased from 1.3×10^8 to 1.9×10^9 m^3, while the net salt fluxes increased from 5.0×10^6 to

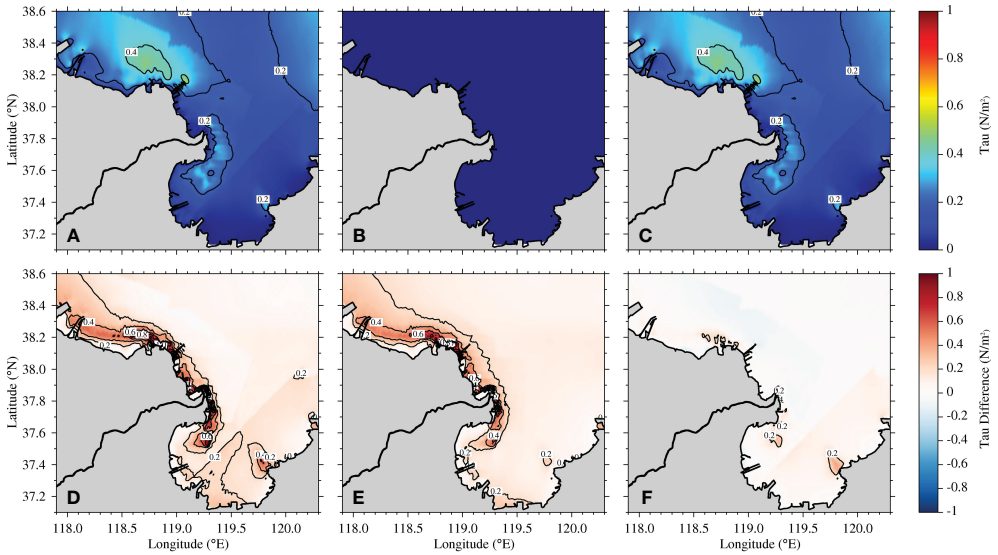

FIGURE 13
Distributions of the total bottom shear stress **(A)**, bottom shear stress induced by wave **(B)**, and bottom shear stress induced by tide **(C)** in Exp 2 and differences in total bottom shear stress **(D)**, bottom shear stress induced by wave **(E)**, and bottom shear stress induced by tide **(F)** in Exp 0 (control run) – Exp 2 (without wave) during spring tide in December 2012.

5.4×10^7 kg, both rising one order of magnitude when tidal forcing was removed from the experiment (Supplementary Table S3). On the other hand, wave forcing strengthened the net upstream transport of water and salt during spring tide. Without tidal forcing, the decreased bottom shear stress resuspended less sediment, resulting in weaker sediment transport across Sec 1. The net sediment flux across Sec 1 in Exp 0 during spring tide was 1.3×10^9 kg in the downstream direction. Without tidal forcing, the sediment flux decreased to 1.9×10^8 kg and turned in the upstream direction. Without wave forcing, the sediment transport was weaker than that without tidal forcing due to the lower bottom shear stress. Therefore, the influence of waves on sediment transport in winter was greater than that of tides. Compared with that in Exp 0, the net sediment flux across Sec 1 in Exp 2 was in the same downstream direction and was reduced to 3.7×10^8 kg during spring tide.

Waves are highly dependent on winds, which vary seasonally. In general, wind waves are stronger in winter and weaker in summer. This paper discusses the effect of waves in winter and the comparison with tides because the sediment transport and resuspension are more significant and the effect of waves is more obvious. On the other hand, the waves in summer may play a less important role in sediment transport compared to tides.

5 Conclusions

In this paper, the transport of water and sediment from the Yellow River mouth was studied and the effects of tide and wave discussed using a 3D numerical model coupled with a hydrodynamic and sediment module. The model was validated using current, salinity, measured, and remote sensing retrieval SSC data. The

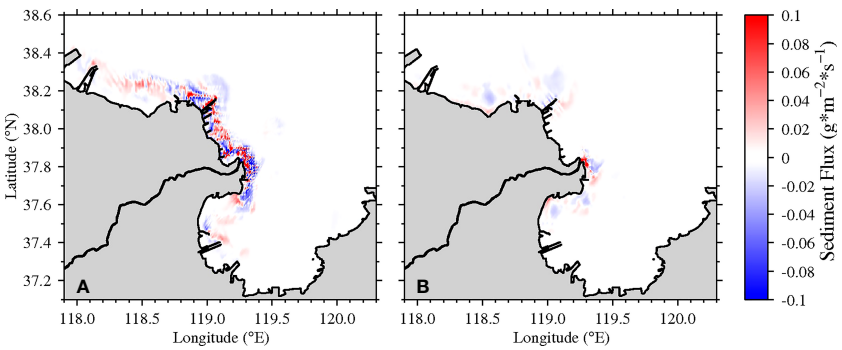

FIGURE 14
Distributions of sediment convergence and divergence during spring tide in December 2012 in Exp 1 **(A)** and Exp 2 **(B)** (*positive value* and *red color* indicate convergence, while *negative value* and *blue color* indicate divergence).

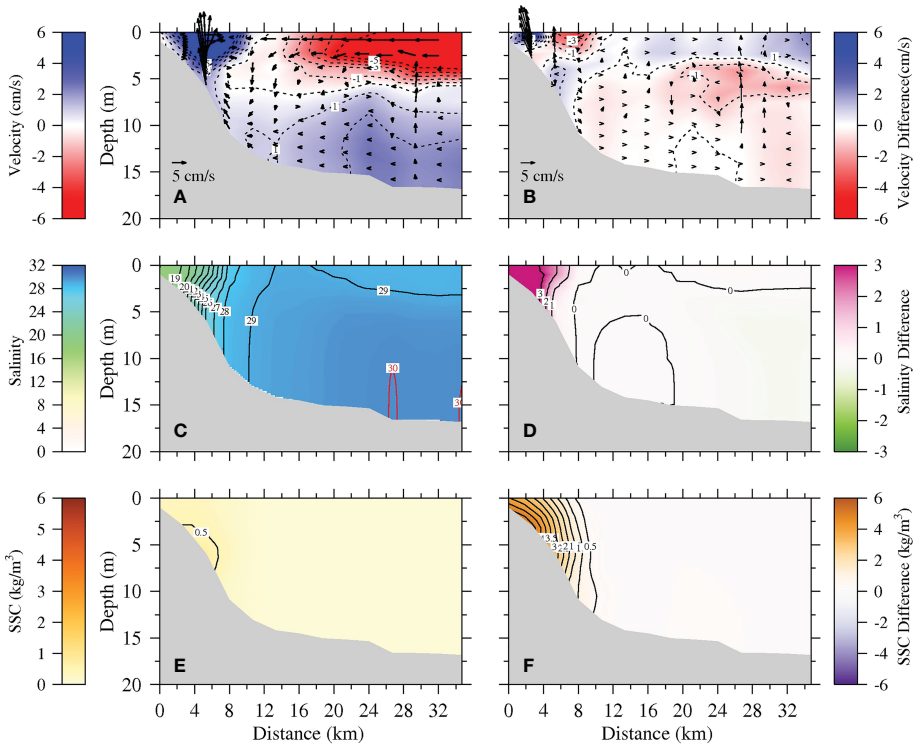

FIGURE 15
Vertical profile distributions of residual velocity **(A)**, salinity **(C)**, and suspended sediment concentration (SSC) **(E)** in Exp 2 and differences in residual velocity **(B)**, salinity **(D)**, and SSC **(F)** in Exp 0 (control run) – Exp 2 (without wave) along Sec 1 during spring tide in December 2012. *Arrows* in **(A, B)** signify current vectors along section, while the *contours* signify the current velocities perpendicular to the section (*positive values* indicate downstream current).

wave parameters simulated by the SWAN model were validated using measured significant wave height and period data.

The transport of water and sediment under the northeasterly prevailing wind in the Bohai Sea during spring tide in December 2012 was simulated. The freshwater off the Yellow River flowed downstream, carrying the river sediment and suspended sediment into Laizhou Bay. The bottom shear stress induced by wave was higher in the shallow water along the coast of the Yellow River Delta. The bottom shear stress induced by tide was higher in the north of Laizhou Bay and south of Bohai Bay due to the larger water velocities.

Tidal forcing induced more freshwater transport downstream along the coast of the Yellow River Delta. Without tidal forcing, the bottom shear stress decreased 0–0.4 N/m^2 in the south of the Yellow River mouth and south of Bohai Bay, resulting in less sediment resuspension in the bottom. The stratification in the water column hindered the upward diffusion of the bottom suspended sediment due to the lack of tidal mixing. Wave forcing had little impact on the water transport. However, without wave forcing, the bottom shear stress decreased 0–1 N/m^2 along the Yellow River Delta, causing less suspended sediment along the delta, which also weakened the sediment transport. Wave mixing was weaker than tidal mixing in the vertical direction. This study explained the effects of tides and waves on the transport of water and sediments off the Yellow River mouth in winter.

Sediment transport is a complicated study that involves sediment flocculation, breakup, erosion, and deposition, among others. This paper mainly concentrated on the dynamic effect of tides and waves on the movement of sediments. It is focused, but not all-inclusive. There are still a lot of aspects of sediment behaviors that are worth a thorough investigation, which are under consideration of the authors' future works.

Data availability statement

The raw data supporting the conclusions of this article will be made available by the authors, without undue reservation.

Author contributions

XC and JZ designed the research and revised the manuscript. XC collected the remote sensing data, conducted the numerical experiments, and wrote an original draft of the manuscript. XC and JZ analyzed the results. SC collected the observed data and acquired the funding. All authors contributed to the article and approved the submitted version.

Funding

This study was supported by the National Key Research and Development Program of China (No. 2017YFC0405503), and the

National Natural Science Foundation of China (NSFC) (No. U1706214).

Acknowledgments

We also acknowledge the reviewers for their valuable comments and suggestions. The sea surface wind data obtained from ECMWF are available at http://apps.ecmwf.int/datasets/. The open-ocean boundary water flux and salinity data were provided by SODA and can be found at http://iridl.ldeo.columbia.edu/SOURCES/.CARTON-GIESE/.SODA/.v2p0p2-4/. Tidal constituents were obtained from the NaoTide dataset (http://www.miz.nao.ac.jp/). The topographic data of the Bohai Sea were observational data from the Yellow River Water Commission. The remote sensing images of Landsat 8 OLI were downloaded from USGS (http://glovis.usgs.gov/).

Conflict of interest

Author XC is employed by Shanghai National Engineering Research Center of Urban Water Resources Co., Ltd.

The remaining authors declare that the research was conducted in the absence of any commercial or financial relationships that could be construed as a potential conflict of interest.

Publisher's note

Supplementary material

The Supplementary Material for this article can be found online at: https://www.frontiersin.org/articles/10.3389/fmars.2023.1181347/full#supplementary-material

References

Arakawa, A., and Lamb, V. R. (1977). Computational design of the basic dynamical processes of the UCLA general circulation model. *Gen. Circ. Models Atmosphere* 17, 173–265. doi: 10.1016/B978-0-12-460817-7.50009-4

Bian, C., Jiang, W., and Greatbatch, R. J. (2013). An exploratory model study of sediment transport sources and deposits in the bohai Sea, yellow Sea, and East China Sea. *J. Geophysical Res.: Oceans* 118, 5908–5923. doi: 10.1002/2013JC009116

Blumberg, A. F. (1994). "A primer for ECOM-si," in *Technical report of HydroQual*, vol. 66. (Mahwah, New Jersey).

Blumberg, A. F., and Mellor, G. L. (1987). "A description of a threedimensional coastal ocean circulation model," in *Coastal and estuarine science, volume 4, three-dimensional coastal ocean models*. Ed. N. S. Heaps (Washington, DC: American Geophysical Union), 1–16.

Brand, A., Lacy, J. R., Hsu, K., Hoover, D., Gladding, S., and Stacey, M. T. (2010). Wind-enhanced resuspension in the shallow waters of south San Francisco bay: mechanisms and potential implications for cohesive sediment transport. *J. Geophysical Res.* 115, C11024. doi: 10.1029/2010JC006172

Burchard, H., Schuttelaars, H. M., and Ralston, D. K. (2018). Sediment trapping in estuaries. *Annu. Rev. Mar. Sci.* 10, 371–395. doi: 10.1146/annurev-marine-010816-060535

Cao, Z., and Wang, Y. (1994). *Hydrodynamic and sediment transport numerical simulation (in Chinese)* (Tianjin, China: Tianjin University Press).

Chapman, D. C., and Lentz, S. J. (1994). Trapping of a coastal density front by the bottom boundary layer. *J. Phys. Oceanography* 24 (7), 1464–1479. doi: 10.1175/1520-0485(1994)024<1464:TOACDF>2.0.CO;2

Chen, S. (2001). Seasonal, neap-spring variation of sediment concentration in the joint area between Yangtze estuary and hangzhou bay. *Sci. China Ser. B.: Chem.* 44, 57–62. doi: 10.1007/BF02884809

Chen, C., Zhu, J., Zheng, L., Ralph, E., and Budd, J. W. (2004). A non-orthogonal primitive equation coastal ocean circulation model: application to lake superior. *J. Great Lakes Res.* 30 (supp-S1), 41–54. doi: 10.1016/S0380-1330(04)70376-7

Cheng, X., Zhu, J., and Chen, S. (2021a). Dynamics of the extension of the yellow river plume in the bohai Sea. *Continental Shelf Res.* 222 (9), 104438. doi: 10.1016/j.csr.2021.104438

Cheng, X., Zhu, J., and Chen, S. (2021b). Extensions of the river plume under various yellow river courses into the bohai Sea at different times. *Estuarine Coast. Shelf Sci.* 249 (107092). doi: 10.1016/j.ecss.2020.107092

Cui, B. L., and Li, X.-Y. (2011). Coastline change of the yellow river estuary and its response to the sediment and runoff, (1976–2005) *Geomorphology* 127, 1-2, 0–40. doi: 10.1016/j.geomorph.2010.12.001

Dou, G. (1999). Incipient motion of coarse and fine sediment (in Chinese). *J. Sediment Res.* 6, 1–9.

Doxaran, D., Froidefond, J. M., and Castaing, P. (2002). A reflectance band ratio used to estimate suspended matter concentrations in sediment-dominated coastal waters. *Int. J. Remote Sens.* 23 (23), 5079–5085. doi: 10.1080/0143116021000009912

Fan, H., and Huang, H. (2005). Changes in huanghe (Yellow) river estuary since artificial re-routing in 1996. *Chin. J. Oceanol. Limnol.* 23 (3), 299–305. doi: 10.1007/BF02847152

Fan, H., Huang, H., Zeng, T. Q., and Wang, K. (2006). River mouth bar formation, riverbed aggradation and channel migration in the modern huanghe (Yellow) river delta, China. *Geomorphology* 74, 124–136. doi: 10.1016/j.geomorph.2005.08.015

Fettweis, M., Sas, M., and Monbaliu, J. (1998). Seasonal, neap-spring and tidal variation of cohesive sediment concentration in the scheldt estuary, Belgium. *Estuarine Coast. Shelf Sci.* 47, 21–36. doi: 10.1006/ecss.1998.0338

Geyer, W. R. (1993). The importance of suppression of turbulence by stra tification on the estuarine turbidity maximum. *Estuaries* 16, 113–125. doi: 10.2307/1352769

Han, Q. (1997). The distribution and application of sediment dry density (in Chinese). *J. Sediment Res.* 2, 10–16.

Huang, S., Han, N., and Zhong, X. (1980). "Analysis of siltation at mouth bar of the Yangtze river estuary," in *Proceedings of the international symposium on river sedimentation, paper C6* (Beijing, China: Chinese Society of Hydraulic Engineering).

Kong, D., Miao, C., Borthwick, A. G. L., Duan, Q., Liu, H., Sun, Q., et al. (2015). Evolution of the yellow river delta and its relationship with runoff and sediment load from 1983 to 2011. *J. Hydrol.* 520, 157–167. doi: 10.1016/j.jhydrol.2014.09.038

Li, G., Tang, Z., Yue, S., Zhuang, K., and Wei, H. (2001). Sedimentation in the shear front off the yellow river mouth. *Continental Shelf Res.* 21, 607–625. doi: 10.1016/S0278-4343(00)00097-2

Li, G., Wei, H., Han, Y., and Chen, Y. (1998a). Sedimentation in the yellow river delta, part I: flow and suspended sediment structure in the upper distributary and the estuary. *Mar. Geol.* 149, 93–111. doi: 10.1016/S0025-3227(98)00031-0

Li, G., Wei, H., Yue, S., Cheng, Y., and Han, Y. (1998b). Sedimentation in the yellow river delta, part II: suspended sediment dispersal and deposition on the subaqueous delta. *Mar. Geol.* 149, 113–131. doi: 10.1016/S0025-3227(98)00032-2

Liang, B., Li, H., and Lee, D. (2008). Bottom shear stress under wave-current interaction. *J. Hydrodynamics* 20 (1), 88–95. doi: 10.1016/S1001-6058(08)60032-3

Lin, J., and Kuo, A. Y. (2001). Secondary turbidity maximum in a partially mixed microtidal estuary. *Estuaries* 24, 707–720. doi: 10.2307/1352879

Liu, G., and Cai, S. (2019). Modeling of suspended sediment by coupled wave-current model in the zhujiang (Pearl) river estuary. *Acta Oceanol. Sin.* 38 (7), 22–35. doi: 10.1007/s13131-019-1455-3

Liu, Y., Maccready, P., Hickey, B. M., Dever, E. P., and Banas, N. S. (2009). Evaluation of a coastal ocean circulation model for the Columbia river plume in summer 2004. *J. Geophysical Res. Oceans.* 114(C2). doi: 10.1029/2008JC004929

Long, C. M., and Pavelsky, T. M. (2013). Remote sensing of suspended sediment concentration and hydrologic connectivity in a complex wetland environment. *Remote Sens. Environ.* 129, 197–209. doi: 10.1016/j.rse.2012.10.019

Luettich, R. A. J., Harleman, D. R. F., and Somlyódy, L. (1990). Dynamic behavior of suspended sediment concentrations in a shallow lake perturbed by episodic wind events. *Limnol. Oceanography* 35 (5), 1050–1067. doi: 10.4319/lo.1990.35.5.1050

Lv, X., Yuan, D., Ma, X., and Tao, J. (2014). Wave characteristics analysis in bohai Sea based on ECMWF wind field. *Ocean Eng.* 91, 159–171. doi: 10.1016/j.oceaneng.2014.09.010

Maréchal, D. (2004). *A soil-based approach to rainfall-runoff modeling in ungauged catchments for England and Wales (PhD thesis)* (Cranfield, UK: Cranfield University).

Marine Atlas of Offshore China—Marine Sediment (2017) (Beijing).

Martin, J. M., Zhang, J., Shi, M. C., and Zhou, Q. (1993). Actual flux of the huanghe (Yellow river) sediment to the western pacific ocean. *J. Sea Res.* 31 (93), 243–254. doi: 10.1016/0077-7579(93)90025-N

Mehta, A. J., and McAnally, W. H. (2008). "Fine grained sediment transport," in *Sedimentation engineering: processes, management, modeling, and practice*, 253–307.

Mellor, G. L., and Yamada, T. (1974). A hierarchy of turbulence closure models for planetary boundary layers. *J. Atmospheric Sci.* 31 (7), 1791–1806. doi: 10.1175/1520-0469(1974)031<1791:AHOTCM>2.0.CO;2

Mellor, G. L., and Yamada, T. (1982). Development of a turbulence closure model for geophysical fluid problems. *Rev. Geophysics Space Phys.* 20 (4), 851–875. doi: 10.1029/RG020i004p00851

Murphy, A. H. (1988). Skill scores based on the mean square error and their relationships to the correlation coefficient *Monthly Weather Review* 116, 12, 990–991. doi: 10.1175/1520-0493(1988)116<2417:SSBOTM>2.0.CO;2

Pang, J. Z., and Si, S. H. (1979). Evolution of the yellow river mouth: i. historical shifts. *Oceanol. Et. Limnol. Sin.* 10 (2), 136–141.

Qin, Y. S., and Li, F. (1983). "Study of influence of sediment loads discharged from huanghe river on sedimentation in bohai Sea and huanghai Sea," in *International symposium on sedimentation on the continental shelf, with special reference to East China Sea* (Hangzhou, China).

Ralston, D. K., Geyer, W. R., and Lerczak, J. A. (2010). Structure, variability, and salt flux in a strongly forced salt wedge estuary. *J. Geophysical Res. Atmospheres* 115 (C6). doi: 10.1029/2009JC005806

Sanford, L. P. (1994). Wave-forced resuspension of upper Chesapeake bay muds. *Estuaries Coasts* 17 (1), 148–165. doi: 10.2307/1352564

Scully, M. E., and Friedrichs, C. T. (2003). The influence of asymmetries in overlying stratification on near-bed turbulence and sediment suspension in a partially-mixed estuary. *Ocean Dynamics* 53, 208–218. doi: 10.1007/s10236-003-0034-y

Scully, M. E., and Friedrichs, C. T. (2007). Sediment pumping by tidal asymmetry in a partially mixed estuary. *J. Geophysical Res.* 112, C07028. doi: 10.1029/2006JC003784

Shi, W. (2008). *3D numerical simulation and analysis of the transportation of suspended sediment in the huanghe estuary, Ph.D. thesis* (Shandong, China: Ocean University of China).

Signell, R. P., Beardsley, R. C., Graber, H. C., and Capotondi, A. (1990). Effect of wave-current interaction on wind-driven circulation in narrow, shallow embayments. *J. Geophysical Res.* 95, 9671–9678. doi: 10.1029/JC095iC06p09671

Simpson, J. H., Brown, J., Matthews, J., and Allen, G. (1990). Tidal straining, density currents, and stirring in the control of estuarine stratification. *Estuaries* 13, 125–132. doi: 10.2307/1351581

Smagorinsky, J. (1963). General circulation experiments with the primitive equations: i. the basic experiment. *Monthly Weather Rev.* 91 (3), 99–164. doi: 10.1175/1520-0493(1963)091<0099:GCEWTP>2.3.CO;2

Sun, X. (2013). *The impact of wave on the sediment erosion and deposition near the yellow river mouth* (Qingdao: Ocean University of China).

Traykovski, P., Geyer, W. R., and Sommerfield, C. (2004). Rapid sediment deposition and fine-scale strata formation in the Hudson estuary. *J. Geophysical Res.* 109, F02004. doi: 10.1029/2003JF000096

van Leussen, W. (1988). "Aggregation of particles, settling velocity of mud flocs: a review," in *Physical processes in estuaries*. Eds. J. Dronkers and W. van Leussen (Springer-Verlag) 347, 403.

Wang, K. (2003). *Study on yellow river estuary sediment transport and it's distributing regulation, master thesis* (Xi'an, China: Xi'an University of Technology).

Wang, N. (2014). *Sedimentary dynamics process and topographic evolution in the modern yellow river mouth* (Shandong: Ocean University of China).

Wang, H., Yang, Z., Li, Y., Guo, Z., Sun, X., and Wang, Y. (2007). Dispersal pattern of suspended sediment in the shear frontal zone off the huanghe (Yellow river) mouth. *Continental Shelf Res.* 27, 854–871. doi: 10.1016/j.csr.2006.12.002

Wolanski, E., King, B. A., and Galloway, D. (1995). Dynamics of the turbidity maximum in the fly river estuary, Papua new Guinea. *Estuarine Coast. Shelf Sci.* 40 (3), 321–337. doi: 10.1016/S0272-7714(05)80013-7

Wu, T., and Wu, H. (2018). Tidal mixing sustains a bottom-trapped river plume and buoyant coastal current on an energetic continental shelf. *J. Geophysical Res.: Oceans* 123 (11), 8026–8051. doi: 10.1029/2018JC014105

Wu, H., and Zhu, J. (2010). Advection scheme with 3rd high-order spatial interpolation at the middle temporal level and its application to saltwater intrusion in the changjiang estuary. *Ocean Model.* 33 (1-2), 33–51. doi: 10.1016/j.ocemod.2009.12.001

Yu, Y., Wang, H., Shi, X., Ran, X., Cui, T., Qiao, S., et al. (2013). New discharge regime of the huanghe (Yellow river): causes and implications. *Continental Shelf Res.* 69, 62–72. doi: 10.1016/j.csr.2013.09.013

Zhan, C., Yu, J., Wang, Q., Li, Y., Zhou, D., Xing, Q., et al. (2017). Remote sensing retrieval of surface suspended sediment concentration in the yellow river estuary. *Chin. Geographical Sci.* 27 (6), 934–947. doi: 10.1007/s11769-017-0921-7

Zhu, J. (2003). *Ocean numerical calculation method and numerical model* (Beijing: China Ocean Press).

frontiers | Frontiers in Marine Science

TYPE Original Research
PUBLISHED 18 September 2023
DOI 10.3389/fmars.2023.1155270

OPEN ACCESS

EDITED BY
Henrik Kalisch,
University of Bergen, Norway

REVIEWED BY
Magda Carr,
Newcastle University, United Kingdom
Edward Robert Johnson,
University College London,
United Kingdom

*CORRESPONDENCE
Thea Josefine Ellevold
theajel@math.uio.no

RECEIVED 31 January 2023
ACCEPTED 09 August 2023
PUBLISHED 18 September 2023

CITATION
Ellevold TJ, Grue J and Sletten JS (2023) Tracer particle motion driven by vortex formation in the bottom boundary layer underneath internal solitary waves. *Front. Mar. Sci.* 10:1155270. doi: 10.3389/fmars.2023.1155270

Tracer particle motion driven by vortex formation in the bottom boundary layer underneath internal solitary waves

Thea Josefine Ellevold*, John Grue and Joakim Soløy Sletten

Department of Mathematics, University of Oslo, Oslo, Norway

Internal solitary waves (ISWs) of large amplitude moving in the coastal ocean induce sizeable horizontal velocities above the sea bed. In turn, these give rise to instability and vortex formation in the bottom boundary layer (BBL), and sediment resuspension and concentration maintenance in the water column. We present two-dimensional laminar simulations in a numerical tank suitable for internal wave motion, including the processes of the BBL. The combined wave and vorticity field encounters a cloud of tracer particles near the bottom. The tracer particles are moved vertically because of the vorticity field during a first encounter. The reflected wave intercepts a second time with the tracer particles, which are then moved further vertically. Numerical experiments with a kinematic viscosity of 1/100 $cm^2\ s^{-1}$ or 1/1000 $cm^2\ s^{-1}$ are used to manipulate the scale of the Reynolds number at a moderate and great laboratory scale. The final vertical position of the tracer particles is found below a vertical level of approximately 0.23 times the water depth (H) after the second passage. The result is independent of the scale. This vertical position matches available field measurements of a summer benthic nepheloid layer reaching a height of $0.19H$. The laminar model predictions compare very well to the ISW-driven vortex formation measured in a three-dimensional laboratory wave tank. Convergence of the calculated vortex formation is documented.

KEYWORDS

internal waves, vortex formation, Lagrangian tracer particle trajectories, probability distribution, upscaling to field dimension

1 Introduction

Internal solitary waves (ISWs) are commonly observed in the coastal ocean and are generally driven by the wind or the tide (Helfrich and Melville, 2006). The ISWs are driven by the acceleration of gravity ($g = 9.81\ m\ s^{-2}$) and may move along the pycnocline of the ocean located at a middle depth d, which is small compared to the local water depth H, implying the dimensionless ratio d/H. The density jump across the pycnocline ($\Delta\rho$) relative to the density of the water below the pycnocline (ρ_3) is typically small, with a dimensionless value of $\Delta\rho$

$/\rho_3 \ll 1$. In practice, $\Delta\rho/\rho_3$ is 1/1000. The wave motion and the velocity field are functions of the wave amplitude a, obtaining another dimensionless variable a/H. The wave-driven velocities scale according to a reference velocity c_0. This is proportional to $\sqrt{dg\Delta\rho/\rho_3}$ times a function of d/H. As regards the bottom boundary layer effect, it is commonly characterized by the Reynolds number based on the total water depth, the wave speed c_0, and the kinematic viscosity ν, obtaining $Re_w = c_0 H/\nu$.

ISWs are often highly nonlinear. The theories, like weakly nonlinear Korteweg–de Vries (KdV) -type theories, have played a primary role in explaining the essential features of the observed wave, even though those theories do not always provide accurate quantitative details. Grue et al. (1999) conducted laboratory experiments of solitary waves propagating in a two-layer fluid. They compared the weakly nonlinear KdV theory and a fully nonlinear interface model towards the experimental results. Having a small amplitude, both theory and model compared excellently. However, above a certain amplitude threshold, the weakly nonlinear theory exhibits systematic deviation from the experiments where the fully nonlinear model still compared excellently for all quantities measured.

Above the pycnocline, the velocities have a dominant horizontal component, a substantial fraction of the wave propagation velocity. Below the pycnocline, the horizontal velocity is opposite of the wave propagation and is also a substantial fraction of the wave propagation speed. The vertically integrated horizontal velocity is zero and satisfies the mass balance. There are also vertical velocities. These are proportional to the horizontal gradient of the displaced pycnocline along the wave propagation times the wave speed.

The wave-induced boundary layer underneath an ISW of depression separates in the adverse pressure gradient region behind the trough. Strong enough instability may give rise to the spontaneous onset of vortex shedding (e.g., Diamessis and Redekopp, 2006; Carr et al., 2008; Aghsaee et al., 2012; Sakai et al., 2020). The vortex structures are formed behind the wave trough, ascend vertically into the water column, and then propagate downstream in the same direction as the mother wave but with a much slower speed (Carr et al., 2008). The instabilities in the bottom boundary layer may contribute to the resuspension of particles due to, e.g., substantial variation of the shear stress (e.g., Bogucki and Redekopp, 1999; Boegman and Stastna, 2019). The ability of nonlinear internal waves to move sediments on the bottom vertically in the water column has been observed by Bogucki et al. (1997), and has been further studied model-wise by, e.g., Bogucki and Redekopp (1999), and in field observations, e.g., Bourgault et al. (2007); Quaresma et al. (2007); Zulberti et al. (2020), see also the review by Boegman and Stastna (2019).

Large eddy simulations (LES) in three dimensions (3D) of the ISW-driven separated boundary layer and its development were carried out by Sakai et al. (2020) for a Reynolds number similar to our ($Re_w = 1.6 \cdot 10^5$). A strong wave of $a/H = 0.35$ was moving on a counter-current of the same magnitude as the wave propagation speed, implying that the excitation is stronger than in our cases. The LES computations were compared to two-dimensional direct numerical simulations finding that the vortex generation was essential two-dimensional down to a distance of six water depths behind the wave trough. Further downstream, vortex breakup and degeneration into turbulent clouds, and relaxation to a spatially developing turbulent boundary layer were found to take place.

In this research, we investigate the ISW-driven vortex formation and tracer particle displacements in the bottom boundary layer. We conduct laminar two-dimensional numerical simulations of a set of laboratory experiments by Carr et al. (2008) where this kind of physical effect has been measured. Several questions are addressed, including:

1. As regards the two-dimensional laminar method: How well can the model reproduce the laboratory measurements conducted in a three-dimensional (3D) wave tank? In particular, how well can the model calculations reproduce the measured vortices at the bottom behind the wave?
2. As regards accuracy: How close are prediction and measurement?
3. As regards flow and motion properties: How can the model be used to evaluate quantities which have not been measured in the laboratory?
4. As regards the tracer particle motion: The wave- and boundary-layer-induced tracer particle motion is of interest to study and visualize. This motion was not measured in the laboratory experiments, even though the experimental visual tracking method is based on neutrally buoyant tracer particles added to the fluid.
5. As regards the vertical tracer particle displacements: In the shallow ocean, the particles at the sea bed contain organic matter that is important to the marine production taking place in the euphotic zone in the upper part of the water column. By the present model calculations, we investigate how high up in the water column the tracer particles may be transported. The wave may intercept a cloud of tracer particles once and twice.
6. Finally, we compare the simulated results with available field observations.

In section 2, we present the numerical wave tank, wave generation, wave characteristics, and the Stokes boundary layer thickness. Further, details of the two-dimensional numerical solver are described. The grid resolution and information regarding the Lagrangian tracer particles used in this study are provided. Section 3 presents the obtained results, including answers to the research questions posed. In section 3.1, similarities between the vortex formation in simulation and experiment at $Re_w = 5.9 \cdot 10^4$ are presented. A convergence study of the calculated vortex separation distance and the vortex strength is performed. In section 3.2, we present the Lagrangian tracer particle displacements and paths. The vertical tracer particle distribution is calculated. The results are briefly compared to available field measurements in section 3.3, and conclusions are given in section 4.

2 Method

This article presents numerical simulations of non-linear internal solitary waves (ISWs) of large amplitude, as visualized in

Figure 1B, where the wave travels from left to right with a speed c. The wave-induced velocity field beneath the wave interacts with the bottom, initiating instabilities in the viscous bottom boundary layer (BBL) (e.g., Carr and Davies, 2006; Diamessis and Redekopp, 2006; Aghsaee et al., 2012; Sakai et al., 2020). Tracer particles are implemented close to the bottom in order to investigate their motion in the fluid induced by the wave (Boegman and Stastna, 2019).

2.1 The numerical wave tank

We are following the same setup of the wave tank and the wave generation procedure as conducted in the laboratory experiments by Carr et al. (2008). The numerical wave tank is filled with a stratified fluid. The upper layer has a depth of h_1 and a density of ρ_1. The pycnocline has a thickness of h_2 and density $\rho(z)$, which varies as a linear function of z. The lower layer has thickness h_3 and density ρ_3. The density is continuous throughout the vertical. The total water depth is $H = h_1 + h_2 + h_3$. Figure 1A is a sketch of the wave tank. The amplitude a is defined as the maximum excursion of the isoline separating layers two and three. The middle depth of the pycnocline is defined by $d = h_1 + h_2/2$. In the present investigation, two different stratifications are studied, where stratification one, denoted by Strat. 1, has $d/H = 0.16$, and stratification two,denoted by Strat. 2, has $d/H = 0.21$. These two stratifications correspond to two of the pycnocline depths studied by Carr et al. (2008). In present calculations, the thickness of the pycnocline is $h_2 \sim 0.12H - 0.14H$, and the wave amplitude $a/d \sim 1.45 - 1.87$.

The physical dimensions of the 2D numerical wave tank are the same as those used in the laboratory setup by Carr et al. (2008). The length $L = 6.4$ m and depth $H = 0.38$ m provide a non-dimensional length of $L/H = 16.84$.

2.2 Generation and wave characteristics

To generate ISWs in the tank (physical or numerical), the trapped volume method is applied where a large volume V, given by $(x_0 \times (d_0 - h_1))$ of density ρ_1, is added behind a gate. The gate is located at a distance of $\Delta x_0 = 0.6$ m from the left tank wall. Its horizontal position defines $x = 0$, where the horizontal x-axis is along the bottom. The total volume can be modified by varying the depth d_0, generating ISWs with different amplitudes, by releasing the volume. In the laboratory, the gate is removed by quickly lifting it upwards. In the numerical simulations, the gate is imposed beforetime zero, and after time zero, we assume it is instantaneously removed. A leading wave of mode 1 is generated in each experiment (physical or numerical).

The wave frequency is defined by $\tilde{\omega} = c_0/L_w$, where c_0 is the linear long wave speed given by the two-layer approximation

$$c_0 = \sqrt{\frac{g(h_3 + h_2/2)(h_1 + h_2/2)(\rho_3 - \rho_1)}{\rho_1(h_3 + h_2/2) + \rho_3(h_1 + h_2/2)}} \cong \sqrt{\frac{g' d(H - d)}{H}}, \quad (1)$$

where $g' = g(\rho_3 - \rho_1)/\rho_3$ and $\Delta\rho/\rho_3 \ll 1$. The wavelength of the ISW is defined by

$$L_w = \frac{1}{a}\int_{-\infty}^{\infty} \eta(x)dx, \quad (2)$$

where η denotes the vertical displacement of the isoline separating layers two and three, and the amplitude a is defined above.

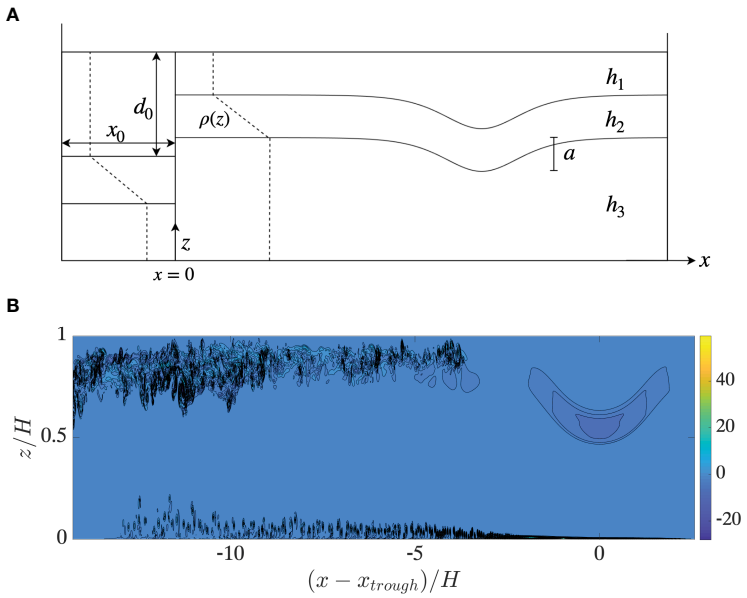

FIGURE 1
(A) Sketch of the wave tank. **(B)** Vorticity field $\omega/(c_0/H)$ (color scale, black contour lines of ω) due to ISW travelling to the right at $tc_0/H = 6.4$ with $a/H = 0.30$ and $Re_w = 5.9 \cdot 10^4$.

The Reynolds number based on the water depth, alternatively denoted the wave Reynolds number, is a helpful quantity used by a group of researchers studying the combined wave and boundary layer effects (e.g., Diamessis and Redekopp, 2006; Carr et al., 2008; Aghsaee et al., 2012; Sakai et al., 2020). The quantity is defined by $Re_w = c_0 H/\nu$ where ν is the kinematic viscosity of the water. In the laboratory experiments by Carr et al. (2008), the Re_w was approximately 60 000. In the field scale, Re_w is 10^8 (e.g., Zulberti et al., 2020). The present calculations are carried out with Re_w between 60 000 and 600 000. The calculations at $Re_w =$ 60 000 are carried out with $\nu = 1/100$ cm^2 s^{-1} for fresh water at 20 °C. In the calculations at $Re_w =$ 600 000, the ν is manipulated with a value put to $\nu = 1/1000$ cm^2 s^{-1}. Alternatively, the water depth may be increased to $\tilde{H} = 10^{2/3}H$, $\tilde{c_0} = 10^{1/3}c_0$, and $\nu = 1/100$ cm^2 s^{-1} producing $Re_w =$ 600 000. Additionally, we define a boundary layer Reynolds number, $Re_\delta = \delta U_{\infty,0}/\nu$, where $U_{\infty,0}$ is the free stream horizontal velocity underneath the wave trough, right above the bottom, and δ is the boundary layer thickness, defined in section 2.3 below.

The wave travels along the pycnocline from left to right. The nonlinear celerity is $c = \Delta x/\Delta t$. There is no background current. A snapshot of an ISW at time $tc_0/H = 6.4$ is visualized by its nondimensional vorticity field in Figure 1B (corresponding to run 1 in Table 1). The simulation is run with a kinematic viscosity of $\nu = 1/100$ cm^2 s^{-1}. The wave drives the instability and vortex formation in the BBL, in addition to the shear instability in the pycnocline (e.g., Fructus et al., 2009; Lamb, 2014). As the volume is released, a local mixing of the fluid taking place across the gate position is confined to a small volume (physical or numerical). This is set into horizontal motion along the pycnocline, generating a short and slower wave of mode 2, observed at approximately nine water depths behind the main wave. Such a wave is measured by Sveen et al. (2002), their Figure 17 and more recently studied by Carr et al. (2019).

The ISW propagating at small speed c, proportional to $(\Delta\rho/\rho_3)^{1/2}$, implies that the effect on the free surface elevation is small. The vertical velocity is approximately zero at the free surface. The small free surface elevation may be calculated a posteriori from the Bernoulli equation giving $\eta = (1/2g)(c^2 - u^2)$, where u is the horizontal speed driven by the ISW at the free surface (e.g., Fructus and Grue, 2004). On the laboratory scale, the wave speed is 0.26 m s^{-1}, $u/c << 1$ for the waves of large amplitude (and the wavelength is approximately 1 m). This obtains a surface elevation of 0.3 cm while the internal wave amplitude is 11 cm. Corresponding estimates of ISWs in the coastal ocean are: wave speed of 0.5 m s^{-1}, a surface elevation of 1 cm, while the internal wave amplitude is typically 30 m. The internal waves are 500 m to 1000 m long.

2.3 Boundary layer thickness

The Stokes boundary layer thickness at the bottom beneath the wave phase is characterized by $\delta = \sqrt{(2\nu/\tilde{\omega})}$, where $\tilde{\omega}$ is defined in § 2.2.

2.4 Finite volume solver

We present numerical simulations of ISWs, utilizing the open-source software Basilisk (Popinet and collaborators, 2013–2023). The important part of the calculation is to resolve the wave-driven viscous boundary layer effect at the bottom of the fluid domain. Basilisk is a second-order finite volume solver, where the two-phase incompressible Navier-Stokes equations are solved and is the successor of Gerris (Popinet, 2003; Popinet, 2009). Basilisk provides ready-to-use finite volume solvers for fluid dynamics and has been widely used in calculations and simulations of several problems, i.e., tsunamies (e.g., Popinet, 2015), shallow water, wave breaking and surface flows (e.g., Popinet, 2011; Mostert and Deike, 2020; Popinet, 2020), incompressible two-phase flow (e.g., López-Herrera et al., 2019), and atmospheric turbulent boundary layer (e.g., van Hooft et al., 2018).

In this two-dimensional (2D) study, the incompressible, non-hydrostatic equations in a Cartesian reference frame become,

$$\frac{\partial \mathbf{u}}{\partial t} + (\mathbf{u}\cdot\nabla)\mathbf{u} = -\frac{1}{\rho}\nabla p + \nu\nabla^2\mathbf{u} + \rho\mathbf{a}, \tag{3}$$

$$\frac{\partial \rho}{\partial t} + \nabla\cdot(\rho\mathbf{u}) = 0, \tag{4}$$

$$\nabla\cdot\mathbf{u} = 0, \tag{5}$$

where ρ, u = $(\mathbf{u}, w)$, p and ν are the density, velocity vector, pressure and kinematic viscosity, respectively. The vector $\mathbf{a} = -g\mathbf{k} = g(0,-1)$, where g is the acceleration due to gravity. Further, t is time, and (x, z) are the (horizontal, vertical) coordinates. The Navier-Stokes equations determine the pressure and the velocity field driven by the wave where mass conservation is included, additionally to set the effect of viscosity in the viscous boundary layer at the bottom.

TABLE 1 Layer depths, stratification (Strat.), calculated amplitude a, numerical values for $U_{\infty,0}/c_0$, δ, Re_δ, Re_w, and x_p/H.

Run	$h_3/h_2/h_1$ (m)	Strat.	a/H	$U_{\infty,0}/c_0$	$\delta \cdot 10^{-3}$ (m)	Re_δ	Re_w	x_p/H
1	0.293/0.052/0.035	1	0.300	0.863	3.68	490	5.9 10^4	7.42
3	0.280/0.047/0.055	2	0.300	0.833	4.44	631	6.5 10^4	7.43
2	0.293/0.052/0.0235	1	0.297	0.858	1.22	1620	5.9 10^5	7.42
4	0.280/0.047/0.055	2	0.301	0.835	1.46	2080	6.5 10^5	7.43

Resolution $N = 12, N_+ = 14$ for Run 1 and 3, and $N = 11, N_+ = 16$ for Run 2 and 4.

The field equations are solved by means of a multilevel Poisson solver. The Bell-Colella-Glaz (Bell et al., 1989) advection scheme integrates the momentum equation. The viscous terms are treated implicitly. The solver employs a geometric volume of fluid method (VOF) to reconstruct the interfaces by the continuous change of the fluid properties; density and viscosity. The cells that include an interface are treated by introducing the volume fraction of the two fluids, $f(x,z,t)$. The implementation of the numerical scheme is briefly described below. The time integration (supplied in Appendix A.1) adheres to the standard Basilisk setup, with a slight modification where the dynamic viscosity is harmonically averaged. For more details, see the Basilisk web page (basilisk.fr), Popinet (2003); Popinet (2009), and references therein.

2.5 The domain

By default, Basilisk defines a computational domain with sides L. Our numerical wave tank is defined as a part of this spatial domain, with horizontal length L and vertical height H ($< L$). At $z = H$ ($z = 0$ at the tank bottom, see Figure 1A), a rigid lid is placed, implying no motion in the domain $z > H$. The effect of viscosity is taken into account within the fluid and at the bottom. This means that the no-slip condition is applied at the lower boundary. Free-slip conditions are used at the upper boundary, vertical end walls, and gate. The depth provides the physical length scale in the calculations. The time and velocity scales are $\sqrt{H/g}$ and $\sqrt{gH}$, respectively.

2.6 Discretization and grid resolution

The discretization of the computational domain utilizes a quad-tree scheme (Popinet, 2003; van Hooft et al., 2018) where the user can choose to run the scheme with either a non-adaptive mesh or an adaptive mesh, further referred to as "refine" and "adapt", respectively.

The size of a cell is characterized by its level N where it is located. The cells are square finite volume cells, providing equal subdivisions vertically and horizontally, creating $\Delta_N = \Delta_x = \Delta_z$. Hence, the grid size of the cell at a given level is $\Delta_N = L/2^N$.

The grid resolution is discussed relative to the boundary layer thickness, i.e., Δ_N/δ. A fine discretization with $\Delta_{N_+} = L/2^{N_+}$ is developed near the bottom for $0 < z < 0.015H$, where the finest resolution becomes $\Delta_{N_+}/\delta = 0.022$ (run 3, Table 1). Hence, $N_+ > N$. This is to ensure grid independence of the results.

Adaptive meshing is widely used and is known to significantly reduce the computation cost. We will utilize adapting meshing when exploring convergence properties of our numerical scheme. When the mesh is adapted, the refinement criterion is based on the discretization error of the velocities u and w, and the criterion for refinement of the volume fraction f is based upon a wavelet algorithm. The threshold values are set to $\epsilon_u^{th} = \epsilon_w^{th} = 3 \times 10^{-4}$ and $\epsilon_f^{th} = 3 \times 10^{-2}$. Further details are provided in the Appendix A.2.

van Hooft et al. (2018), their Figure 8, have compared the numerical dissipation in the "refine" and "adapt" versions of Basilisk, finding that small discrepancies on the order of 5 % were present between the runs with the fixed uniform grid and the adaptive grid, where this discrepancy decreased with increasing refinement. Numerical tests diagnosed with a lower dissipation rate were associated with lower kinetic energy, indicating that a small part of the dissipation was of numerical/non-physical origin.

The advantage of the Basilisk framework is that it includes OpenMP/MPI parallelism capability. The simulations were run in parallel using shared memory (OpenMP), and the computations were performed on the Norwegian Research and Education Cloud (NREC).

2.7 Lagrangian tracer particles

Tracking of Lagrangian tracer particles is performed using a two-stage Runge-Kutta (RK2) scheme. The seeded neutrally buoyant tracer particles are purely Lagrangian tracers, and their settling velocity, added mass, history effects, etc., are ignored (Necker et al., 2005; Stastna and Lamb, 2008).

The tracer particles are seeded close to the bottom in a two-dimensional rectangular grid. More precisely, 160×160 tracer particles are equally distributed horizontally between $x_p - H < x < x_p + H$ and vertically between $z_1 < z_p < z_2$ before time zero. Table 1 provides the x_p/H values. The tracer particle positions are presented relative to the total water depth H and the boundary layer's height δ (§2.3). The vertical extent is $z_p/H \sim 0.0037 - 0.0283$.

However, the boundary layer thickness, δ, is a better vertical scale of the tracer particle vertical motion, providing vertical extension between $0.31 < z_p/\delta < 2.93$ for $Re_w = 5.9 \cdot 10^4$ and $6.5 \cdot 10^4$, and $0.96 < z_p/\delta < 8.82$ for $Re_w = 5.9 \cdot 10^5$ and $6.5 \cdot 10^5$.

The tracer particles displacement $\mathbf{r}_p = (x_p, z_p)$ and the path driven by the wave-induced instabilities are calculated by integrating:

$$\frac{dx_p}{dt} = u(x_p, z_p, t), \tag{6}$$

$$\frac{dz_p}{dt} = w(x_p, z_p, t), \tag{7}$$

obtaining

$$x_p = x_{p,0} + \int_{t_0}^{t} u(x_p, z_p, t)dt, \tag{8}$$

$$z_p = z_{p,0} + \int_{t_0}^{t} w(x_p, z_p, t)dt\,. \tag{9}$$

The RK2 scheme employs

$$\mathbf{r}_{p,n+1} = \mathbf{r}_{p,n} + \Delta t(b_1 k_1 + b_2 k_2), \tag{10}$$

$$k_1 = \mathbf{u}(\mathbf{r}_{p,n}, t_n), \tag{11}$$

$$k_2 = \mathbf{u}(\mathbf{r}_{p,n} + c_2 k_1, t_n + \Delta t\alpha), \tag{12}$$

where $c_2 = \alpha$, $b_1 = 1 - \frac{1}{2\alpha}$ and $b_2 = \frac{1}{2\alpha}$, and $b_1 + b_2 = 1$, $b_2 c_2 = 1/2$, and $b_2 \alpha = 1/2$ (Sanderse and Veldman, 2019). The tracer particles paths are visualized both in a fixed frame of reference and a frame of reference following the wave.

3 Results

3.1 Vortex formation

3.1.1 Simulation of the laboratory experiments by Carr et al.

In this section, a numerical simulation of the wave-induced instability is presented. We simulate one of the laboratory experiments by Carr et al. (2008), their experiment dated 080207, and directly compare our results. The parameters of the numerical simulation corresponding to the experiment are provided in Table 1, denoted by Run 1. In the table, a/H is the non-dimensionalized amplitude and is similar in the computation and experiment (as $a/H = 0.30$).

The created wave, numerically and physically, is strong enough to induce instability and vortices. Figure 2A shows the instability and vortex ejection from the boundary layer due to the wave illustrated in Figure 1B. The horizontal axis is $(x - x_{trough})/H$, where x_{trough} denotes the position of the wave trough. The instability grows exponentially between $(x - x_{trough})/H = -1.7$ and -2.5, whereafter the vortices are formed. The series of vortex rolls in the instability growth area have a shorter separation length than the vortices found further downstream. The vortex formation goes on continuously, producing the vortex wake. Specifically, we compare to the experiment in which Carr et al. (2008) presented the vertical velocity corresponding to the vortices, their Figure 13, reproduced here in Figure 2C.

The separation distance λ_v between the vortices located in the vortex wake is set to be the center-to-center distance between the vortices. The computational result (Figure 2B) shows five vortices, the same number as in the experiment for the similar horizontal extension (Figure 2C). In the experiment, the separation distance between the vortices is between $0.069H$ and $0.122H$, with an average of $\lambda_v \sim 0.103H$. The similar average distance in the computation is $\lambda_v \sim 0.103H$, which is exactly the same result. The maximum vertical extent of the vortices was 8.7 % of the water depth in the laboratory and 6.6 % in the simulation. The results in Figure 2 were simulated with $N = 12$ and $N_+ = 14$, see section 2.6.

3.1.2 Convergence of the separation distance, vorticity, amplitude and wave speed

We now discuss research question two of the introduction: how close are prediction and measurement?

Two different numerical representations are included in Basilisk, as described in section 3.6. Calculations using both representations are presented.

The resolution level is in the range of $N = 10 - 12$. When running with "refine", there is no additional refinement close to the bottom. The minimum and maximum refinement levels in "adapt" are set to $N_{min} = N - 1$ and $N_{max} = N$.

Each simulation was performed ten times with the same settings and executed with and without parallelization. The average values and standard deviations of the variables: distance, vorticity, amplitude, and speed were calculated over the ten runs with the same settings. Hence, a total of 120 simulations were run.

The vortices measured in Carr et al. (2008) (Figure 2C) exhibit an individual distance that slightly varies. Figure 3 illustrates the respective computational distance, calculated over the same area, further referred to as the local area, as a function of the resolution level N. The distance is further explored over a broader range in the wave tank where $-13.3 < (x - x_{trough})/H < -4.3$ (results are not shown). The simulations converge for increasing resolution level. A small anomaly for $N = 12$ "adapt" in the result presented in Figure 3 is observed. However, if we increase the respective local area three times, its average distance reduces from $0.134H$ to $0.108H$ (marked by a green circle in the figure). When simulating with the lowest resolution, the vortex formation formed is the main difference between "refine" and "adapt". However, this discrepancy decreases with increasing resolution. For our purposes, the advantages of utilizing "adapt" instead of "refine" are minor.

An additional convergence check is conducted where the results are analyzed after a downscaling of the resolution in the post-processing procedure. Hence, the simulations are executed with "refine" and $N = 11$ and 12. In the post-processing procedure, the simulations conducted with $N = 11$ are downscaled to level $N = 10$, and the simulations performed with $N = 12$ are downscaled to level $N = 11$. The results are plotted in Figures 3, 4C with black $*$ and are marked with an asterisk in the figure legend.

The measured average amplitude a and wave speed c are visualized in Figures 4A, B, respectively. The amplitude in the simulation is ~ 3.3 % higher than the amplitude measured in the laboratory experiments by Carr et al. (2008). The average wave speed in the computations converges to 0.262 m s^{-1}, corresponding to the upper limit of the wave speed measured in the laboratory of 0.242 ± 0.022 m s^{-1}.

The vorticity in the numerical simulations is obtained by evaluating the circulation integral in each grid cell, divided by the area A enclosed by the integration contour obtaining $\omega(x, z) = [\oint (u, w) \cdot d\mathbf{l}]/A$. Here $d\mathbf{l}$ is the vector length along the side of the grid cell. An average of the non-dimensional maximum vorticity $\omega^* = \bar{\omega}_{max}/(c_0/H)$ is calculated over the vortices located in the local area and in the global area $-13.3 < (x - x_{trough})/H < -4.3$. The results of averaging over the broader range are illustrated in Figure 4C. The respective standard deviation of ω^* is found to be 1 % ($N = 10, 11$), "refine" and "adapt", 2 % ($N = 12$), "refine", and 3 % ($N = 12$), "adapt".

3.1.3 Proximity between prediction and measurement

The comparison between the computations and the laboratory experiments by Carr et al. (2008), presented in § 3.1.1, is also included in Figure 3. The simulation conducted with $N = 12, N_+ = 14$ is marked in the figure by 14_+.

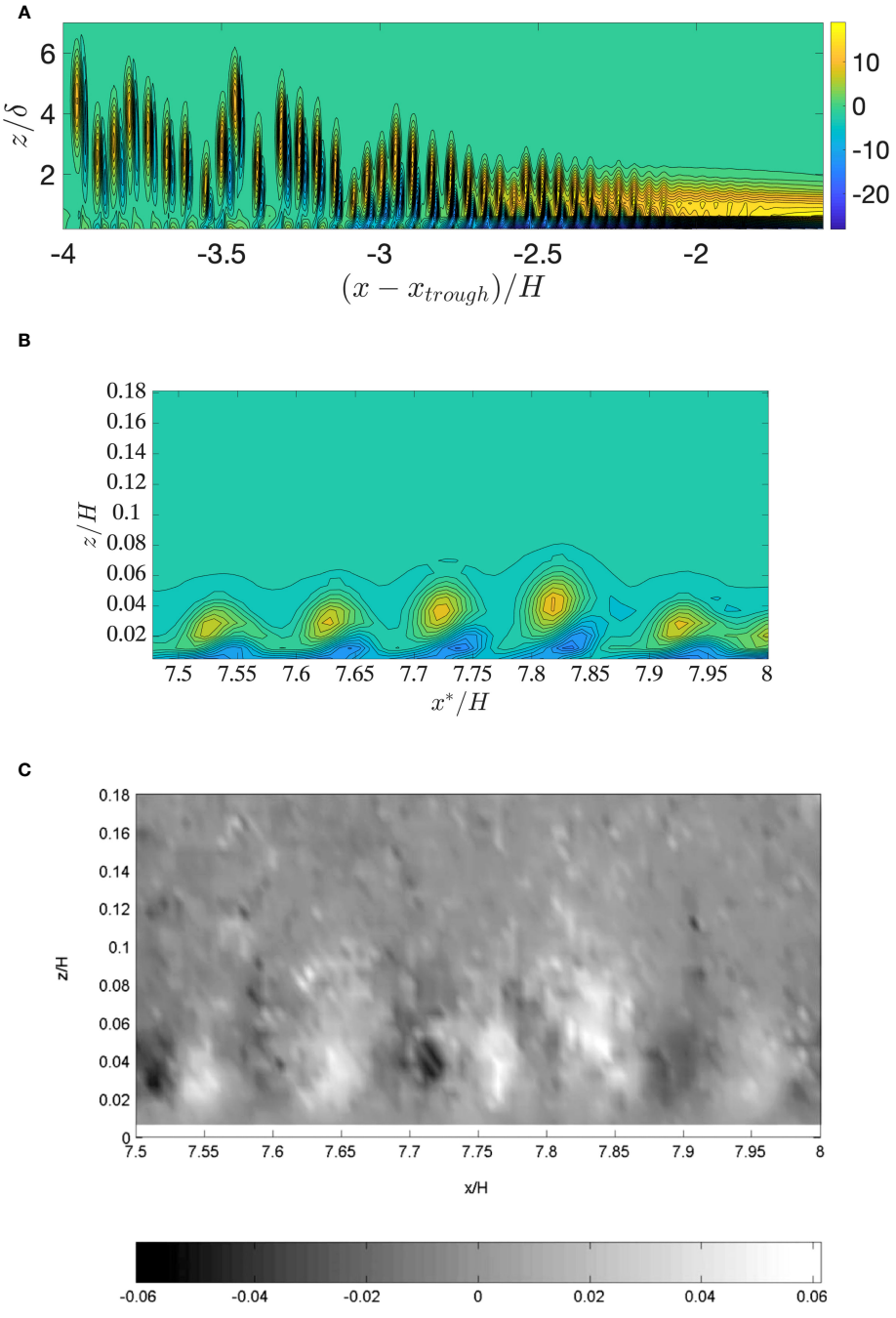

FIGURE 2
(A) Vorticity field $\omega/(c_0/H)$ (color scale, black contour lines of ω) vs. horizontal position. **(B)** $\omega/(c_0/H)$ with horizontal position $x^*/H = ct/H$ + constant corresponding to the measurement area in c). **(C)** Image: Reprinted from Carr et al., (2008), with the permission of AIP Publishing. Vortices displayed by their vertical velocity at time tc_0/H = 6.4.

This subsection illustrates that the model very well reproduces the laboratory experiment in the 3D wave tank by Carr et al. (2008). The predictions and measurements are very close. Moreover, the 2D laminar calculations illustrate that the dominant processes in the laboratory experiments are dominated by 2D processes. The processes investigated by Carr et al. (2008) are indeed dominated by two-dimensionality. This correspondence lasts up to a distance of eight water depths behind the wave trough.

The computations in this section illustrate the convergence of the method where the vorticity and the distance between the vortices are evaluated. The computed and measured averaged separation distance at 7.8 ± 0.2 water depths behind the trough correspond. The vorticity strength is computed, where this motion property was not measured in the laboratory. The calculated amplitude and wave speed were both converged. These findings respond to research points 1 – 3 of the introduction.

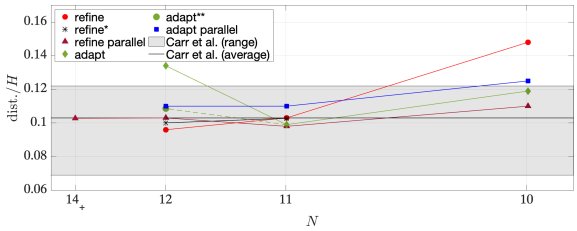

FIGURE 3
Vortex separation distance (dist.) over the local area versus the resolution level N. The result from the simulation with N = 12, N+ = 14 is marked by N = 14+. The black line corresponds to the experimental average local distance. The grey-shaded area corresponds to the measured individual separation distance in Figure 2C. Simulations without parallelization: refine ○, refine*∗, adapt ♦ and adapt** ○.Simulations with parallelization: refine △ and adapt □.

3.2 Tracer particles

3.2.1 Trajectories

As seen in section 3.1.1, the wave-induced velocity field interacts with the bottom, and vortices are being ejected from the bottom boundary layer (BBL). In this section we explore how the wave-induced velocity field moves a cloud of tracer particles, initially found in the BBL, upstream of the ISW. The tracer particles are located approximately between $x/H = 6.4$ and 8.4 before time zero, and the simulations are conducted with wave Reynolds number in the range $Re_w \sim 5.9 \cdot 10^4 - 6.5 \cdot 10^5$ (Table 1).

In our numerical simulations, we can only generate one wave and not a train of waves as may be observed in the coastal ocean (e.g., Quaresma et al., 2007; Zulberti et al., 2020). We let the wave intercept the tracer particle cloud twice, first during the propagation along the undisturbed fluid and second as a reflected wave from the right end of the tank. When the wave becomes a reflected wave, the horizontal velocity changes the sign, while the vertical velocity maintains the sign. During wave passage one, the time runs from 0 to $tc_0/H \simeq 19.6$ and 21.0 for Strat.1 and Strat.2, respectively, and is defined as the transit until the wave encounters the right end wall. Then the wave passage two stage starts and endures until $tc_0/H \simeq$ 40.7 and 44.7 for Strat.1 and Strat.2, respectively.

The wave propagating from left to right induces a velocity of the lower fluid layer in the opposite direction of the wave propagation, pushing the fluid backward. The vertical velocity in the forward part of the wave is also negative, pushing the fluid downward. When the wave encounters the cloud of tracer particles, the tracer particles are first driven backward, approximately a horizontal distance of $1H$ for Strat. 1 (visualized in in Figures 5, 6) and $1.5H$ for Strat. 2 (results are not shown). The figures display the traces of 12 random tracer particles out of the 25 600 tracer particles implemented. The colors are constant according to the vertical position of tracer particles before time zero.

The trajectory of the tracer particles has the same shape as the wave displacement before the vortices intercept the tracer particles' movement. The tracer particles are then displaced vertically. The vortices intercept the cloud of the leftmost tracer particles when the wave trough is at approximately $x_{trough}/H \simeq 7.7$ when $Re_w = 5.9 \cdot 10^4$, see Figures 5A, B. The integration illustrates how the displacements and paths depend on the location of the tracer particle before time zero.

Figures 5B, D illustrate the trajectories in a reference frame that follows the wave. The time period illustrated lies between $ct/H = -10$ to -69. In the figures, the black vertical line indicates when the wave trough is at $x_{trough}/H = 7.6$. The solid red line is a time $tc_0/H = 6.4$ later and shows the position x_{trough}/H at this time. The dashed red line indicates x_{trough}/H when the wave begins its encounter with the wall.

The trajectories at the beginning are almost horizontal, with some small fluctuations. The vortices behind the trough intercept the tracer particles, where the tracers acquire an oscillatory behavior of a range of wavelengths. They are in the range from $0.3H$ (Run 4) up to $16H$ (Run 1). The shortest wavelengths are in the same order of magnitude as the separation distance of the vortices generated behind the trough when the instability saturates. Run 4 exhibits very short wavelengths and a wavelength of $10H$.

The wave propagates to the end of the tank and returns. The wave intercepts again with the group of tracer particles, visualized in Figures 5, 6, plots C and D. During the second passage, the tracer particles are moved further upward. The vertical position, relative to the boundary layer δ, depends on the Reynolds number. In Figure 6C, the uppermost position after wave passage one is $z/\delta \simeq$ 13 and $z/\delta \simeq 55$ after wave passage two.

Figures 7 and 8 show paths due to 128 tracer particles. Plots A and C display that the downstream vortices transport the tracer particles upwards and out of the boundary layer. In plots b and d, the second wave encounter and its induced instabilities move the tracer particles even higher.

3.2.2 Displacements

The terminal position of a number of 25 600 particles are then discussed (Figure 9). The 50th (median) and 90th percentile of the vertical tracer particle position are evaluated. For the 90th percentile, the vertical height increases by a factor of three between passage one and passage two. The vertical displacement of the 50th percentile is similar, although there are some large variations at the moderate Re_w (Table 2). For the same percentile, the height relative to δ increases by a factor of 2.4, approximately, when the wave Reynolds number increases by a factor of 10. The horizontal position of the tracer particle cloud is negative during the first passage and positive during the second passage due to the reflected wave. The net horizontal displacement of the tracer

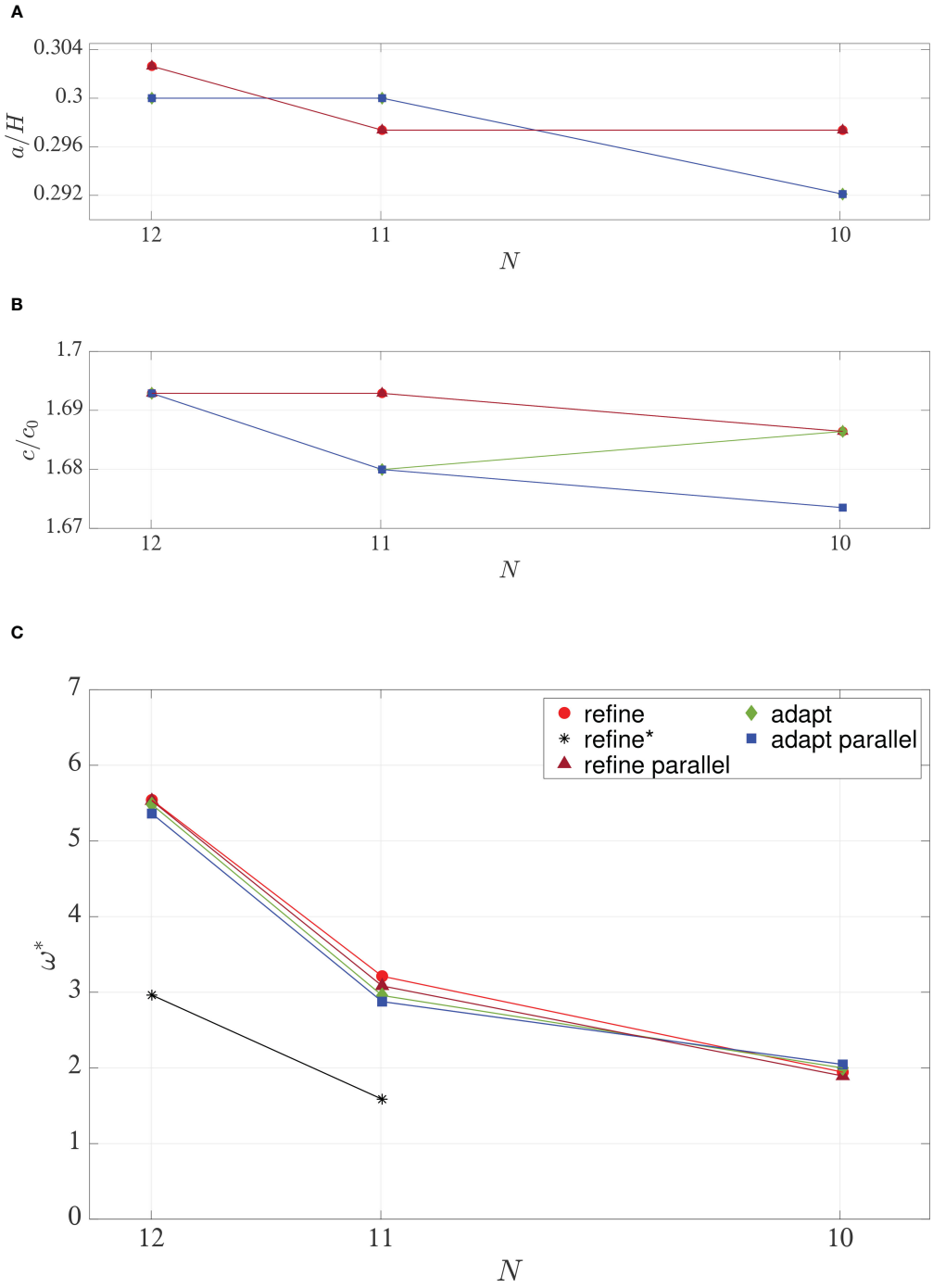

FIGURE 4
(A) Wave amplitude *a/H*, **(B)** speed c/c0 and **(C)** maximum vorticity $\omega^* = \bar{\omega}_{max}/(c_0/H)$ versus resolution level *N*. Simulations without parallelization: refine ○, refine* ∗, and adapt ◆. Simulations with parallelization: refine △ and adapt □.

particle cloud is approximately zero. The red lines in the figure indicate the tracer particles' left and right most horizontal seeded position before time zero.

The probability density function (PDF) of the tracer particles' vertical position as a function of time is illustrated in Figure 10. The black line indicates the initial uppermost vertical position of the tracer particles. The blue line indicates the tracer particle distribution after wave passage one. The red line provides the tracer particle distribution when the wave has intercepted the cloud of tracer particles for the second time. After passage one, tracer particle distribution is below 20δ, and after passage two, below 65δ for the large $Re_w \sim 5.9 - 6.5 \cdot 10^5$. The similar numbers for the smaller $Re_w \sim 5.9 - 6.5 \cdot 10^4$ are 10δ and 25δ, respectively.

The results imply that the particles are found below a vertical level of approximately $0.23H$ after the second passage for both Reynolds numbers.

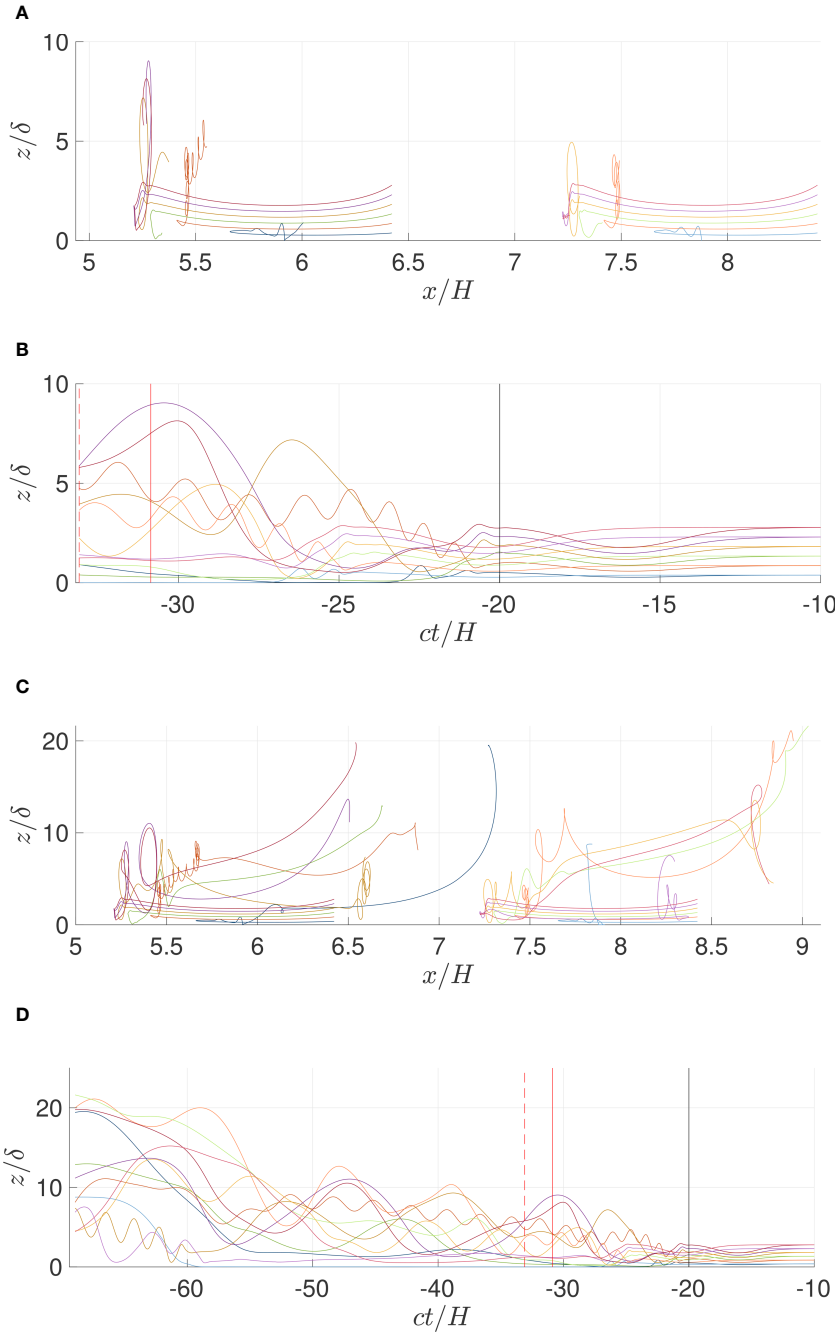

FIGURE 5
Tracer particle trajectories for Re_w = 5.9 · 10^4. **(A, C)** Fixed frame of reference. **(B, D)** Frame of reference following the wave. In **(A, B)** wave passage one, tc_0/H = 0 – 19.6. In **(C, D)** wave passage two, tc_0/H = 0 – 40.7.

3.3 Comparison to field measurements

Quaresma et al. (2007) conducted a field study of internal waves propagating over the northern shelf of Portugal over a canyon head. The local water depth was measured to be ∼ 80 m with a middle depth of the pycnocline of $d/H = 0.19$. The wave amplitudes were in the range $a/H = 0.13 - 0.38$. The measured local sediment concentration mainly consists of sandy sediments (∼ 93 %) of a settling velocity of 2 cm s^{-1}. The remaining sediments, silt and clay components with diameters in the range ∼ 1 – 20 μm were found to remain suspended. Their measurements showed that only the strongest waves were capable of suspending the sediments, contributing to a summer bottom nepheloid layer (BNL) of 10 – 15 m thickness, corresponding to $0.13 - 0.19H$.

We note that the vertical height of the tracer particles after wave passage two was found to be approximately $0.23H$ in our numerical computations and was insensitive to the Re_w. This tracer particle height is in correspondence with the height of the BNL measured by Quaresma et al. (2007).

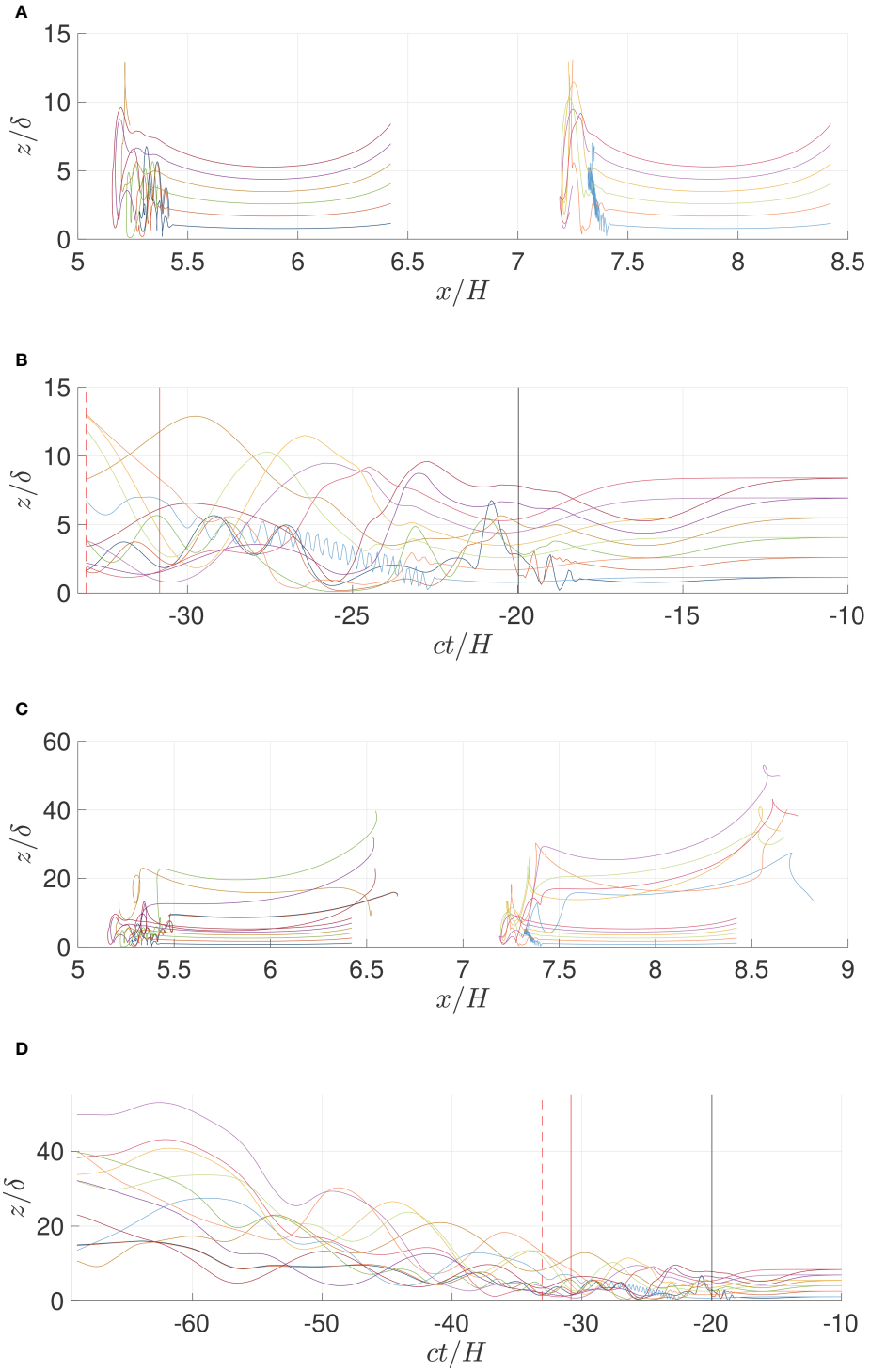

FIGURE 6
Same as Figure 3 **(A–D)** but with $Re_w = 5.9 \cdot 10^5$.

Quaresma et al. (2007) also measured a strong local sediment concentration up to a height of $0.56H$ below the leading wave. Our present computation does not exhibit such an effect.

Zulberti et al. (2020) conducted field observations of nonlinear internal waves over a low-gradient topography on Australia's Northwest Shelf. They observed that large-amplitude internal waves of depression greatly enhanced the sediment transport. From sediment grab samples, they deduced that the bed sediment was of typical silt. The settling velocity of silt particles of density $\rho_s = 1350$ kg m^{-3} and diameter of 30 μm, may be calculated to be $U = 0.014$ cm s^{-1}. They measured sediment resuspension to exceed 20 m ($0.08H$) beneath the leading wave of amplitude $a/H = 0.3$. However, they measured a density gradient at this level, limiting the advancement of bottom sediments. A direct correspondence

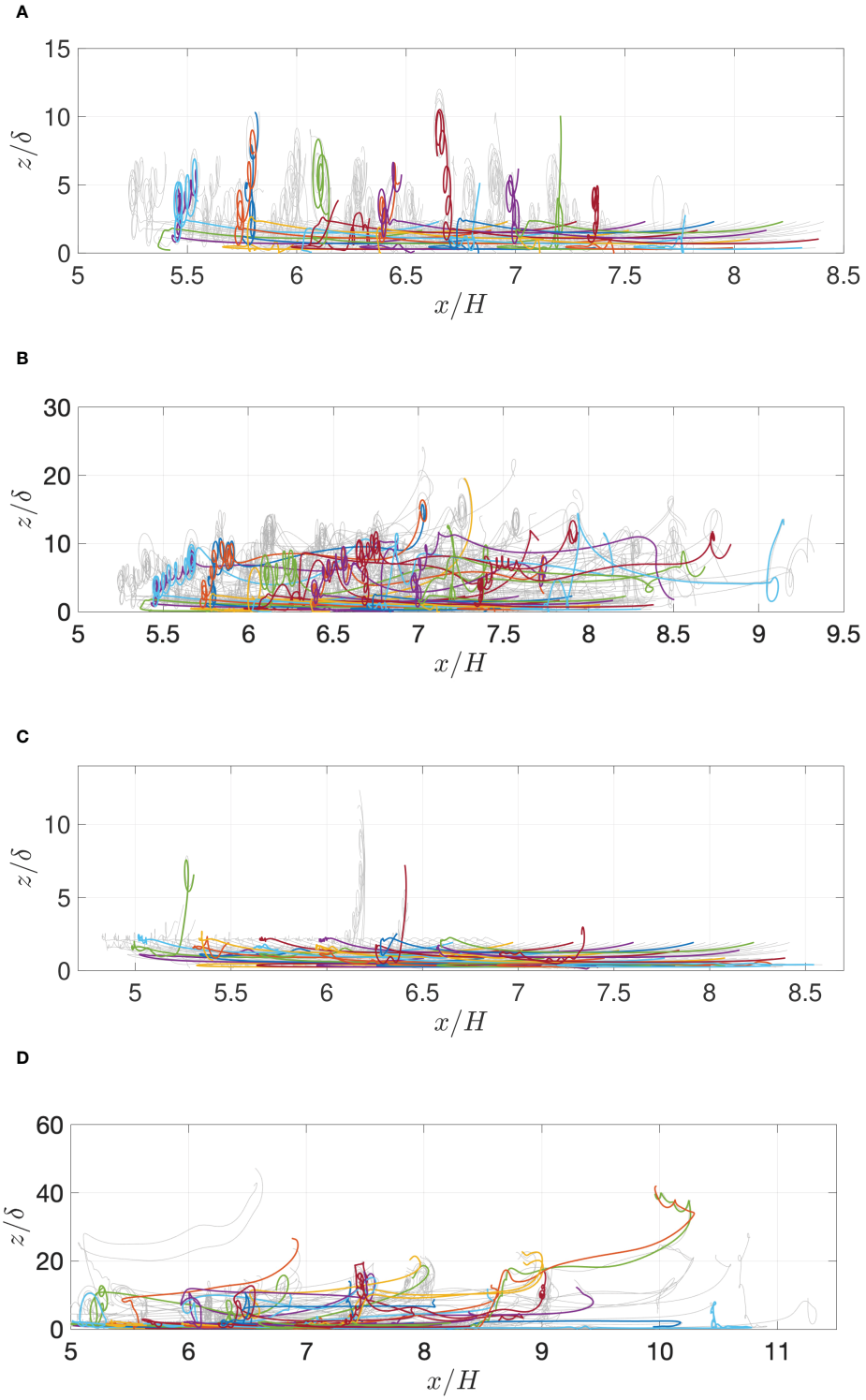

FIGURE 7
Tracer particle trajectories of 128 particles. **(A)** $Re_w = 5.9 \cdot 10^4$. Wave passage one, $tc_0/H = 0 - 19.6$. **(B)** $Re_w = 5.9 \cdot 10^4$. Wave passage two, $tc_0/H = 0 - 40.7$. **(C)** $Re_w = 6.5 \cdot 10^4$. Wave passage one, $tc_0/H = 0 - 21.0$. **(D)** $Re_w = 6.5 \cdot 10^4$. Wave passage two, $tc_0/H = 0 - 44.7$.

between the measurements and the present computations are not realistic because we have not included a weak stratification layer at the bottom. One of the factors driving the resuspension mechanism in the measurement of Zulberti et al. (2020), was a vertical pumping mechanism associated with the compression underneath the wave trough followed by a subsequent expansion of the mixing-layer at the bottom. This effect is included in our simulations, however.

Finally, the subjects discussed in these result sections 3.2 and 3.3 include the tracer particles, the vertical tracer particle displacement during the wave encounters, as well as comparison to observations

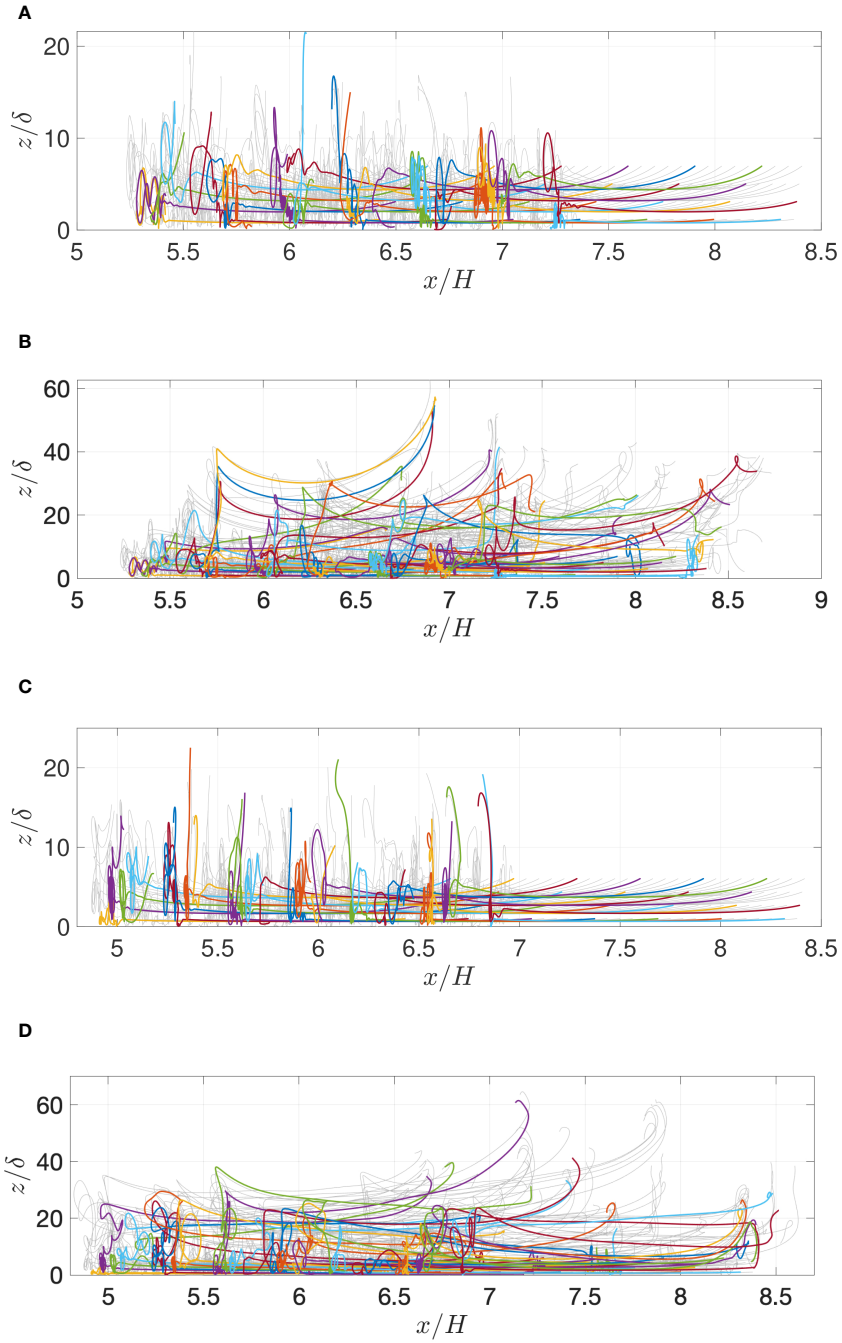

FIGURE 8
Same as Figure 7 but with **(A)** and **(B)** $Re_w = 5.9 \cdot 10^5$. **(C, D)** $Re_w = 6.5 \cdot 10^5$.

in the field, and response to the research subject 4, 5, and 6 as presented in the introduction.

4 Conclusions

By a 2D laminar method, the vortex formation and the tracer particle motion in the bottom boundary layer of the water column of a fluid layer, driven by large internal solitary waves of depression, are calculated. The motion in a numerical wave tank for internal waves is simulated. Comparison is made to a set of available laboratory observations, and a very good match between the model and the laboratory measurements is found. Convergence of the numerical calculation of the vortex formation is documented.

A cloud of tracer particles in the bottom boundary layer obtains vertical displacements because of the wave-driven vortices. The paths exhibit the following properties: when the wave approaches the tracer particle cloud, the tracer particles are first moved horizontally in the opposite direction of the wave. Behind the wave trough, the tracer particles are transported vertically in the

10.3389/fmars.2023.1155270

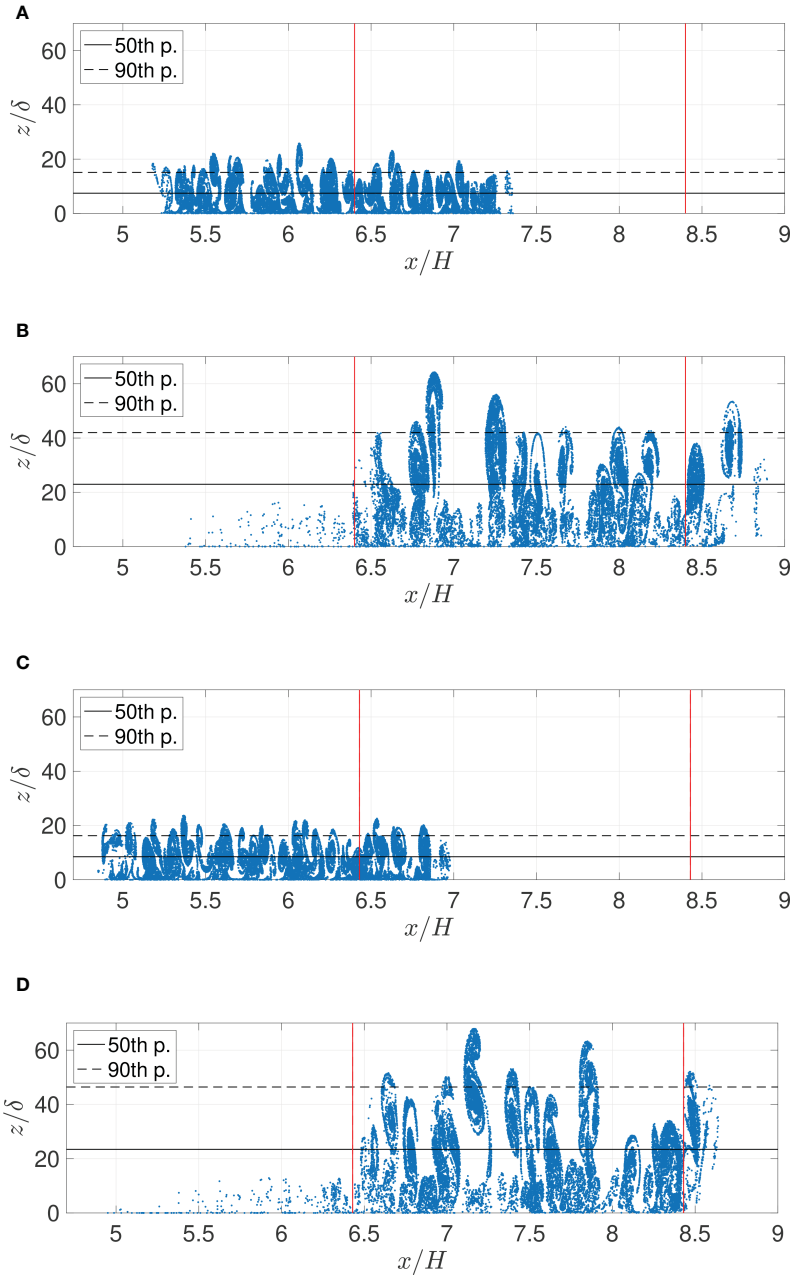

FIGURE 9
Snapshots of the Lagrangian tracer particle density field. The black solid line indicates the 50th percentile (median depth) of the tracer particles vertical height and the black dashed line indicates the layer containing up to 90% of all of the tracer particles. The red lines indicate the tracer particles' left and right most horizontal seeded position before time zero. **(A)** Rew = 5.9 · 10^5. Wave passage one, tc_0/H = 19.6. **(B)** Re_w = 5.9·10^5. Wave passage two, tc_0/H = 40.7. **(C)** Re_w = 6.5·10^5. Wave passage one, tc_0/H = 21.0. **(D)** Re_w = 6.5 · 10^5. Wave passage two, tc_0/H = 44.7.

TABLE 2 The vertical location z/δ corresponding to the 50th and 90th percentiles of the tracer particle density field for wave passage one and two.

	Passage one		Passage two				
Run	50%	90%	50%	90%	$\delta \cdot 10^{-3}$ (m)	Re_δ	Re_w
1	4.5	8.3	7.1	15.6	3.68	490	5.9 10^4
3	1.4	4.7	9.2	20.4	4.44	631	6.5 10^4
2	7.4	15.1	23.0	42.0	1.22	1620	5.9 10^5
4	8.9	16.2	23.5	46.4	1.46	2080	6.5 10^5

Boundary layer thickness, Re_δ, Re_w. Runs 1 – 4.

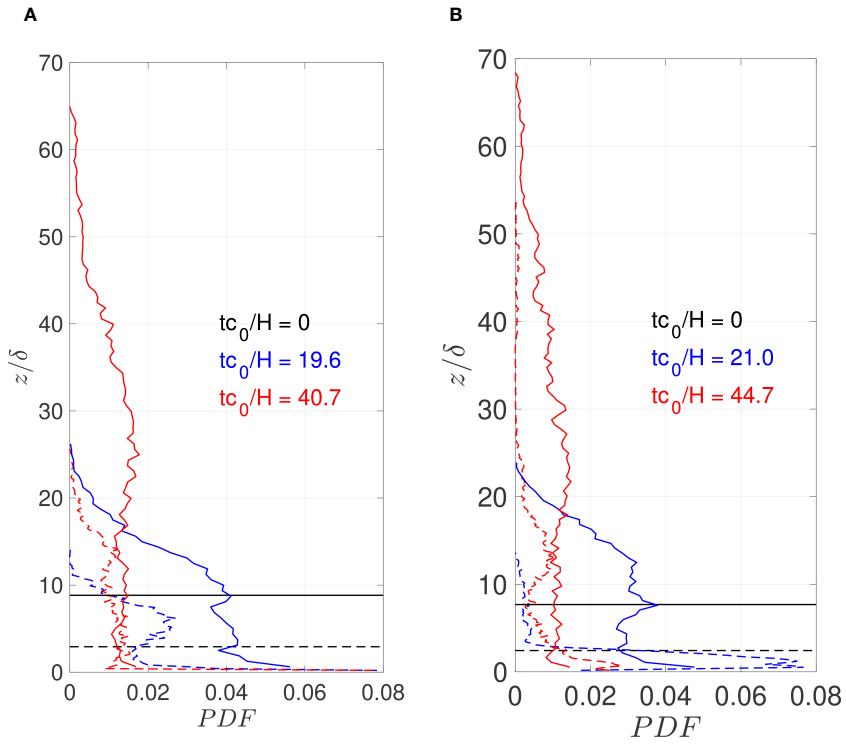

FIGURE 10
Probability distribution function of the vertical position of the tracer particles relative to the boundary layer thickness δ. **(A)** $Re_w = 5.9 \cdot 10^4$ (dashed lines) and $5.9 \cdot 10^5$ (solid lines). Black line, $tc_0/H = 0$; blue line, tc0/H = 19.6 (wave passage one); red line, $tc_0/H = 40.7$ (wave passage two). **(B)** $Re_w = 6.5 \cdot 10^4$ (dashed lines) and $6.5 \cdot 10^5$ (solid lines). Black line, $tc_0/H = 0$; blue line, $tc_0/H = 21.0$ (wave passage one); red line, $tc_0/H = 44.7$ (wave passage two).

water column. The wave is reflected and returns to the tracer particle cloud. At the second passage, the tracer particles are moved in the opposite direction of the wave propagation. The vortices behind the trough transport the tracer particles further vertically. The tracer particles are found below a vertical level of approximately $0.23H$ after the second passage, for the Reynolds number in the range $Re_w \sim 5.9 \cdot 10^4 - 6.5 \cdot 10^5$. The net horizontal transport of the tracer particle cloud is approximately zero.

We have compared the results to available field observations by Quaresma et al. (2007), obtained at the northern shelf of Portugal, where the local depth was 80 m. The wave amplitude was in the range $a/H = 0.13 - 0.38$, and a summer bottom nepheloid layer was measured to be 10 – 15 m, corresponding to $0.13 - 0.19H$. Our computational results are in a fair match with that observation. We note that the processes in the computations at the moderate scale and the processes at the field scale may not be directly similar, however. In another field measurement by Zulberti et al. (2020), large amplitude internal waves of depression were found to resuspend the sediments at the sea bed greatly. In their measurements, a density gradient at 20 m ($0.08H$) above the sea bottom was found to limit the vertical advancement of the bottom sediments. Direct correspondence to the present computations is not realistic.

Data availability statement

The raw data supporting the conclusions of this article will be made available by the authors, without undue reservation.

Author contributions

TE, JG, and JS contributed to the conception and methodology of the study. TE and JS wrote the code. TE performed the processing of the data. Visualization by TE and JG. TE wrote the first draft of the manuscript. TE and JG wrote the submitted manuscript. All authors contributed to the article and approved the submitted version.

Funding

The funding by the Research Council of Norway (Ecopulse, NFR300329) is gratefully acknowledged.

Acknowledgments

The discussions with Dr. Johannes Röhrs are acknowledged. The computations were performed on the Norwegian Research and Education Cloud (NREC), using resources provided by the University of Bergen and the University of Oslo. http://www.nrec.no/. The authors would like to acknowledge the referees for helpful comments.

Conflict of interest

The authors declare that the research was conducted in the absence of any commercial or financial relationships that could be construed as a potential conflict of interest.

Publisher's note

References

Aghsaee, P., Boegman, L., Diamessis, P. J., and Lamb, K. G. (2012). Boundary-layer-separation driven vortex shedding beneath internal solitary waves of depression. *J. Fluid Mech.* 690, 321–344. doi: 10.1017/jfm.2011.432

Bell, J. B., Colella, P., and Glaz, M. G. (1989). A second-order projection method for the incompressible Navier-Stokes equations. *J. Comp. Phys.* 85, 257–283. doi: 10.1016/0021-9991(89)90151-4

Boegman, L., and Stastna, M. (2019). Sediment resuspension and transport by internal solitary waves. *Annu. Rev. Fluid Mech.* 51, 129–154. doi: 10.1146/annurev-fluid-122316-045049

Bogucki, D., Dickey, T., and Redekopp, L. G. (1997). Sediment resuspension and mixing by resonantly generated internal solitary waves. *J. Phys. Oceanogr.* 27, 1181–1196. doi: 10.1175/1520-0485(1997)027(1181:SRAMBR)2.0.CO;2

Bogucki, D. J., and Redekopp, L. G. (1999). A mechanism for sediment resuspension by internal solitary waves. *Geophys. Res. Lett.* 26, 1317–1320. doi: 10.1029/1999GL900234

Bourgault, D., Blokhina, M. D., Mirshak, R., and Kelley, D. E. (2007). Evolution of a shoaling internal solitary wave train. *Geophys. Res. Lett.* 34, L03601–1–5. doi: 10.1029/2006GL028462

Carr, M., and Davies, P. A. (2006). The motion of an internal solitary wave of depression over a fixed bottom boundary in a shallow, two-layer fluid. *Phys. Fluids* 18, 016601. doi: 10.1063/1.2162033

Carr, M., Davies, P. A., and Shivaram, P. (2008). Experimental evidence of internal solitary wave-induced 454 global instability in shallow water benthic boundary layers. *Phys. Fluids* 20, 066603. doi: 10.1063/1.2931693

Carr, M., Stastna, M., Davies, P. A., and van de Wal, K. J. (2019). Shoaling mode-2 internal solitary-like waves. *J. Fluid Mechanics* 879, 604–632. doi: 10.1017/jfm.2019.671

Chorin, A. (1968). Numerical solution of the Navier-Stokes equations. *Math. Comp.* 22, 745–762. doi: 10.1090/S0025-5718-1968-0242392-2

Diamessis, P. J., and Redekopp, L. G. (2006). Numerical investigation of solitary internal wave-induced global instability in shallow water benthic boundary layers. *J. Phys. Oceanogr.* 36, 784–812. doi: 10.1175/JPO2900.1

Fructus, D., Carr, M., Grue, J., Jensen, A., and Davies, P. A. (2009). Shear-induced breaking of large internal solitary waves. *J. Fluid Mech.* 620, 1–29. doi: 10.1017/S0022112008004898

Fructus, D., and Grue, J. (2004). Fully nonlinear solitary waves in a layered stratified fluid. *J. Fluid Mechanics* 505, 323–347. doi: 10.1017/S0022112004008596

Grue, J., Jensen, A., Rusås, P.-O., and Sveen, J. K. (1999). Properties of large-amplitude internal waves. *J. Fluid Mech.* 380, 257–278. doi: 10.1017/S0022112098003528

Helfrich, K. R., and Melville, W. K. (2006). Long nonlinear internal waves. *Annu. Rev. Fluid Mech.* 38, 395–425. doi: 10.1146/annurev.fluid.38.050304.092129

Lamb, K. G. (2014). Internal wave breaking and dissipation mechanisms on the continental slope/shelf. *Annu. Rev. Fluid Mech.* 46, 231–254. doi: 10.1146/annurev-fluid-011212-140701

López-Herrera, J. M., Popinet, S., and Castrejón-Pita, A. A. (2019). An adaptive solver for viscoelastic incompressible two-phase problems applied to the study of the splashing of weakly viscoelastic droplets. *J. Non-Newtonian Fluid Mech.* 264, 144–158. doi: 10.1016/j.jnnfm.2018.10.012

Mostert, W., and Deike, L. (2020). Inertial energy dissipation in shallow-water breaking waves. *J. Fluid Mechanics* 890, A12. doi: 10.1017/jfm.2020.83

Necker, F., Härtel, C., Kleiser, L., and Meiburg, E. (2005). Mixing and dissipation in particle-driven gravity currents. *J. Fluid Mechanics* 545, 339–372. doi: 10.1017/S0022112005006932

Popinet, S. (2003). Gerris: a tree-based adaptive solver for the incompressible Euler equations in complex geometries. *J. Comp. Phys.* 190, 572–600. doi: 10.1016/S0021-9991(03)00298-5

Popinet, S. (2009). An accurate adaptive solver for surface-tension-driven interfacial flows. *J. Comp. Phys.* 228, 5838–5866. doi: 10.1016/j.jcp.2009.04.042

Popinet, S. (2011). Quadtree-adaptive tsunami modelling. *Ocean Dyn.* 61, 1261–1285. doi: 10.1007/s10236-011-0438-z

Popinet, S. (2015). A quadtree-adaptive multigrid solver for the Serre-Green-Naghdi equations. *J. Comp. Phys.* 302, 336–358. doi: 10.1016/j.jcp.2015.09.009

Popinet, S. (2020). A vertically-Lagrangian, non-hydrostatic, multilayer model for multiscale free-surface flows. *J. Comp. Phys.* 418, 109609. doi: 10.1016/j.jcp.2020.109609

Popinet, S. and collaborators (2013–2023)Basilisk. Available at: http://basilisk.fr (Accessed 18.10.2021).

Quaresma, L. S., Vitorino, J., Oliveira, A., and da Silva, J. (2007). Evidence of sediment resuspension by nonlinear internal waves on the western Portuguese mid-shelf. *Mar. Geol.* 246, 123–143. doi: 10.1016/j.margeo.2007.04.019

Sakai, T., Diamessis, P. J., and Jacobs, G. B. (2020). Self-sustained instability, transition, and turbulence induced by a long separation bubble in the footprint of an internal solitary wave. I. Flow topology. *Phys.Rev. Fluids* 5, 103801. doi: 10.1103/PhysRevFluids.5.103801

Sanderse, B., and Veldman, A. (2019). Constraint-consistent Runge–Kutta methods for one-dimensional incompressible multiphase flow. *J. Comput. Phys.* 384, 170–199. doi: 10.1016/j.jcp.2019.02.001

Stastna, M., and Lamb, K. G. (2008). Sediment resuspension mechanisms associated with internal waves in coastal waters. *J. Geophys. Res.* 113, C10016–1–19. doi: 10.1029/2007JC004711

Sveen, J. K., Guo, Y., Davies, P. A., and Grue, J. (2002). On the breaking of internal solitary waves at a ridge. *J. Fluid Mech.* 469, 161–188. doi: 10.1017/S0022112002001556

van Hooft, J. A., Popinet, S., van Heerwaarden, C. C., van der Linden, S. J. A., de Roode, S. R., and van de Wiel, B. J. H. (2018). Towards adaptive grids for atmospheric boundary-layer simulations. *Boundary-Layer Meteorol.* 167, 421–443. doi: 10.1007/s10546-018-0335-9

Zulberti, A., Jones, N. L., and Ivey, G. N. (2020). Observations of enhanced sediment transport by nonlinear internal waves. *Geophys. Res. Lett.* 47, 1–11. doi: 10.1029/2020GL088499

Appendix A: Finite Volume Solver

A.1. Time integration

The discretization in time is staggered and second-order accurate. The advection term is calculated using the Bell-Colella-Glaz scheme Bell et al., 1989. The unsplit, upwind scheme reads:

$$\rho_{n+\frac{1}{2}}\left[\frac{\mathbf{u}_{n+1}-\mathbf{u}_n}{\Delta t}+\mathbf{u}_{n+\frac{1}{2}}\cdot\nabla\mathbf{u}_{n+\frac{1}{2}}\right] = -\nabla p_{n+\frac{1}{2}}+\nabla\cdot[\mu_{n+\frac{1}{2}}(\mathbb{D}_n+\mathbb{D}_{n+1})]+\rho_{n+\frac{1}{2}}\mathbf{a}_{n+\frac{1}{2}}, \quad (13)$$

$$\frac{f_{n+\frac{1}{2}}-f_{n-\frac{1}{2}}}{\Delta t}+\nabla\cdot(f_n\mathbf{u}_n)=0, \quad (14)$$

$$\nabla\cdot\mathbf{u}_n=0, \quad (15)$$

where $\mathbb{D}=(\nabla u+(\nabla u)^T)/2)$ is the strain rate tensor, where $()^T$ denotes transpose. The index n indicates time t_n, and likewise for $n+1$, $n+1/2$, $n-1$, etc.

An equivalent advection equation of the volume fraction replaces the advection equation of the density. The density and viscosity are defined using the averages $\rho(\tilde{f})=\tilde{f}(\rho_1-\rho_2)+\rho_2$ and $\mu(\tilde{f})=[\tilde{f}(1/\mu_1-1/\mu_2)+1/\mu_2]^{-1}$, where ρ_1, μ_1, and ρ_2, μ_2 are the densities and dynamic viscosities of the upper and lower fluid layers, respectively. The field $\tilde{f}$ is constructed by applying a smoothing spatial filter to f. This is accomplished by averaging the four corner values of f obtained from the cell-centered values by bilinear interpolation. The fluid properties are updated by:

$$\rho_{n+\frac{1}{2}}=\tilde{f}_{n+\frac{1}{2}}(\rho_1-\rho_2)+\rho_2, \quad (16)$$

$$\mu_{n+\frac{1}{2}}=[\tilde{f}_{n+\frac{1}{2}}(1/\mu_1-1/\mu_2)+1/\mu_2]^{-1}. \quad (17)$$

By using a classical time-splitting projection method Chorin, 1968, the system is further simplified:

$$\rho_{n+\frac{1}{2}}\left[\frac{\mathbf{u}_\star-\mathbf{u}_n}{\Delta t}+\mathbf{u}_{n+\frac{1}{2}}\cdot\nabla\mathbf{u}_{n+\frac{1}{2}}\right] = \nabla\cdot[\mu_{n+\frac{1}{2}}(\mathbb{D}_n+\mathbb{D}_\star)]+\rho_{n+\frac{1}{2}}\mathbf{a}_{n+\frac{1}{2}}, \quad (18)$$

$$\frac{f_{n+\frac{1}{2}}-f_{n-\frac{1}{2}}}{\Delta t}+\nabla\cdot(f_n\mathbf{u}_n)=0. \quad (19)$$

The velocity at the new time is found by combining equations 13 and 18. Hence,

$$\mathbf{u}_{n+1}=\mathbf{u}_\star-\frac{\Delta t\,\nabla p_{n+\frac{1}{2}}}{\rho_{n+\frac{1}{2}}}. \quad (20)$$

The equation for the pressure is found by requiring

$$\nabla\cdot\mathbf{u}_{n+1}=0. \quad (21)$$

This leads to a Poisson equation for the pressure

$$\nabla\cdot\left[\frac{\Delta t\,\nabla p_{n+\frac{1}{2}}}{\rho_{n+\frac{1}{2}}}\right]=\nabla\cdot\mathbf{u}_\star. \quad (22)$$

The time step in each iteration is controlled by the Courant-Friedrich-Levy CFL condition.

A.2. Spatial discretization

The quadtree structure can be seen as a family tree. An important parameter is the level N of a given cell of the tree. The *root* cell is that corresponding to N=0, from which the cells at the next level hang down. A *parent* cell at (level N) can have zero or four *children* cells, where the children are at level $N+1$. If the cell has no *children* it is called a *leaf* cell. The size of a cell is characterized by its level N, where it is located. Hence, the grid size of the cells at that level is $\Delta_N=L/2^N$. The cells are square finite volume cells, providing $\Delta_N=\Delta x=\Delta z$, where (x,z) are the horizontal and vertical coordinates.

Further, a few restrictions apply. For example, the maximum difference of the level between two neighboring *leaf* cells is one; each cell has a direct neighbor at the same level; the level increases by one for each successive generation; the grid can be refined and coarsened dynamically adapted as the simulation proceeds, where this occurs at an affordable computational cost. We have used two central representations of the numerical grid, a non-adaptive static grid mesh and an adaptive mesh.

1. *"Refine"*:

Refine static grid refinement is referred to when the simulation is run with the same level of refinement in the mesh hierarchy.

2. *"Adapt"*:

The adaptive mesh hierarchy enables increase/decrease of the grid resolution where necessary. Such an approach can significantly reduce the memory required to obtain a given level of accuracy. The algorithm is based on the estimation of the numerical errors in the representation of the spatially discretized fields. This analysis is used to determine which grid cells require refinement, and wherein the domain cells can be coarsened. Following van Hooft et al. (2018) and López-Herrera et al. (2019), a scalar field g_N discretized at grid level N, can be coarsened one level down utilizing a downsampling operation denoted by *restriction*, g_{N-1}=*restriction*(g_N). Next, the upsampled (or prolongated) operator, which upsamples the coarser field distribution, g_{N-1}, to the original level, g_N^0=*prolongation*(g_{N-1}), is defined. The prolongation procedure is second-order accurate. Noting that in general $g_N\neq g_N^0$, a comparison provides an estimation of the absolute discretization error, $\zeta_N=|g_N-g_N^0|$. A particular cell i with level N in which the error is ζ_N^i, will be,

- refined if $\zeta_N^i>\zeta$,
- coarsened if $\zeta_N^i<2\zeta/3$,
- remain unchanged otherwise,

where ζ is called the refinement criterion and is the error threshold set in the numerical scheme. The "refine" and "adapt" procedures are used in the present study. Further details of the algorithm can be found in Popinet (2003) and van Hooft et al. (2018).

Near the resolution boundaries, ghost cells are generated as virtual cells. This allows for simple Cartesian stencil operations, for the typically uneven grid at the boundary. The ghost cells have neighbours with the same refinement level N, whereas their values are defined by interpolating the original field values.

frontiers | Frontiers in Marine Science

TYPE Original Research
PUBLISHED 27 March 2024
DOI 10.3389/fmars.2024.1364960

OPEN ACCESS

EDITED BY
Yan Li,
University of Bergen, Norway

REVIEWED BY
Hailun He,
Ministry of Natural Resources, China
Xingya Feng,
Southern University of Science and Technology, China

*CORRESPONDENCE
Ting Yu
julia_yu_nmdis@163.com
Zengan Deng
dengzengan@163.com

RECEIVED 03 January 2024
ACCEPTED 04 March 2024
PUBLISHED 27 March 2024

CITATION
Yu T, Deng Z, Zhang C and Hamdi Ali A (2024) Detecting the role of Stokes drift under typhoon condition by a fully coupled wave-current model.
Front. Mar. Sci. 11:1364960.
doi: 10.3389/fmars.2024.1364960

Detecting the role of Stokes drift under typhoon condition by a fully coupled wave-current model

Ting Yu[1*], Zengan Deng[2*], Chi Zhang[2] and Amani Hamdi Ali[3]

[1]National Marine Data and Information Service, Tianjin, China, [2]School of Marine Science and Technology, Tianjin University, Tianjin, China, [3]Egyptian Meteorology Authority, Cairo, Egypt

The impacts of Stokes drift and sea-state-dependent Langmuir turbulence (LT) on the three-dimensional ocean response to a tropical cyclone in the Bohai Sea are studied through two-way coupled wave-current simulations. The Stokes drift is calculated from the simulated wave spectrum of the wave model, Simulating Waves Nearshore (SWAN), and then input to the Princeton Ocean Model with the generalized coordinate system (POMgcs) to represent the Langmuir effect. The Langmuir circulation is included in the vertical mixing of the ocean model by adding the Stokes drift to the shear of the vertical mean current and by including LT enhancements to the Mellor-Yamada 2.5 turbulent closure submodel. Simulations are assessed through the case study of Typhoon Masta in 2005 with a set of diagnostic experiments that incorporated different terms of Stokes production (SP) respectively. It is shown that with the consideration of SP, a deeper mixed layer, an enhanced vertical mixing coefficient K_{MS}, and a more accurate representation of the vertical temperature distribution could be derived. Moreover, the effect of LT in elevating the turbulence mixing is stronger than that of Coriolis Stokes force (CSF) and Craik-Leibovich vortex force (CLVF). LT has a greater influence on the vertical mixing during typhoon than that in normal weather.

KEYWORDS

Bohai Sea, Langmuir turbulence, Stokes drift, Typhoon Matsa, wave-current interaction

1 Introduction

Surface gravity waves can influence the upper ocean in a variety of ways, among which Stokes drift and wave breaking are two main contributors to turbulent kinetic energy (TKE) and turbulent mixing throughout the mixed layer (ML). Compared with wave breaking that injects none-consistent and random energy to a layer a few meters near the air-sea interface (Kantha and Clayson, 2004; Noh et al., 2004; Li et al., 2013; Wu et al., 2015), the Stokes drift plays a stronger large-scale coherent role in influencing the dynamic and thermodynamic structure of the ML (McWilliams and Restrepo, 1999; Zhang et al., 2018; Cao et al., 2019).

The presence of Stokes drift increases the vertical shear instability of the upper ocean, directly contributing to the TKE thus enhancing the upper turbulent mixing. It transports the momentum and heat from the upper ocean to deeper layers, thereby deepening the ML (Kantha and Clayson, 2004; Mellor and Blumberg, 2004; Deng et al., 2012). Consequently, the Stokes drift must be considered in numerical ocean models (Deng et al., 2013) to improve modeling performance and the skill of the operational forecast.

Previous studies suggested that three terms of Stokes drift effect, namely the Stokes production (SP), jointly affect the turbulent mixing in the upper ocean and should be numerically considered. These terms are the large-scale Coriolis-Stokes forcing (CSF) that represents the interaction between the Stokes drift and planetary vorticity (Huang, 1979; Polton et al., 2005; Deng et al., 2012), the small-scale Langmuir turbulence (LT) (Langmuir, 1938; Craik and Leibovich, 1976; McWilliams et al., 1997), and the resolved-scale Craik-Leibovich vortex force (CLVF) (Craik and Leibovich, 1976). A schematic of mixing processes in the upper ocean is provided in Figure 1. Understanding the role of SP in the dynamic and thermal processes of the upper ocean is particularly crucial and useful under extreme weather conditions like typhoons and storm surges.

The sea surface temperature (SST) and ocean current are required by the typhoon/hurricane forecasting model to calculate the air-sea heat and momentum fluxes which are the main contributors to the energy budget of typhoons, thus have a significant impact on the intensity of typhoon. Typhoons/hurricanes cause the upper ocean to react vigorously (Price, 1981; Reichl et al., 2016a, Reichl et al., 2016b), such as the generation of surface waves higher than 20m and the sea surface current > 1m/s, resulting in significant sea surface cooling (Ginis, 2002). The turbulent mixing in the upper ocean boundary layer plays a major role in determining how the SST and current respond to typhoons. When a typhoon passes through a specific location, the large sea surface frictional velocity and surface gravity waves are generated, intensifying the wind-driven mean current shear and Stokes drift. The turbulence caused by vertical shear below the developing surface current significantly deepens the ML (Reichl et al., 2016b). Many studies (Webb and Fox-Kemper, 2011, among others) suggest that SP is the main contributor to the vertical mixing of momentum and temperature/salinity. Accurate knowledge of the kinetic and thermodynamic processes of the ML under strong winds is crucial for marginal waters that are vulnerable to typhoons. By using one-way wave-current coupled model to examine the effects of SP on ocean dynamics in the Bohai Sea during summer, Cao et al. (2019) contend that LT is a common occurrence in the Bohai Sea and has a significant role in modifying the turbulent mixing. Moreover, the role of SP in the upper ocean dynamics under extreme weather such as typhoons deserves further study, since in the operational forecasting, SP terms were not always incorporated in the numerical model.

In this study, we attempt to apply a two-way coupled wave-current model to investigate the upper ocean thermal and dynamic structure responses to SP in typhoon scenarios. Typhoon Matsa (2005) swept over the Bohai Sea is selected as a case. The roles of CSF, CLVF, and LT in modifying the turbulent mixing, thus in changing the thermal and dynamic processes in Bohai Sea, are analyzed through numerical experiments. Parameterizations of the CSF, resolved-scale CLVF, and LT in the dynamic equation are described in Section 2. Section 3 provides information on model coupling and configurations. Section 4 analyzes the numerical results. Conclusions and discussions are presented in Section 5.

2 Parameterization of Stokes production

2.1 Calculation of Stokes drift

Sullivan et al. (2012) suggested that the calculation of Stokes drift should be based on wave spectra, instead of the single-wave assumption or wind-wave equilibrium. After comparative study of several existing computations for Stokes drift, Zhang et al. (2018) also concluded that the Stokes drift might be underestimated when using bulk parameterization. Therefore, here we use directional wave spectra derived by the wave model to calculate Stokes drift. Webb and Fox-Kemper (2011) proposed the leading-order expression for the Stokes drift from an arbitrary spectral shape:

$$U_s(z) = \frac{16\pi^3}{g}\int_0^{\infty}\int_{-\pi}^{\pi}(\cos\theta, \sin\theta, 0) f^3 S_{f\theta}(f,\theta) e^{\frac{8\pi^2 f^2}{g}z} d\theta df \quad (1)$$

In Equation 1 U_s is Stokes drift, $S_{f\theta}$ is the directional-frequency spectral density, θ is wave direction, f is the real wave frequency, and g is the gravitational acceleration.

2.2 Parameterization of CSF and resolved-scale CLVF

According to the schema of McWilliams and Restrepo (1999), we added CSF and CLVF to the horizontal dynamic equations of POMgcs.

$$\frac{\partial UD}{\partial t} + \frac{\partial U^2 D}{\partial x} + \frac{\partial UVD}{\partial y} + \frac{\partial U\omega}{\partial \sigma} - fVD + g\frac{D^2}{\rho_0}\int_{\sigma}^{0}\left[\frac{\partial \rho'}{\partial x} - \frac{\sigma'}{D}\frac{\partial D}{\partial x}\frac{\partial \rho'}{\partial \sigma'}\right]d\sigma' \quad (2)$$
$$+ gD\frac{\partial \eta}{\partial x} = \frac{\partial}{\partial \sigma}\left[\frac{K_M}{D}\frac{\partial U}{\partial \sigma}\right] + F_x + CSFX + CLVFX$$

$$\frac{\partial VD}{\partial t} + \frac{\partial UVD}{\partial x} + \frac{\partial V^2 D}{\partial y} + \frac{\partial V\omega}{\partial \sigma} + fUD + g\frac{D^2}{\rho_0}\int_{k}^{0}\left[\frac{\partial \rho'}{\partial y} - \frac{\sigma'}{D}\frac{\partial D}{\partial y}\frac{\partial \rho'}{\partial \sigma'}\right]d\sigma' \quad (3)$$
$$+ gD\frac{\partial \eta}{\partial y} = \frac{\partial}{\partial k}\left[\frac{K_M}{D}\frac{\partial V}{\partial \sigma}\right] + F_y + CSFY + CLVFY$$

where

$$CSFX = fV_sD \quad (4)$$

$$CSFY = -fU_sD \quad (5)$$

$$CLVFX = V_s\left[D\left(\frac{\partial V}{\partial x} - \frac{\partial U}{\partial y}\right) - \sigma'\frac{\partial D}{\partial x}\frac{\partial V}{\partial \sigma} + \sigma'\frac{\partial D}{\partial y}\frac{\partial U}{\partial \sigma}\right] \quad (6)$$

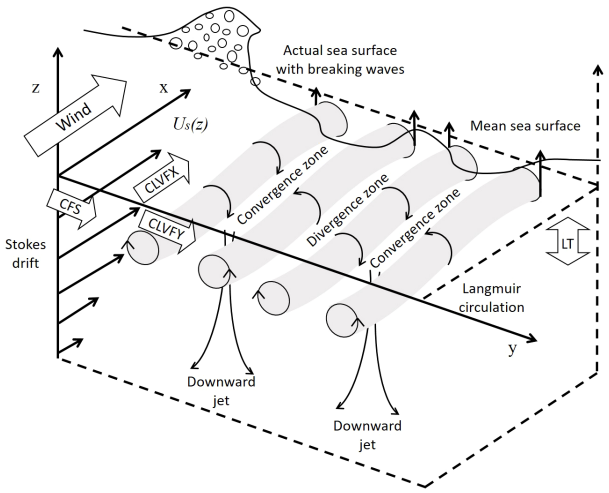

FIGURE 1
Mixing processes in the upper ocean schematic with vertically sheared Stokes drift and Langmuir cells (grey rolls) created by strong, sustained winds (thick arrow). Stokes drift is a reflection of large-scale wave transportation which contributes directly to the upper ocean mixing. As a result of the interaction between wave-induced Stokes drift and mean-current, downwelling convergence zones and upwelling divergence zones are formed below the surface by the counter-rotating neighboring cells, mostly aligned with the wind. CLVF is an approximation of vortex force acting Eulerian current in the horizontal direction. LT is a continuous source of coherent vertical vorticity.

$$\mathrm{CLVFY} = -U_s\left[D\left(\frac{\partial V}{\partial x}-\frac{\partial U}{\partial y}\right)-\sigma'\frac{\partial D}{\partial x}\frac{\partial V}{\partial \sigma}+\sigma'\frac{\partial D}{\partial y}\frac{\partial U}{\partial \sigma}\right] \quad (7)$$

In the Equation 2–7, (x, y) are the horizontal coordinates, (U, V) and (U_s, V_s) are eastern-western and northern-southern components of Eulerian mean current and Stokes drift, respectively, *CSFX* and *CSFY* are the horizontal components of CSF, and *CLVFX* and *CLVFY* are the horizontal components of resolved-scale CLVF.

In addition to vortex force, wave radiation stress is also considered as a mechanism of wave-current interaction. In comparing the effects of the two mechanisms, Moghimi et al. (2013) discovered that vortex force and radiation stress formulations typically produced comparable outcomes. According to Lane et al. (2007), radiation stress may ignore the low-order effect of waves and vortex force is the dominant effect of wave-current interaction. Thus in this study, we merely consider the vortex force.

2.3 Parameterization of LT

It is confirmed that the modification of turbulence parameterization scheme based on Mellor Yamada 2.5 turbulence closure submodel (Mellor and Yamada, 1982, hereinafter MY-2.5) can reveal the wave-induced turbulent mixing. To better simulate the turbulent mixing, a second-moment turbulent closure model of LT, (Harcourt, 2015, hereinafter H15), is used in the present study. H15 changes the corresponding effect of the stability function on Stokes shear, so that the CLVF is directly included in the turbulence closure model. The revised turbulence closure equation can be written as follows:

$$\frac{\partial q^2 D}{\partial t}+\frac{\partial U q^2 D}{\partial x}+\frac{\partial V q^2 D}{\partial y}+\frac{\partial \omega q^2}{\partial \sigma}-\frac{\partial}{\partial \sigma}\left[\frac{K_q}{D}\frac{\partial q^2}{\partial \sigma}\right] \quad (8)$$
$$=-\frac{2}{D}\overline{u\omega}\left(\frac{\partial U}{\partial \sigma}+\frac{\partial U_s}{\partial \sigma}\right)-\frac{2}{D}\overline{v\omega}\left(\frac{\partial V}{\partial \sigma}+\frac{\partial V_s}{\partial \sigma}\right)+\frac{2g}{\rho_0}K_H\frac{\partial \tilde{\rho}}{\partial \sigma}-2\frac{Dq^3}{B_1 l}+F_q$$

$$\frac{\partial q^2 lD}{\partial t}+\frac{\partial U q^2 lD}{\partial x}+\frac{\partial V q^2 lD}{\partial y}+\frac{\partial \omega q^2 l}{\partial \sigma}-\frac{\partial}{\partial \sigma}\left[\frac{K_q}{D}\frac{\partial q^2 l}{\partial \sigma}\right] \quad (9)$$
$$=E_1E_3 l\frac{g}{\rho_0}K_H\frac{\partial \tilde{\rho}}{\partial \sigma}+\frac{E_1 l}{D}\left(-\overline{u\omega}\frac{\partial U}{\partial \sigma}-\overline{v\omega}\frac{\partial V}{\partial \sigma}\right)+\frac{E_6 l}{D}\left(-\overline{u\omega}\frac{\partial U_s}{\partial \sigma}-\overline{v\omega}\frac{\partial V_s}{\partial \sigma}\right)-\frac{Dq^3}{B_1}\tilde{W}$$
$$+F_l$$

where

$$\overline{u\omega}=-\left(K_M\frac{\partial U}{\partial \sigma}+K_{MS}\frac{\partial U_s}{\partial \sigma}\right) \quad (10)$$

$$\overline{v\omega}=\left(K_M\frac{\partial V}{\partial \sigma}+K_{MS}\frac{\partial V_s}{\partial \sigma}\right) \quad (11)$$

$$K_{MS}=qlS_{MS} \quad (12)$$

$$S_{MS}=\frac{A_1(1-f_z^s)(1-6A_1/B_1)}{1-9A_1A_2G_H-9A_1^2(1-f_z^s)l^2q^{-2}D^{-2}\frac{\partial U}{\partial \sigma}\frac{\partial U_s}{\partial \sigma}} \quad (13)$$

In Equation 8–13, $\overline{u\omega}$ and $\overline{v\omega}$ are the components of the vertical turbulent fluxes. According to Kantha and Clayson (2004), q is a turbulence velocity scale, l is a turbulence length scale, D is the water depth. $E_1 = E_3 = 1.8$, and $B_1 = 16.6$ are recommended by MY-2.5. E_6 is an LT-related constant, here we choose $E_6 = 4E_1$. K_{MS} denotes the new vertical mixing coefficient. S_{MS} is stability function from H15, A_1 and A_2 are model constants, G_H=-$l^2q^{-2}N^2$, N is buoyancy frequency, and f_z^s is the surface-proximity function.

3 Study area and numerical settings

The Bohai Sea, located on the west bank of the Pacific Ocean, is a semi-closed marginal sea in China that may be attacked by typhoons in summer and autumn. In the event of a typhoon, the coastal cities in Bohai Rim Economic Circle, Tianjin, Dalian, and Qinhuangdao may suffer from serious economic loss. It is desirable to build a more accurate operational ocean forecasting and disaster mitigation model with the improved physical mechanism, for example, with the numerical consideration of the effects of SP on the Bohai ocean dynamics in typhoon scenario.

3.1 Wave model configuration

The Simulating Waves Nearshore model (SWAN) that includes processes of wind-wave generation, wave breaking, bottom dissipation, and nonlinear wave-wave interactions, is hired as a wave model to obtain wave parameters and wave spectra (Booij et al., 1999). The input wind field of SWAN is the European Centre

for Medium-Range Weather Forecasts (ECMWF) ERA-Interim reanalysis winds, with the input time interval of 6h and a spatial resolution of 0.125°. The wave spectrum was discretized by 32 logarithmically spaced frequencies (with a minimum frequency of 0.05Hz) and 36 evenly spaced directions (with an interval of 10°). The time step is set at 200s, consistent with the internal-mode time step used in the circulation model. The output interval is 6h which is equal to the input interval for the forcing of the circulation model.

The simulation domain covers [37.083°N - 41.033°N, 117.52°E - 122.47°E] (Figure 2) with a horizontal resolution of 0.05°, resulting in grids of 80×100. This setup was carefully chosen to strike a balance between computational efficiency and model accuracy, taking into account the available resolution of bottom topographic data in Bohai Sea. ETOPO2 Global 2' Elevations dataset is used for bottom topography. The feasibility of such grid configuration had been verified by Cao et al. (2019) and Wang and Deng (2022). The major geographic locations inside the Bohai Sea are: the Liaodong Bay to the north, the Laizhou Bay to the south, the Bohai Bay to the west, the Central Sea Area in the middle, and the Bohai Strait to the east which are connecting the Yellow Sea and are also marked in the right panel of Figure 2.

3.2 Ocean current model configuration

Princeton Ocean Model with generalized sigma-coordinate system (POMgcs, Ezer and Mellor, 2004), a free surface and 3D coastal circulation model, is used to simulate the circulation in the Bohai Sea. The MY-2.5 turbulence closure scheme is included in POMgcs to parameterize the vertical turbulent mixing. Since the majority of Bohai Sea's water depth is less than 60m, and the ML is where SP has the most influence, the vertical stratification is set at 6 layers, namely 0m, 5m, 15m, 25m, 35m, and 65m. The time step of the internal-mode of POMgcs is set as 200s, and that of the external-mode is set as 0.33s. The initial fields of temperature, salinity, water level, and current velocity are obtained from China Ocean ReAnalysis (CORA), a reanalysis dataset for China's coastal waters and adjacent seas. They are then interpolated into the computational grid of the model. The model's domain, bottom topography, and horizontal resolution are the same as those of the wave model specified in section 3.1.

Winds and thermal fluxes are serving as the dynamic driving force of POMgcs. The input wind field of POMgcs is the same as that of wave model SWAN. Nearest neighbor interpolation is applied to reach the model resolution of 0.05°×0.05°, which is adequate to resolve the main dynamic and thermodynamic processes under typhoons. The surface heat fluxes, including long-wave radiation, short-wave radiation, latent heat flux, and sensible heat flux, with a spatial resolution of 1.875°×1.875°, are from the US National Centers for Environmental Prediction (NCEP). To better simulate the vertical structure of temperature in the Summer Bohai Sea, four main tidal components of M2, S2, K1, and O1 are imposed on the open boundary condition of the model. Their feasibility had been well verified by Zhao et al. (2019) and Cao et al. (2019).

3.3 Two-way coupling scheme and experiment setup

POMgcs and SWAN are fully coupled through the model-coupling toolkit (MCT) in two-way data exchange (Figure 3) with an exchange frequency of 1800s. The input to the SWAN is the output of real-time current and sea surface height from POMgcs. The CSF, CLVF, and LT are calculated using wave spectrum and parameters output from the SWAN, then fed to POMgcs.

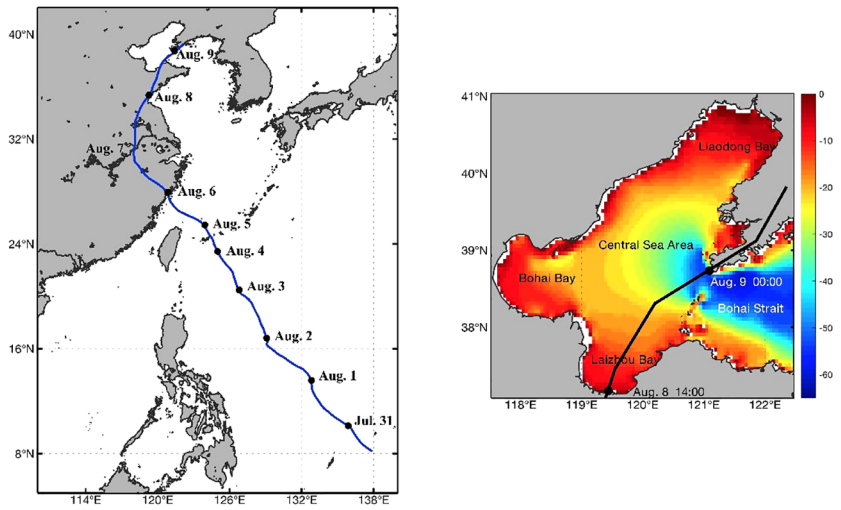

FIGURE 2
Left: The track of Typhoon Matsa (2005) from 30th July 2005 to 9th Aug 2005 from Zhejiang Provincial Water Resources Department (data source: http://typhoon.zjwater.gov.cn/default.aspx.). Right: Simulation domain of Bohai Sea with the color shading as the water depth (m) and with the major geographic locations names marked. Black line in the right panel represents the track of Typhoon Matsa from 8th Aug to 9th Aug 2005 that directly affected the Bohai Sea.

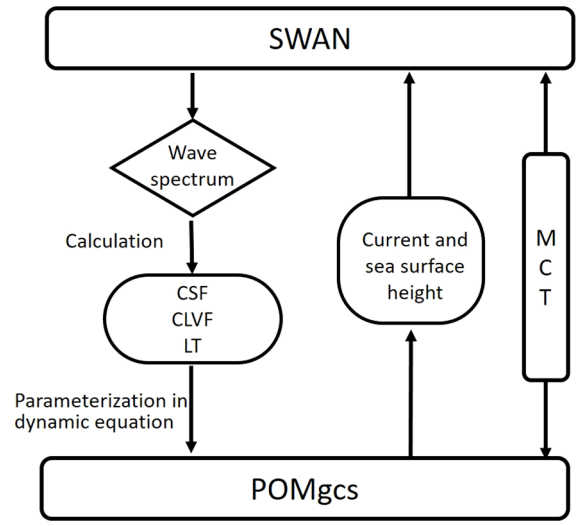

FIGURE 3
Schematic of POMgcs-SWAN two-way coupling.

Comparing to the one-way coupling model (without the feedbacks from POMgcs to SWAN), we are expecting that this coupling would allow for a more comprehensive examination of the intricate interplay between waves and currents, enabling a more accurate representation of the dynamic processes occurring in the Bohai Sea under typhoon conditions.

The integration time of the numerical experiment is half a year, from 1st January to 31st July 2005, in order to obtain a stable current field. The vertical stratification of the Bohai Sea in summer is stronger and more stable, and the influence of convective mixing on the mixing layer is relatively weak, which makes the influence of SP more significant. Four diagnostic experiments are designed in this study (Table 1): (1) the control run (WAVE-NONE), in which the wave effects are not considered, serves as the benchmark to measure the effects of CSF, CLVF, and LT on ocean dynamics, (2) adding both CSF and CLVF (WAVE-CSVF) in the horizontal momentum equations, (3) only introducing LT parameterization (WAVE-LT), and (4) including CSF, CLVF, and LT parameterization (WAVE-ALL).

4 The modeling results

Typhoon Matsa, which swept over the Bohai Sea in 2005, was selected as the case study. Initiated at 2000 UTC+8, 31st July 2005 in the ocean east of Philippine at [134°E, 11.7°N], Typhoon Matsa developed into a tropical storm on 2nd August and then strengthened to a mature typhoon by 5th August 2005 with steady winds of around 150 km/h. Moving northwest, Masta made landfall at Yuhuan County Zhejiang Province at 0340 UTC+8, 6th August 2005 with a peak intensity and maximum sustained wind (MSW) of 45m/s (Song, 2012). The weakening tropical cyclone then passed through Zhejiang, Anhui, Jiangsu, and Shandong Provinces successively before the center of Matsa entered the Bohai Sea from Lazhou Bay around 1400 UTC+8, on 8th August, with a maximum sustained wind speed up to 18m/s and a central mean-sea-level pressure of 995 hpa. Matsa was downgraded to a temperate cyclone at 0500 UTC+8, on 9th August in the central area of Bohai Sea, then it made a second landfall at Dalian, Liaoning Province two hours later.

The Bohai Sea was primarily affected by Typhoon Masta between 8th and 9th August 2005. Three stages are set in the present study with 0000UTC on 7th August representing pre-typhoon condition, 0000UTC on 8th and 9th August standing for the typhoon stage, and 0000UTC 10th August as the after-typhoon stage. LT on the ocean dynamic process of Bohai Sea under typhoon condition is then studied. This allows for the analysis of the upper ocean response of the Bohai Sea to Typhoon Masta. ECMWF ERA-Interim reanalysis wind field are hired to study the wind speed distribution over Bohai Sea during the four days mentioned above.

On 7th Aug, low winds ranging between 4 and 8 m/s were observed, which are the typical of what the Bohai Sea experiences during the summer. The wind speed in the entire sea area elevated dramatically on 8th and 9th August, when Typhoon Masta was in the Bohai Sea, reaching a maximum wind speed of ~20m/s on 8th August. The typhoon center gradually moved from the Bohai Strait to the

TABLE 1 Experiment setup.

Experiment name	Inclusion of Coriolis-Stokes force (CSF)	Inclusion of Craik-Leibovich vortex force (CLVF)	Inclusion of Langmuir turbulence (LT)	Description
WAVE-NONE	No	No	No	The control run, in which the Stokes drift effects are not considered in the POMgcs–SWAN coupled model, thus serving as the benchmark.
WAVE-CSVF	Yes	Yes	No	The same integration time as in WAVE-NONE, with CSF and CLVF included through the wave–current interaction. LT is absent.
WAVE-LT	No	No	Yes	The same integration time as in WAVE-NONE, with only LT effect included. CSF and CLVF are absent.
WAVE-ALL	Yes	Yes	Yes	Integrated diagnose run, with the same integration time as in WAVE-NONE with the effect of CSF, CLVF, and LT all included.

northeast, then reached the central sea area, with a rapid weakening of typhoon intensity. The maximum wind speed on 9th August decreased to 12 m/s. Then, the wind speed after typhoon (10th August) dropped quickly, with slightly higher winds than the pre-typhoon stage. However, Typhoon Masta did alter the wind direction over the Bohai Sea on 10th August, which was opposite to that on 7th August.

The harshness of the sea is typically measured by the significant wave height (H_s), one of the most important wave parameters for characterizing wave energy. Table 2 shows the single-point H_s comparison of the model simulation with the in-situ observations at the tide gauge stations of Laohutan[1] from 7 to 10 August 2005. The RMSE (Root Mean Square Error) of less than 0.01, and the CC (Correlation Coefficient) exceed 90%, indicating that the model is relatively reliable in simulating the significant wave height. A typhoon can easily generate large gravity waves thus leading to a significant increase in H_s. The distribution of H_s output by SWAN shows relatively good agreement with the wind field on 7th August, when the wind speed was low or moderate across the entire Bohai Sea, and on 8th August when Typhoon Matsa first stepped into the study region with strong power and high speed (Figures 4A, B). During these stages of pre-typhoon and during-typhoon, the directions of Stokes drift were basically as same as that of wind (Figures 4E, F), suggesting a generally positive correlation between them. When the Matsa exerted its influence on the Bohai Sea as a complete cyclone on 9th August, the typhoon center (39°N, 120°45′ E) in the central sea area was inconsistent with the counter-clockwise drift center (38°30′N, 120°E) formed by Stokes drift (Figure 4G), and the direction deviation in wind and Stokes drift was large within this area. It is interesting to find that the area with large H_s(>0.4m) was located east to the Bohai Strait adjacent to (38°N, 120°45′E) (Figure 4C). In after-typhoon stage of 10th August, the H_s in the Bohai Bay and west Liaozhou Bay dropped to<0.2m while remaining high in the Bohai Strait (Figure 4D). A relatively large Stokes drift of 0.01~0.015 showed up in the northeast Laizhou Bay and southwest Bohai Strait, with direction aligned with that of the wind field. The maximum Stokes drift of the study region appeared in the Yellow Sea near the southern tip of Liaodong Peninsula which agrees well with the largest H_s (Figure 4H).

Through the above analysis, we were able to observe the numerical response of wave field to wind, where high wind causes big H_s, as well as the complicated variation of Stokes drift due to the wave-current interactions under severe weather. Stokes drift responds to normal wind relatively quickly and simply, while there seems to be a temporal lag in a typhoon scenario. The magnitude and direction of Stokes drift are also influenced by the elevated current in high winds, thus not aligned with the winds.

4.1 Temperature

To quantitatively study the influence of different SP terms on sea temperature, the deviations between different diagnostic experiments and control run WAVE-NONE were calculated. The sea surface temperature (SST) simulated by WAVE-ALL was found to be lower than that of WAVE-NONE on 7th August 2005, prior to the arrival of Typhoon Masta in the majority of the Bohai Sea. In particular, the temperature decreased evidently by about 0.3°C in the south of Liaodong Bay, the east of Bohai Bay, and the sea area near Miaodao islands. Under normal weather conditions, the Bohai Sea has a clear and stable vertical temperature stratification. However, the presence of SP in the numerical model slightly reduced the temperature at sea surface and a few meters below, while slightly increased the temperature of the deeper layer (such as the layers of 15m and 25m). In general, the overall vertical temperature change was insignificant, and the temperature stratification structure essentially remained unchanging, suggesting a minimal effect of SP on the vertical temperature profile in the Bohai Sea. When comparing our current two-way coupling approach with the one-way coupling employed in Cao et al. (2019), which demonstrated a reduction in sea surface temperature (SST) by less than 0.4°C across most of the Bohai Sea region under normal conditions, we observe an increase in the maximum SST deviation to 0.5356°C in our (WAVE-ALL)-(WAVE-NONE). Although the simulations were not conducted on the exact same day, this discrepancy partly underscores the influence of wave-current feedback on local thermodynamics. Given the absence of in-situ observation during our simulation experiments, it is premature to definitively assert the superiority of either approach. However, it is evident that the two-way coupling incorporates a more comprehensive physical mechanism, rendering it theoretically advantageous.

When Typhoon Masta entering the Bohai Sea (8th August), the SST decreased rapidly, and the SP aggravated the “cold absorption” of the sea water, resulting in a maximum decline of 0.4°C in the SST. Reichl et al. (2016a) discovered that when the SST drops by 0.5°C, the total air sea heat flux falls by at least 10%, suggesting this SST cooling caused by SP cannot be ignored in the ML parameterization under severe weather. By comparing with the pre-typhoon stage, it can be seen that, owing to the enhancement of sea surface wind and the deterioration of sea state by typhoon, the SP effect intensified, resulting in a significant increase in both the cooling magnitude and range of the SST (Figure 5B).

Masta did not induce a significant change in the vertical temperature structure when it initially entered the Bohai Sea. However, after one day’s working, the temperature difference of the whole central sea area and the Bohai Strait became evident, with the maximum temperature change exceeding 0.41°C. This occurred because these areas have a deeper water depth, which allows the SP to continue bringing colder water up to the surface. Even though the intensity of Typhoon Masta on 9th August was substantially lower than it was one day before, the heat exchange between the upper and lower sea water caused by SP was still in progress, causing a lag in temperature change. Vertically, the temperature stratification gradually weakened, and the upper and lower layers became increasingly mixed (Figure 5G). The SP makes the cooling of the sea surface more obvious. The difference of the vertical temperature profile is greater (comparing Figures 5E, G), with a maximum decrease of 0.54 °C. It is anticipated that if the typhoon persists for longer, the SP will cause more intense vertical heat exchange. The similar pattern of Figures 5G, H implies that the effect of LT in

1 Oceanographic station observations are available at NMDIS, http://www.nmdis.org.cn.

TABLE 2 Model validation with in-situ observations.

Date	Time	H_s (m)		RMSE	CC	Location
		Simulated	Observed			
20050807	08:00 11:00 14:00 17:00	0.168 0.173 0.178 0.184	0.193 0.192 0.199 0.204	0.021	93.0%	38°52′ N 121°41′ E
20050808	08:00 11:00 14:00 17:00	0.400 0.420 0.427 0.444	0.484 0.493 0.502 0.508	0.074	97.9%	
20050809	08:00 11:00 14:00 17:00	0.364 0.366 0.370 0.376	0.402 0.422 0.425 0.437	0.053	90.2%	
20050810	08:00 11:00 14:00 17:00	0.530 0.548 0.556 0.563	0.599 0.612 0.624 0.643	0.071	94.9%	

elevating the turbulence mixing is stronger than that of CSF and CLVF.

4.2 The ocean currents

Along with the increased wind speed caused by Masta starting from 8th August, the surface current speed increased accordingly, especially in the marginal areas of east Bohai Bay and the northwest Laizhou Bay (Figure 6A). The Liaodong Bay in northeast Bohai Sea had not been affected by the typhoon, thus the surface currents there for four experiments remained close to the pattern on 7th August. With the consideration of CSF and CLVF in WAVE-CSFV case (Figure 6B), the maximum current speed increase of 0.018m/s and maximum reduction of 0.013m/s all appeared in the Bohai Strait. From Figure 6C, the maximum change of surface current speed brought by LT under typhoon weather was 0.04m/s, and the maximum speed change area basically coincides with that of the maximum temperature change. The similar pattern of Figures 6C, D suggests that among the SP terms, LT has a greater influence on the vertical mixing intensity and TKE during typhoon.

The vertical profiles of current and related changes along the 38.333°N section simulated by four experiments on 8th August 2005 are shown in Figure 6E to Figure 6H. Numerically, the presence of SP occupied a portion of the energy transmitted to the upper ocean by winds. Typhoon Masta generally made the current distribution in the whole shallow sea become more uniform, and the presence of SP further promoted the decrease of simulated speed throughout the entire water depth. However, because of the short time of typhoon, the intensification of wind force led to a rapid increase in surface current speed, and the kinetic energy transmitted from the atmosphere to the sea was mainly limited to a depth of several meters below the sea surface. In other words, within a short time period, energy transfer to the lower layers was insufficient, resulting in the vertically stratified currents in the central sea area and the Bohai Strait, and there was a significant difference between the surface velocity and the bottom velocity. In certain areas, there is a noticeable change in the direction of the current vectors.

With 24h action of typhoon winds, the increased sea surface current speed agreed well with the areas of high wind speed, while the speed was quite low near the center of the typhoon. The influence of the wind direction can be reflected in the current direction. At the pre-typhoon stage, the current mainly converged from other areas to the Laizhou Bay. On 9th Aug, the current direction in the Laizhou Bay gradually became parallel to the wind direction, indicating that the wind was the dominant factor affecting the current during the typhoon, rather than the tidal currents. When the typhoon continued to act, the influence of SP on the surface current speed was further enhanced, and the decrease of sea surface speed was most obvious in the northern Laizhou Bay and the Bohai Strait. Vertically, the energy transported by the atmosphere to the ocean has been fully propagated to the whole depth. Because of the shallow water depth, the current velocity at the surface and bottom were almost the same. In the Bohai Bay and the central sea area, the current speed increased significantly because of the consistent wind direction and the circulation direction, while in the Bohai Strait the speed was smaller due to its proximity to the typhoon center and the opposite wind direction to the original circulation. With SP under typhoon conditions, the vertical structure of the current changed noticeably, with the speed decreasing more along the vertical direction.

On 10th Aug, as Matsa passed, the currents were mostly flowing eastward, from the Liaodong Bay and the Bohai Bay to the Laizhou Bay and the Bohai Strait. In the Bohai Bay and the central sea area, the current speed decreased, while in the Bohai Strait, the speed increased. With the weakening of the sea surface winds, the ocean current started to change from the surface to the bottom, thus forming a temporary current stratification. Comparing the distribution of WAVE-NONE and WAVE-ALL (Figure 7), the consideration of SP promoted the synergetic current change at the upper and lower layers, making the current distribution more uniform in the vertical direction. In other words, the SP weakened the current stratification to a certain extent.

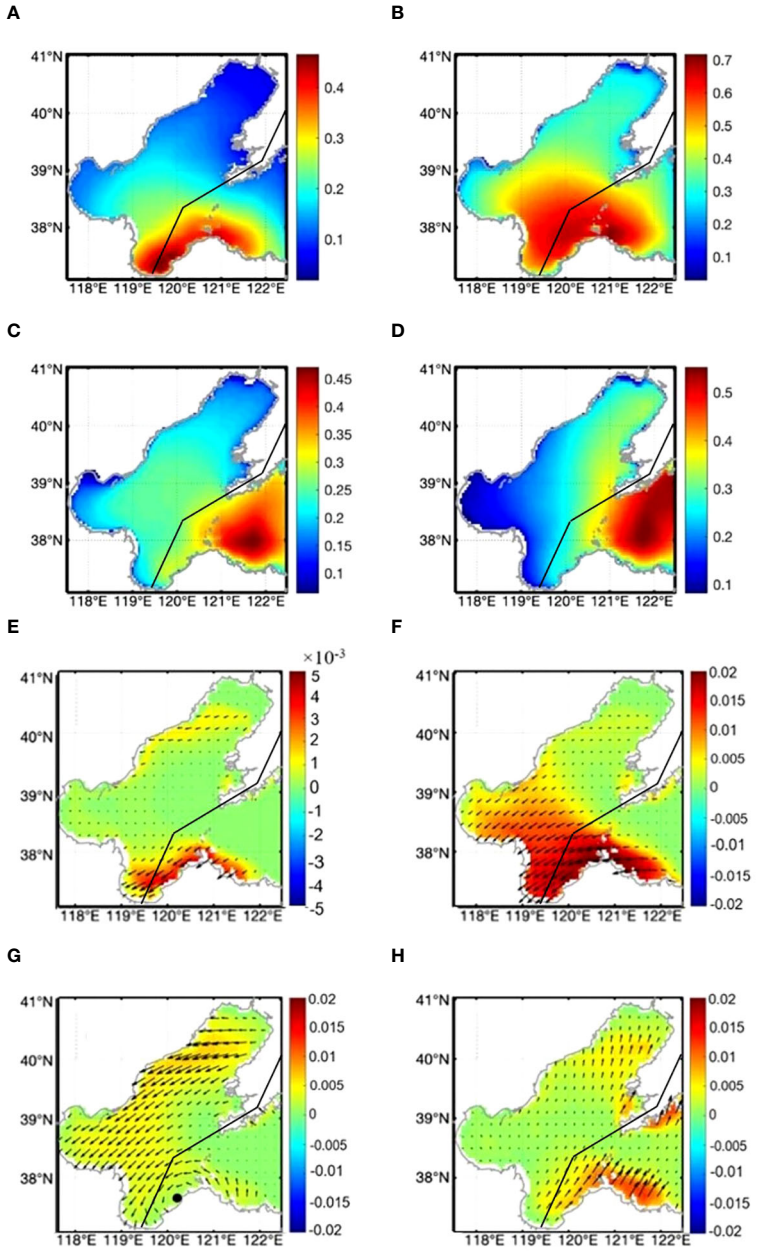

FIGURE 4
POMgcs simulated horizontal distribution of significant wave height (m) without coupling at 0000 UTC on **(A)** 7th, **(B)** 8th, **(C)** 9th, and **(D)** 10th August 2005. Horizontal distribution of simulated Stokes drift direction and speed (10^{-3} m/s) on **(E)** 7th, **(F)** 8th, **(G)** 9th, and **(H)** 10th of August 2005. Black line represents the track of Typhoon Matsa from 8th to 9th Aug 2005. Black dot in **(G)** represents the center of counter-clock-wise Stokes drift.

4.3 Turbulent Langmuir number and vertical mixing coefficient

Turbulent Langmuir number (L_a) is an indicator representing the relative influence of wind driven shear and Langmuir turbulence (McWilliams et al., 1997). By using the parameterization proposed by Harcourt and D'Asaro (2008), the nondimensional number $L_a = \sqrt{(|\rho_a C_d|\overrightarrow{u_{10}}|\overrightarrow{u_{10}}/\rho|)^{1/2}/|\langle U_s\rangle_{SL} - U_s(z_{ref})|}$, spatial distribution of the Langmuir turbulence is calculated. In the calculation, ρ is the sea water density and ρ_a is the air density, u_{10} is the 10-m wind speed, C_d is the wind drag coefficient and following the form proposed by Zijlema et al. (2012), $\langle U_s\rangle_{SL}$ is the Stokes drift averaged over the surface layer, $U_s(z_{ref})$ is the reference Stokes drift, and z_{ref} represents the mixed layer depth.

The daily-mean L_a values in the Bohai Sea during the whole typhoon event are given in Figure 8. L_a represents the ratio of viscous to inertial forces in the water column, i.e., in negative correlation with sea surface Stokes drift. At pre-typhoon stage, although some high L_a values appeared near the central line in Bohai Strait, most of the Bohai Sea had L_a less than 0.3 (Figure 8A). This is lower than the typical range of 0.35~0.5 reported by Belcher et al. (2012) for the Northern Hemisphere in summertime,

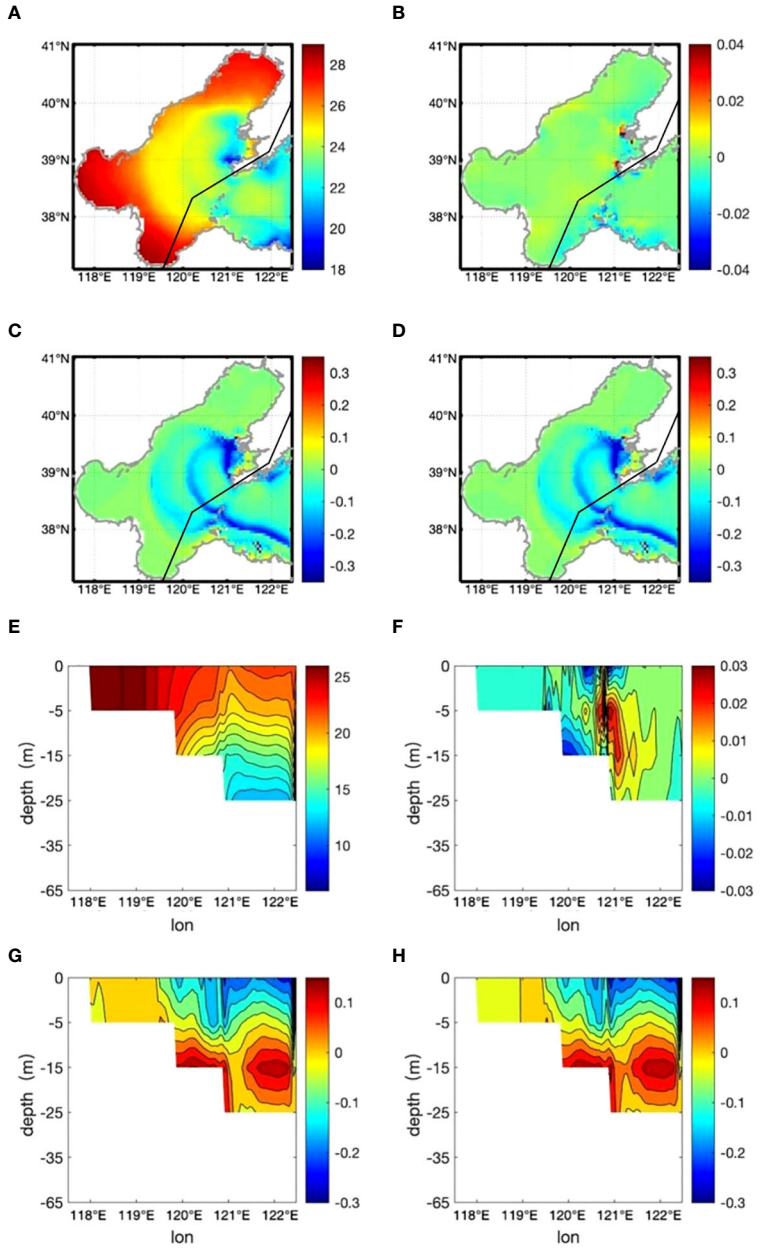

FIGURE 5
Horizontal distribution of **(A)** SST from WAVE-NONE, and SST difference between **(B)** (WAVE-CSVF) - (WAVE-NONE), **(C)** (WAVE-LT) - (WAVE-NONE), and **(D)** (WAVE-ALL) - (WAVE-NONE) at 0000UTC on 8th August 2005 (°C). Black line represents the track of Typhoon Matsa from 8th to 9th Aug 2005.Vertical temperature profile along the widest section in Bohai Sea 38.333°N from **(E)** WAVE-NONE, and the temperature differences between **(F)** (WAVE-CSVF) - (WAVE-NONE), **(G)** (WAVE-LT) - (WAVE-NONE), and **(H)** (WAVE-ALL) - (WAVE-NONE) at 0000UTC on 9th August 2005 (°C).

indicating the important role of Langmuir turbulence in the Bohai Sea. During the typhoon, strong atmospheric forcing caused a decrease in L_a throughout the Bohai Sea, with the value falling below 0.14 on 9th Aug (Figure 8C), and below 0.16 on 10th Aug 2005 (Figure 8D).

Wind can directly affect the turbulent mixing of the upper ocean. The distribution of vertical mixing coefficient was positively correlated with the wind field. This study compares the K_M (without LT) and K_{MS} (with LT) that was calculated by Equation 12 following H15 parameterization for Langmuir circulation.

Under normal weather conditions (represented by 7th Aug), the vertical mixing coefficient K_{MS} that includes the SP effect, was greater than the original vertical mixing coefficient K_M at the surface, 5m, and 15m layers. However, the SP did not alter the horizontal structure of the vertical mixing coefficient, thus the vertical profile of K_{MS} was basically identical to K_M, especially at depths greater than 35m (Figure 9A). This indicates that although Stokes drift decayed exponentially within a few meters below the sea surface, the LT it generated continued to transmit downward and enhanced the turbulent mixing of the entire upper ocean. Under

10.3389/fmars.2024.1364960

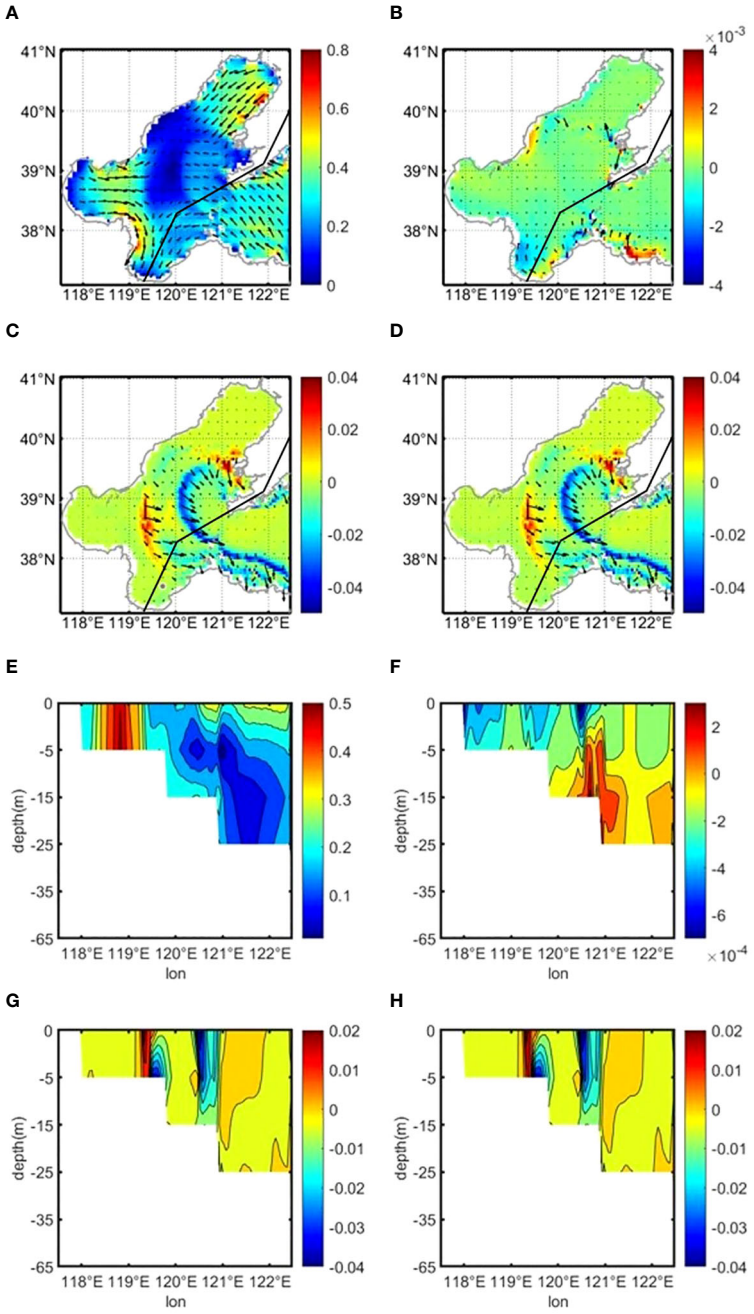

FIGURE 6
Horizontal distribution of **(A)** surface current (unit: m/s) of WAVE-NONE, **(B)** current difference (unit: m/s)between WAVE-NONE and WAVE-CSVF, **(C)** current difference between WAVE-NONE and WAVE-LT, and **(D)** current difference between WAVE-NON and WAVE-ALL at 0000UTC on 8th August 2005. The color shading represents the magnitude of current velocity, and the arrows represent the current direction. Black line represents the track of Typhoon Matsa. The Vertical profile of current velocity along the 38.333°N section at 0000UTC on 8th August 2005 from **(E)** WAVE-NONE, and the differences between **(F)** (WAVE-CSVF) - (WAVE-NONE), **(G)** (WAVE-LT) - (WAVE-NONE), and **(H)** (WAVE-ALL) - (WAVE-NONE).

typhoon condition, K_{MS} was obviously larger than K_M at the upper 25m on 8th Aug and extended to upper 55m on 9th Aug (Figures 9B, C). One day after Typhoon Matsa's passage, K_{MS} slightly decreased but was still larger than K_M at almost all depths (Figure 9D).

Through examination of the horizontal distribution of the sea surface mixing coefficient in the Bohai Sea, it is found that the vertical mixing coefficient increased significantly when Typhoon Matsa swept the sea surface with a maximum increase of $O(10\ m^2/s)$ on 8th August near the north boundary of Laizhou Bay (~38.2°N). The higher the wind speed, the greater the vertical mixing coefficient. K_{MS} was larger than K_M with a maximum difference of 0.02 m^2/s, suggesting that the wind speed has a greater impact on K_{MS} when SP is taken into account. On 9th August, the regions with enlarged mixing coefficient were in the Laizhou Bay and the southern Bohai Strait, both of which experienced strong winds. In the typhoon center and the regions with large difference between

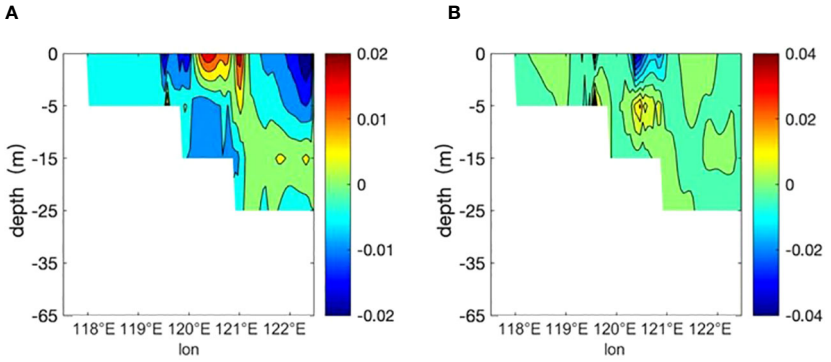

FIGURE 7
The vertical profile of current velocity differences (unit: m/s) between (WAVE-ALL) - (WAVE-NONE) along the 38.333°N section at 0000UTC on **(A)** 9th and **(B)** 10th August 2005.

Stokes drift direction and wind direction, the vertical mixing coefficient was very small. This agrees with the previous studies (Van Roekel et al., 2012; Zhang et al., 2018) which found that wind wave misalignment can obviously suppress Stokes drift and turbulent mixing caused by shear effect. After the wind speed dropped to be less than 8m/s on 10th Aug, the mixing coefficient in the Lazhou Bay and Bohai Strati remained at a higher level than that of the pre-typhoon stage. The presence of SP significantly influenced the K_{MS}, with a maximum difference of $2.8\times10^{-3}m^2/s$ between K_{MS} and K_M.

4.4 The mixed layer depth (MLD)

The MLD is another important feature for the vertical temperature distribution in typhoon simulations. In this study, MLD is computed based on a constant temperature difference criterion, specifically the 0.5°C temperature difference between the ocean surface and the bottom of ML (Monterey and Levitus, 1997). We first interpolated the simulated sea water temperature layer by layer in horizontal direction, and then calculated the depth of ML by using the above criterion. Figure 10 shows the MLD simulated by

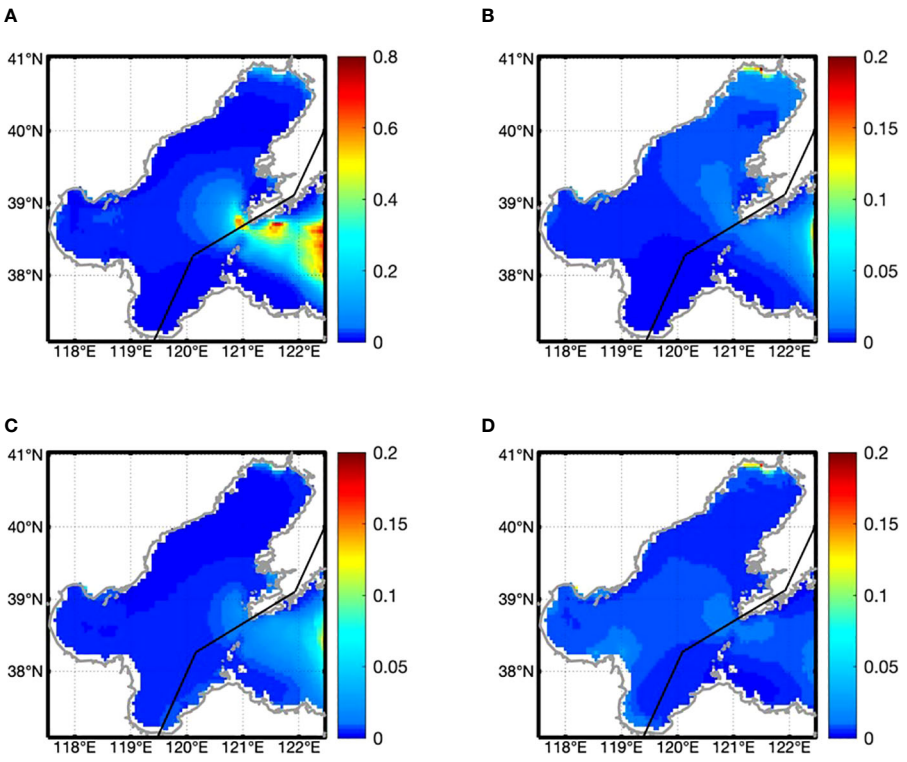

FIGURE 8
Horizontal distribution of daily mean Langmuir number on **(A)** 7th, **(B)** 8th, **(C)** 9th, and **(D)** 10th August 2005. Black line represents the track of Typhoon Matsa.

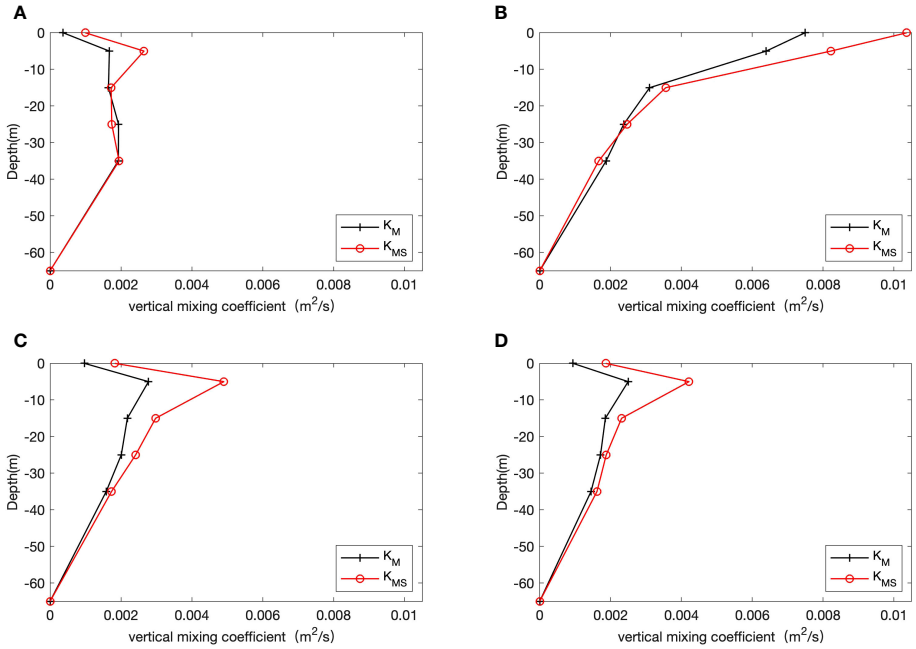

FIGURE 9
The profile of horizontally averaged vertical mixing coefficients K_M and K_{MS} (m^2/s) simulated at 0000UTC on **(A)** 7th, **(B)** 8th, **(C)** 9th, and **(D)** 10th August 2005 in Bohai Sea, where the black line with + represents the profile without wave effect (WAVE-NONE), while the red line with circle shows the situation with CSF, CLVF, and LT (WAVE-ALL).

the cases of WAVE-NONE, WAVE-CSVF, WAVE-LT, and WAVE-ALL along the 38.333°N section at pre-, during-, and after- Typhoon stages, respectively. Under normal and typhoon weathers, the MLD was basically equivalent to the depth of water in shallow offshore regions, where the whole depth of sea water was well mixed with similar temperature at the sea surface and bottom layer. When the longitude exceeds 119°E, the thickness of the ML decreased rapidly and remained stable within 1m on 7th Aug 2005 (Figure 10A). This is due to the strong vertical stratification in the summer Bohai Sea, with a large temperature difference between the sea surface and subsurface. Comparing the results of four experiments at the pre-typhoon stage, we found little variation in MLD, which could be ignored from the perspective of the whole Bohai Sea.

When Typhoon Matsa entered the Bohai Sea on 8th Aug, the MLD in the deep sea area began to deepen, especially for [119.5°E-120.7°E] (Figure 10B). The MLD is sensitive to different mixing schemes, with MLD generated by WAVE-ALL and WAVE-LT thicker than those simulated by WAVE-NONE and WAVE-CSVF, indicating that the incorporation of additional SP terms does affect the deepening of the ML. Under the continuous action of typhoon, the MLD in the Bohai Sea was further deepened on 9th Aug, and the MLD in deep water areas (east of 119°, >20m depth) was all larger than 1m. Only at 120°50′E close to the center of typhoon, the MLD decreased rapidly to about 1.1m (Figure 10C), which is consistent with the results of Reichl et al. (2016b). The largest MLD difference between WAVE-ALL and WAVE-NONE was 0.65m. Compared with temperature section in Figure 5, it can be found that the seawater within the ML was fully mixed and exhibited a uniform vertical temperature distribution. From the results of WAVE-NONE and WAVE-ALL, we can see the continued influence of SP on strengthening of the upper mixing.

Without strong atmospheric forcing at the after-typhoon stage, the MLD gradually returned to smaller value on 10th Aug. The MLD obtained by WAVE-ALL simulation was deeper than that of WAVE-NONE, with a larger difference of 0.5m around [120°E-120.4°E], and about 0.1~0.2m in other areas. Because of the lag of ocean response to atmospheric force, these changes of MLD induced by SP were of the same magnitude with that on 9th Aug when typhoon passed by.

5 Conclusion and discussion

This paper studies the influence of the SP on the ocean dynamics and thermal processes of the Bohai Sea during Typhoon Matsa based on fully coupled wave-current model simulations. The 0000UTC of each day from 7th to 10th August, 2005 are selected to represent the pre-, during-, and after-typhoon stages, respectively. The main findings include:

(1) Before typhoon arrived in the Bohai Sea, on 7th August 2005, the Stokes drift caused slight decrease of the SST and an increase in temperature at deeper layers, but the temperature stratification structure generally remained unchanging. The SP terms had little effect on the MLD and sea surface current speed in the Bohai Sea. By analyzing the vertical mixing coefficient K_M and K_{MS}, it can be found

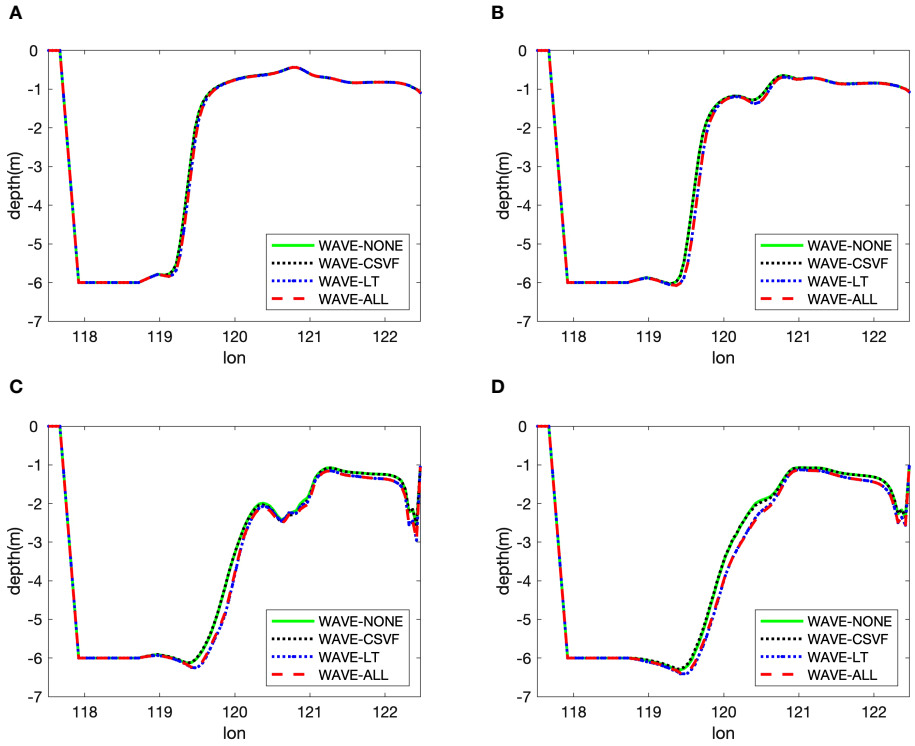

FIGURE 10
Mixed layer depth (M) along the section 38.333°N in Bohai Sea at 0000UTC on **(A)** 7th, **(B)** 8th, **(C)** 9th, and **(D)** 10th August 2005, in which the green solid lines represent coordinate run without consideration of wave, black dots are the simulation with CLVF and CSF, blue dots show the simulation with LT, and the dashed red line are the result of all wave effects.

that the mixing coefficient is positively correlated with the wind speed, and the SP strengthens the vertical mixing intensity.

(2) On 8th August 2005 when Typhoon Matsa was sweeping over the Bohai Sea, the Stokes drift intensified the turbulent mixing in the upper ocean, resulting in a significant decrease in SST and current speed, and a thicker ML. However, due to the short action time of typhoon in the Bohai Sea, the vertical temperature structure was not changed dramatically, and the kinetic energy transmitted from the atmosphere to the sea was mainly limited to the surface layer. The current starts to be stratified in the vertical direction with relatively large speed difference between the surface and the bottom. From the distribution of vertical mixing coefficient, it can be seen that wind speed has a higher impact on K_{MS} when taking the SP into account.

(3) On 9th August 2005, one day after typhoon influencing the Bohai Sea, the continuous effect of SP brought deeper colder water to the surface, leading to the significant surface water cooling and the gradually weakened temperature stratification. The vertical temperature structure was almost changed, and the MLD decreased rapidly to about 1.1m. The presence of SP makes the speed decrease more in the vertical direction, while the vertical structure of current tends to be more uniform. The magnitude of K_{MS} is mainly controlled by the wind speed and the angle between wind direction and Stokes drift direction, and the misaligned wind and wave fields can obviously suppress the turbulent mixing caused by SP.

(4) After the passage of Typhoon on 10th August 2005, the SST in the Bohai Strait and the central sea area decreased in the SP involved parameterization. The magnitude and range of the temperature decrease were similar to those on 9th August. This suggests that the SP not only affects the SST on the synoptic time scale, but also has a longer time scale influence, which is correlated with the total heat budget on the monthly and seasonal scales. Comparing the vertical temperature simulated by WAVE-ALL and WAVE-NONE, it can be found that with SP the temperature difference of -0.01°C largely occurred in ML, while from the bottom of ML downward to the seafloor only a small positive value scattered. Actually, from the simulation of successive days, it is suggested that the warming trend in the ML is slow, and the depth of the ML changes slowly, indicating the response lag of seawater temperature to the SP. The current gradually returned to the normal wind condition, with the SP terms promoting the coordinated change of upper- and lower-layer currents, thus making the current velocity distribution more uniform in the vertical direction. Although the wind speed in most areas of the Bohai Sea dropped to<8m/s, the vertical mixing coefficient maintained a large value in some areas.

The above findings are consistent with the previous studies that the improvement of surface gravity waves parameterizations for mixing is essential to depict the upper ocean dynamic and thermodynamic structure. In the typhoon scenario, the intensified wave-induced mixing led to the elevated vertical mixing coefficient, deepened MLD, and sea surface cooling as expected. High wave regions tend also to be regions of high Stokes drift, however, in some areas it is not the case, since stokes drift is also correlated with other characteristics of surface gravity waves, such as wave speed. Our statistical analysis reveals marginal improvements in results with the two-way coupling over one-way coupling of POMgcs and SWAN, as it also integrates the feedback of currents on waves, leading to localized adjustments in simulation outcomes without inducing significant changes. For instance, in our pre-typhoon experiment, the average difference between (WAVE-ALL) and (WAVE-NONE) current speed is approximately -0.0013 m/s. This finding aligns closely with Cao et al.'s (2019) one-way coupling simulation, indicating that velocities derived from (WAVE-NONE) tend to be larger than those from (WAVE-ALL). In the present study, we use limited buoy observation data to validate and illustrate the simulation's efficacy in representing H_s, further reinforcing the credibility of our two-way coupling model. However, due to article length constraints and limited field observations, we refrain from presenting a detailed comparative analysis between two-way and one-way coupling simulations in this paper. Our focus lies on utilizing modeling tools to delve into Stokes drift and Langmuir turbulence effects. Nevertheless, it's crucial to underscore that two-way coupling offers a more comprehensive physical mechanism, theoretically enhancing the fidelity of numerical simulations in shallow marginal seas.

It is also worth noting that the present study focuses on the impact of three SP terms on upper ocean dynamics under typhoon scenario based on a two-way coupled wave-current model, rather than providing an exhaustive analysis of specific regional characteristics. This methodological framework can be adapted and applied to various other coastal sea areas, enabling researchers to explore and understand the dynamics of Stokes drift in diverse marine environments. In the future, the numerical study of the role of SP in normal weather conditions and typhoon scenario in a fully coupled system of atmospheric-wave-current model would be desirable. As mentioned in Section 1, this study does not discuss the effect of wave-breaking, which has a considerable effect on the near-surface distributions of current, temperature, and salinity. Also, the integration of wave-breaking together with SP in the coupled ocean model remains a direction to be explored, as under high-wind conditions, the wave-breaking injects TKE to near-surface depths and the sea spay it induced can impact the exchange processes of momentum and heat through air-sea interface thus affecting ocean circulation modeling.

The impact of SST on hurricane intensity forecasts is a good example that emphasizes its importance in the air-sea interaction. A decrease of SST due to entrainment of the cooler waters from the thermocline in the ML under hurricane wind forcing produces a significant change in storm intensity.

Data availability statement

The original contributions presented in the study are included in the article/supplementary material. Further inquiries can be directed to the corresponding authors.

Author contributions

TY: Conceptualization, Funding acquisition, Validation, Writing – original draft, Writing – review & editing. ZD: Conceptualization, Formal Analysis, Funding acquisition, Investigation, Methodology, Resources, Validation, Writing – review & editing, Writing – original draft. CZ: Formal Analysis, Validation, Visualization, Writing – review & editing. AA: Formal Analysis, Validation, Writing – review & editing.

Funding

The author(s) declare that financial support was received for the research, authorship, and/or publication of this article. This research was supported by the National Key Research and Development Program under contract No. 2022YFC3105002; the National Natural Science Foundation under contract No. 42176020; and the Chinese Academy of Engineering Advisory Project under contract No. 2022-XBZD-11.

Conflict of interest

The authors declare that the research was conducted in the absence of any commercial or financial relationships that could be construed as a potential conflict of interest.

Publisher's note

References

Belcher, S., Grant, A., and Hanley, K. (2012). A global perspective on Langmuir turbulence in the ocean surface boundary layer. *Geophys. Res. Lett.* 39, L18605. doi: 10.1029/2012GL052932

Booij, N., Ris, R. C., and Holthuijsen, L. H. (1999). A third-generation wave model for coastal regions - 1. Model description and validation. *J. Geophysical Research-Oceans* 104, 7649–7666. doi: 10.1029/98JC02622

Cao, Y., Deng, Z., and Wang, C. (2019). Impacts of surface gravity waves on summer ocean dynamics in Bohai Sea. *Estuarine Coast. Shelf Science.* 230, 106443. doi: 10.1016/j.ecss.2019.106443

Craik, A. D. D., and Leibovich, S. (1976). A rational model for Langmuir circulation. *J. Fluid Mechanics* 73, 401–426. doi: 10.1017/S0022112076001420

Deng, Z., Li'an, X., Guijun, H., Xuefeng, Z., and Kejian, W. (2012). The effect of Coriolis-Stokes forcing on upper ocean circulation in a two-way coupled wave-current model. *Chin. J. Oceanology Limnology* 30, 321–335. doi: 10.1007/s00343-012-1069-z

Deng, Z., Lian, X., Ting, Y., Suixiang, S., Jiye, J., and Kejian, W. (2013). Numerical study of the effects of wave-induced forcing on dynamics in ocean mixed layer. *Adv. Meteorology* 2013 (10), 365818. doi: 10.1155/2013/365818

Ezer, T., and Mellor, G. L. (2004). A generalized coordinate ocean model and a comparison of the bottom boundary layer dynamics in terrain-following and in z-level grids. *Ocean Modell.* 6, 379–403. doi: 10.1016/S1463-5003(03)00026-X

Ginis, I. (2002). "Tropical cyclone–ocean interactions," in *Advances in Fluid Mechanics Series*, vol. 1 . Ed. W. Perrie (WIT Press), 83–114. Available at: https://www.researchgate.net/publication/266479137.

Harcourt, R. R. (2015). An improved second-moment closure model of langmuir turbulence. *J. Phys. Oceanography* 45, 84–103. doi: 10.1175/JPO-D-14-0046.1

Harcourt, R. R., and D'Asaro, E. A. (2008). Large-eddy simulation of Langmuir turbulence in pure wind seas. *J. Phys. Oceanogr.* 38, 1542–1562. doi: 10.1175/2007JPO3842.1

Huang, N. E. (1979). On surface drift currents in the ocean. *J. Fluid Mech.* 91, 191–208. doi: 10.1017/S0022112079000112

Kantha, L. H., and Clayson, C. A. (2004). On the effect of surface gravity waves on mixing in the oceanic mixed layer. *Ocean Modell.* 6, 101–124. doi: 10.1016/S1463-5003(02)00062-8

Lane, E. M., Restrepo, J. M., and McWilliams, J. C. (2007). Wave current interaction: A comparison of radiation-stress and vortex-force representations. *J. Phys. Oceanography* 37, 1122. doi: 10.1175/JPO3043.1

Langmuir, I. (1938). Surface motion of water induced by wind. *Science Am. Assoc. Advancement Sci.* 87, 119–123. doi: 10.1126/science.87.2250.119

Li, S., Li, M., Gerbi, G. P., and Song, J.-B. (2013). Roles of breaking waves and Langmuir circulation in the surface boundary layer of a coastal ocean. *J. Geophys. Res.* 118, 5173–5187. doi: 10.1002/jgrc.20387

McWilliams, J. C., and Restrepo, J. M. (1999). The wave-driven ocean circulation. *J. Phys. Oceanography* 29, 2523–2540. doi: 10.1175/15200485(1999)029<2523:TWDOC>2.0.CO;2

McWilliams, J., Sullivan, P., and Moeng, C. (1997). Langmuir turbulence in the ocean. *J. Fluid Mechanics* 334, 1–30. doi: 10.1017/S0022112096004375

Mellor, G. L., and Blumberg, A. (2004). Wave breaking and ocean surface thermal response. *J. Phys. Oceanogr.* 34, 693–698. doi: 10.1175/2517.1

Mellor, G. L., and Yamada, T. (1982). Development of a turbulence closure models for geophysical fluid problems. *Rev. Geophys.* 20, 851–875. doi: 10.1029/RG020i004p00851

Moghimi, S., Klingbeil, K., Gräwe, U., and Burchard, H. (2013). A direct comparison of a depth-dependent Radiation stress formulation and a Vortex force formulation within a three-dimensional coastal ocean model. *Ocean Model.* 70, 132–144. doi: 10.1016/j.ocemod.2012.10.002

Monterey, G., and Levitus, S. (1997). *Seasonal variability of mixed layer depth for the World Ocean* (Washington, D.C: NOAA Atlas, NESDIS 14). 100 pp.

Noh, Y., Min, H. S., and Raasch, S. (2004). Large eddy simulation of the ocean mixed layer: The effects of wave breaking and Langmuir circulation. *J. Phys. Oceanogr.* 34, 720–735. doi: 10.1175/1520-0485(2004)034<0720:LESOTO>2.0.CO;2

Polton, J. A., Lewis, D. M., and Belcher, S. E. (2005). The role of wave-induced Coriolis-Stokes forcing on the wind-driven mixed layer. *J. Phys. Oceanography Amer Meteorological Soc.* 35, 444–457. doi: 10.1175/JPO2701.1

Price, J. F. (1981). Upper ocean response to a hurricane. *J. Phys. Oceanogr.* 11, 153–175. doi: 10.1175/1520-0485(1981)011<0153:UORTAH>2.0.CO;2

Reichl, B. G., Ginis, I., Hara, T., Thomas, B., Kukulka, T., Wang, D., et al. (2016a). Impact of sea-state-dependent langmuir turbulence on the ocean response to a tropical cyclone. *Monthly Weather Rev.* 144, 4569–4590. doi: 10.1175/MWR-D-16-0074.1

Reichl, B. G., Wang, D., Hara, T., Ginis, I., and Kukulka, T. (2016b). Langmuir turbulence parameterization in tropical cyclone conditions. *J. Phys. Oceanogr* 46, 863–886. doi: 10.1175/JPO-D-15-0106.1

Song, D. (2012). Effect of activity characteristics of Typhoon Matsa on aviation meteorological observation and support. *Meteorological Hydrographical Mar. Instruments* 1, 99–104. doi: 10.19441/j.cnki.issn1006-009x.2012.01.026

Sullivan, P. P., Romero, L., McWilliams, J. C., and Melville, W. K. (2012). Transient evolution of langmuir turbulence in ocean boundary layers driven by hurricane winds and waves. *J. Phys. Oceanography* 42, 1959–1980. doi: 10.1175/JPO-D-12-025.1

Van Roekel, L. P., Fox-Kemper, B., Sullivan, P. P., Hamlington, P. E., and Haney, S. R. (2012). The form and orientation of Langmuir cells for misaligned winds and waves. *J. Geophys. Res.* 117, C05001. doi: 10.1029/2011JC007516

Wang, M., and Deng, Z. (2022). On the role of wave breaking in ocean dynamics under typhoon Matsa in the Bohai Sea, China. *Acta Oceanol. Sin.* 41, 1–18. doi: 10.1007/s13131-022-1995-3

Webb, A., and Fox-Kemper, B. (2011). Wave spectral moments and Stokes drift estimation. *Ocean Model.* 40, 273–288. doi: 10.1016/j.ocemod.2011.08.007

Wu, L., Rutgersson, A., and Sahlee, E. (2015). Upper-ocean mixing due to surface gravity waves. *J. Geophys. Res.* 120, 8210–8228. doi: 10.1002/2015JC011329

Zhang, X., Chu, P. C., Li, W., Liu, C., Zhang, L., Shao, C., et al. (2018). Impact of langmuir turbulence on the thermal response of the ocean surface mixed layer to supertyphoon haitang, (2005). *J. Phys. Oceanography* 48, 1651–1674. doi: 10.1175/JPO-D-17-0132.1

Zhao, Y., Deng, Z., Yu, T., and Wang, H. (2019). Numerical study on tidal mixing in the bohai sea. *Mar. Geodesy* 42 (1), 46–63. doi: 10.1080/01490419.2018.15390

Zijlema, M., van Vledder, G. P., and Holthuijsen, L. H. (2012). Bottom friction and wind drag for wave models. *Coast. Eng.* 65, 19–26. doi: 10.1016/j.coastaleng.2012.03.002

frontiers | Frontiers in Marine Science

TYPE Brief Research Report
PUBLISHED 12 June 2024
DOI 10.3389/fmars.2024.1374144

OPEN ACCESS

EDITED BY
Donald B. Olson,
University of Miami, United States

REVIEWED BY
Alessandro Stocchino,
Hong Kong Polytechnic University,
Hong Kong SAR, China
Dan Liberzon,
Technion Israel Institute of Technology, Israel

*CORRESPONDENCE
Henrik Kalisch
henrik.kalisch@uib.no

RECEIVED 21 January 2024
ACCEPTED 21 May 2024
PUBLISHED 12 June 2024

CITATION
Bondehagen A, Kalisch H and Roeber V (2024) Infragravity waves and cross-shore motion–a conceptual study. *Front. Mar. Sci.* 11:1374144. doi: 10.3389/fmars.2024.1374144

Infragravity waves and cross-shore motion–a conceptual study

Andreas Bondehagen[1], Henrik Kalisch[1]* and Volker Roeber[2]

[1]Department of Mathematics, University of Bergen, Bergen, Norway, [2]Université de Pau et des Pays de l'Adour, E2S-UPPA, chair HPC-Waves, SIAME, Anglet, France

It is widely known that Infragravity (IG) waves induce cross-shore fluid motion in the nearshore, and multiple recent observational studies have identified IG waves as the dominant factor for a range of nearshore processes such as particle drift in the surf zone, transport of suspended sediment and river plume oscillations. While it is clear that the underlying orbital motion linked to IG wave excursions correlates with IG wave periods, the exact relation between the IG wave amplitude and the strength of the cross-shore motion has not been investigated in great detail. In the present contribution, we aim to quantify the cross-shore motion as a function of the IG wave amplitude. Indeed, it is shown that IG waves of even the most minute amplitude induce a large horizontal movement of particles, and the cross-shore movement is often several orders of magnitude larger than the particle movement induced by ordinary gravity waves. The results hold across a number of situations including monochromatic waves, sea states given by a spectrum as well as nonlinear waves with and without strong bathymetric forcing.

KEYWORDS

infragravity waves, particle transport, linear wave theory, numerical modeling, Boussinesq model, numerical tracers

1 Introduction

A sea state can be thought of as a superposition of surface waves of different periods with suitably randomized amplitudes and phase parameters, providing a theoretical description of wave conditions at a particular location in the ocean. The energy distribution of a sea state is given in terms of a wave spectrum that can often be approximated with simple expressions, which are understood to have fairly broad applicability. Commonly used expressions include the JONSWAP spectrum (Hasselmann et al., 1973) for typical North Sea waves, its extension to shallow water, the TMA spectrum (Holthuijsen, 2010), or the Pierson-Moskowitz (Pierson and Moskowitz, 1964) spectrum suitable for the description of fully developed open-ocean swells. As the individual waves that compose these spectra propagate through the ocean, fluid particles move in tandem with the waves, but at a slower pace, with the particle velocity

typically being only a fraction of the wave celerity. In the linear approximation, fluid particles trace out nearly circular to elliptic orbits that do not effectively lead to a mass displacement except for a small forward drift, commonly known as the Stokes drift (Stokes, 1847; Lamb, 1924; Kundu and Cohen, 2015). While the Stokes drift is the main driving force for wave-induced mass transport in the open ocean (Kenyon, 1969; McWilliams and Restrepo, 1999), in the nearshore and in particular in the surf zone, wave breaking is the dominant mechanism for mass transport, affecting processes such as undertow (Svendsen, 1984), surf beat, circulation patterns (Davidson-Arnott et al., 2019), and rip currents (Castelle et al., 2016).

In contrast to ordinary wind-generated gravity waves which have periods of 1 sec to about 30 sec (Munk, 1951; Kinsman, 1984), *Infragravity* (IG) waves feature much larger periods, usually well above 25 seconds. Generally, waves in the 30- to 300-second range are attributed to the IG spectrum; though very long IG waves with periods of up to 15 min have been reported through observations and numerical modeling efforts (Péquignet et al., 2014). While gravity waves are generated by wind forcing, IG waves appear due to secondary generation mechanisms. In fact, there are two types of IG waves, bound IG waves, connected to wave groups originating from the deep open ocean, and free IG waves, generated in and around the surf zone. Regarding bound IG waves, recall that it is well established that ocean waves conventionally appear in groups or sets (see (Longuet-Higgins, 1984; Thompson et al., 1984)) and that these groups carry long-period oscillations of the mean water level based on the mechanisms outlined in (Longuet-Higgins and Stewart, 1962). These oscillations of the mean water level are known as bound IG waves. Once these bound waves enter shallow water, they are released and propagate freely. This is usually happening close to the break point in shallow water where the waves' group speed depends less on the frequencies of the individual swell waves, but increasingly on the local water depth (Baldock, 2012). In addition, the horizontal movement of the break point location can contribute to the energy in the IG wave band as pointed out by (Symonds et al., 1982). This is essentially based on the fact that individual nearshore waves exhibit varying heights and periods so that wave breaking occurs over a range of different depths and consequently at slightly different distances from shore.

IG waves in the surf zone explain the well-known surf beats observed in (Munk, 1949; Tucker, 1950), and are connected to various nearshore and coastal processes such as rip currents, run-up and overtopping, as well as beach and dune erosion (Russell, 1993; van Thiel de Vries et al., 2008; Roeber and Bricker, 2015; Castelle et al., 2016; Bertin et al., 2018). It is also known that IG waves are crucial for the movement of sandbars along the beach (Aagaard and Greenwood, 2008), and recent field measurements have revealed the importance of IG waves for several nearshore transport phenomena such as river plume oscillations (Flores et al., 2022), movement of particle tracers (Bjørnestad et al., 2021), and transport of suspended sediment (Mendes et al., 2020).

The present study aims to quantify how IG waves drive cross-shore currents. The basic mechanism can be observed in a simple - yet fundamental - linear analysis of the water-wave problem. In fact, in Section 2 linear wave theory will be used to show that waves of small - even minute - amplitude but very long period can cause large horizontal excursions of the particles in the underlying fluid. This effect can be observed for both monochromatic waves as well as a superposition of wave modes defined by a wave spectrum. In fact, it will be shown that IG frequencies always dominate the lateral forward-backward movement of the fluid particles.

Section 3 investigates cross-shore motions in a more realistic setting in the presence of nonlinear interactions and wave breaking. Here, the well-established numerical nearshore wave model BOSZ (Boussinesq Ocean & Surf Zone model) (Roeber et al., 2010) is used to study the influence of IG waves on cross-shore motion. First, the ability of the BOSZ model to generate dynamic (bound) IG-waves on a flat bathymetry and free IG waves through wave breaking at a beach is ascertained. We impose wave signal with an empirical JONSWAP spectrum through boundary forcing and look at the wave development on a flat bathymetry and at a couple of idealized beaches. It is observed that free IG waves usually dominate over bound IG waves, inline with observational findings, such as for example Herbers et al. (1994). Finally, a more realistic beach with multiple bars is studied, and by following fluid particles throughout the computation, it is shown that IG-waves dominate the cross-shore back-and-forth movement to an even larger degree than in the linear case.

2 Linear theory

Consider a single wave component in a fluid of depth H. For a monochromatic wave with the free-surface excursion given by $\eta(x,t) = a\cos(kx - \omega t)$, the velocity potential is obtained from the linearized free-surface Euler equations as

$$\phi(x,z,t) = \frac{\omega a}{k}\frac{\cosh\,[k(H+z)]}{\sinh\,(kH)}\sin\,(kx-\omega t)\,. \tag{1}$$

Here a is the wave amplitude, $k = 2\pi/\lambda$ is the wave number, λ is the wavelength, $\omega = 2\pi/T$ is the radial frequency, and T is the wave period. Taking the spatial derivative of ϕ in Equation (1) for the horizontal and vertical component, the fluid particle paths ($\xi(t), \zeta(t)$) are given as a solution of the system

$$\begin{aligned}\frac{d\xi}{dt} &= \phi_x(\xi,\zeta,t) = \omega a\frac{\cosh\,[k(H+\zeta)]}{\sinh\,(kH)}\cos\,(k\xi-\omega t)\\ \frac{d\zeta}{dt} &= \phi_z(\xi,\zeta,t) = \omega a\frac{\sinh\,[k(H+\zeta)]}{\sinh\,(kH)}\sin\,(k\xi-\omega t)\,.\end{aligned} \tag{2}$$

Assuming that the particle position stays close to the center (x_0, z_0) allows replacement of the position $(\xi(t), \zeta(t))$ on the right hand side by the center position, leading to closed elliptic orbits of the form

$$\begin{aligned}\xi &= x_0 - a\frac{\cosh\,[k(H+z_0)]}{\sinh\,(kH)}\sin\,(kx_0-\omega t),\\ \zeta &= z_0 + a\frac{\sinh\,[k(H+z_0)]}{\sinh\,(kH)}\cos\,(kx_0-\omega t)\,.\end{aligned} \tag{3}$$

The total extent of horizontal movement of a particle due to a single wave can then be seen from Equation (3) to be $L(a,k,z) = 2a\frac{\cosh\,[k(H+z_0)]}{\sinh\,(kH)}$, and for long waves in shallow water, and particular for IG waves, this can be approximated by $L \sim a\lambda/\pi H$. Note that the second-order approximation of the paths yields a net movement

in the direction of the waves, the *Stokes drift velocity* $\bar{u}_L$, already alluded to in the introduction. The Stokes drift during one wave cycle can be computed from (2) (see Debnath (1994) for example), and is given by

$$x_L(a,k,z) = T\bar{u}_L = a^2\omega kT\frac{\cosh\ [2k(H+z_0)]}{2\sinh^2(kH)}, \tag{4}$$

and in shallow water, this can be approximated by the expression $x_L \sim a^2\lambda/2H^2$. It can be seen that in the nearshore zone where the shallow-water approximation is valid, the ratio between these two quantities is

$$\frac{x_L}{L(a,k,z)} \sim \frac{\pi}{2}\frac{a}{H}.$$

Since IG wave amplitudes are usually only a small fraction of the water depth (except during severe sea conditions), $L(a,k,z)$ dominates substantially over the Stokes drift, and we neglect the Stokes drift in the present section. However, in a general situation, a wavefield will feature both IG and gravity wave components, and the Stokes drift for the gravity-wave components will be considered later.

The above formula relates the horizontal extent of the particle motion L and the Stokes drift x_L specifically in terms of the wave period while considering shallow water with a fixed depth H. One may also relate the expressions for L and x_L in terms of the wave period T by using the relationship between wave period and $\lambda = cT$, where c is the wave speed or celerity. For long waves, we have

$$L \sim \frac{acT}{\pi H},$$

while for short waves the Stokes drift is

$$x_L \sim \frac{a^2cT}{2H^2}.$$

So, in shallow water with a fixed depth, the horizontal particle motion and the Stokes drift both have a linear dependence on the wave period, but with different coefficients that depend on the wave speed, wave amplitude, and depth. It should be kept in mind that gravity waves decay in amplitude due to wave breaking in the surf zone. As already mentioned, wave breaking is also an energy transfer process from short to long waves, i.e. as gravity waves decrease towards the shore, IG waves increase and the difference between L and x_L increases rapidly.

In Figure 1A, particle trajectories associated to surface waves for four different parameter combinations are shown. It is apparent that the extent of horizontal movement is much larger for IG waves than for gravity waves (in the figure, we compare waves of period 10 seconds and 100 seconds). Comparing the upper and lower panels in Figure 1A shows that the difference in the horizontal extent of the particle movement diminishes with larger depth. Plotting the total extent of the horizontal movement of waves in the same depth, with the same amplitude but different periods yields the black curve in the left panel of Figure 1B. The plot also shows the movement associated with a superposition of linear waves from a JONSWAP spectrum with an added small infragravity component. The right panel shows the spectrum, and the green and dashed curves in the left panel show the extent of horizontal movement at difference depths. For both these examples the infragravity waves dominate the movement by far.

Using linear wave theory allows adding an arbitrary number of wave components in the form

$$\eta_i(x,t) = A_i\cos(k_ix - \omega_it + \phi_i), \tag{5}$$

where the amplitude A_i is Rayleigh distributed and the phase ϕ is uniformly distributed. The free surface is then written as a superposition $\eta(x,t) = \sum_i \eta_i$ and the fluid velocity at the free surface is given by

$$u(x,z,t) = \sum_i \omega_iA_i\frac{\cosh(k_i(H+z))}{\sinh(k_iH)}\cos\left(k_ix - \omega_it + \phi_i\right) \tag{6}$$

and

$$v(x,z,t) = \sum_i \omega_iA_i\frac{\sinh\ (k_i(H+z))}{\sinh\ (k_iH)}\sin\left(k_ix - \omega_it + \phi_i\right). \tag{7}$$

The movement of a fluid particle can then be described by a coupled system of differential equations similar to (2) as

$$\frac{d\xi}{dt} = u(\xi,\zeta,t), \frac{d\zeta}{dt} = v(\xi,\zeta,t). \tag{8}$$

Since the expressions for u and v are known explicitly, these equations can be solved with a standard numerical solver, such as a Runge-Kutta scheme. Instead of assuming that the velocity of the particle is close to that near the original center, we compute the particle paths directly which is feasible as long as the expressions for u and v are known in closed form [for a similar process applied to cnoidal-wave solutions, see (Borluk and Kalisch, 2012)].

Modelling the waves with Equations (5–7) and following the particle for 1800s with a time discretization of 0.25s, using the classical four-stage Runge-Kutta scheme to evolve (Equation 8) in time, and removing the linear Stokes drift, we get the results from Figure 2. Notice here that the position of the tracer is dominated by the components in the infragravity spectrum to a larger degree than predicted by the analytical case, while the amplitudes and the velocity are reminiscent of the input spectrum. Together with the analytical results, this shows that IG waves have a much larger influence on particle transport and dominate that of higher frequency waves, although they carry only a small part of the total energy of the wave field.

3 Nonlinear model

The next objective is to show that the results detailed above also hold for realistic conditions in the nearshore. To this end, we utilize BOSZ, a phase-resolving nearshore wave model based on the Nwogu equations (Roeber et al., 2010), which has been shown to yield accurate results in various situations. In particular, the model has been compared to both laboratory results (Wong et al., 2019), data from field campaigns (Roeber and Bricker, 2015) and with other models (Lynett et al., 2017). The model allows evaluation of wave-driven currents and tracking of particles.

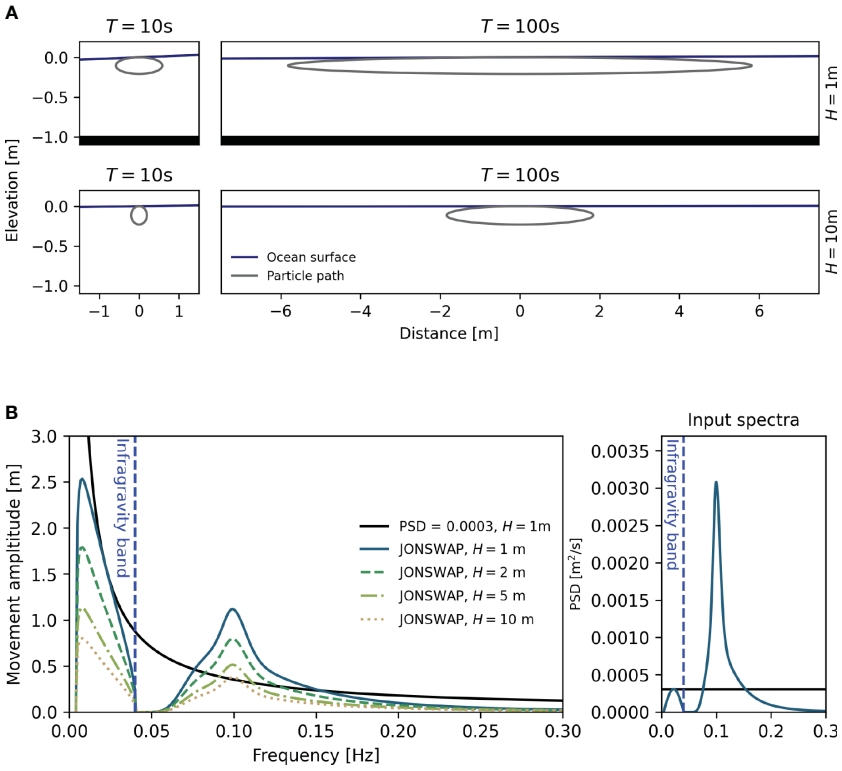

FIGURE 1
Fluid particle movement associated with a single wave component: **(A)** Pathlines for one period of a monochromatic wave with 0.1 m amplitude. Particle trajectories are found by solving Equation (2) with RK4. Left panels: a 10-second wave with amplitude for depth H = 1m and H = 10m. Right: a 100-second wave with the same amplitude and for the same two depths. It is apparent that the infragravity wave induces a much larger extent of horizontal movement. **(B)** Horizontal extent of particular orbit based on analytical solutions of the movement of the particle in a surface wave of a single frequency. The black curve in the left panel shows the horizontal movement associated with different wave components with equal amplitude a = 0.025m. The remaining curves show the maximum horizontal transport due to linear waves with amplitudes chosen from a JONSWAP spectrum with H_s = 0.1m and T_m = 10s, with an added infragravity component with 10% of the peak energy, and with varying depths. The right panel shows a representation of the power spectra for the case of a single wave (black line) and for the case of a JONSWAP spectrum with additional infragravity component (blue curve).

The model is driven by imposing a sea state from a JONSWAP spectrum near the left boundary. The sea state is the same as in the earlier tests, but without the infragravity component (see Figure 3 upper right panel). In the present case, we first aim to observe IG wave generation due to nonlinear interactions in the governing equations.

To verify that BOSZ can model IG-generation a computation is run for 3 hours with a 1 hour ramping time for 3 different bathymetry configurations. The wave's free surface elevation is recorded at 1 Hz at a virtual gauge in form of a time series, from which the power spectral density is calculated. In Figure 3 one can see the bathymetries and corresponding power spectral densities (PSD). In the flat beach case both ends of the domain are padded with a sponge layer so that no reflection takes place. Thus IG wave components that are visible in the spectrum must be bound IG waves as described in (Longuet-Higgins and Stewart, 1962). For the other two bathymetries, a plane beach and a trilinear beach, the IG-band is more pronounced by a factor of 2 to 4 (see Table 1 for an overview of the bathymetries). This is likely due to free IG waves generated around the limit of the surf zone by the break point and shallow water mechanisms outlined in (Symonds et al., 1982; Baldock, 2012). In fact, applying a band-pass filter isolating the IG-wave frequencies between f = 0.004 and f = 0.04 Hz, reveals a correlation of 0.99 between the free surface and the horizontal velocity in the case of a flat bathymetry, indicating that IG waves are traveling in the direction of increasing values of x. On the other hand the correlation in the two cases with the sloping beach is 0.16 and −0.15, indicating IG waves traveling in both directions. The finding that free waves dominate vis-a-vis bound IG waves in the cases with the beach is also in line with the measurements reported on in (Smit et al., 2018).

The bathymetry of the applied test of movement can be seen in the top panel of Figure 4 and in the last row in Table 1, with the locations of three measurement points (gauges) and the corresponding tracked drifters marked. The numerical domain is one-dimensional with a spatial resolution of DX = 2m. This bathymetry features a simple but realistic concept that allows us to observe the effect of IG waves on wave-induced particle transport.

The model is run for 3600 seconds of which the first 1800 seconds are dedicated to the full development of the sea state before the fluid particles are introduced, after which they are sampled every 1 second. This yields a fundamental frequency of $f_0 = \frac{1}{T} \approx 0.001$Hz and Nyquist frequency of f_{max} = 0.5 Hz.

Results of an in-depth time series analysis are shown in Figure 4. In the panels in row 2, the total signal as well as the low-pass filtered data recorded at the gauges is plotted. Combining this with the PSD as seen in row 3, one can see in the left column that the JONSWAP

10.3389/fmars.2024.1374144

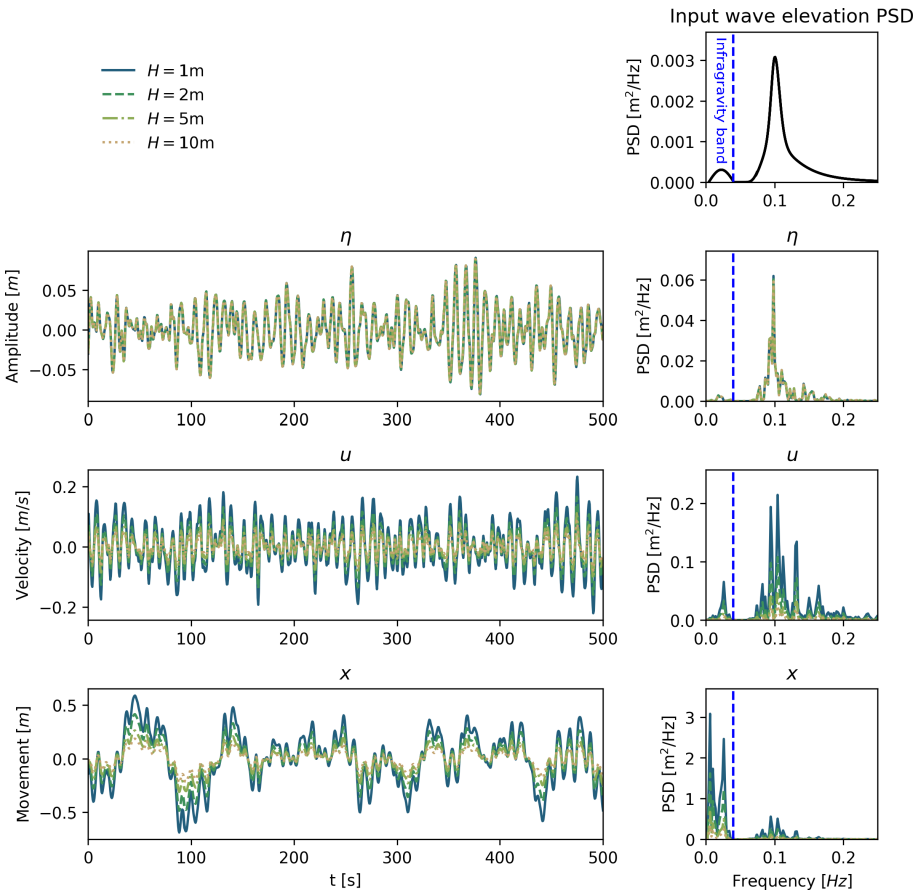

FIGURE 2
Experimental results from following a fluid particle moved by a superposition of waves. Top: Amplitudes of waves encountered by the particle. Middle: Velocity experienced by the particle. Bottom: Position of particle over time. Left: Time series of values. Right: Power spectral density of the time series. Colors and line-styles indicate corresponding to water depths: whole 1m, dashed 2m, dash-dot 5m, dotted 10m. For the computations shown in this Figure, 500 wave components with frequencies between 0.004*Hz* and 0.5*Hz* were used.

spectrum has been correctly generated by the wavemaker, but with some extra energy in the frequency band at 0.2Hz. This appears to be the result of reflected waves twice the frequency of the original JONSWAP peak. In the middle column the waves have travelled over the 1:10 slope, so that the water depth is now 2.5 meters, as opposed to 10 meters in the left column. It can be seen in the middle plot of row 3 that energy from the ordinary gravity wave spectrum has almost vanished due to bathymetry-driven wave breaking while energy starts to appear in the IG-band. Continuing on to the rightmost gauge on a now much milder slope in 1 meter depth these processes continue and the free surface is now dominated by waves in the IG band.

In row 4 the position of the three numerical drifters over time is shown. Since the numerical drifters move in the direction of the waves due to Stokes drift, it is necessary to detrend their time series signal around a moving mean position as shown in row 4 of Figure 4. For the drifter in 10 meters depth, the Stokes drift as defined in Equation 4 is constant due to the flat bathymetry, so that a first-order linear regression can be used to remove the Stokes drift from the observed drifter path. For the drifters in the shallower locations, subtracting the Stokes drift is not as straightforward. As the numerical drifters move to shallower water, the wave field and hence Stokes drift change yielding a non-constant drift, which makes a linear curve fit problematic. In such cases, a 3rd and 4th-order polynomial provided a much better fit as indicated by the black line in the middle and right column in row 4. The movement about the changing mean position for the three drifters can be seen in row 5 in Figure 4. Lastly, the Fourier transformation of this signal was taken resulting in the plots of row 6. Comparing row 3 and 6 shows the importance of the IG band on the particle movement. In the left column it is impossible, on a linear scale, to see the component of the IG band in the PSD. Nevertheless, as observed in the row 6, the IG band still has a significant influence on the movement of the drifter. For the middle row it is possible to notice the PSD component in the IG band, but it is still small compared to the size of the ordinary gravity waves. However, the particle movement is dominated by the IG wave component. Lastly, as shown in the right column of plots concerning the drifter very close to shore, the horizontal movement is almost entirely controlled by waves in the IG band. Comparing the right column with the middle and left columns, it is clear that the increased energy associated with IG waves yields a much larger movement even though the wave field is much smaller.

10.3389/fmars.2024.1374144

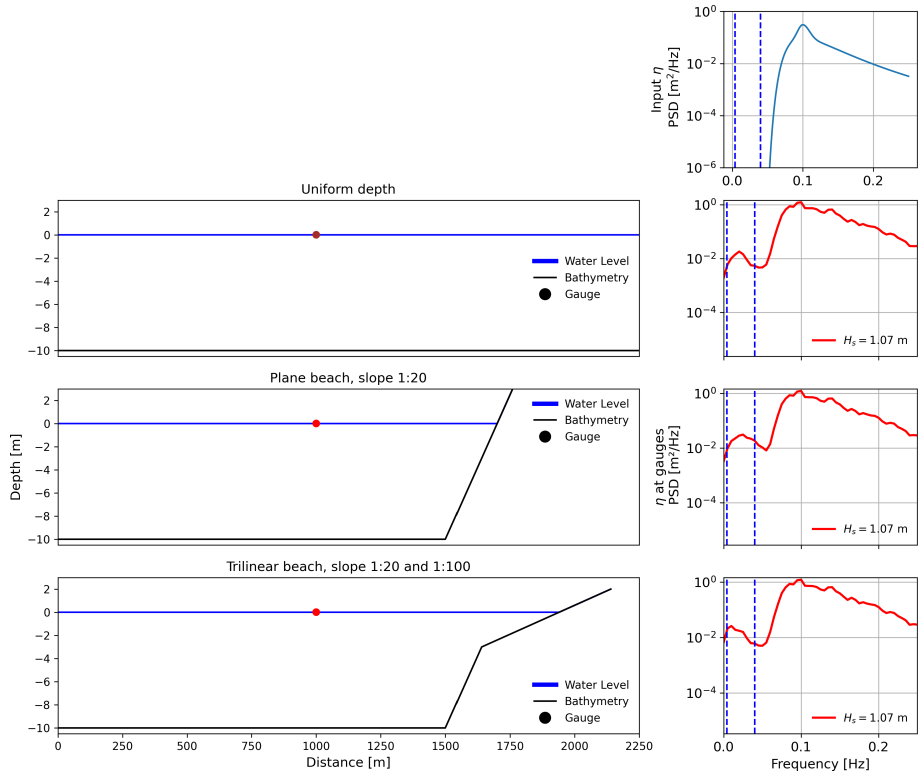

FIGURE 3
Comparison of infragravity wave generation from BOSZ. Upper right: the input JONSWAP spectrum to the model with H_s = 1m and T_p = 10s. Notice the lack of IG wave components in the input. Second row: A flat beach is simulated, and bound IG waves are generated as expected given the theory in (Longuet-Higgins and Stewart, 1962). Third and fourth row: with the inclusion of a beach where waves can break the IG band is increasingly significant. This is likely due to free IG waves generated in shallow water around the break point (Symonds et al., 1982; Baldock, 2012).

4 Conclusion

In the present work, the importance of IG waves on particle motion in the nearshore area has been considered in a two-dimensional setting, i.e. along a shore-normal transect. In this simplified situation, a direct link between the presence of IG waves and the main cross-shore fluid particle movement has been explored. While it is generally accepted that infragravity-wave components correlate with perturbations in the shorter-wave velocity and with horizontal velocities (see (Tissier et al., 2015) for example), the present study provides a fundamental explanation using linear wave theory and a quantification of the cross-shore motion as a function of the wave amplitude both in the linear and nonlinear case.

The study highlights what is essentially evident from linear wave theory, namely the dependence of the fluid particle excursion under waves on wave amplitude and period. It is shown in a simple yet realistic way that the horizontal motion of fluid particles in shallow water is mostly controlled by underlying IG waves, nearly independent of their amplitude, and that usual gravity waves are only of secondary importance.

This transport is essentially oscillatory in nature, i.e. it describes a back-and-forth motion of the fluid particles. This is in contrast to the Stokes drift of gravity waves that is always acting in the direction of wave propagation. The IG wave-induced motion is very large in proportion to the IG wave amplitude. In fact, even an IG wave with a tiny amplitude can lead to very large back-and-forth motions in the fluid. In the non-linear case this ratio approaches

TABLE 1 Bathymetries used in BOSZ.

Fig	Length	Depth	Slope 1	Depth	Slope 2	Depth	Slope 3	Depth	Slope 4	Depth	Slope 5	Depth
	[m]	[m]		[m]		[m]		[m]		[m]		[m]
3a	2250	10	–	–	–	–	–	–	–	–	–	–
3b	1750	10	1:20	-5	–	–	–	–	–	–	–	–
3c	2150	10	1:20	3	–	–	1:100	-2	–	–	–	–
4	2500	10	1:10	2.7	-1:2000	2.8	1:200	0.5	-1:500	0.7	1:50	-1.3

For Figure 4 the slopes are the means of each squared sine function.

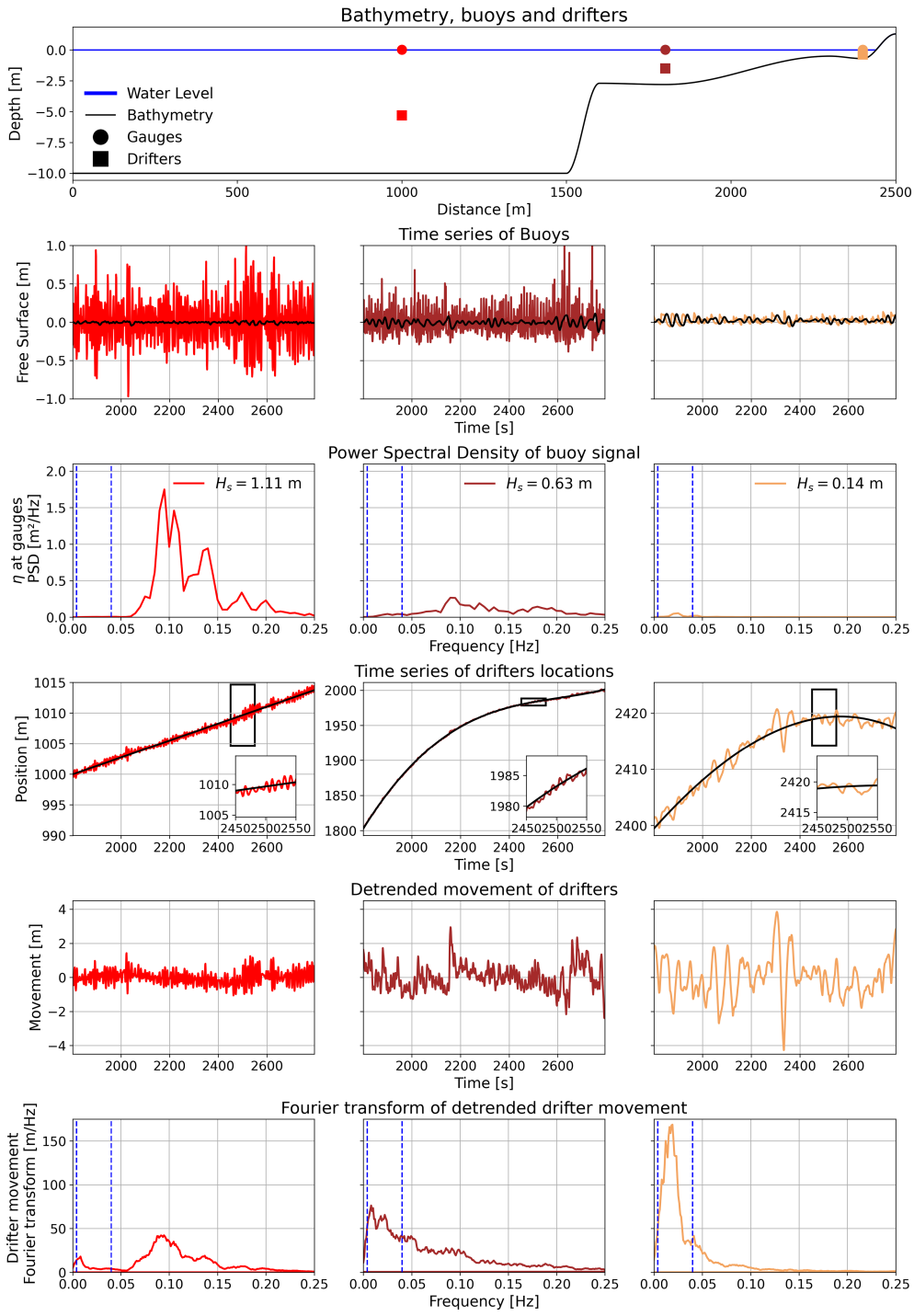

FIGURE 4
Numerical results for particle tracer movements. Row 1: Bathymetry and locations. Row 2: The time series of the wave elevation at the gauges. The colors and column correspond to the locations in the top plot, and the black curves are the IG-signal. Row 3: PSD of the wave elevation at the gauges. Row 4: Raw time series of the drifters location (color) together with the regression line (black). Row 5: Time series of the movement about the regression line. Row 6: PSD of the movement of the particles after the Stokes drift has been removed.

quickly 1/100. The phenomenon essentially applies in the same way to a single wave component or a spectrum, and it also occurs in a similar fashion in nonlinear waves as shown by a Boussinesq-type model. The principles also hold consistently for non-uniform seabeds.

In nature, the behavior of IG waves depends at various levels on other factors such as the direction of the incoming wave field (Herbers et al., 1995a), local beach morphology (Bryan et al., 1998), or the tide stage (Melito et al., 2022), to name only a few. Obviously, three-dimensional dynamics will generally affect the

IG wave signal, in particular in connection with the appearance of edge waves (Herbers et al., 1995b), IG wave reflection (Sheremet et al., 2002), as well as eventual propagation off-shore and refraction at the shelf break (Smit et al., 2018).

As already mentioned, IG waves are connected to a wide range of nearshore processes, and the results in this paper are in line with recent observations of horizontal movement of freshwater plumes (Flores et al., 2022) and also with wave-by-wave motions of tracer particles in the nearshore (Bjørnestad et al., 2021).

While the objective of this study is not to identify the processes responsible for sediment transport, this work validates and quantifies the findings by (Aagaard and Greenwood, 2008) about the underlying physics of IG wave-driven motion of sediment. In reality, the mechanism showcased in this article will rarely be the only controlling process and may not always be easily detectable in a three-dimensional setting. However, as shallow water regimes naturally tend to exhibit waves in the IG band due to non-linear bathymetric effects, the results provided here suggest that the horizontal motion induced by IG waves always plays a key role.

Data availability statement

The original contributions presented in the study are included in the article/supplementary material. Further inquiries can be directed to the corresponding author.

Author contributions

AB: Conceptualization, Formal analysis, Investigation, Methodology, Software, Visualization, Writing – original draft, Writing – review & editing. HK: Conceptualization, Formal analysis, Funding acquisition, Investigation, Methodology, Supervision, Writing – original draft, Writing – review & editing. VR: Conceptualization, Formal analysis, Methodology, Resources, Software, Supervision, Validation, Writing – original draft, Writing – review & editing.

Funding

The author(s) declare financial support was received for the research, authorship, and/or publication of this article. HK acknowledges support from *Bergen Universitetsfond*. VR acknowledges financial support from the I-SITE program *Energy & Environment Solutions* (E2S), the Communauté d'Agglomération Pays Basque (CAPB), and the Communauté Région Nouvelle Aquitaine (CRNA) for the E2S chair position HPC-Waves.

Acknowledgments

The authors would like to thank Alexander Horner-Devine for providing some inspiration for undertaking the present study. The authors would like to thank Dr. Tomohiro Suzuki for providing the raw data of the laboratory experiment referenced in Suzuki et al. (2017).

Conflict of interest

The authors declare that the research was conducted in the absence of any commercial or financial relationships that could be construed as a potential conflict of interest.

Publisher's note

References

Aagaard, T., and Greenwood, B. (2008). Infragravity wave contribution to surf zone sediment transport—the role of advection. *Mar. Geology* 251, 1–14. doi: 10.1016/j.margeo.2008.01.017

Baldock, T. (2012). Dissipation of incident forced long waves in the surf zone — implications for the concept of "bound" wave release at short wave breaking. *Coast. Eng.* 60, 276–285. doi: 10.1016/j.coastaleng.2011.11.002

Bertin, X., De Bakker, A., Van Dongeren, A., Coco, G., Andre, G., Ardhuin, F., et al. (2018). Infragravity waves: From driving mechanisms to impacts. *Earth-Science Rev.* 177, 774–799. doi: 10.1016/j.earscirev.2018.01.002

Bjørnestad, M., Buckley, M., Kalisch, H., Streßer, M., Horstmann, J., Frøysa, H. G., et al. (2021). Lagrangian measurements of orbital velocities in the surf zone. *Geophysical Res. Lett.* 48, e2021GL095722. doi: 10.1029/2021GL095722

Borluk, H., and Kalisch, H. (2012). Particle dynamics in the KdV approximation. *Wave Motion* 49, 691–709. doi: 10.1016/j.wavemoti.2012.04.007

Bryan, K., Howd, P., and Bowen, A. (1998). Field observations of bar-trapped edge waves. *J. Geophysical Research: Oceans* 103, 1285–1305. doi: 10.1029/97JC02938

Castelle, B., Scott, T., Brander, R., and McCarroll, R. (2016). Rip current types, circulation and hazard. *Earth-Science Rev.* 163, 1–21. doi: 10.1016/j.earscirev.2016.09.008

Davidson-Arnott, R., Bauer, B., and Houser, C. (2019). *Introduction to coastal processes and geomorphology*. (Cambridge: Cambridge University Press).

Debnath, L. (1994). *Nonlinear water waves*. (San Diego: Academic Press).

Flores, R. P., Williams, M. E., and Horner-Devine, A. R. (2022). River plume modulation by infragravity wave forcing. *Geophysical Res. Lett.* Academic Press: San Diego 49, e2021GL097467.

Hasselmann, K., Barnett, T. P., Bouws, E., Carlson, H., Cartwright, D. E., Enke, K., et al. (1973). Measurements of wind-wave growth and swell decay during the joint north sea wave project (jonswap). *Ergaenzungsheft zur Deutschen Hydrographischen Zeitschrift Reihe A*. 12, 7–93

Herbers, T., Elgar, S., and Guza, R. (1994). Infragravity-frequency (0.005–0.05 hz) motions on the shelf. part i: Forced waves. *J. Phys. Oceanography* 24, 917–927. doi: 10.1175/1520-0485(1994)024<0917:IFHMOT>2.0.CO;2

Herbers, T., Elgar, S., and Guza, R. (1995a). Generation and propagation of infragravity waves. *J. Geophysical Research: Oceans* 100, 24863–24872. doi: 10.1029/95JC02680

Herbers, T., Elgar, S., Guza, R., and O'Reilly, W. (1995b). Infragravity-frequency (0.005–0.05 hz) motions on the shelf. part ii: Free waves. *J. Phys. Oceanography* 25, 1063–1079. doi: 10.1175/1520-0485(1995)025<1063:IFHMOT>2.0.CO;2

Holthuijsen, L. H. (2010). *Waves in oceanic and coastal waters*. (Cambridge: Cambridge university press).

Kalisch, H., Lagona, F., and Roeber, V. (2024). Sudden wave flooding on steep rock shores: a clear but hidden danger. *Natural Hazards* 120, 3105–3125. doi: 10.1007/s11069-023-06319-w

Kenyon, K. E. (1969). Stokes drift for random gravity waves. *J. Geophysical Res.* 74, 6991–6994. doi: 10.1029/JC074i028p06991

Kinsman, B. (1984). *Wind waves: their generation and propagation on the ocean surface*. (New York: Courier Corporation).

Kundu, P. K., and Cohen, I. M. (2015). *Fluid mechanics*. (San Diego: Academic Press).

Lamb, H. (1924). *Hydrodynamics*. (Cambridge: University Press).

Longuet-Higgins, M. S. (1984). Statistical properties of wave groups in a random sea state. Philosophical Transactions of the Royal Society of London. *Ser. A Math. Phys. Sci.* 312, 219–250.

Longuet-Higgins, M. S., and Stewart, R. W. (1962). Radiation stress and mass transport in gravity waves, with application to 'surf beats'. *J. Fluid Mechanics* 13, 481–504. doi: 10.1017/S0022112062000877

Lynett, P. J., Gately, K., Wilson, R., Montoya, L., Arcas, D., Aytore, B., et al. (2017). Inter-model analysis of tsunami-induced coastal currents. *Ocean Model.* 114, 14–32. doi: 10.1016/j.ocemod.2017.04.003

McWilliams, J. C., and Restrepo, J. M. (1999). The wave-driven ocean circulation. *J. Phys. Oceanography* 29, 2523–2540. doi: 10.1175/1520-0485(1999)029<2523:TWDOC>2.0.CO;2

Melito, L., Parlagreco, L., Devoti, S., and Brocchini, M. (2022). Wave-and tide-induced infragravity dynamics at an intermediate-to-dissipative microtidal beach. *J. Geophysical Research: Oceans* 127, e2021JC017980.

Mendes, D., Fortunato, A. B., Bertin, X., Martins, K., Lavaud, L., Nobre Silva, A., et al. (2020). Importance of infragravity waves in a wave-dominated inlet under storm conditions. *Continental Shelf Res.* 192, 104026. doi: 10.1016/j.csr.2019.104026

Munk, W. (1949). *Surf beats* Vol. 30. (EOS, Transactions American Geophysical Union), 849–854.

Munk, W. H. (1951). *Origin and generation of waves*. (La Jolla: Tech. rep., Scripps Institution of Oceanography La Jolla Calif).

Péquignet, A.-C. N., Becker, J. M., and Merrifield, M. A. (2014). Energy transfer between wind waves and low-frequency oscillations on a fringing reef, Ipan, Guam. *J. Geophysical Research: Oceans* 119, 6709–6724. doi: 10.1002/2014JC010179

Pierson, W. J. Jr., and Moskowitz, L. (1964). A proposed spectral form for fully developed wind seas based on the similarity theory of sa kitaigorodskii. *J. geophysical Res.* 69, 5181–5190. doi: 10.1029/JZ069i024p05181

Roeber, V., and Bricker, J. D. (2015). Destructive tsunami-like wave generated by surf beat over a coral reef during typhoon haiyan. *Nat. Commun.* 6, 7854. doi: 10.1038/ncomms8854

Roeber, V., Cheung, K. F., and Kobayashi, M. H. (2010). Shock-capturing boussinesq-type model for nearshore wave processes. *Coast. Eng.* 57, 407–423. doi: 10.1016/j.coastaleng.2009.11.007

Russell, P. E. (1993). Mechanisms for beach erosion during storms. *Continental Shelf Res.* 13, 1243–1265. doi: 10.1016/0278-4343(93)90051-X

Sheremet, A., Guza, R., and Herbers, T. (2002). Observations of nearshore infragravity waves: Seaward and shoreward propagating components. *J. Geophysical Research: Oceans* 107, 10–11. doi: 10.1029/2001JC000970

Smit, P., Janssen, T., Herbers, T., Taira, T., and Romanowicz, B. (2018). Infragravity wave radiation across the shelf break. *J. Geophysical Research: Oceans* 123, 4483–4490. doi: 10.1029/2018JC013986

Stokes, G. G. (1847). On the theory of oscillatory waves. *Trans. Cam. Philos. Soc* 8, 441–455.

Suzuki, T., Altomare, C., Veale, W., Verwaest, T., Trouw, K., Troch, P., et al. (2017). Efficient and robust wave overtopping estimation for impermeable coastal structures in shallow foreshores using swash. *Coast. Eng.* 122, 108–123. doi: 10.1016/j.coastaleng.2017.01.009

Svendsen, I. A. (1984). Wave heights and set-up in a surf zone. *Coast. Eng.* 8, 303–329. doi: 10.1016/0378-3839(84)90028-0

Symonds, G., Huntley, D. A., and Bowen, A. J. (1982). Two-dimensional surf beat: Long wave generation by a time-varying breakpoint. *J. Geophysical Research: Oceans* 87, 492–498. doi: 10.1029/JC087iC01p00492

Thompson, W. C., Nelson, A. R., and Sedivy, D. G. (1984). Wave group anatomy of ocean wave spectra. *Coastal Engineering Proceedings*. 1 (19), 45. doi: 10.9753/icce.v19.45

Tissier, M., Bonneton, P., Michallet, H., and Ruessink, B. (2015). Infragravity-wave modulation of short-wave celerity in the surf zone. *J. Geophysical Research: Oceans* 120, 6799–6814. doi: 10.1002/2015JC010708

Tucker, M. (1950). Surf beats: Sea waves of 1 to 5 min. period. *Proc. R. Soc. London. Ser. A. Math. Phys. Sci.* 202, 565–573.

van Thiel de Vries, J., van Gent, M., Walstra, D., and Reniers, A. (2008). Analysis of dune erosion processes in large-scale flume experiments. *Coast. Eng.* 55, 1028–1040. doi: 10.1016/j.coastaleng.2008.04.004

Wong, W.-Y., Bjørnestad, M., Lin, C., Kao, M.-J., Kalisch, H., Guyenne, P., et al. (2019). Internal flow properties in a capillary bore. *Phys. Fluids* 31. doi: 10.1063/1.5124038

Appendix: validation of BOSZ

For validation of the BOSZ model's ability in replicating the evolution of the wave field and generation of IG-waves across a varying bathymetry we include the replication of the results from the laboratory test described in Suzuki et al. (2017). The test is useful for validation of the numerical model's ability in handling the process of wave shoaling and transformation of energy levels across an entire spectrum including the breaking process with subsequent transfer and dissipation of energy. This test consists of a 1D channel with a 1:35 slope. The wave field is based on a Pierson-Moskowitz spectrum. The boundary condition in the model uses a free surface times series initially recorded at an offshore wave gauge during the experiment.

The test was run with a grid of $\Delta x = 0.01$ m, the results of which can be seen in Figure A1. Significant for this article, BOSZ is able to capture the evolution of the wave field from generation to very small depths. Further, it is evident that it manages to account for the shift of energy to higher frequencies in the shoaling process and the dissipation in the wave breaking process and the subsequent transfer to lower frequencies in the IG band. For more details, please consult Kalisch et al. (2024).

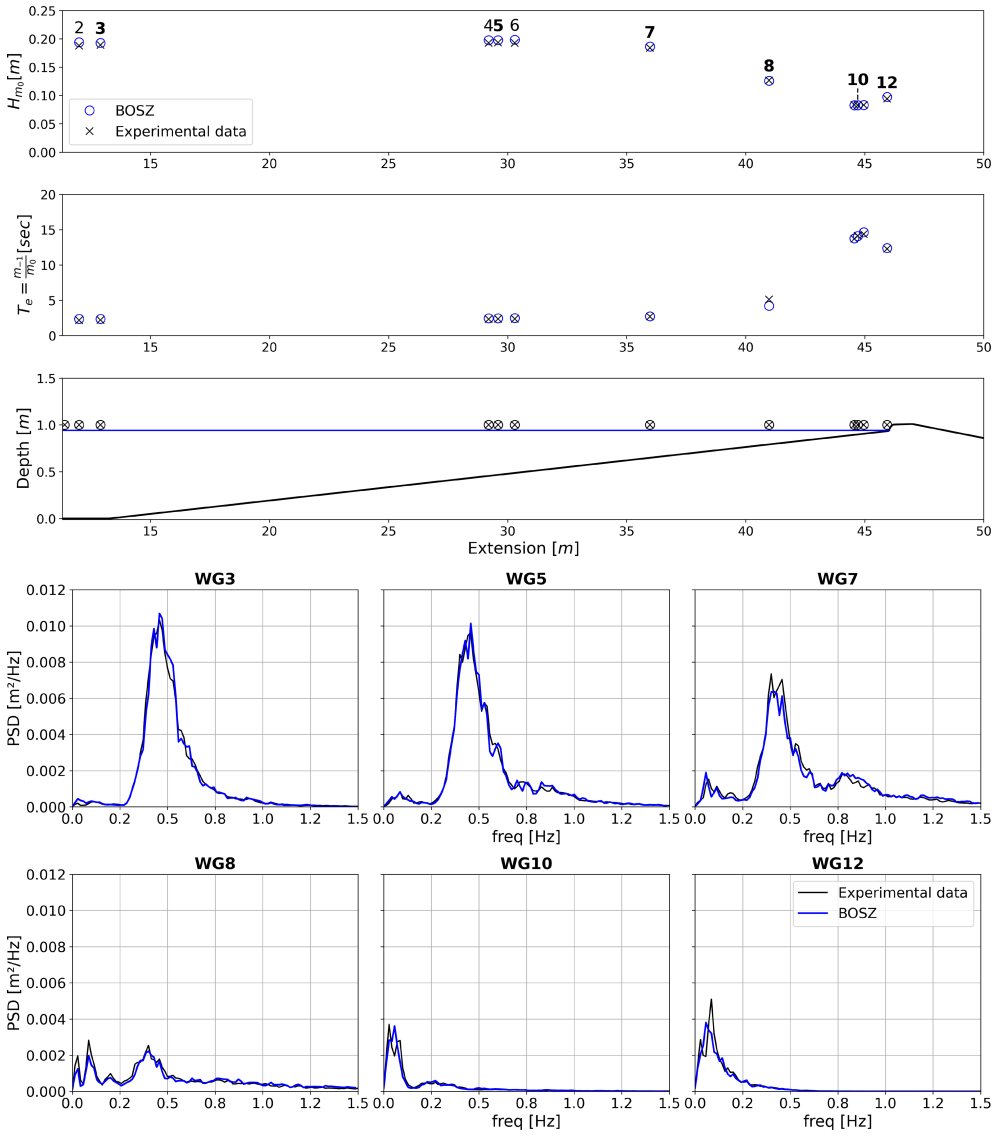

FIGURE A1
Comparison between the numerical solution of BOSZ and the laboratory data from Suzuki et al. (2017). Row 1 shows the comparison of significant wave height at multiple gauge locations, and row 2 to the corresponding energy period. Row 3 shows the locations of the gauges in the wave channel. The last two rows show the entire spectrum for 6 of the locations.

frontiers | Frontiers in Marine Science

TYPE Original Research
PUBLISHED 05 July 2024
DOI 10.3389/fmars.2024.1425697

OPEN ACCESS

EDITED BY
Henrik Kalisch,
University of Bergen, Norway

REVIEWED BY
José Pinho,
University of Minho, Portugal
Hailun He,
Ministry of Natural Resources, China

*CORRESPONDENCE
Yongzhi Liu
yzliu@fio.org.cn
Ruichen Cao
crc@stu.ouc.edu.cn

RECEIVED 30 April 2024
ACCEPTED 14 June 2024
PUBLISHED 05 July 2024

CITATION
Chen L, Zhang Y, Liu Y, Cao R and Lv X (2024) Research on scallop shells transport of the Yantai coastal region in the Bohai Sea. *Front. Mar. Sci.* 11:1425697. doi: 10.3389/fmars.2024.1425697

Research on scallop shells transport of the Yantai coastal region in the Bohai Sea

Le Chen[1], Yibo Zhang[1], Yongzhi Liu[2]*, Ruichen Cao[1]* and Xianqing Lv[1]

[1]Frontier Science Center for Deep Ocean Multispheres and Earth System (FDOMES), Physical Oceanography Laboratory, Ocean University of China, Qingdao, China, [2]Center for Ocean and Climate Research, First Institute of Oceanography, Ministry of Natural Resources, and Laboratory for Regional Oceanography and Numerical Modeling, Qingdao Marine Science and Technology Center, Qingdao, China

Introduction: Bivalve aquaculture is an important pillar of China's fisheries, with over 1 million tonnes of scallop shells produced annually. However, most of these shells are directly discarded into the sea, leading to continuous pollution of the marine and coastal environments, especially the coast of Yantai in the Bohai Sea where a large number of discarded scallop shell have accumulated.

Methods: To trace the fate of scallop shells in the ocean, this study established a model for the transport of scallop shells, coupling a two-dimensional tidal current model using the adjoint method with a Lagrangian particle model. By simulating nested tidal models, the distribution of tidal residual current in the Yantai coastal region was obtained. Then, a Lagrangian particle model was used to track the transport pathways of pollutants in the sea.

Results: Driven by the residual current calculated from the tidal model with the actual situation, possible pollutant release areas were inferred. The results of Lagrangian particle tracking experiments indicate that pollutants were released from the upstream accumulation area, specifically the area near Penglai Hulushan, confirming previous speculation.

Discussion: The scallop shells transport model can accurately simulate the spatiotemporal profile of scallop shells, which is helpful for managing scallop shell resources and improving the level of shell reuse.

KEYWORDS

adjoint assimilation, Lagrangian particle tracking, Bohai Sea, tidal residual current, pollutant transport

1 Introduction

Bivalves aquaculture constitutes one of the pillar industries in China's fisheries. In 2020, the total output of marine aquaculture bivalves nationwide exceeded 14 million tons (Wang and Wu, 2021). About 11.8% of China's total marine aquaculture bivalves are scallops, amounting to around 1.7 million tons. The abundant bivalve products not only drive the circulation of the seafood market, but also generate a large amount of discarded shells. Based on calculations that shell weight accounts for 60% of the total weight of scallops (Yan et al., 2012; Li et al., 2019a), approximately 1 million tons of shells are produced annually. Discarded shells have two main destinations, some are reused as resources, while others are wasted as solid waste. In recent years, China's resource utilization of waste shells has made certain progress, with an annual output of construction materials using shells as raw materials exceeding 2,000 tons (Li, 2017). Research and applications in fields such as soil remediation (Zhang et al., 2021b) and artificial reefs (Shi et al., 2019) are also continuously advancing. However, overall, China's work on shell resource utilization is still in its infancy. The vast majority of scallop shells are simply buried or discarded in landfills and oceans as solid waste, occupying valuable land and causing serious environmental pollution. In fact, the large amount of scallop shells discarded in public waters, drifting with the tide to the coast, has become a significant environmental issue. Zhifu Island beach in Yantai City, Shandong Province, was found to be piled with scallop shells covering an area equivalent to three basketball courts (Figure 1, where the reddish-brown material represents scallops). After ruling out the possibility of local fishermen illegally discarding scallop shells, it can be reasonably inferred that these scallop shells were carried from other areas to the coast of Yantai by seawater. Therefore, it is necessary to determine the source of the discarded scallop shells on the Yantai coast and the maritime transport path, and establish a "one-stop" collection, transportation, and disposal system for shells from the sea to landfills or recycling facilities.

The diffusion and transportation of pollutants such as oil (Li et al., 2019b; Aslan and Otay, 2021; Cervantes-Hernández et al., 2024), microplastics (Sterl et al., 2020; Frishfelds et al., 2022), and heavy metals (Zhang et al., 2023) in the ocean are hot topics among many scholars, while little attention has been paid to the fate of scallop shells discarded in the sea. Therefore, the origins of the accumulated shells on nearshore coasts are mostly unknown, making it difficult for relevant departments to trace them, and consequently, greatly reducing the efficiency of shell resource utilization. The scallop shells transport model established in this study is coupled with a two-dimensional tidal model using the adjoint method and a Lagrangian particle tracking model to simulate the transport of scallop shells, improve shell statistics systems, and enhance the level of shell resource utilization in China. Currently, many researchers adopt two-dimensional hydrodynamic models to simulate tides and tidal currents in China's marginal seas (Choi et al., 2014; Kuang et al., 2021; Wang et al., 2022a), with improved performance after adjoint assimilation (Jiao et al., 2023). The two-dimensional tidal model with the adjoint assimilation method can improve the accuracy of the model by assimilating data (Wang et al., 2021), separate tidal waves, simulate the current of single (Qian et al., 2021) or multiple tidal components (Wang et al., 2022b), and obtain tidal currents and residual currents. The residual current is a flow phenomenon generated when water points within a tidal wave deviate from their initial positions due to nonlinear effects after passing through one tidal cycle. Residual currents persist for a long time in nearshore areas and make significant contributions to the distribution of suspended sediment. The use of the residual current field in the research process can intuitively reflect the net transport of water (Liu et al., 2023) and serve as a basis for inferring the transport trajectories of suspended matter in seawater (Zhang et al., 2021a). To simulate the spatiotemporal profile of scallop shells in the residual current field, we can solve the partial differential equations governing advection and diffusion from a Lagrangian perspective (Capecelatro, 2018). The Lagrangian perspective solves the laws of particle displacement over time in the flow field, and can describe the particle movement process on a time scale (Das et al., 2000). Therefore, the Lagrangian model is widely used in the field of oceanography, especially in the study of particle transport in seawater, such as oil particles (Varona et al., 2024), biological larvae (Wong-Ala et al., 2022), plastic particles (Liang et al., 2021; Wisha et al., 2022), phytoplankton (Rowe et al.,

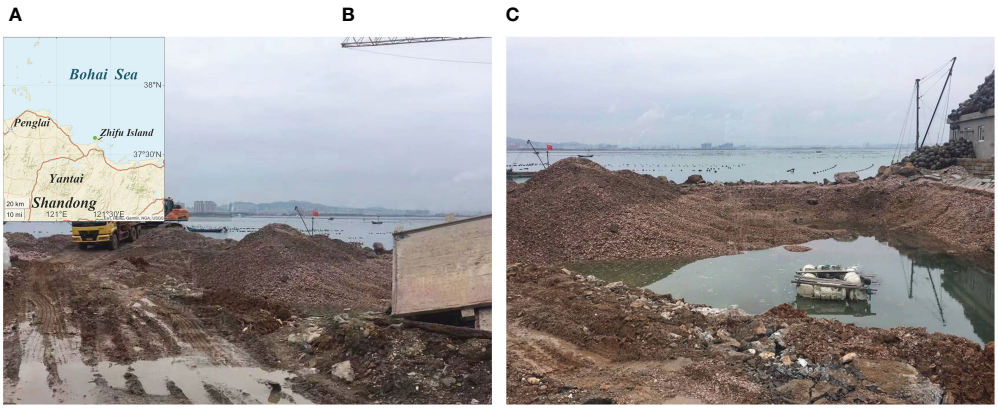

FIGURE 1
Accumulated scallop shells on Zhifu Island beach, Yantai city, Shandong province. **(A)** The green point is the area where scallop shells accumulate. **(B, C)** Show the specific accumulated scenario of scallop shells.

2016), suspended sediment (Nakada et al., 2018), all of which can be simulated by the Lagrangian particle tracking model to study the transport process of suspended matter in the ocean.

The Bohai Sea, as a semi-enclosed marginal sea of China, is characterized mainly by shallow water features and significant tidal effects (Fang, 1986; Zhu et al., 2021). In this study, a two-dimensional tidal model with the adjoint assimilation method is established to conduct hydrodynamic research on the sea area near Yantai in the Bohai Sea. Then, a Lagrangian particle tracking model is coupled to establish a transport model for scallop shells in the Bohai Sea, simulating the transport paths of scallop shells after release under the action of dynamic factors such as residual flow, nearshore waves, and environmental factors such as temperature and salinity. The structure of this paper is as follows. Section 2 introduces the main principles and establishment of the models, and the settings of the main experimental methods. In Section 3, the experimental results are analyzed. Section 4 summarizes the results obtained, highlights the innovative points, and prospects for the future development of the model.

2 Methods

2.1 Two-dimensional tidal model with adjoint assimilation method

Under the assumptions of hydrostatic pressure, incompressible fluid, and depth-averaging, the control equations for the two-dimensional tidal model in a Cartesian coordinate system are as follows:

$$\begin{aligned}
&\frac{\partial \varsigma}{\partial t}+\frac{\partial[(h+\varsigma)u]}{\partial x}+\frac{\partial[(h+\varsigma)v]}{\partial y}=0,\\
&\frac{\partial u}{\partial t}+u\frac{\partial u}{\partial x}+v\frac{\partial u}{\partial y}-fv+\frac{ku\sqrt{u^2+v^2}}{h+\varsigma}-A\left(\frac{\partial^2 u}{\partial x^2}+\frac{\partial^2 u}{\partial y^2}\right)+g\frac{\partial \varsigma}{\partial x}=0,\\
&\frac{\partial v}{\partial t}+u\frac{\partial v}{\partial x}+v\frac{\partial v}{\partial y}+fu+\frac{kv\sqrt{u^2+v^2}}{h+\varsigma}-A\left(\frac{\partial^2 v}{\partial x^2}+\frac{\partial^2 v}{\partial y^2}\right)+g\frac{\partial \varsigma}{\partial y}=0.
\end{aligned} \tag{1}$$

In Equation 1, t is time, x and y are Cartesian coordinates (with eastward and northward directions considered positive, respectively), $h(x,y)$ is the static water depth at location (x,y), $\zeta(x,y,t)$ is the variation in height of the free surface relative to the stationary water surface at time t, $u(x,y,t)$ and $v(x,y,t)$ are the depth averaged velocity components of tidal currents in the x and y directions at time t, f is the Coriolis parameter, k is the bottom friction coefficient, and A is the horizontal eddy viscosity coefficient.

The boundary condition for the M_2 tidal elevation is described as follows:

$$\zeta = a\cos(\omega t) + b\sin(\omega t). \tag{2}$$

In Equation 2, a and b are Fourier coefficients, and ω is the angular frequency of the M_2 constituent ($1.405189025 \times 10^{-4} s^{-1}$).

To construct the adjoint equation, the cost function is defined as follows:

$$J(\zeta)=\frac{1}{2}K_\zeta\sum_{j=1}^{ite}\sum_{(m,n)\in D_\zeta}\left(\zeta^j_{m,n}-\hat{\zeta}^j_{m,n}\right)^2. \tag{3}$$

In Equation 3, K_ζ is a constant ($K_\zeta = 1$), D_ζ is the model spatial domain, $\zeta^j_{m,n}$ is the simulated value, $\hat{\zeta}^j_{m,n}$ is the observed value, and *ite* is the time step of the forward mode.

The Lagrangian function can be roughly defined as follows (Zhang and Lu, 2010):

$$L(\mu,\nu,\tau)=\sum_{j=1}^{ite}\sum_{(m,n)\in D_\zeta} Eq.(1)+J(\zeta). \tag{4}$$

In Equation 4, μ, ν, and τ represent the adjoint variables (i.e., Lagrange multipliers) corresponding to u, v, and ζ, respectively. The adjoint model employs the method of discretization before differentiation as described by Gunzburger (2000). For simplicity, the indices of discrete variables have been omitted in the following equations. According to the theory of Lagrange multipliers, Equation 4 can be reformulated as follows:

$$\frac{\partial L}{\partial u}=0 \quad \frac{\partial L}{\partial v}=0 \quad \frac{\partial L}{\partial \zeta}=0, \tag{5.1}$$

$$\frac{\partial L}{\partial \mu}=0 \quad \frac{\partial L}{\partial \nu}=0 \quad \frac{\partial L}{\partial \tau}=0, \tag{5.2}$$

$$\frac{\partial L}{\partial k}=0 \quad \frac{\partial L}{\partial a}=0 \quad \frac{\partial L}{\partial b}=0. \tag{5.3}$$

Equation 5.1 represents the control equation. The adjoint equation can be expanded from Equation 5.2. Equation 5.3 can continuously optimize the model's bottom friction coefficient and open boundary conditions during iterative computations.

Residual current is the net current velocity after a complete M_2 tidal cycle. The residual current velocity $\overrightarrow{U_r}$ on the calculation point of the model can be described as follows:

$$\overrightarrow{U_r}=\sum_{i=1}^{lt}\overrightarrow{U_i}. \tag{6}$$

In Equation 6, *lt* is the number of times steps for the model to simulate one M_2 tidal cycle (4.471416363×10^4s), and $\overrightarrow{U_i}$ is the instantaneous current velocity when running for i time steps.

The finite-difference formulation of the control equations and adjoint equations for the tidal flow model is similar to that described by Lu and Zhang (2006). However, due to the relatively small latitude span of the Bohai Sea (approximately 4°), we constructed the finite-difference scheme in a Cartesian coordinate system rather than a spherical coordinate system.

The model adopts the Arakawa-C grid, where the water level is located on the grid center, and the current velocity is located on the grid edges. Topex/Poseidon data, an important product of satellite remote sensing technology for observing ocean dynamics systems, are commonly used to validate the scientific integrity of constructed models (Prakash et al., 2021) and can be used for further computations. The water depth is obtained from the ETOPO 2022 dataset, with varying resolutions for different study areas. Actual Coriolis parameters are employed to study the primary M_2

tide in the Bohai Sea. The main study area of this paper is the sea area adjacent to Yantai city in the Bohai Sea, where a large accumulation of scallop shells is observed (green point in Figure 2). Due to the limited availability of satellite observation data in the sea area adjacent to Yantai, we divided the Bohai Sea region into three nested areas (Figure 2A): Bohai Region I, Bohai Strait Region II, and Yantai Adjacent Region III. More specific parameters about areas are provided in Table 1.

When setting the model grid, refinement and optimization were applied to the boundary grid points based on the actual coastline and resolution. The specific division of each study area and the model grid settings are shown in Figure 2. Observation data from the Topex/Poseidon satellite altimeter was used for Region I, while data from the satellite altimeter were too sparse for Regions II and III. Therefore, in the process of nested regionalization, the simulation results from the previous level were incorporated as "observed" data into the simulation process of the next level to ensure an adequate amount of observation data for each region. For example, in Figure 2B, the black grid points in Region I correspond to the blue grid points in Region II. The simulation results from the black grid points in Region I were used as "observed" data for the blue grid points in Region II. Similarly, the simulation results from grid points in Region II were used as "observed" data for the blue grid points in Region III. Finally, using the two-dimensional tidal model, the distribution of tidal residual currents in each region was calculated.

2.2 Lagrangian particle tracking method

The simulation of pollutants based on the Lagrangian particle tracking method has been widely applied and used in studies related to green tides (Han et al., 2022), oil spills (Wang et al., 2023b), and the transportation of fish feed (Wang et al., 2023a). In this study, we employed the Lagrangian particle tracking method to simulate the transport of scallop shells. Scallop shells have a three-layer structure with air pockets between the layers, which increases their actual displaced volume and decreases their density. Additionally, the discarded shells assume an open position, which is favorable for resuspension under the influence of natural forces such as tides, waves, and turbulence. Considering all these factors, we assumed

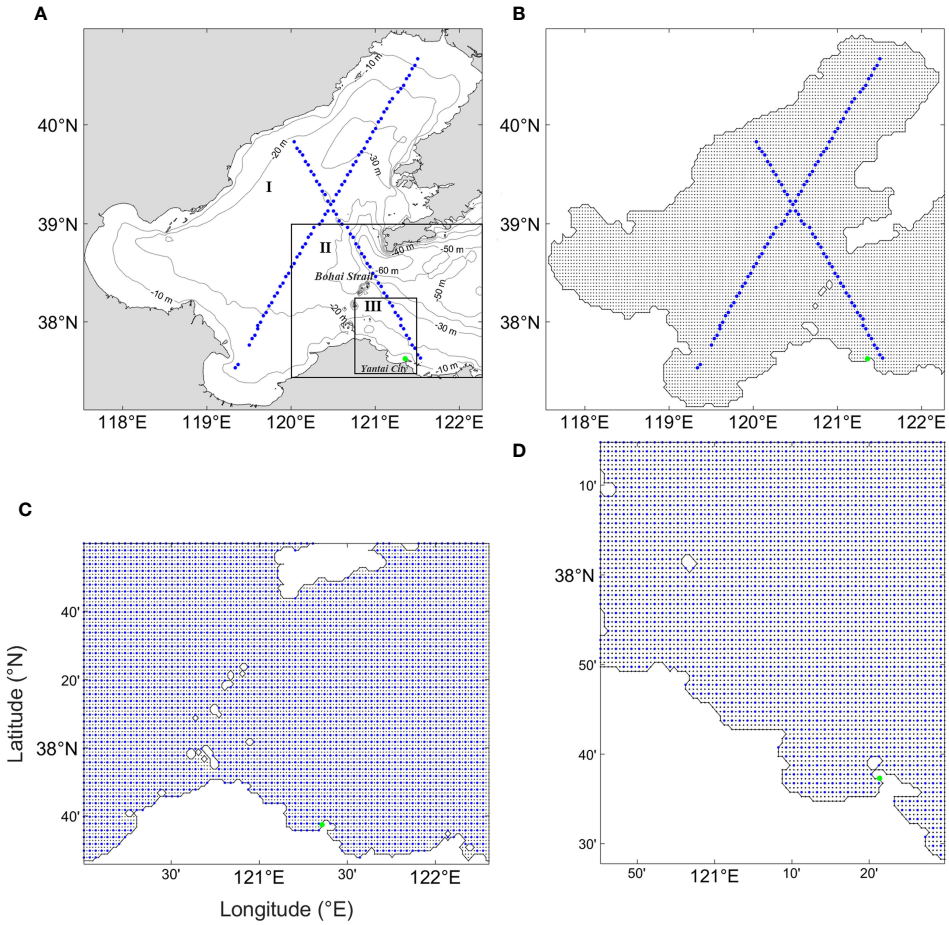

FIGURE 2
The specific division and grid settings of each study area. **(A)** Study areas of the tidal model, with Bohai Sea Region I at a resolution of 2′×2′, Bohai Strait Region II at a resolution of 1′×1′, and the adjacent area of Yantai Region III at a resolution of 30″×30″. **(B)** Distribution of adjoint assimilation grid points and observation data in Region I, where black points represent model grid points, blue points represent satellite observation data, and the green point indicates the area of pollutant accumulation. **(C, D)** Show the distribution of adjoint assimilation grid points and observation data in Regions II and III, respectively, with black points representing model grid points, blue points representing observation data, and the green point indicating the area of pollutant accumulation.

TABLE 1 Specific settings for each study area of the experiment.

Study area	Coverage range	Horizontal resolution	Time step
I	117.5375°-122.2709°E, 37.1022°-40.9689°N	2′×2′	62.103 s
II	120.0042°-122.2709°E, 37.4293°-38.9959°N	1′×1′	62.103 s
III	120.7542°-121.4959°E, 37.4626°-38.2459°N	30″×30″	62.103 s

that scallop shells undergo suspended motion in near-seabed areas and transport in the form of particles within the model. Therefore, during the computation, the discarded shells suspended in near-seabed areas and subject to dynamic processes. The coordinates of particles released into the sea surface can be determined as follows:

$$\frac{d\vec{P}(t)}{dt} = \vec{U}_c + \vec{U}_s + \vec{U}_w + \vec{U}_d \,. \tag{7}$$

In Equation 7, $\vec{P} = (x, y, z, t)$ is the displacement vector of the particles in the Cartesian coordinate system, which is also a function of time t, $\vec{U}_c$ is the current velocity, $\vec{U}_s$ is the current velocity driven by waves, $\vec{U}_w$ is the current velocity driven by wind, $\vec{U}_d$ is the diffusion velocity of the particles induced by turbulence. The sum of the first three terms on the right side represents the drift velocity $\vec{U}$ of the particles.

Our study focuses on the transport of scallop shells, a process that typically occurs near the seabed, rather than at the surface. Since wind stress directly affects surface waters, the influence of wind-induced currents is most significant in the upper layers of the water column, the effect of wind stress on the particles can be neglected. In this case, the drift velocity of the particles is mainly composed of the current velocity vector and the Stokes wave velocity vector. The velocity components in each direction can be expressed as (Zhang and Ozer, 1992):

$$\begin{aligned} \langle u \rangle &= u_c + u_s, \\ \langle v \rangle &= v_c + v_s, \\ \langle w \rangle &= w_c \,. \end{aligned} \tag{8}$$

In Equation 8, u_c and v_c are the horizontal velocity components of the current, with specific data provided by the residual current field output from the two-dimensional tidal model, u_s and v_s are the Stokes wave-induced velocity, which affects the movement trajectory of particles, causing them to tend more towards the shore in the motion simulation, aligning better with real-world conditions, w_c is the vertical velocity of the particles.

The diffusion caused by turbulence exhibits randomness, and the diffusion velocity $\vec{U}_d = (u', v', w')$ is calculated as follows:

$$(u', v', w') = \sqrt{\frac{6}{\Delta t}}\left(R_x\sqrt{K_h}, R_y\sqrt{K_h}, R_z\sqrt{K_z}\right) . \tag{9}$$

In Equation 9, R_x, R_y, and R_z are mutually independent and uniformly distributed random numbers in the interval [-1, 1], Δt is the time step, K_h is the horizontal diffusion coefficient, and K_z is the vertical diffusion coefficient.

The horizontal diffusion coefficient K_h is approximated using an exponential function of time t (Equation 10) proposed by Pan et al. (2020):

$$K_h = 0.027t^{1.34} \,. \tag{10}$$

The vertical diffusion coefficient K_z is calculated based on the relationship proposed by Boufadel et al. (2020):

$$K_z = \left(\frac{\kappa u_*}{0.9}\right) z\left(1 - \frac{z}{MLD}\right)^2 = \left(\frac{\kappa u_*}{0.9}\right)(z + z_0)\left(1 - \frac{z}{MLD}\right) . \tag{11}$$

In Equation 11, $\kappa = 0.4$ is the von Kármán constant, u_* is the water friction velocity, MLD is the mixed layer depth, representing the maximum depth of the boundary layer formed by the interaction between air and sea, defined here as the depth where the temperature is 0.2 °C lower than the sea surface temperature (Cao et al., 2021), and z_0 is the roughness length of the surface under regular wave action. When $z = 0$ (at the sea surface), $K_z(z = 0) = \left(\frac{\kappa \cdot u*}{0.9}\right) \neq 0$. The introduction of the non-zero value z_0 allows substances at the sea surface to diffuse downwards into the water column through turbulent diffusion. z_0 is calculated using the following relationship (Bandara et al., 2011):

$$z_0 = 1.38 \times 10^{-4} H_s \left(\frac{U_{wind}}{c_p}\right)^{2.66} . \tag{12}$$

In Equation 12, H_s is the significant wave height, U_{wind} is the wind speed at 10 meters above sea level, $c_p = \frac{gT}{2\pi}$ is the phase velocity of the wave, which depends on the wave period.

The water friction velocity u_* is calculated according to the following relationship in Equation 11 (Craig and Banner, 1994; Bandara et al., 2011):

$$u_* = \begin{cases} \sqrt{\frac{\rho_a C_{d1} U_{wind}(U_{wind} - U_{sur})}{\rho_w}}, & z = 0, \\ \frac{\sqrt{\frac{\rho_a}{\rho_w}}\kappa U_{wind}}{ln\left(\frac{10}{z_0}\right)}, & z \neq -H \text{ and } z \neq 0, \\ \sqrt{\frac{C_{d2} U_{bot}}{\rho_w}}, & z = -H \,. \end{cases} \tag{13}$$

In Equation 13, ρ_a and ρ_w are the air and water densities, U_{sur} and U_{bot} are the flow velocities at the sea surface and the seabed respectively, $C_{d1} = 1.13 \times 10^{-3}$ is the surface drag coefficient, and C_{d2} is the bottom drag coefficient, which can be calculated from (Li et al., 2018):

$$C_{d2} = max\left[\frac{\kappa^2}{ln\left(\frac{z_{ab}}{z_0}\right)}, \; 0.0025\right] . \tag{14}$$

In Equation 14, z_{ab} represents the height of the water column above the seabed, and z_0 represents the thickness of the mixed layer.

The calculation domain of the Lagrangian particle tracking model matches that of Region III, the sea area adjacent to Yantai, Bohai Sea, in the tidal model. The grid resolution of the model is 30”×30”, with a temporal resolution of 1 day. The total grid number is 95×90, and the model is divided into 10 layers vertically. Depth data is sourced from

the ETOPO 2022 dataset, while the current field data is obtained from the adjoint assimilation model of the two-dimensional tidal flow simulation in Region III. Wind speed data is calculated from NCEP dataset, and the nearshore wave data is generated by the SWAN model, which is validated by Jiang et al. (2022).

In this study, based on the Lagrangian particle tracking method, two experimental schemes are employed to simulate the transport pathways of shells. Scheme one involves continuously releasing 100,000 Lagrangian particles at the center of the aquaculture area (121.165229°E, 37.692156°N) for 240 days to simulate the movement of pollutants. The specific parameters of the model are listed in Table 2. Scheme two applies simultaneously and randomly releasing 100,000 Lagrangian particles within the aquaculture area (121.165229 ± 0.01°E, 37.692156 ± 0.01°N) to simulate the movement of pollutants. The specific parameters of the model are listed in Table 3.

3 Results

3.1 Tidal residual current field

The tidal residual current distribution in each region is illustrated in Figures 3–5. Due to the large coverage ranges of Regions I and II, it is challenging to depict the residual current distribution near the pollutant accumulation areas effectively. Hence, we magnify the tidal residual flow distribution near the pollutant accumulation areas in Regions I and II (Figures 3, 4).

The residual current field (Figures 3B, 4B) can, to a certain extent, characterize the net transport process of water masses near the pollutant accumulation area, it can be observed that the water mass near the pollutant accumulation point mainly originates from the northwest and northeast currents. The northeast current is blocked by Zhifu Island. If pollutants were to be transported along the northeast current, they would accumulate north of Zhifu Island instead of the southwest, suggesting a higher possibility of pollutant movement along the northwest current. Examination of the actual situation in the northwest direction reveals shellfish aquaculture farms and processing plants near Penglai Liujiagou and Hulushan (Figure 5B), further increasing the possibility of waste shells accumulation originating from the northwest direction. Therefore, we reduce the coverage area to Region III and increase the grid resolution to 30". Region III focuses on the western sea area near the pollutant accumulation point, including the two suspected pollution sources. The simulation result of Region II is used as observed data for Region III simulation, yielding the residual current distribution shown in Figure 5A.

By magnifying the western sea area near the pollutant accumulation point (Figure 5B), clockwise residual currents are observed near Liujiagou, which may carry pollutants away from the coast. Subsequently, these pollutants may move southeastward along with the residual current, possibly passing near Hulushan. Likewise, clockwise residual currents near Hulushan could further propel pollutants eastward, then southward, these pollutants could eventually aggregate near the pollutant accumulation point, influenced by counterclockwise residual currents and nearshore wave effects. These pathways are speculative based on the residual current field. Next, we will use the Lagrangian particle tracking method to simulate the transport pathways of pollutants to validate our speculations.

3.2 Lagrangian particle tracking experiments

In the Lagrangian particle tracking model, pollutants are considered particles, and simulations are conducted to study the pollutant accumulation area (Figure 5A), in the sea area adjacent to Yantai, in the Bohai Sea. Among the two suspected pollution sources near Penglai Liujiagou and Hulushan, we selected the sea area adjacent to Hulushan (121.165229°E, 37.692156°N) as the pollutant release area based on the proximity principle, residual current field, and field inspections. The model applies onshore waves in the nearshore sea areas to facilitate the shoreline movement of pollutants. To further observe the transport pathways of pollutants, two sets of Lagrangian particle tracking experiments are designed in this study to validate the possibility of pollutants aggregating near Zhifu Island (121.353758°E, 37.626160°N) originating from the sea area adjacent to Hulushan. The first set involves a single-point release experiment to observe the trajectory of pollutants released from the sea area adjacent area of Hulushan. The second set comprises a regional release experiment where pollutants are randomly released within the domain of 121.165229 ± 0.01°E, 37.692156 ± 0.01°N, simulating the movement of pollutants. Since pollutants are not

TABLE 2 Parameters for single-point release experiment.

Parameter	Value
Release point	121.165229°E, 37.692156°N
Release depth	0 m
Release time	240 days
Number of released particles	100,000
Simulation time	480 days
Pollutant density	1000 kg·m^{-3}

TABLE 3 Parameters for regional release experiment model.

Parameter	Value
Release area	121.165229 ± 0.01°E, 37.692156 ± 0.01°N
Release depth	0 m
Release time	1 day
Number of released particles	100,000
Simulation time	480 days
Pollutant density	1000 kg·m^{-3}

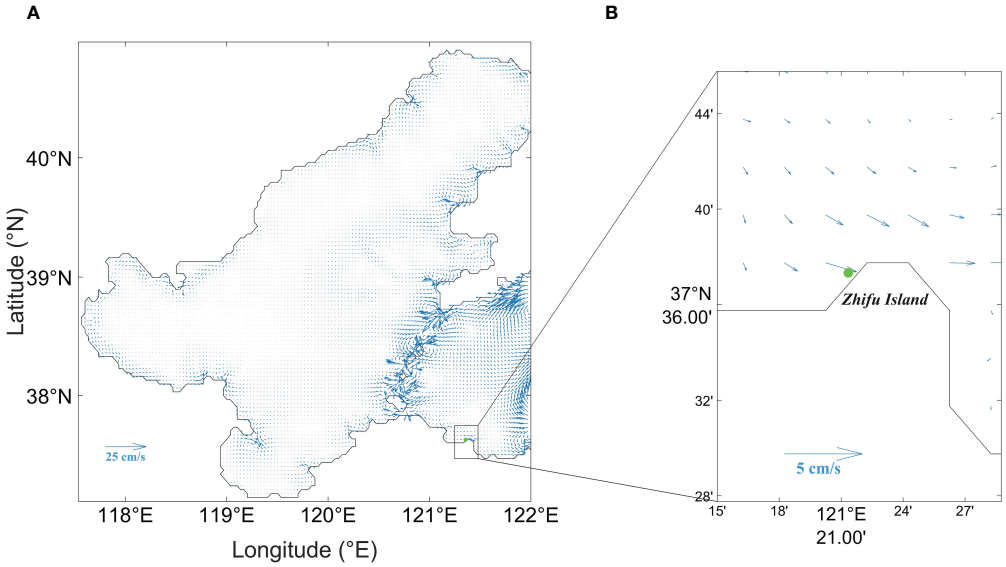

FIGURE 3
Tidal residual current distribution in Region I **(A)** (scale of 25 cm/s) and near the pollutant accumulation area **(B)** (scale of 5 cm/s). The green point is the pollutant accumulation point at 121.353758°E, 37.626160°N.

released solely at one point in actual scenarios but within a certain range, the second set of experiments better reflects reality.

3.2.1 Single-point release experiment

In this experiment, 100,000 pollutant particles were continuously released for 240 days near Hulushan (red diamond point in Figure 6), simulating the transport trajectory of pollutants. The specific parameters of the model are listed in Table 2. The experiment comprehensively considers the effects of residual current, turbulence, and nearshore waves. The transport trajectories of pollutants at different times under the influence of environmental dynamics are shown in Figure 6.

In the simulation of the single-point release experiment, under the drive of environmental dynamics, pollutants move northeastward from the red point within 20 days after release (Figure 6B). After 40 days, pollutants begin to move southeastward (Figure 6C), exhibiting a clockwise trajectory, largely influenced by the clockwise residual current in the area. Over the next 100 days, pollutants continue to move southeastward until day 180 (Figure 6E), when their direction shifts slightly. By day 240 (Figure 6F), pollutants have started moving eastward, slightly northward, and gradually approaching the coast. On day 254 (Figure 6G), some pollutants are closer to the coast, with nearshore waves dominating environmental dynamics, pushing pollutants toward the shore. By day 260 (Figure 6H), some have

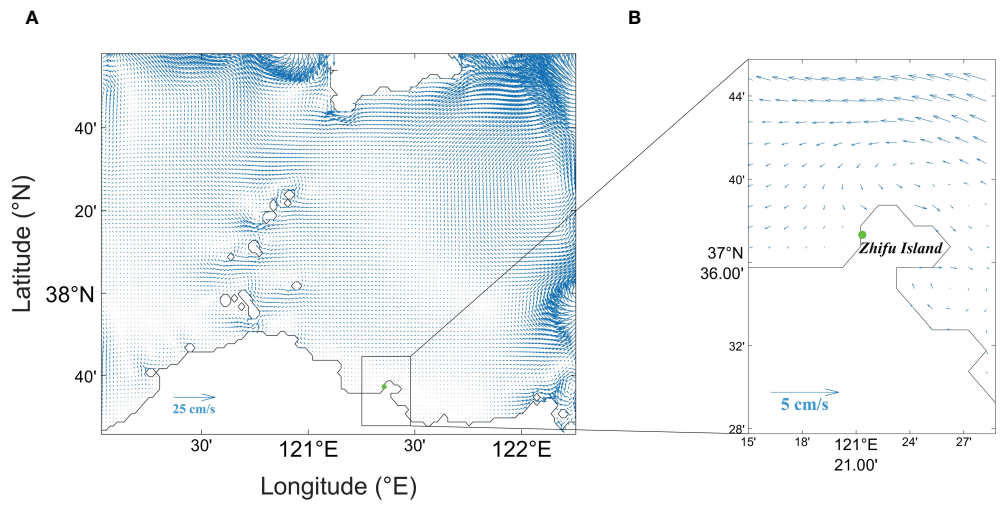

FIGURE 4
Tidal residual current distribution in Region II **(A)** (scale of 25 cm/s) and near the pollutant accumulation area **(B)** (scale of 5 cm/s). The green point is the pollutant accumulation point at 121.353758°E, 37.626160°N.

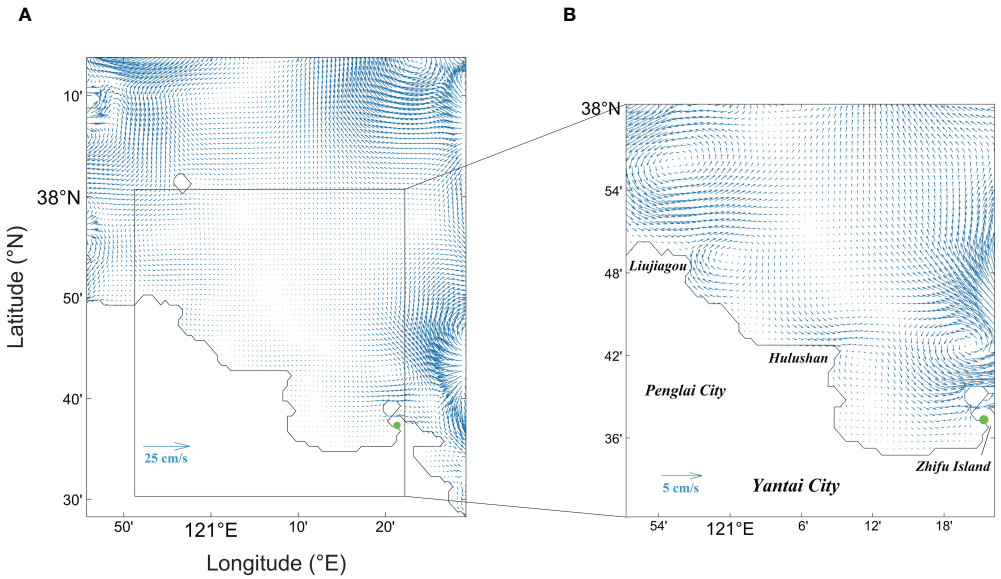

FIGURE 5
Tidal residual current distribution in Region III **(A)** (scale of 25 cm/s) and near the pollutant accumulation area **(B)** (scale of 5 cm/s). The green point is the pollutant accumulation point at 121.353758°E, 37.626160°N.

reached the shore, near the pollutant accumulation point (green point in Figure 6). By day 240, all pollutant particles have entered the ocean. Once pollutants reach the shore, their movement stops as the model sets their velocity to zero. Subsequently, 93.88% of pollutants have reached the accumulation area by day 480. The results of the experiment indicate that pollutants released from a single point near Hulushan can reach the actual pollutant accumulation area under the influence of residual current, turbulence, and nearshore waves. This also suggests a high possibility that pollutants, in reality, may be released from the Hulushan.

3.2.2 Regional release experiment

In this experiment, pollutants were simultaneously and randomly released within the domain of 121.165229 ± 0.01°E, 37.692156 ± 0.01° N (the black square centered around a red diamond point in Figure 7), simulating the diffusion and transport pathways of pollutants in the study area over different time periods (Figure 7). The specific parameters of the model are listed in Table 3.

In this experiment, 100,000 pollutant particles are released (Figure 7A) in one day. These pollutants then enter the seawater, where they are suspended and gradually disperse under the influence of a clockwise residual current. Initially, owing to release together, pollutants collectively move clockwise in the sea near the release area within 40 days (Figures 7B, C). However, at day 80 (Figure 7D), due to a smaller residual current in the southeast of the release area and varying current velocities at different positions, the pollutants experience different environmental dynamics during this period. Consequently, the pollutant cluster gradually stretches out, and experiences more complex environmental dynamics. Under the influence of significant counterclockwise residual current and turbulence near the pollutant accumulation area, part of the pollutants spread eastward and eventually ashore on day 108 (Figure 7E) driven by the nearshore waves. Meanwhile, other pollutants, affected by the clockwise residual current near the release area, circulated back towards the initial release area, leaving a clockwise trajectory (Figure 7F). After 300 days (Figure 7G), pollutants are separately transported southeastward and northwestward due to residual current and turbulence. By day 400 (Figure 7H), a significant portion of the pollutants had been transported close to the accumulation area, while others began moving northwestward, influenced by the clockwise currents near the release site. By day 480 (Figure 7I), at the end of the regional release experiment, 82.57% of pollutants have reached the shore, the remaining pollutants are either stranded on other coasts or still undergone suspension in the Bohai Sea. Interestingly, the pollutants in the regional release experiment reached the accumulation area faster than in the single-point release experiment. This difference can be attributed to the fact in the latter, the residual current direction in the single-point experiment is not directly toward the accumulation point, whereas some release points in the regional release experiment have residual current directions toward the accumulation area. Overall, the results of the regional release experiment further demonstrate that pollutants released near Penglai Hulushan can be transported to the accumulation area under the influence of residual current, turbulence, and nearshore waves, consistent with real scenarios.

These two sets of experiments, designed based on known tidal residual current and nearshore wave conditions in the study area, use the Lagrangian particle tracking model to determine the specific transport pathways and dispersion ranges of suspended pollutants. Scientifically validated speculations suggest that pollutants accumulating along the Yantai coast are likely released from or pass through the vicinity of Penglai Hulushan.

10.3389/fmars.2024.1425697

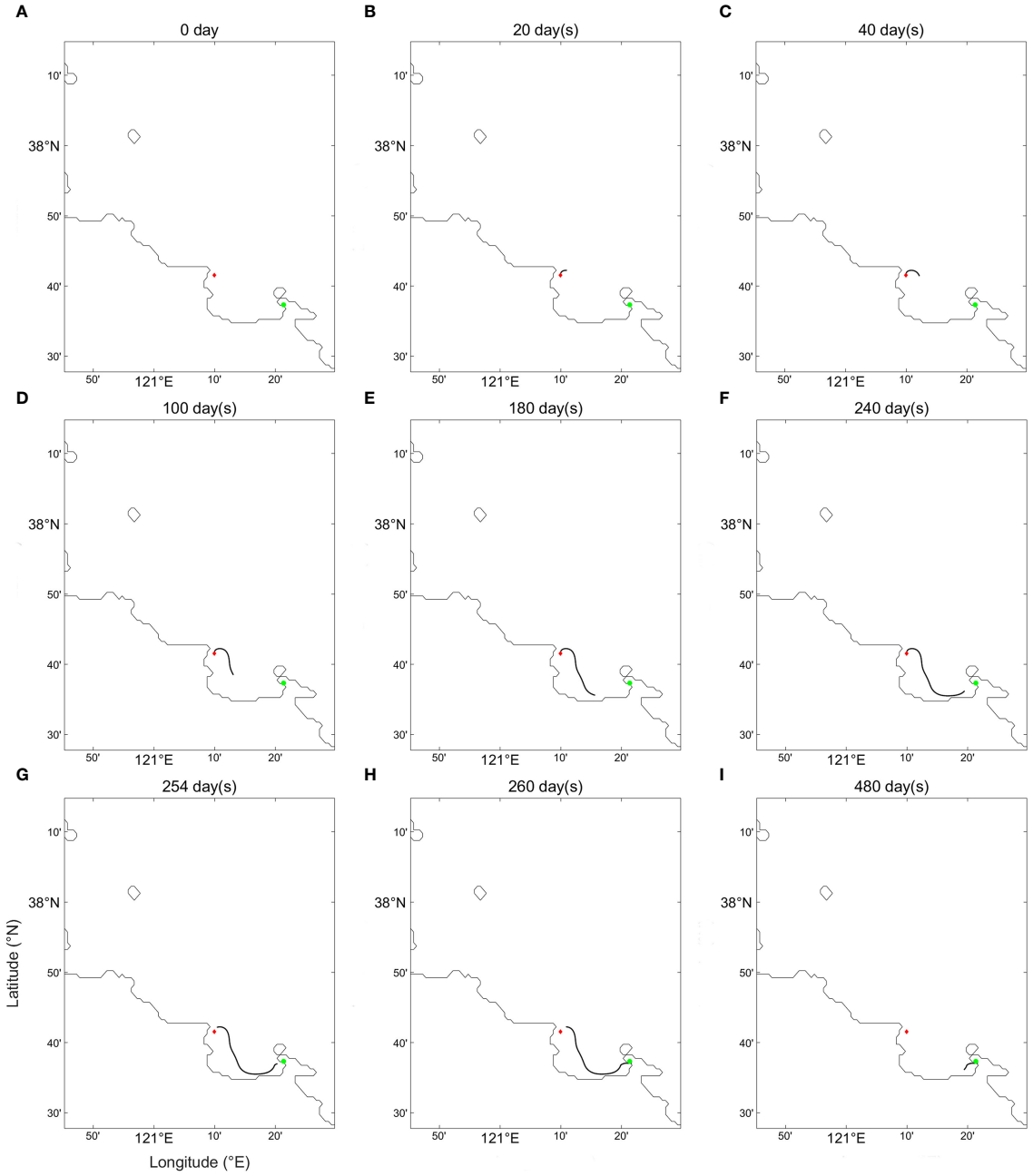

FIGURE 6
Transport trajectories of pollutants in the single-point release experiment at different time points: **(A)** 0 day, **(B)** 20 days, **(C)** 40 days, **(D)** 100 days, **(E)** 180 days, **(F)** 240 days, **(G)** 254 days, **(H)** 260 days, **(I)** 480 days.

4 Conclusion and discussion

This study employed a method coupling a Lagrangian particle tracking model with a two-dimensional tidal model to simulate the transport and movement of discarded scallop shells in the Bohai Sea. Given that the M_2 tidal constituent dominates in the Bohai Sea, the M_2 tidal residual current field was selected as the input flow field for the Lagrangian particle tracking model. Through hierarchical nested simulations in the Bohai Sea region, high-resolution M_2 tidal residual current distributions near the accumulation area of scallop shells were obtained. The simulation results indicated the presence of a clockwise residual current near Hulushan in the scallop farming area and a counterclockwise residual current near Zhifu Island. Based on this, we inferred the approximate release area and likely transport direction of scallop shells. Considering the uncertainty of the release location of the shells, two sets of particle tracking experiments were designed. The experiments revealed that after entering the sea, shells initially moved northeastward under the influence of a rotating residual current, then southeastward, followed by a northeastern shift, and finally approached the coast

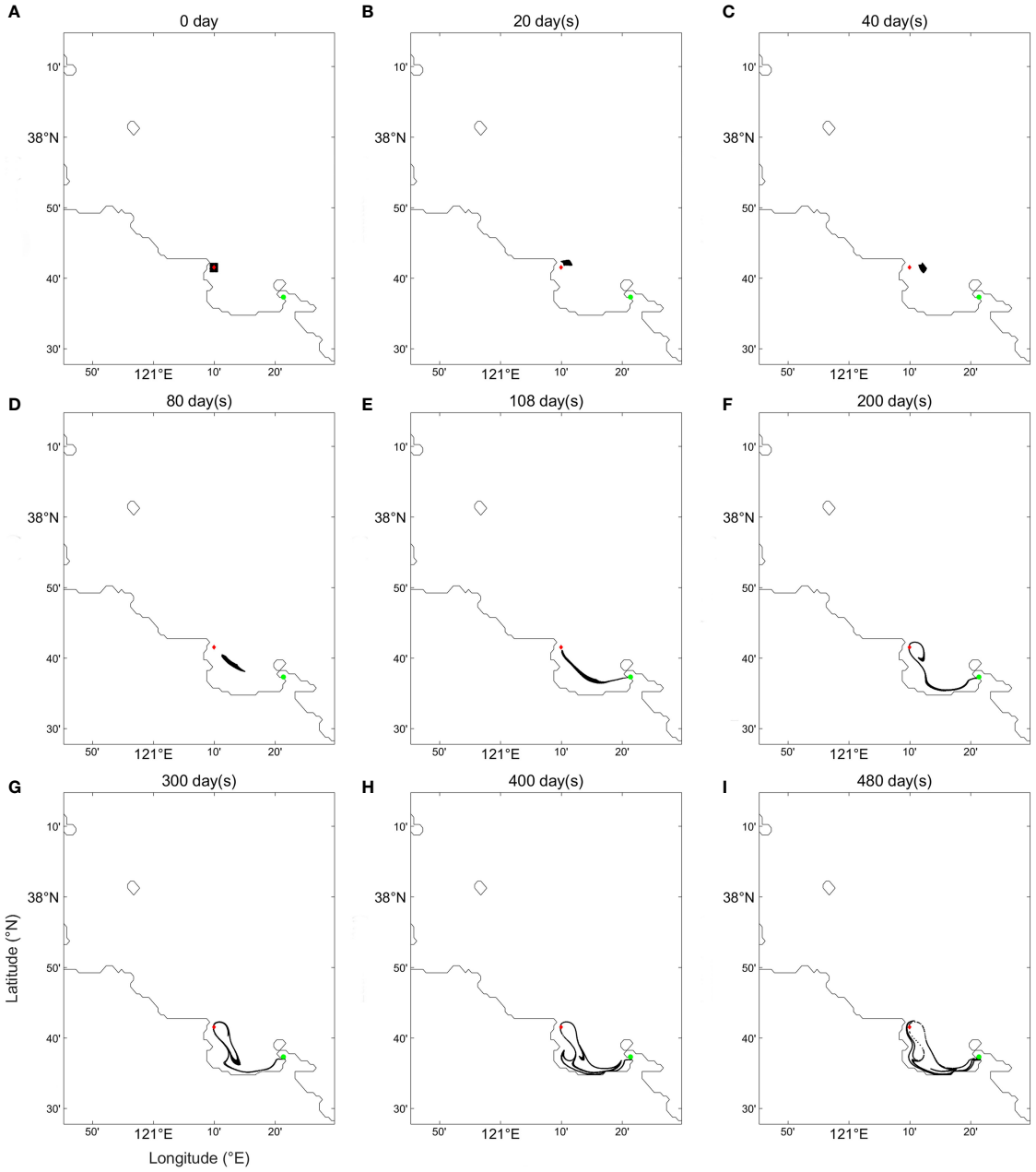

FIGURE 7
Transport trajectories of pollutants in the regional release experiment at different time points: **(A)** 0 day, **(B)** 20 days, **(C)** 40 days, **(D)** 80 days, **(E)** 108 days, **(F)** 200 days, **(G)** 300 days, **(H)** 400 days, **(I)** 480 days.

under the influence of nearshore waves. From the moment the scallop shells were released into the sea to their arrival on the coast of Zhifu Island, it took at least 108 days. Moreover, shells were continually dispersed during their movement. By the end of the regional release experiment, scallop shells had not only accumulated on the coast of Zhifu Island, but also remained on other coasts of Yantai. The study found that most of the shells accumulated on the coast of Yantai Zhifu Island originated from or passed by Hulushan after being discarded.

However, the coupled model used in this study still has some limitations. The model ignored the shape and size of the shells themselves, treating them as homogeneous Lagrangian particles. Additionally, we assumed that the shells remained suspended in seawater and neglected the possibility of sinking due to factors other than dynamic forces, such as attachment of other organisms increasing density and causing sinking. Furthermore, it's important to notice that the dynamic factors considered in this study only included M_2 tidal residual current, turbulence, and nearshore waves, but M_2 tidal residual current does not represent all tidal dynamics in the area, and the influence of ocean current in the region was not considered. Lastly, this study is only an idealized experiment and has not considered seasonal variations, such as wind, temperature and

duration of scallop shells released. In future research, we plan to incorporate the residual currents of the four major tidal constituents (M_2, S_2, K_1, O_1) as well as the effect of the Bohai Sea current to improve model accuracy. In addition, we will also conduct practical experiments, setting the release time of the scallop shells based on the results of these experiments and the scallop market season, and actually considering the effects of tidal currents, wind, turbulence, and coastal waves on the transport of the scallop shells. Field visits to scallop farming bases near Penglai Hulushan will be conducted to validate the model's conclusions and enhance its reliability. Overall, this study provides new insights into the mechanisms of discarded scallop shell pollutants transport in the Bohai Sea region, contributing to a better understanding of environmental pollution issues and marine ecological impacts in the area.

Data availability statement

The original contributions presented in the study are included in the article/supplementary material. Further inquiries can be directed to the corresponding authors.

Author contributions

LC: Conceptualization, Data curation, Formal analysis, Investigation, Methodology, Software, Validation, Visualization, Writing – original draft, Writing – review & editing. YZ: Conceptualization, Methodology, Software, Writing – review & editing. YL: Conceptualization, Funding acquisition, Supervision, Writing – review & editing. RC: Conceptualization, Methodology, Software, Supervision, Writing – review & editing. XL: Conceptualization, Formal analysis, Methodology, Project administration, Resources, Supervision, Writing – review & editing.

Funding

The author(s) declare financial support was received for the research, authorship, and/or publication of this article. This work is supported by the Key R&D Program of Shandong Province (S & T Demonstration Project) (No. 2021SFGC0701) and the National Natural Science Foundation of China (Grant No. 42076011 and Grant No. U2006210).

Acknowledgments

Special thanks to Rushui Xiao, Nan Wang, and Shengyi Jiao for participating in the discussion on the study method and manuscript with useful suggestions.

Conflict of interest

The authors declare that the research was conducted in the absence of any commercial or financial relationships that could be construed as a potential conflict of interest.

Publisher's note

References

Aslan, M., and Otay, E. N. (2021). Exchange of water and contaminants between the Strait of Istanbul and the Golden Horn. *Ocean Eng.* 230, 108984. doi: 10.1016/j.oceaneng.2021.108984

Bandara, U. C., Yapa, P. D., and Xie, H. (2011). Fate and transport of oil in sediment laden marine waters. *J. Hydro-environment Res.* 5, 145–156. doi: 10.1016/j.jher.2011.03.002

Boufadel, M., Liu, R., Zhao, L., Lu, Y., Özgökmen, T., Nedwed, T., et al. (2020). Transport of oil droplets in the upper ocean: impact of the eddy diffusivity. *JGR Oceans* 125, e2019JC015727. doi: 10.1029/2019JC015727

Cao, R., Chen, H., Rong, Z., and Lv, X. (2021). Impact of ocean waves on transport of underwater spilled oil in the Bohai Sea. *Mar. pollut. Bull.* 171, 112702. doi: 10.1016/j.marpolbul.2021.112702

Capecelatro, J. (2018). A purely Lagrangian method for simulating the shallow water equations on a sphere using smooth particle hydrodynamics. *J. Comput. Phys.* 356, 174–191. doi: 10.1016/j.jcp.2017.12.002

Cervantes-Hernández, P., Celis-Hernández, O., Ahumada-Sempoal, M. A., Reyes-Hernández, C. A., and Gómez-Ponce, M. A. (2024). Combined use of SAR images and numerical simulations to identify the source and trajectories of oil spills in coastal environments. *Mar. pollut. Bull.* 199, 115981. doi: 10.1016/j.marpolbul.2023.115981

Choi, B., Hwang, C., and Lee, S. (2014). Meteotsunami-tide interactions and high-frequency sea level oscillations in the eastern Yellow Sea. *JGR Oceans* 119, 6725–6742. doi: 10.1002/2013JC009788

Craig, P. D., and Banner, M. L. (1994). Modeling wave-enhanced turbulence in the ocean surface layer. *J. Phys. Oceanography* 24, 2546–2559. doi: 10.1175/1520-0485(1994)024<2546:MWETIT>2.0.CO;2

Das, P., Marchesiello, P., and Middleton, J. H. (2000). Numerical modelling of tide-induced residual circulation in Sydney Harbour. *Mar. Freshw. Res.* 51, 97. doi: 10.1071/MF97177

Fang, G. (1986). Tide and tidal current charts for the marginal seas adjacent to China. *Chin. J. Ocean. Limnol.* 4, 1–16. doi: 10.1007/BF02850393

Frishfelds, V., Murawski, J., and She, J. (2022). Transport of microplastics from the daugava estuary to the open sea. *Front. Mar. Sci.* 9. doi: 10.3389/fmars.2022.886775

Gunzburger, M. (2000). Adjoint equation-based methods for control problems in incompressible, viscous flows. *Flow Turbulence Combustion.* 65, 249–272. doi: 10.1023/A:1011455900396

Han, X., Kuang, C., Li, Y., Song, W., Qin, R., and Wang, D. (2022). Numerical modeling of a green tide migration process with multiple artificial structures in the Western Bohai Sea, China. *Appl. Sci.* 12, 3017. doi: 10.3390/app12063017

Jiang, Y., Rong, Z., Li, P., Qin, T., Yu, X., Chi, Y., et al. (2022). Modeling waves over the Changjiang River Estuary using a high-resolution unstructured SWAN model. *Ocean Model.* 173, 102007. doi: 10.1016/j.ocemod.2022.102007

Jiao, S., Zhang, Y., Pan, H., and Lv, X. (2023). Improved estimation of the open boundary conditions in tidal models using trigonometric polynomials fitting scheme. *Remote Sens.* 15, 480. doi: 10.3390/rs15020480

Kuang, C., Han, X., Zhang, J., Zou, Q., and Dong, B. (2021). Morphodynamic evolution of a nourished beach with artificial sandbars: field observations and numerical modeling. *JMSE* 9, 245. doi: 10.3390/jmse9030245

Li, C. (2017). "A new way of handling shells," in *People's Daily Oversea*, vol. 4. (China: Chenyang Li), vol. 4. Available at: http://paper.people.com.cn/rmrbhwb/html/2017-07/04/content_1787897.htm.

Li, Y., Chen, H., and Lv, X. (2018). Impact of error in ocean dynamical background, on the transport of underwater spilled oil. *Ocean Model.* 132, 30–45. doi: 10.1016/j.ocemod.2018.10.003

Li, Y., Yan, L., Yu, D., Tian, Y., and Liu, J. (2019a). Comparison of air exposure stress resistances of post-harvested yesso scallop with different sizes. *Fisheries Sci.* 38, 443–450. doi: 10.16378/j.cnki.1003-1111.2019.04.002

Li, Y., Yu, H., Wang, Z., Li, Y., Pan, Q., Meng, S., et al. (2019b). The forecasting and analysis of oil spill drift trajectory during the Sanchi collision accident, East China Sea. *Ocean Eng.* 187, 106231. doi: 10.1016/j.oceaneng.2019.106231

Liang, J., Liu, J., Benfield, M., Justic, D., Holstein, D., Liu, B., et al. (2021). Including the effects of subsurface currents on buoyant particles in Lagrangian particle tracking models: Model development and its application to the study of riverborne plastics over the Louisiana/Texas shelf. *Ocean Model.* 167, 101879. doi: 10.1016/j.ocemod.2021.101879

Liu, L., Yuan, D., Li, X., and Mao, Y. (2023). Influence of reclamation on the water exchange in Bohai Bay using trajectory clustering. *Stoch Environ. Res. Risk Assess.* 37, 3571–3583. doi: 10.1007/s00477-023-02463-8

Lu, X., and Zhang, J. (2006). Numerical study on spatially varying bottom friction coefficient of a 2D tidal model with adjoint method. *Continental Shelf Res.* 26, 1905–1923. doi: 10.1016/j.csr.2006.06.007

Nakada, S., Hayashi, M., and Koshimura, S. (2018). Transportation of sediment and heavy metals resuspended by a giant tsunami based on coupled three-dimensional tsunami, ocean, and particle-tracking simulations. *J. Wat. Envir. Tech* 16, 161–174. doi: 10.2965/jwet.17-028

Pan, Q., Yu, H., Daling, P. S., Zhang, Y., Reed, M., Wang, Z., et al. (2020). Fate and behavior of Sanchi oil spill transported by the Kuroshio during January–February 2018. *Mar. pollut. Bull.* 152, 110917. doi: 10.1016/j.marpolbul.2020.110917

Prakash, N., Ashly, K. U., Seelam, J. K., Bhaskaran, H., Yadhunath, E. M., Lavanya, H., et al. (2021). Investigation of near-shore processes along North Goa beaches: A study based on field observations and numerical modelling. *J. Earth Syst. Sci.* 130, 242. doi: 10.1007/s12040-021-01755-3

Qian, S., Wang, D., Zhang, J., and Li, C. (2021). Adjoint estimation and interpretation of spatially varying bottom friction coefficients of the M 2 tide for a tidal model in the Bohai, Yellow and East China Seas with multi-mission satellite observations. *Ocean Model.* 161, 101783. doi: 10.1016/j.ocemod.2021.101783

Rowe, M. D., Anderson, E. J., Wynne, T. T., Stumpf, R. P., Fanslow, D. L., Kijanka, K., et al. (2016). Vertical distribution of buoyant *Microcystis* blooms in a Lagrangian particle tracking model for short-term forecasts in Lake Erie. *JGR Oceans* 121, 5296–5314. doi: 10.1002/2016JC011720

Shi, B., Gong, P., Guan, C., Zhao, R., and Li, J. (2019). Influence of different replacement rates of argopecten irradias aggregate on physical properties of artificial reefs and carbon sequestration. *Prog. Fishery Sci.* 40, 1–8. doi: 10.19663/j.issn2095-9869.20181222002

Sterl, M. F., Delandmeter, P., and Van Sebille, E. (2020). Influence of barotropic tidal currents on transport and accumulation of floating microplastics in the global open ocean. *JGR Oceans* 125, e2019JC015583. doi: 10.1029/2019JC015583

Varona, H. L., Noriega, C., Calzada, A. E., Medeiros, C., Lobaina, A., Rodriguez, A., et al. (2024). Effects of meteo-oceanographic conditions on the weathering processes of oil spills in northeastern Brazil. *Mar. pollut. Bull.* 198, 115828. doi: 10.1016/j.marpolbul.2023.115828

D. Wang and F. Wu (Eds.) (2021). "Part II. Production," in *CHINA FISHERY STATISTICAL YEARBOOK* (China: China Agriculture Press), 15 + 17–46. doi: 10.43455/y.cnki.yzytn.2022.000001

Wang, D., Zhang, J., and Wang, Y. P. (2021). Estimation of bottom friction coefficient in multi-constituent tidal models using the adjoint method: temporal variations and spatial distributions. *JGR Oceans* 126, e2020JC016949. doi: 10.1029/2020JC016949

Wang, J., Kuang, C., Ou, L., Zhang, Q., Qin, R., Fan, J., et al. (2022a). A simple model for a fast forewarning system of brown tide in the coastal waters of Qinhuangdao in the Bohai Sea, China. *Appl. Sci.* 12, 6477. doi: 10.3390/app12136477

Wang, N., Cao, R., Lv, X., and Shi, H. (2023a). Research on the transport of typical pollutants in the yellow sea with flow and wind fields. *JMSE* 11, 1710. doi: 10.3390/jmse11091710

Wang, Q., Lü, Y., He, L., Huang, X., and Feng, J. (2023b). Simulating oil droplet underwater dispersal from a condensate field spill in the South China Sea. *Ocean Eng.* 284, 115090. doi: 10.1016/j.oceaneng.2023.115090

Wang, Q., Zhang, Y., Wang, Y., Xu, M., and Lv, X. (2022b). Fitting cotidal charts of eight major tidal components in the bohai sea, yellow sea based on chebyshev polynomial method. *JMSE* 10, 1219. doi: 10.3390/jmse10091219

Wisha, U. J., Gemilang, W. A., Wijaya, Y. J., and Purwanto, A. D. (2022). Model-based estimation of plastic debris accumulation in Banten Bay, Indonesia, using particle tracking - Flow model hydrodynamics approach. *Ocean Coast. Manage.* 217, 106009. doi: 10.1016/j.ocecoaman.2021.106009

Wong-Ala, J. A. T. K., Ciannelli, L., Durski, S. M., and Spitz, Y. (2022). Particle trajectories in an eastern boundary current using a regional ocean model at two horizontal resolutions. *J. Mar. Syst.* 233, 103757. doi: 10.1016/j.jmarsys.2022.103757

Yan, C., Gu, Z., Zhang, H., Wang, Y., Shi, Y., Zhan, X., et al. (2012). Correlation and path analysis of major quantitative traits of Chlamys nobilis in Sanya. *South China Fisheries Sci.* 8, 34–38. doi: 10.3969/j.issn.2095-0780.2012.03.005

Zhang, B., and Ozer, J. (1992). *SURF -A simulation model for the behaviour of oil slicks at sea*. Available online at: https://api.semanticscholar.org/CorpusID:221993828.

Zhang, B., Pu, A., Jia, P., Xu, C., Wang, Q., and Tang, W. (2021a). Numerical simulation on the diffusion of alien phytoplankton in Bohai Bay. *Front. Ecol. Evol.* 9. doi: 10.3389/fevo.2021.719844

Zhang, J., and Lu, X. (2010). Inversion of three-dimensional tidal currents in marginal seas by assimilating satellite altimetry. *Comput. Methods Appl. Mechanics Eng.* 199, 3125–3136. doi: 10.1016/j.cma.2010.06.014

Zhang, L., Wu, Y., Ni, Z., Li, J., Ren, Y., Lin, J., et al. (2023). Saltwater intrusion regulates the distribution and partitioning of heavy metals in water in a dynamic estuary, South China. *Mar. Environ. Res.* 186, 105943. doi: 10.1016/j.marenvres.2023.105943

Zhang, R., Gao, B., Guo, L., Wu, J., Peng, Y., and Chen, Q. (2021b). Advances in research on the use of shellfish wastes to passivate heavy metals in soil. *J. Agric. Resour. Environ.* 38, 787–796. doi: 10.13254/j.jare.2020.0504

Zhu, Z., Zhu, X., Zhang, C., Chen, M., Wang, M., Dong, M., et al. (2021). Dynamics of tidal and residual currents based on coastal acoustic tomography assimilated data obtained in Jiaozhou Bay, China. *JGR Oceans* 126, e2020JC017003. doi: 10.1029/2020JC017003

frontiers | Frontiers in Marine Science

TYPE Original Research
PUBLISHED 15 October 2024
DOI 10.3389/fmars.2024.1445116

OPEN ACCESS

EDITED BY
Xiaohui Xie,
Ministry of Natural Resources, China

REVIEWED BY
Emilian Parau,
University of East Anglia, United Kingdom
Yu Qin,
University of Florida, United States

*CORRESPONDENCE
Yan Li
yan.li@uib.no

RECEIVED 06 June 2024
ACCEPTED 12 August 2024
PUBLISHED 15 October 2024

CITATION
Li Y, Zheng Z and Kalisch H (2024) Stokes drift and particle trajectories induced by surface waves atop a shear flow.
Front. Mar. Sci. 11:1445116.
doi: 10.3389/fmars.2024.1445116

Stokes drift and particle trajectories induced by surface waves atop a shear flow

Yan Li[1,2]*, Zibo Zheng[3] and Henrik Kalisch[1]

[1]Department of Mathematics, University of Bergen, Bergen, Norway, [2]Bjerknes Centre for Climate Research, University of Bergen, Bergen, Norway, [3]Department of Mathematical Sciences, New Jersey Institute of Technology, Newark, NJ, United States

Surface waves and currents are crucial to the mass transfer in the air-sea interaction as they can drive a variety of dynamical processes. How mass can be transported by surface waves and current coupling is addressed through a study of their induced motions of fluid parcels. To this end, a weakly nonlinear wavetrain is imposed on the background flow whose direction and magnitude are permitted to vary with water depth and second-order features of this configuration are investigated. A leading-order approximation to the Stokes drift is derived, correct to the second order in wave steepness, and applicable to an arbitrarily depth-dependent background flow. The reduced forms of the approximate Stokes drift are provided in a few limiting cases such as a current with an exponential profile or propagating in an orthogonal direction to the wave propagation. Novel features related to the Stokes drift and particle trajectories have been reported for the first time as a result of the rotation induced by the wave and current coupling. A non-vanishing component of the Stokes drift velocity and net-mean displacement of fluid parcels in the span-wise direction to the wave propagation are observed in the cases where a shear current propagates obliquely to the waves direction. A non-monotonic dependence on water depth of the stream-wise component of the Stokes drift is shown, and thereby the largest mass transport induced no longer occurs on the still water surface but some depth beneath. The non-monotonic behavior occurs beyond the regime of the near-irrotational assumption of wave-induced motions. It can also lead to the change of the signs for the stream-wise Stokes drift throughout the water column, and thus an overall cancellation of the integrated mass transport by waves over the water column, indicating that the depth-integrated models can likely lead to underestimated effects of the mass transport which is non-trivial at a local depth. The results from this study have far-reaching impact. The Stokes drift profile is a direct input to the parametrization of the surface waves forcing in ocean circulations and the obliquely propagating Stokes drift can be plausibly responsible for the formation of oblique Langmuir rolls to wave propagation in the open ocean.

KEYWORDS

Stokes drift, surface waves (fluid), shear current, ocean modelling, wave-current interaction (WCI), wave forcing in the upper ocean, particle trajectories

1 Introduction

Surface waves are ubiquitous in the ocean. They are an essential factor driving dynamical processes near the ocean surface including the exchange of mass, momentum, and energy in the upper ocean with both the atmosphere and deeper sea. One particularly important process involves the interaction of waves with ocean currents which has been widely investigated for example in the context of ocean circulations and the occurrence of rogue waves (Kharif and Pelinovsky, 2003; Sullivan and McWilliams, 2010; Onorato et al., 2011). In the present contribution, attention is given to mass transport due to the interaction of waves with depth-dependent currents, and in particular how the wave-induced Stokes drift changes if the waves propagate on a pre-existing depth-dependent background flow.

The net forward drift of fluid particles in a steady periodic wavetrain was discovered in Stokes (1847). This celebrated result is very well known and has been famously illustrated in the collection (Van Dyke, 1982). The Stokes drift has been verified in various recent wave tank experiments (Chen et al., 2010; van den Bremer et al., 2019), but it is also well known that the result needs to be modified when dealing with finite depth due to bottom drag (Longuet-Higgins, 1953; Ursell, 1953; Monismith et al., 2007), when considering the more realistic case of wave groups (Smith, 2006; Li and Li, 2021), the influence of infragravity waves (Bjørnestad et al., 2021), mean currents and rotation (Constantin and Monismith, 2017), or random sea states (Myrhaug et al., 2014; Myrhaug, 2015). Nevertheless, Stokes drift correlates well with the transport of small objects by surface waves in field observations, for example in the case of oil spills (Yang et al., 2021). In particular when dealing with wave groups, the depth-dependent net displacement of fluid parcels in the form of a mean flow should be taken into account (Dysthe, 1979; McIntyre, 1981; Davey and Stewartson, 1974; Higgins et al., 2020; Li, 2021). In the last couple of decades, environmental concerns over plastic pollution in the oceans have led to several studies assessing the role of surface waves in the transport of plastic particles near the ocean surface, see, e.g., van den Bremer and Breivik (2018); Chamecki et al. (2019); Calvert et al. (2021); Larsen et al. (2023); Sutherland et al. (2023) among others.

While the interaction of surface waves and currents occurs naturally in the oceans at all times, there are many features which have not been investigated thoroughly, owing partially to the technical difficulties in describing various configurations analytically. On the other hand, understanding wave-current interaction better is of utmost importance in various applications. For example, wave-current interactions have been reported as a plausible mechanism for the generation of rogue waves, i.e. unexpected and abnormally large waves which pose a great risk to maritime transportation and man-made structures in coastal waters. The physical origins of such unexpected waves are indicated as linear refraction (White and Fornberg, 1998) or nonlinear effects like modulational instability and crest amplification as a result of bound waves (Shrira and Slunyaev, 2014; Pizzo et al., 2023; Zheng et al., 2023; Li and Chabchoub, 2024).

Stokes drift has been considered in a few regional ocean models in the last few decades as it is the main physical origin for various forces sometimes called *Stokes forces*, as has been explained in-depth by Suzuki and Fox-Kemper (2016) and Zippel et al. (2022). Craik and Leibovich (1976) have demonstrated the role of Stokes drift in triggering Langmuir circulations through the so-called Craik-Lebovich Type 2 (CL2) Instability. Based on large-eddy simulations, McWilliams et al. (1997) first showed that Stokes drift in wind-induced mean current leads to Langmuir turbulence in the ocean which represents flow structures similar to Langmuir cells but considerably more irregular in both time and space. The role of Langmuir turbulence in both vertical mixing and the horizontal transport of materials has been addressed in a variety of papers, see, e.g., Sullivan and McWilliams (2010); McWilliams (2016). Stokes velocity profiles are parameterized in the form of explicit expressions for better numerical efficiency in oceanic models, accounting for different sea states like short-crested waves, swell, or well-developed wind seas, see, e.g., Kenyon (1969); Ardhuin et al. (2009); Breivik et al. (2014); Webb and Fox-Kemper (2011), Webb and Fox-Kemper, 2015); Breivik and Christensen (2020). In contrast to the Stokes forces, there are various models which have accounted for the roles of surface waves in ocean models through radiation stress (Lane et al., 2007; Qiao et al., 2010; Mellor, 2015) and steep wave-induced turbulence (Babanin, 2006; Babanin and Chalikov, 2012; Ghantous and Babanin, 2014).

Among the works which have examined the effect of a depth-dependent flow on waves at the free surface, most have considered the special case of a linearly sheared current. This configuration induces a number of mathematical simplifications which have been exploited by many authors (see Ali and Kalisch (2013); Flamarion et al. (2023) and many others). Constant background vorticity introduces a directional asymmetry in the linear dispersion relation and rotational wave-induced motions (Peregrine, 1976; Ellingsen, 2014a), giving rise to novel features in the pattern of both ship waves and these generated by a moving oscillating body, see, e.g., Ellingsen (2014b); Li and Ellingsen (2016a); Li and Ellingsen, (2016b); Li (2018). Touboul et al. (2016) derived a mild envelope equation for waves in a water region with a slowly varying bathymetry and linearly sheared current. In accordance with Craik (1970), a second-order theory for three-dimensional waves in a linearly sheared current has been derived by Akselsen and Ellingsen (2019). Expressions for Stokes drift velocity and particle trajectories are particularly presented, which differ from Hsu (2013) by that the linearly current advection effects in the linear orbital velocity of fluid parcels have been properly considered. Thomas et al. (2012) have derived a nonlinear Schrödinger (NLS) equation for the evolution of the energy of surface waves with constant vorticity. It is especially shown that different vorticity strengths can result in various instability regions and growth rates when a Stokes wavetrain is subject to modulational instability, which is experimentally validated by Steer et al. (2020). Curtis et al. (2018) have extended the NLS equation to a higher order and additionally considered the surface tension, where a formula for the Stokes drift velocity on a still surface has also been obtained.

In contrast, studies on waves atop an arbitrarily depth-dependent flow have been scarce. A majority of the very few exceptions have placed their focus on the linear dispersive properties of surface waves, see, e.g., Stewart and Joy (1974); Skop (1987); Kirby and Chen (1989); Shrira (1993); Ellingsen and Li (2017); Li and Ellingsen (2019);

Ellingsen et al. (2024). Both Quinn et al. (2017) and Li and Ellingsen (2019) lead to the linear wave action equation which in addition to the shear flow can handle non-trivial bathymetry in a consistent manner. Based on a newly derived second-order theory for narrowband waves in a depth-dependent flow, Xin et al. (2023) report that the wave-current coupling leads to much amplified loads on a bottom-fixed vertically installed slender cylinder, posing a big risk to the safety and reliability of offshore structures. Zheng et al. (2023) extended Xin et al. (2023) and Li and Ellingsen (2019) to permit broadband waves, where statistical features of surface elevation altered by a depth-dependent flow are examined, showing the important relevance of depth-dependent structure of current to extremely large wave events. In both Xin et al. (2023) and Zheng et al. (2024), considerably different wave kinematics are shown as a result of shear current-modified second-order bound waves, where a non-vanishing velocity field forced by second-harmonic deep-water waves is shown by both and the latter in addition a considerable Eulerian mean flow even in the limit of extremely narrow-banded waves.

Through laboratory observations, Pizzo et al. (2023) have, for the first time, reported how modulational instability can be suppressed by a background current whose profile is similar to the Stokes drift as a result of the Stokes wave. Using a newly derived higher-order Shear-Current Modified NLS (SC-MNLS) equation, Li and Chabchoub (2024) also lead to a similar conclusion but due to a wave-modified rotational flow whose profile is arbitrarily dependent on depth instead. Interestingly, Li and Chabchoub (2024) have led to a hypothesis that states the plausible link between the formation of rogue waves owing to modulational instability and the CL2 instability, addressing the need for resolving wave phases in ocean circulations for the test of the hypothesis. Fully nonlinear depth-integrated models for two-dimensional waves in a depth-dependent current have been developed by Yang and Liu (2022).

Despite of the aforementioned extensive literature, Stokes drift accounting for the effects of an arbitrary depth-dependent flow in both the dispersion relation and the magnitude of wave-induced orbital motions has, to the best of the authors' knowledge, not been derived before, and thus never been physically elucidated. The main objective of this work is to fill in this gap by deriving the Stokes drift and the particle trajectories of passive fluid parcels in such a physical setting. Novel physical features are demonstrated. With the widely recognized role of Stokes drift, the results from this work can be used to assessing shear current-modified wave effects in ocean circulations, particularly in wave phase resolved oceanic models, as addressed by Li and Chabchoub (2024). We highlight that Stokes drift itself will be shown to possess a misalignment with the wave propagation, and thereby likely to trigger misaligned Langmuir rolls in realistic scenarios. Such misaligned Langmuir rolls would differ from Van Roekel et al. (2012) in the physical origin, where they are a result of wind surface stress and Stokes drift which is assumed to be aligned with the wave propagation direction.

This paper is laid out as follows. A theoretical description of the system is introduced in section 2, covering the underlying assumptions, perturbation expansion, and the solution to a linearized boundary value problem. The quadratic features of surface waves atop a depth-dependent flow have been newly derived in section 3 with a special focus on the Stokes drift and particle trajectories. Approximations to Stokes drift in a few limiting cases are particularly derived. Novel features of Stokes drift and particular trajectories are demonstrated in section 4 in which the approximations are tested. The conclusions from this paper are drawn in section 5.

2 Theoretical description

2.1 System description

Let $\mathbf{U}(z) = (U_x(z), U_y(z))$ be the velocity vector of a horizontally-oriented depth-dependent flow and $\mathbf{V}(\mathbf{x},z,t) = [\mathbf{u}(\mathbf{x},z,t), w(\mathbf{x},z,t)]$ be the flow velocity induced by surface waves in an Eulerian frame which has accounted for the modified effects by the depth-dependent flow, where $\mathbf{u}$ and w denote the velocity vector in the horizontal plane and the vertical velocity, respectively; $\mathbf{x} = (x,y)$ denotes the position vector in the horizontal plane and z is the vertical axis with $z = 0$ denoting a still water surface, U_x and U_y are the component of the flow velocity in the x and y direction, respectively. Assuming an incompressible flow, negligible viscosity, and Coriolis force, the fluid system of surface waves in a large-scale flow is described by the continuity and Euler momentum equations given by

$$\nabla_3 \cdot \mathbf{V} = 0, \tag{1}$$

$$\partial_t (\mathbf{V} + \mathcal{U}) + [(\mathbf{V} + \mathcal{U}) \cdot \nabla_3](\mathbf{V} + \mathcal{U}) + \nabla_3 p = 0, \tag{2}$$

where $\mathcal{U} = [\mathbf{U}, 0]$ is the velocity vector due to a background depth-dependent flow; $\nabla_3 = (\nabla, \partial_z)$ denotes the spatial gradient operator in three dimensions with $\nabla = (\partial_x, \partial_y)$ the gradient operator in the horizontal plane, $p(\mathbf{x}, z, t) = P(\mathbf{x}, z, t)/\rho + gz$ is the dynamic pressure, with P the total pressure, ρ the water density which is assumed constant, and g the gravitational acceleration. The system is described by the dynamic and kinematic boundary conditions at the free water surface $z = \zeta$, respectively,

$$p - gz = 0 \quad \text{and} \quad \partial_t \zeta + (\mathbf{u} + \mathbf{U}) \cdot \nabla \zeta = w; \tag{3}$$

and the finite-water seabed boundary condition

$$w = 0 \quad \text{for} \quad z = -h, \tag{4}$$

where h denotes the water depth. The perturbed approximate solution to the boundary value problem described by Equations 1–4 are obtained with additional assumptions detailed in the following sections.

2.2 Perturbation expansion

Following the derivations by Zheng et al. (2023); Xin et al. (2023), the wave-induced velocity is expressed in an approximate form of power series in wave steepness ε which is a non-dimensional scaling parameter,

$$[\mathbf{u}, w, p, \zeta] = \epsilon[\mathbf{u}^{(1)}, w^{(1)}, p^{(1)}, \zeta^{(1)}] + \epsilon^2[\mathbf{u}^{(2)}, w^{(2)}, p^{(2)}, \zeta^{(2)}], \quad (5)$$

where the corrections at the third and higher orders are truncated, and the superscript '(j)' denotes $\mathcal{O}(\epsilon^j)$. The leading order approximations to the unknowns are solved in the context of a prescribed train of monochromatic waves whose perturbed elevation is given by

$$\zeta^{(1)} = a\cos\ \psi \equiv \frac{1}{2}ae^{i\psi} + \text{c.c.}, \quad (6)$$

where c.c. denotes the complex conjugates, $\psi = \mathbf{k}\cdot\mathbf{x} - \omega t + \theta_0$ denotes the wave phase, a, $\mathbf{k}$, and ω are the (real) *current-modified* amplitude, wave vector, and angular frequency of monochromatic waves, respectively. The prescribed linear elevation leads to the linear velocity and pressure to be solved for in the form as

$$\begin{aligned}&[\mathbf{u}^{(1)}, w^{(1)}] = -\tfrac{1}{2}i\omega a[\hat{\mathbf{u}}^{(1)}(\mathbf{k}, z), \hat{w}^{(1)}(\mathbf{k}, z)]e^{i\psi}\\ &+\text{c.c.} \quad \text{and}\\ &p^{(1)} = \tfrac{1}{2}ga\hat{p}^{(1)}(\mathbf{k}, z)e^{i\psi} + \text{c.c.},\end{aligned} \quad (7)$$

where $\hat{\mathbf{u}}^{(1)}$, $\hat{w}^{(1)}$, and $\hat{p}^{(1)}$ are the dimensionless and depth-dependent horizontal velocity vector, vertical velocity, and pressure, respectively. These dimensionless quantities are solved for in the next sub-section.

2.3 Linear waves

Substituting the expression for the linear vertical velocity into the linearized boundary value problem based on Equations 1–4 gives rise to [see, e.g., Li and Ellingsen (2019)]

$$\begin{aligned}&(\mathbf{k}\cdot\mathbf{U} - \omega)(\partial_{zz} - k^2)\hat{w}^{(1)} - \mathbf{k}\cdot\mathbf{U}''\hat{w}^{(1)}\\ &= 0 \quad \text{for} \quad -h \le z \le 0\end{aligned} \quad (8)$$

$$\begin{aligned}&(\omega - \mathbf{k}\cdot\mathbf{U}_0)^2\,\partial_z\,\hat{w}^{(1)} - \left[gk^2 - (\omega - \mathbf{k}\cdot\mathbf{U}''_0)\mathbf{k}\cdot\mathbf{U}''_0\right]\hat{w}^{(1)}\\ &= 0 \quad \text{for} \quad z = 0,\end{aligned} \quad (9)$$

$$\hat{w}^{(1)} = 0 \quad \text{for} \quad z = -h, \quad (10)$$

where $\Re$ the prime denotes the derivative with respect to z (e.g., $\mathbf{U}' = \partial_z\,\mathbf{U}$ and $\mathbf{U}'' = \partial_{zz}\,\mathbf{U}$) and subscript '0' denotes the evaluation at $z = 0$. Following Li and Ellingsen (2019), the dispersion relation and the linearized boundary value problem are solved together for the unknown dimensionless velocity and angular velocity using the Direct Integration Method (DIM). Specifically, the dispersion relation is described by

$$\left(\coth\ kh + \int_{-h}^{0}\frac{\mathbf{k}\cdot\mathbf{U}''(z)}{\mathbf{k}\cdot\mathbf{U}(z) - \omega}\frac{\sinh k(z+h)}{\sinh\ kh}\hat{w}^{(1)}dz\right) \quad (11)$$

$$(\omega - \mathbf{k}\cdot\mathbf{U}_0)^2 + \frac{\mathbf{k}\cdot\mathbf{U}'_0}{k}(\omega - \mathbf{k}\cdot\mathbf{U}_0) - gk = 0.$$

Furthermore, the horizontal velocity vector and pressure of linear wave-induced flow in the presence of an arbitrary depth-dependent background current are given by, respectively

$$\hat{\mathbf{u}}^{(1)} = \frac{(\mathbf{k}\cdot\mathbf{U}')\mathbf{k} - k^2\mathbf{U}'}{k^2(\omega - \mathbf{k}\cdot\mathbf{U})}i\hat{w}^{(1)} + \frac{i\mathbf{k}}{k^2}(\hat{w}^{(1)})', \quad (12)$$

$$\hat{p}^{(1)} = \frac{\omega - \mathbf{k}\cdot\mathbf{U}}{k^2}i\left(\hat{w}^{(1)}\right)' + \frac{\mathbf{k}\cdot\mathbf{U}'}{k^2}i\hat{w}^{(1)}. \quad (13)$$

We remark that a current propagating in the orthogonal direction to the wave propagation, which means $\mathbf{k}\cdot\mathbf{U} = 0$, $\mathbf{k}\cdot\mathbf{U}' = 0$, and $\mathbf{k}\cdot\mathbf{U}'' = 0$, does not affect the dispersion relation and dimensionless vertical velocity described together by Equations 8–11. Nevertheless, the orbital velocity in the span-wise direction remains altered by the vorticity of the shear current when $U'_y \neq 0$ in Equation 12. This non-vanishing orbital velocity has far-reaching effects on the Stokes drift and particle trajectories, as elaborated in sub-section 3.2.2 and section 4.

2.4 Linear velocity of fluid parcels and particle trajectories

The particle trajectories of fluid motions due to linear waves can be directly obtained by noting that the linear particle velocity

$$\mathbf{V}_p^{(1)} = [\mathbf{u}^{(1)} + \mathbf{U}(z), w^{(1)}], \quad (14)$$

which gives rise to

$$\begin{aligned}\Delta\mathbf{r}^{(1)} &\equiv [\Delta\mathbf{x}_p(t), \Delta z_p(t)]\\ &= [\mathbf{U}(z)(t - t_0), 0] + \Re\left(\left[\hat{\mathbf{u}}^{(1)}, \hat{w}^{(1)}\right]ae^{i(\psi + \omega t_0)}\right),\end{aligned} \quad (15)$$

where $\Re$ denotes the real component, $\Delta\mathbf{r}^{(1)} = \mathbf{r}^{(1)}(t) - \mathbf{r}(t_0)$ denotes the linear displacement related to the position of the particle at an initial time instant $t = t_0$. For later reference, we introduce a time-averaging operator '$\overline{(\ldots)}$' defined as

$$\overline{(\ldots)} = \frac{\omega}{2\pi}\int_0^{2\pi/\omega}(\ldots)dt, \quad (16)$$

which denotes the time averaging with respect to the period of the wave phase.

3 Quadratic properties of linear waves

3.1 Stokes drift and net mean trajectories in an arbitrary shear current

Assuming infinitesimal waves where $\mathcal{O}(ka) \ll 1$, the particle velocity in the second order in wave steepness can be obtained by a Taylor expansion about $\mathbf{r}(t) = \mathbf{r}^{(1)}(t)$

$$\mathbf{V}_p^{(2)} = \left[\mathbf{u}^{(2)}, w^{(2)}\right] + (\Delta\mathbf{r}^{(1)}\cdot\nabla_3)\mathbf{V}_p^{(1)}, \quad (17)$$

where $\nabla_3 = (\nabla, \partial_z)$, $\nabla = (\partial_x, \partial_y)$, $\mathbf{u}^{(2)}$ and $w^{(2)}$, as noted, denote the Eulerian velocity vector in the horizontal plane and the vertical

velocity due to second-order waves, respectively. The Stokes drift $\mathbf{V}_S$ denotes the net mean transport velocity of particles correct to second order in wave steepness. It is obtained by averaging the second term on the right-hand side of Equation 17, and thus

$$\begin{aligned}\mathbf{V}_S &\equiv \overline{[\Delta\mathbf{r}^{(1)}\cdot\nabla_3]\mathbf{V}_{\mathrm{P}}^{(1)}}\\ &= \frac{\omega a^2}{4}\mathrm{i}\left(\partial_z\hat{w}^{(1)}+\hat{w}^{(1)}\partial_z\right)\left(\hat{\mathbf{V}}^{(1)}\right)^{*}+\mathrm{c.c.}\end{aligned}\tag{18}$$

where $\hat{\mathbf{V}}^{(1)}=[\hat{\mathbf{u}}^{(1)},\hat{w}^{(1)}]$ by definition, the continuity equation $\mathrm{i}\mathbf{k}\cdot\hat{\mathbf{u}}^{(1)}+\partial_z\hat{w}^{(1)}=0$ was used, both c.c. and the asterisk denote the complex conjugates. We note that the vertical velocity of the mean motion of particles vanishes (as $\mathrm{i}|\partial_z\hat{w}^{(1)}|^2+\mathrm{c.c.}=0$), and thus

$$\mathbf{V}_S=\left[\frac{\omega a^2}{4}\mathrm{i}\left(\partial_z\hat{w}^{(1)}+\hat{w}^{(1)}\partial_z\right)(\hat{\mathbf{u}}^{(1)})^{*}+\mathrm{c.c.},0\right].\tag{19}$$

Substituting (12) for $\hat{\mathbf{u}}^{(1)}$ into (19) gives rise to

$$\begin{aligned}&\mathbf{V}_S\left(\mathbf{k},z;\hat{w}^{(1)},\omega\right)\\ &=\frac{\mathbf{k}\omega a^2}{4k^2}[|\partial_z(\hat{w}^{(1)})|^2+\partial_{zz}\left(\hat{w}^{(1)}\right)^{*}\hat{w}^{(1)}]\\ &+\frac{\omega a^2}{4}\frac{(\mathbf{k}\cdot\mathbf{U}')\mathbf{k}-k^2\mathbf{U}'}{k^2(\omega-\mathbf{k}\cdot\mathbf{U})}\partial_z|\hat{w}^{(1)}|^2\\ &+\frac{\omega a^2}{4}|\hat{w}^{(1)}|^2\partial_z\left[\frac{(\mathbf{k}\cdot\mathbf{U}')\mathbf{k}-k^2\mathbf{U}'}{k^2(\omega-k\cdot\mathbf{U})}\right]+\mathrm{c.c.}\end{aligned}\tag{20}$$

In the absence of a shear current, i.e., $\mathbf{U}(z)=[0,0]$, and $\hat{w}=\hat{w}_{\mathrm{noC}}$ with $\hat{w}_{\mathrm{noC}}$

$$\hat{w}_{\mathrm{noC}}=\frac{\sinh\ k(z+h)}{\sinh\ kh},\tag{21}$$

the Stokes drift denoted by Equation 20 becomes

$$\mathbf{V}_S(\mathbf{k},z)=\frac{1}{2}\frac{\cosh\ 2k(z+h)}{(\sinh\ kh)^2}\frac{\omega}{k}(ka)^2\mathbf{e}_{\mathbf{k}},\tag{22}$$

where $\mathbf{e}_{\mathbf{k}}$ denotes the unit vector in the direction of the wave vector $\boldsymbol{k}$. We remark that the dimensionless vertical velocity given by Equation 21 also corresponds the vertical velocity for linear waves atop a linearly sheared current, which will be used in §3.2.1. The Stokes drift velocity given by Equation 22 agrees with the net mean horizontal displacement driven by a train of linear Stokes waves on a finite water depth and also on deep water in the limit of $kh\to+\infty$ (Kenyon, 1969). For later reference and convenience, we introduce

$$\mathbf{V}_{s,0}=\mathbf{V}_s(\mathbf{k},0),\tag{23}$$

corresponding to the Stokes drift velocity at a still water surface in the absence of a current.

It is worth noting that the Stokes drift velocity given by Equation 20 has a non-vanishing component as long as the profile shear of the current is non-zero in the spanwise direction, giving rise to a non-vanishing component of the vorticity of fluid parcels in the wave propagation direction.

3.2 Limiting cases of different current profiles

We proceed to the explicit expression for the profiles of Stokes drift velocity in three limiting cases which are elaborated below.

3.2.1 A linearly sheared current

A linearly sheared current whose velocity profile $\mathbf{U}=\mathbf{S}z$ is firstly assumed, where $\mathbf{S}$ denotes the constant vorticity vector of the shear. For a train of Stokes wave, the vertical velocity of the particles induced by linear waves are the same as these in the absence of a shear current, i.e., Equation 21 [see, e.g (Peregrine, 1976; Ellingsen, 2014a)]. Substituting both the linear shear current profile and the dimensionless vertical velocity $\hat{w}^{(1)}$ in the form of Equation 21 into Equation 20 gives rise to

$$\begin{aligned}\mathbf{V}_S(\mathbf{k},z;\hat{w}_{\mathrm{noC}},\omega)&=\frac{1}{2}\frac{\cosh\ 2k(z+h)}{(\sinh\ kh)^2}\omega a^2\mathbf{k}\\ &+\frac{1}{2}\frac{(\mathbf{k}\cdot\mathbf{S})\mathbf{k}-k^2\mathbf{S}}{k(\omega-z\mathbf{k}\cdot\mathbf{S})}\frac{\sinh\ 2k(z+h)}{\sinh^2kh}\omega a^2+\\ &\frac{[(\mathbf{k}\cdot\mathbf{S})\mathbf{k}-k^2\mathbf{S}](\mathbf{k}\cdot\mathbf{S})}{2k^2(\omega-z\mathbf{k}\cdot\mathbf{S})^2}\frac{\sinh^2k(z+h)}{\sinh^2kh}\omega a^2.\end{aligned}\tag{24}$$

where the linear dispersion relation of waves atop a linearly shear current admits an accurate expression (Peregrine, 1976; Li and Ellingsen, 2016a)

$$\begin{aligned}\omega(k)=\mathbf{k}\cdot\mathbf{U}_0+\sqrt{gk\tanh\ kh+\frac{(\mathbf{k}\cdot\mathbf{S})^2\tanh^2\ kh}{4k^2}}\\ -\frac{\mathbf{k}\cdot\mathbf{S}\ \tanh kh}{2k}.\end{aligned}\tag{25}$$

We notice that there exists a pole at $\omega/(\mathbf{k}\cdot\mathbf{S})=z_c$ for $\mathbf{k}\cdot\mathbf{S}<0$ in Equation 24, where z_c denotes a critical depth which may trigger the instability of the flow system, as discussed in previous works like Shrira (1993) and Li and Ellingsen (2019, their §4.3). From a physical point of view, it is nevertheless typical that either $|z_c|\gg h$ on a finite depth or the current projection in the wave propagation direction cannot reach the same magnitude as the phase velocity in deep water in practice. As a result, the critical depth does not bear much physical meaning in the applicability regime considered in this work.

3.2.2 A shear current propagating orthogonal to the wave propagation

We proceed to consider the limiting cases of a nonlinear profile of shear current propagating in the direction orthogonal to the wave propagation direction, i.e., $\mathbf{k}\cdot\mathbf{U}(z)=0$ is understood, leading to simplifications for the Stokes drift velocity given by Equation 20. In particular, such current profiles are unidirectionally oriented at different depths, and the Stokes drift velocity possesses a reduced form as follows

$$\begin{aligned}\mathbf{V}_S(\mathbf{k},z)=\frac{ka^2\omega}{2}\left[\frac{\cosh\ 2k(z+h)}{(\sinh\ kh)^2}\frac{\mathbf{k}}{k}-\frac{\sinh\ 2k(z+h)}{\sinh^2kh}\frac{\boldsymbol{U}'}{\omega}\right.\\ \left.-\left(\frac{\sinh\ k(z+h)}{\sinh\ kh}\right)^2\frac{\boldsymbol{U}''}{k\omega}\right]\end{aligned}\tag{26}$$

where $\hat{w}$ is understood to be in the form as Equation 21 (Li and Ellingsen, 2019) and $\omega=\sqrt{gk\ \tanh\ kh}$ is admitted. Evidently, the

Stokes drift velocity in the limiting cases where a shear current orients in the direction which is constant in the vertical direction and normal to the wave propagation has a non-vanishing component in the direction normal to wave propagation, in contrast to the cases in the absence of a shear current where the Stokes drift induced by a train of monochromatic waves always follows the direction of wave propagation.

3.2.3 A weakly-sheared current under the near-potentiality assumption

As has been detailed in Ellingsen and Li (2017) and Shrira (1993), the near-potentiality (or irrotationality) assumption can be made when the dimensionless parameter ϵ_c is small, i.e., $\epsilon_c \ll 1$, with ϵ_c being defined as

$$\epsilon_c = \int_{-h}^{0} \frac{\mathbf{k}\cdot\mathbf{U}'(\xi)\sinh\ 2k(\xi+h)}{\omega_0 \sinh\ (2kh)}\mathrm{d}\xi, \tag{27}$$

with $\omega_0 = \sqrt{gk\ \tanh\ kh}$. The dimensionless small parameter ϵ_c bears the physical meaning of the wave vector weighted, depth-integrated, and current-modified effect on the dispersion relation as a leading-order approximation to the wave dispersion relation given by (see, Ellingsen and Li (2017))

$$\omega \approx \omega_{\approx,1\mathrm{st}} \quad \text{with} \quad \omega_{\approx,1\mathrm{st}} = \mathbf{k}\cdot\mathbf{U}_0 + \omega_0\left(\sqrt{1+\epsilon_c^2} - \epsilon_c\right), \tag{28}$$

where the approximate dispersion relation (Equation 28) is correct to $\mathcal{O}(\epsilon_c)$. The higher-order approximations to the dispersion relation of waves than Equation 28 are derived by Kirby and Chen (1989) and Ellingsen and Li (2017). Under the near-irrotationality assumption, the normalized vertical velocity $\hat{w}$ is given by Equation 21, inserting which into Equation 20 gives rise to a leading-order approximation to the Stokes drift velocity $\mathbf{V}_s = \mathbf{V}_{s,\approx}$ with

$$\begin{aligned}\mathbf{V}_{s,\approx} = &\frac{1}{2}\frac{\cosh\ 2k(z+h)}{(\sinh\ kh)^2}\omega_{\approx}a^2\mathbf{k}\\ &+\frac{1}{2}\frac{(\mathbf{k}\cdot\mathbf{U}')\mathbf{k} - k^2\mathbf{U}'}{k^2(\omega_{\approx}-\mathbf{k}\cdot\mathbf{U})}\frac{\sinh 2k(z+h)}{\sinh^2 kh}ka^2\omega_{\approx}+\\ &\partial_z\left[\frac{(\mathbf{k}\cdot\mathbf{U}')\mathbf{k} - k^2\mathbf{U}'}{k^2(\omega_{\approx}-\mathbf{k}\cdot\mathbf{U})}\right]\frac{\sinh^2 k(z+h)}{2\sinh^2 kh}ka^2\omega_{\approx},\end{aligned} \tag{29}$$

where the approximation by Equation 28 to the angular frequency was used. We remark that Equation 29 is an approximation to the Stokes drift for any current profiles in the applicability regime while Equations 24, 26 are second-order accurate expressions of the Stokes drift velocity due to waves in a linearly sheared current and a depth-dependent current propagating in the span-wise direction, respectively.

Following Ellingsen and Li (2017), a higher-order approximation to the Stokes drift velocity can be readily obtained by inserting a higher-order approximation to the dimensionless vertical velocity and angular frequencies, respectively,

$$\hat{w} \approx \hat{w}_{\mathrm{noC}} + \hat{w}_{\approx} \text{ and } \omega \approx \omega_{\approx,\,1\mathrm{st}} + \omega_{\approx,\,2\mathrm{nd}}, \tag{30}$$

where

$$\hat{w}_{\approx}(\boldsymbol{k},z) = \mathcal{W}(\boldsymbol{k},z) - \mathcal{W}(\boldsymbol{k},0)\hat{w}_{\mathrm{noC}}(\boldsymbol{k},z), \tag{31}$$

$$\mathcal{W}(\mathbf{k},z) = \frac{1}{k}\int_{-h}^{z}\frac{\mathbf{k}\cdot\mathbf{U}''(\xi)}{\mathbf{k}\cdot\mathbf{U}(\xi)-\omega_{\approx,1st}}\frac{\sinh\ k(\xi+h)\sinh\ k(z-\xi)}{\sinh\ kh}\mathrm{d}\xi, \tag{32}$$

and

$$\omega_{\approx,\,2\mathrm{nd}} = -\frac{\Delta(\omega_{\approx,1st})}{2\sqrt{1+\epsilon_c^2}}\ \omega_0, \tag{33}$$

$$\begin{aligned}\Delta(\sigma) = -\frac{2\sigma}{\omega_0^2}\int_{-h}^{0}\frac{\mathbf{k}\cdot\mathbf{U}''(z)\sinh\ k(z+h)}{k(\mathbf{k}\cdot\mathbf{U}(z)-\sigma)}\Bigg[\frac{\sinh\ kz}{\sinh\ kh}(\omega_0\epsilon_c\\ -\mathbf{k}\cdot\mathbf{U}_0) - \int_{z}^{0}\frac{2\mathbf{k}\cdot\mathbf{U}(\xi)\cosh\ k(2\xi+h-z)}{-\sinh\ 2kh}k\mathrm{d}\xi\Bigg]\mathrm{d}z\,.\end{aligned} \tag{34}$$

Here, the second term on the right hand side of Equation 31 corresponds to the solution of the homogeneous Laplace equation. The boundary conditions at the still water surface and seabed for the dimensionless vertical velocity are well satisfied; i.e., $\hat{w}_{\mathrm{noC}}(k,0) + \hat{w}_{\approx}(k,0) = 1$ and $\hat{w}_{\mathrm{noC}}(k,-h) + \hat{w}_{\approx}(k,-h) = 0$

$$\mathbf{V}_{s,\,\approx,\,2_{\mathrm{nd}}} = \mathbf{V}_s(\mathbf{k},z;\hat{w}_{\mathrm{noC}}+\hat{w}_{\approx},\omega_{\approx,\,1\mathrm{st}}+\omega_{\approx,\,2\mathrm{nd}}), \tag{35}$$

being an approximation to $\mathbf{V}_s$ which is correct to $\mathcal{O}(\epsilon^2\epsilon_c)$ and with an accuracy at one higher order of magnitude in ϵ_c than the approximation given by Equation 29.

3.3 Particle trajectories

The particle trajectories in the first and second order in wave steepness are given by definition according to, respectively,

$$\begin{aligned}\mathbf{r}^{(1)}(t) &= \mathbf{r}_0 + \int_0^t \mathbf{V}_p^{(1)}(\tau)\mathrm{d}\tau \ \rightarrow\ \mathbf{r}^{(1)}(t)\\ &= \mathbf{r}_0 + \frac{1}{2}[\hat{\mathbf{u}}^{(1)},\hat{w}^{(1)}]a\mathrm{e}^{\mathrm{i}\psi} + \mathrm{c.c.},\end{aligned} \tag{36}$$

$$\mathbf{r}^{(2)}(t) = \int_0^t \mathbf{V}_p^{(2)}(\mathbf{r}^{(1)}(\tau))\mathrm{d}\tau, \tag{37}$$

which denote the time integration of the respective particle velocities. The initial time instant t_0 is set 0 without any loss of generality. A leading-order approximation to the total particle transport can thus be given by

$$\mathbf{r}_p(t) = \mathbf{r}^{(1)} + \mathbf{r}^{(2)} \quad \text{and} \quad \Delta\mathbf{r}_p = \mathbf{V}_s t, \tag{38}$$

where the definition $\Delta\mathbf{r}_p = \overline{\mathbf{r}(t)}$ is introduced to denote the net mean displacement of flow parcels due to waves or wave and current interaction. This means that the mean displacement due to the current alone is not included in $\Delta\mathbf{r}_p$ as it is not the focus of this work. We note that the trajectories predicted by Equations 36, 37

are leading-order approximations in contrast to the approach from a known velocity field via systems of ordinary differential equations, the latter of which has been used by a number of authors in different settings (Borluk and Kalisch, 2012; Chen et al., 2021).

4 Results

In this section, the analytical and semi-analytical solutions derived in § 3 are numerically implemented for the analysis. The setup for the numerical implementations is explained in subsection 4.1, where a few current profiles are assumed. The novel features related to the Stokes drift are demonstrated in subsection 4.2 due to a background current and the approximations to Stokes drift presented in 3.2 are validated. The trajectories and the net mean displacement of fluid parcels are presented in subsection 4.3 using the expressions derived in subsection 3.3.

4.1 Setup for numerical implementations

Three different vertically sheared current profiles are chosen for numerical implementations, including a linearly sheared, exponential, and realistic profile measured at a river mouth implemented in Li and Ellingsen (2019). The linearly and exponential profiles admit analytical expressions as follows, respectively,

$$\mathbf{U}_L(z) = [\mathrm{Fr}_x\alpha_x, \mathrm{Fr}_y\alpha_y]\sqrt{\frac{g}{k}}(kz), \tag{39}$$

$$\mathbf{U}_{\exp}(z) = [\mathrm{Fr}_x(\mathrm{e}^{\alpha_x kz} - 1), \mathrm{Fr}_y(\mathrm{e}^{\alpha_y kz} - 1)]\sqrt{\frac{g}{k}}, \tag{40}$$

where Fr_x and Fr_y are non-dimensional parameters which measure the magnitude of a profile velocity component of the background current in the x and y direction, respectively, relative to the phase velocity of deepwater waves; and the dimensionless parameters α_x and α_y are a measure of the shear strength of the current velocity at a still water surface in the x and y direction, respectively, compared with the decay of the magnitude of the wave-induced orbital velocity. When $\alpha_{x,y} > 1$, it denotes that the decay rate of the magnitude of the current velocity component with depth is larger than that of the wave-induced orbital velocity.

Specific values in various cases are chosen for the four dimensionless parameters, Fr_x, Fr_y, α_x, and α_y. We remark that, as a result of the profile variation with depth being the focus of this work, the profile velocity of both the linear and exponential current is set zero; i.e., $\mathbf{U}_L(0) = 0$ m/s and $\mathbf{U}_{\exp}(0) = 0$ m/s. Doing so permits the profile variation to be better assessed as the physics origin differs from the effects from a uniform current which has been extensively investigated (see, e.g., Peregrine (1976)). The neglect of current velocity on a still water surface can be physically represented as that the wave frequency considered here is intrinsic, i.e., $\omega - \mathbf{k}\cdot\mathbf{U}_0$, corresponding to the difference between the absolute wave frequency and the effect of a background uniform current on the linear dispersion of waves.

The exponential profiles and velocity profile measured at a river mouth against the dimensionless water depth are shown in Figure 1, the latter of which are referred to as the river profile for later references. Moreover, the dimensionless parameter ϵ_c based on Equation 27 has been given for a specific current profile shown in Figure 1, where a larger value of ϵ_c indicates a stronger profile shear of current 'felt' by the chosen wave. Any current oriented in the direction orthogonal to the wave propagation admits $\epsilon_c = 0$ as the identity of $\mathbf{k}\cdot\mathbf{U}' = 0$ holds.

4.2 Stokes drift

4.2.1 Novel features

The Stokes drift profiles against depth in various currents are shown in Figure 2. Three novel features are demonstrated as a result of wave and shear current interaction, compared with the classic conclusion for Stokes drift. Firstly, the Stokes drift has a non-vanishing component in the direction orthogonal to the wave propagation as a result of a non-vanishing depth-dependent component of the current in the span-wise direction, as is observed in panels (d, e, f) of Figure 2. This feature is regardless of the specific dependence of the current component $U_y(z)$, as long as the inequality $U_y'(z) \neq 0$ holds, being consistent with the physical interpretation of the Stokes drift expression given by Equation 20. This feature can only be demonstrated without the assumption of two-dimensional cases which have been extensively examined, see, e.g., Akselsen and Ellingsen (2019); Ellingsen (2014a). Hence, it can be expected in many realistic situations due to the three-dimensional nature of physical processes in the open ocean, although it is, for the first time, physically elucidated here. A few relevant examples of currents can be found in previous works that are expected to result in such a novel feature reported here, should it be physically resolved in the models. For example, depth-dependent wind drifts being misaligned with waves propagation as highlighted in Van Roekel et al. (2012). The Ekman currents are also typical of possessing a non-uniform directionality (McWilliams et al., 1997).

The second feature is demonstrated in panels (b, e) in Figure 2 which correspond to an exponentially sheared current, that the magnitude of the Stokes drift does not decrease exponentially with water depth but experiences firstly an increase in magnitude and thereafter a decrease as depth increases from the surface to a sufficiently large depth. The non-monotonically varying magnitude of the Stokes drift with depth is due to Equation 20 which consists of both the wave following and opposing terms, the latter of which relies on a non-vanishing shear and curvature of the current profile. In other words, such a non-monotonic nature mainly arises from the contribution of the shear production of current opposing to the wave propagation while noting that the cases of waves alone produce a Stokes drift which decreases exponentially with depth in the wave-propagation direction. The second feature is examined more in detail in Figure 3 where the

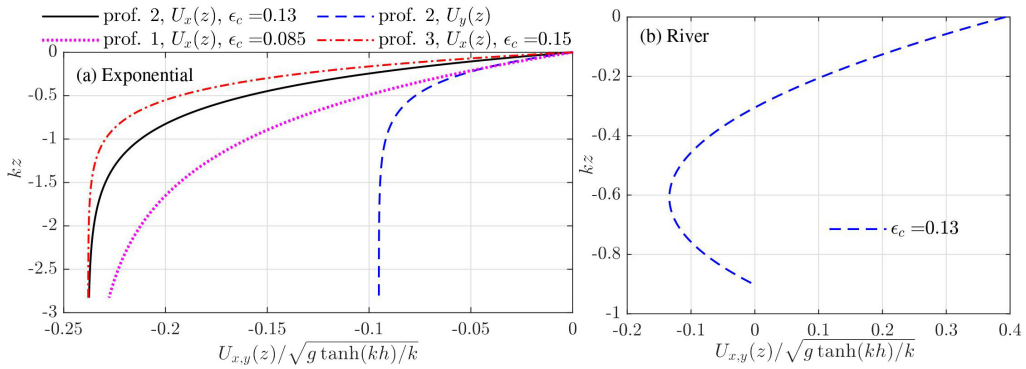

FIGURE 1
Current profiles used for numerical demonstrations. Panel **(A)** exponential profiles and **(B)** current profile measured at a river mouth [see, e.g., Li and Ellingsen (2019)].

Stokes drift is depicted against an exponential current with an increase in the shear strength from panel (a) to (c) indicated by an increasing value of ϵ_c. It is seen from panel (a) that the behavior of the Stokes drift is monotonic with depth when the shear strength of the current is small, which becomes non-monotonic as the shear strength is sufficiently large in panel (b) and remains so in panel (c).

The third feature is demonstrated in panel (c) of both Figures 2 and 3 that the Stokes drift profile experiences a change of sign in the magnitude over the water column from the surface to a deeper depth. From the perspective of mass transport over an entire water column, the change of the sign indicates a cancellation in the depth integrated manner, thereby likely leading to an underestimated role of shear current on mass transport in depth-integrated models such as Yang and Liu (2022). Furthermore, different from the general understanding, the Stokes drift holds a sign opposing the wave propagation near the water surface, which again arises from the terms having a negative sign in Equation 20 being more dominant, i.e., the terms proportional to $-U_x^{'}$ where $U_x^{'}$ holds a positive sign in all examples in panels (b, c) of Figures 2 and 3.

We stress that the aforementioned three features are strikingly different from the cases in the absence of the currents (or in the presence of uniform currents) which are also depicted in Figure 2, where the Stokes drifts have a magnitude that decreases exponentially with depth as $\sim \cosh[2k(z+h)]/\cosh(2kh)$, as well as a direction only aligned with the propagation direction of the 'parent' wave (i.e., the positive x direction). With real-life example profiles of tidal currents shown in Figure 4 where the current profiles were measured at the

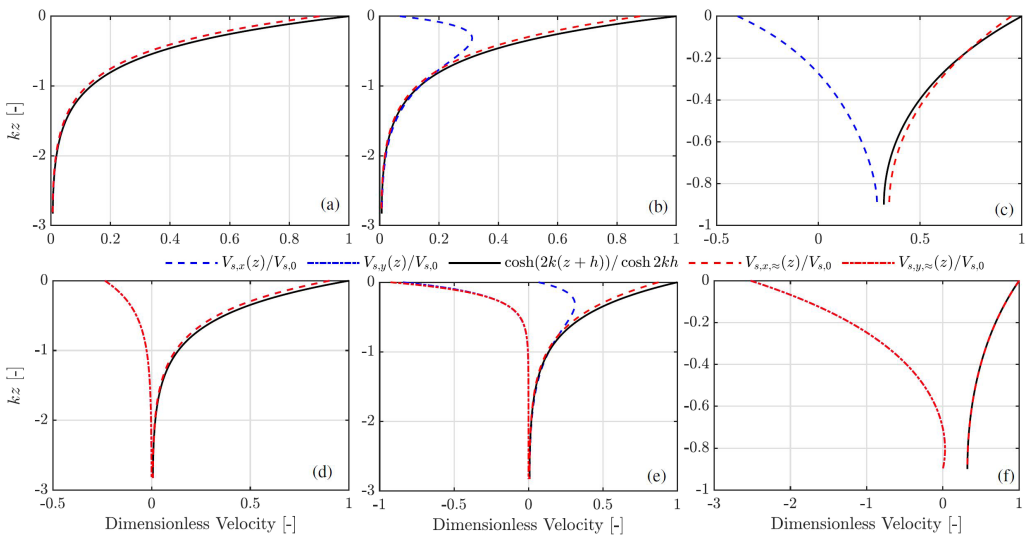

FIGURE 2
Stokes drift velocity profiles at various depths; two main aspects to highlight; (1) Novel physics illustrated (e.g., 2D cases and 2D versus 3D; linear versus profiles with non-vanishing curvature); (2) general and approximate results: clearly state the overlapping blue and red lines); panels **(A, D)** linearly sheared current and $kh = \pi$; panels **(B, E)** exponential currents and $kh = \pi$, where profile 2 in Figure 1A was used but $U_y(z) = 0$ m/s was set instead for the two dimensional case; **(C, F)** $kh = 1$ and the river profile with $[U_x(z),0]$ and $[0,U_y(z)]$ was chosen for the 2D and 3D case, respectively, where $U_{x,y}$ is according to Figure 1B.

10.3389/fmars.2024.1445116

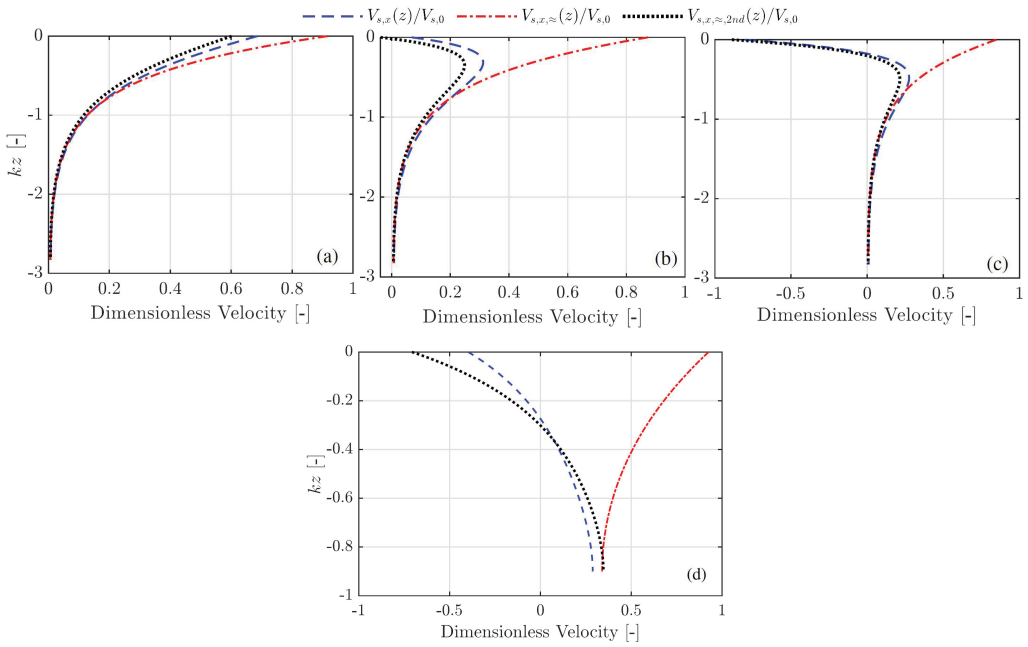

FIGURE 3
Comparison of the approximations to the Stokes drift and the general Stokes drift given by Equation 20, where U_y = 0 m/s was used for all cases. The first- and second-order approximations are based on Equations 29, 35, respectively. Panel **(A–C)** used exponential profile (1,2,3) in Figure 1B) with ϵ_c = 0.085, ϵ_c = 0.13, and ϵ_c = 0.15, respectively. Panel **(D)** used the river profile.

mouth of Columbia river by Zippel and Thomson (2017) and used in Zheng et al. (2024), the novel features of the Stokes drift in 2D cases are confirmed. The non-monotonic behavior of the Stokes drift with depth is clearly demonstrated again in Figure 4B, owing to the change of the sign of the profile shear of the opposing current and the respective moderate value measured by ϵ_c.

4.2.2 Approximate Stokes drift

We proceed to examine the Stokes drift profiles derived in subsection 3.2 in limiting cases through the comparisons with the expression (Equation 20) for general cases shown in both Figures 2 and 3. Figure 2 shows three example current profiles for both two and three-dimensional waves, including a linearly and exponentially

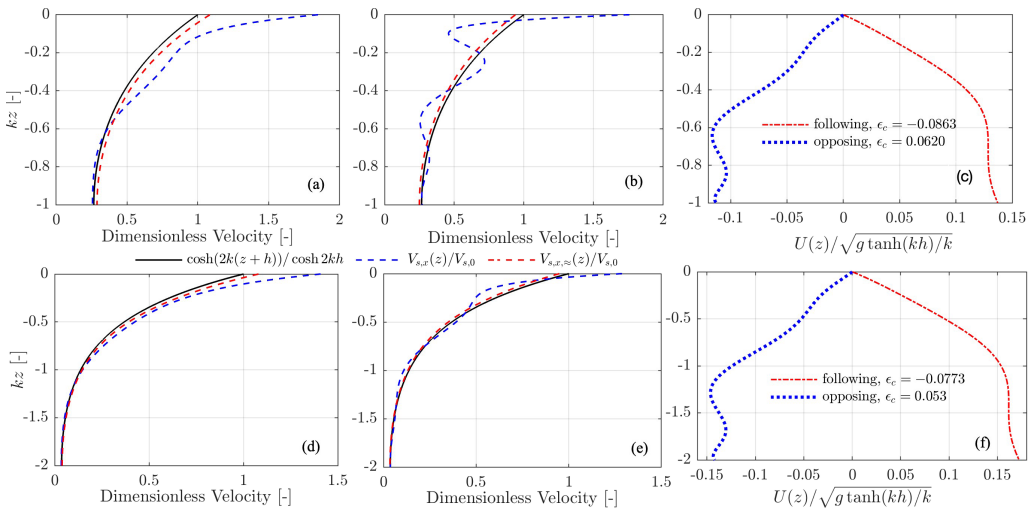

FIGURE 4
Stokes drift velocity profiles against the depth (panels **(A, B, D, E)** atop a following (panels **(A, D)** and opposing (panels **(B, E)** tidal current measured at the mouth of Columbia river (Zippel and Thomson, 2017; Zheng et al., 2024), where the water depth of 25 m was used and the dimensionless parameter ϵ_c was estimated based on Equation 27. The scaled velocity profiles of the following (with negative surface shear) and opposing (with positive surface shear) tidal currents are shown in both panel **(C, F)** due to two different monochromatic waves chosen in panels **(A, B)** and panels **(D, E)**, where kh = 1 and kh = 2 were set for the top and lower rows, respectively.

sheared current and a current representing the profile measured at the mouth of a river. The Stokes drift profile (Equation 24) is analytic for the cases in the presence of a linearly sheared current and a spanwise oriented current profile, which is demonstrated by panels (a, d) and panel (f), respectively as expected. Specifically, the results from either Equations 24 or 26 and 20 are not distinguishable to the numerical extent of the thickness of the lines. When the currents propagate along the spanwise direction or are not linearly sheared, the differences between the approximate Stokes drift (Equation 29) and the general expression given by Equation 20 are noticeable. The differences are considerable in the case of an exponential current in both the two- (panel (b)) and three-dimensional (panel (e)) cases, where the non-monotonic depth-dependent structure is not well predicted by the first-order approximation using Equation 29. A similar observation is reported in panel (c) of Figure 2 where the first-order approximation represents more similar profile features as the Stokes drift in the absence of a current but far off the accurate prediction. It is worth noting that the component of the approximate Stokes drifts in the y direction which is orthogonal to the wave propagation, shows a good agreement with Equation 20 in panel (e), which corresponds to when the shear strength of the current profile is considered to be large. This good agreement may be explained by that the Stokes drift component in the span-wise direction is more shear-production dominated and less affected by shear-current modified wave dispersion properties and $\epsilon_c = 0$ is admitted.

4.3 Particle trajectories

The wave-induced particle trajectories are shown in Figures 5 and 6 for two- and three-dimensional waves in a current modeled by 3 different depth-dependent profiles, respectively, together with the net mean displacement due to the Stokes drift given by Equation 20. Similar to the classic conclusion, it is seen from Figures 5 and 6 that the particle trajectories are not closed arising from a net mean horizontal displacement accumulated per period. In contrast, a striking difference is demonstrated in Figure 6 for three-dimensional cases in which rotational particle trajectories are observed, owing to the non-vanishing transverse y particle motions and the respective net mean displacements. Interestingly, the net mean displacement of particles at various depths shown in panels (a, b, c) behaves in a spiral manner as the depth increases in the presence of an exponentially sheared current. The largest net mean displacement in the wave-propagation direction over a fixed time interval does not appear for the particles at the surface but these below a certain depth. For the special case examined in panels (a, b, c) of Figure 6, it appears for particles at $kz_{p,0} \approx -0.3$, where $z_{p,0}$ is the vertical position of a particle at rest as noted. Generally, the net displacement of particle motions in Figures 5 and 6 show consistent results with the predictions using the Stokes drift velocity as they should, which well validate the expression of Stokes drift given by Equation 20, in addition to these shown in Appendix 1.

5 Concluding remarks and perspectives

This paper has derived explicit formulae for the Stokes drift velocity and particle trajectories by monochromatic waves in an arbitrarily depth-dependent flow, following the Direct Integration Method (DIM) proposed by Li and Ellingsen (2019) for the linear dispersion relation and orbital velocity of fluid parcels. Numerical implementation has been carried out based on the analytical results derived by this work using a few cases which involve different current profiles. Three novel features related to the Stokes drift, and thereby the particle trajectories, have been demonstrated for the first time, as a result of rotational motions of fluid parcels due to the coupling between a shear current and surface waves.

i. When the depth-dependent flow poses a non-vanishing shear in the span-wise direction, the Stokes drift velocity is no longer aligned with the direction of the wave propagation. This feature naturally introduces a misalignment to the wave propagation, being a likely cause to the misaligned Langmuir rolls which have been widely observed in nature, see, e.g., Van Roekel et al. (2012).
ii. When the depth-dependent structure of the flow velocity affects the features of surface waves in a nonweak

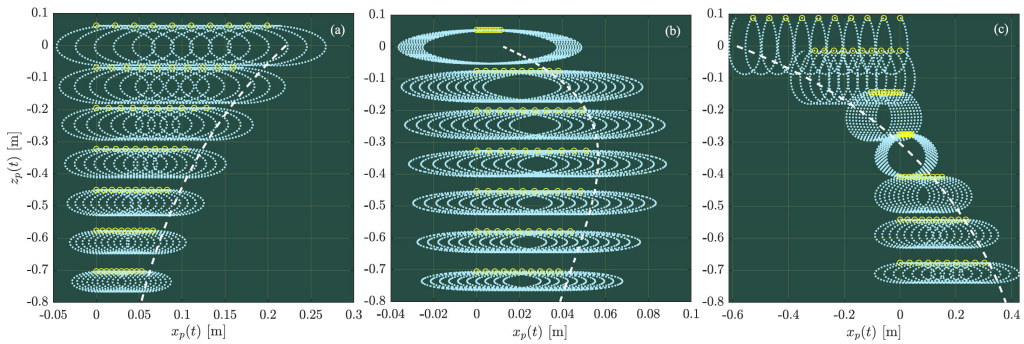

FIGURE 5
Wave-induced trajectories for two-dimensional waves from the initial time instant of $t = 0$ s to $t = 10T_p$, where T_p denotes the period of waves and the net mean displacement due to current alone was not included. The net horizontal displacement is computed due to Stokes drift velocity (white dashed) based on Equation 20.

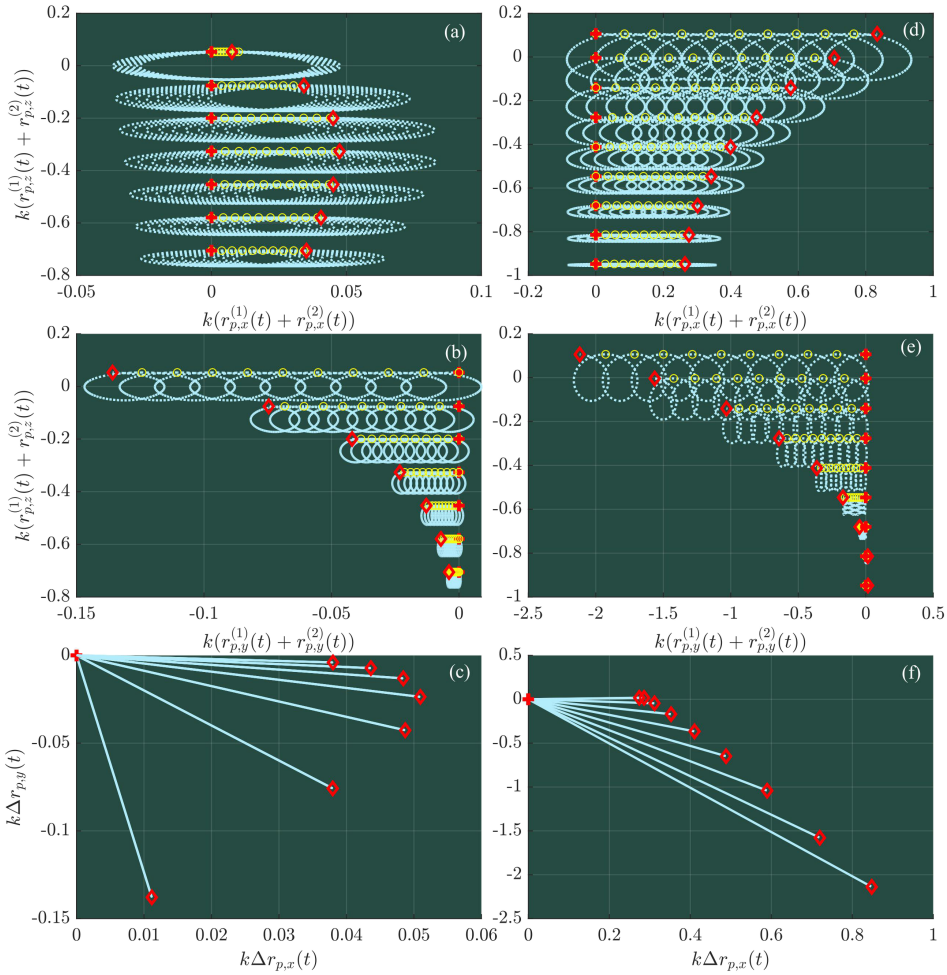

FIGURE 6
Wave-induced trajectories for 3D cases: The top, middle, and bottom rows show the particle trajectories in the *xoz*, *yoz*, and *xoy* planes, respectively.

manner, which corresponds to the wavenumber and depth weighted dimensionless parameter defined in expression (Equation 27) in the regime of $\epsilon_c \gtrsim 0.1$, the magnitude of the Stokes drift does not decrease with depth in a monotonic manner. We show that this leads to that the maximum of the net mean displacement of fluid parcels by waves after a fixed duration is no longer at the surface but at a depth below a still water surface. The physical implications of this feature in other physical processes in the air-sea interaction remain to be demonstrated in future works.

iii. When the surface shear is strong, i.e., $\epsilon_c \gtrsim 0.1$, a change of the direction (or sign) of Stokes drift velocity has been observed, and thereby a cancellation in the mass transport over a water column can develop, given that the mass transport by monochromatic waves can be estimated through integratingthe Stokes drift over the entire water column. This indicates that a depth-integrated model such as Yang and Liu (2022) can likely lead to underestimated effects of a current on the local mass transport.

Reduced forms of the approximate Stokes drift velocity have been derived under the assumption of weak irrotationality of wave-induced flow motions as explained in Shrira (1993); Ellingsen and Li (2017). The first and second-order approximations are compared with the more general formulae derived by this work. The former provides a good approximation when $\epsilon_c \lesssim 0.05$ but the second-order approximation is necessary for demonstrating the key features of the Stokes drift for $\epsilon_c \gtrsim 0.1$. It shall be noted that the numerical implementation of the second-order approximation demands a much larger computational cost than the direct implementation of the Stokes drift given by Equation 20 based on the DIM and thus is not recommended from a practical point of view. Nevertheless, good agreement between the second-order approximation and the predictions by Equation 20 has been consistently observed.

Although based on an asymptotic approximate model, the aforementioned three novel features enable unconventional insights into Stokes drift induced by surface waves, producing far-reaching impact on physical processes in the open oceans as well as suggesting potential directions for future studies. The results obtained from here can be directly used for a more accurate parameterization of the Stokes

drift as a driving force due to surface waves in regional circulation models, see such as Breivik et al. (2014); Suzuki and Fox-Kemper (2016) for an example. This work can also be used to shed light on the question: how the misalignment between the Stokes drift velocity and waves in an obliquely oriented depth-dependent current affect the formation of Langmuir rolls to an oblique angle to the wave propagation.

Data availability statement

The original contributions presented in the study are included in the article/Supplementary Material. Further inquiries can be directed to the corresponding author.

Author contributions

YL: Conceptualization, Formal analysis, Funding acquisition, Investigation, Methodology, Validation, Visualization, Writing – original draft. ZZ: Investigation, Methodology, Validation, Writing – review & editing. HK: Conceptualization, Investigation, Methodology, Writing – review & editing.

Funding

The author(s) declare financial support was received for the research, authorship, and/or publication of this article. YL acknowledges the support from the Research Council of Norway through a POS-ERC grant (project no. 342480).

Acknowledgments

The authors would like to thank Simen A. Å Ellingsen for the useful discussions which have contributed to the preparation of this work.

Conflict of interest

The authors declare that the research was conducted in the absence of any commercial or financial relationships that could be construed as a potential conflict of interest.

Publisher's note

References

Akselsen, A. H., and Ellingsen, S. (2019). Weakly nonlinear transient waves on a shear current: Ring waves and skewed Langmuir rolls. *J. Fluid Mech.* 863, 114–149. doi: 10.1017/jfm.2018.960

Ali, A., and Kalisch, H. (2013). Reconstruction of the pressure in long-wave models with constant vorticity. *Eur. J. Mech.-B/Fluids* 37, 187–194. doi: 10.1016/j.euromechflu.2012.09.009

Ardhuin, F., Marié, L., Rascle, N., Forget, P., and Roland, A. (2009). Observation and estimation of Lagrangian, Stokes, and Eulerian currents induced by wind and waves at the sea surface. *J. Phys. Oceanography* 39, 2820–2838. doi: 10.1175/2009JPO4169.1

Babanin, A. V. (2006). On a wave-induced turbulence and a wave-mixed upper ocean layer. *Geophys. Res. Lett.* 33, L20605. doi: 10.1029/2006GL027308

Babanin, A. V., and Chalikov, D. (2012). Numerical investigation of turbulence generation in non-breaking potential waves. *J. Geophys. Res.: Oceans* 117, C06010. doi: 10.1029/2012JC007929

Bjørnestad, M., Buckley, M., Streßer, M., Horstmann, J., Cysewski, M., and Carrasco-Alvarez, R. (2021). Lagrangian measurements of orbital velocities in the surf zone. *Geophys.Res. Lett.* 48, e2021GL095722. doi: 10.1029/2021GL095722

Borluk, H., and Kalisch, H. (2012). Particle dynamics in the KdV approximation. *Wave Motion* 49, 691–709. doi: 10.1016/j.wavemoti.2012.04.007

Breivik, Ø., and Christensen, K. H. (2020). A combined Stokes drift profile under swell and wind sea. *J. Phys. Oceanogr.* 50, 2819–2833. doi: 10.1175/JPO-D-20-0087.1

Breivik, Ø., Janssen, P. A., and Bidlot, J.-R. (2014). Approximate Stokes drift profiles in deep water. *J. Phys. Oceanogr.* 44, 2433–2445. doi: 10.1175/JPO-D-14-0020.1

Calvert, R., McAllister, M., Whittaker, C., Raby, A., Borthwick, A., and Van Den Bremer, T. (2021). A mechanism for the increased wave-induced drift of floating marine litter. *J. Fluid Mech.* 915, A73. doi: 10.1017/jfm.2021.72

Chamecki, M., Chor, T., Yang, D., and Meneveau, C. (2019). Material transport in the ocean mixed layer: recent developments enabled by large eddy simulations. *Rev. Geophys.* 57, 1338–1371. doi: 10.1029/2019RG000655

Chen, L., Basu, B., and Martin, C.-I. (2021). On rotational flows with discontinuous vorticity beneath steady water waves near stagnation. *J. Fluid Mech.* 912, A44. doi: 10.1017/jfm.2020.1057

Chen, Y.-Y., Hsu, H.-C., and Chen, G.-Y. (2010). Lagrangian experiment and solution for irrotational finite-amplitude progressive gravity waves at uniform depth. *Fluid Dyn. Res.* 42, 045511. doi: 10.1088/0169-5983/42/4/045511

Constantin, A., and Monismith, S. (2017). Gerstner waves in the presence of mean currents and rotation. *J. Fluid Mech.* 820, 511–528. doi: 10.1017/jfm.2017.223

Craik, A. D. (1970). A wave-interaction model for the generation of windrows. *J. Fluid Mech.* 41, 801–821. doi: 10.1017/S0022112070000939

Craik, A., and Leibovich, S. (1976). A rational model for Langmuir circulations. *J. Fluid Mech.* 73, 401–426. doi: 10.1017/S0022112076001420

Curtis, C., Carter, J., and Kalisch, H. (2018). Particle paths in nonlinear Schrodinger¨ models in the presence of linear shear currents. *J. Fluid Mech.* 855, 322–350. doi: 10.1017/jfm.2018.623

Davey, A., and Stewartson, K. (1974). On three-dimensional packets of surface waves. *Proc. R. Soc London Ser. A. Math. Phys. Sci.* 338, 101–110. doi: 10.1098/rspa.1974.0076

Dysthe, K. B. (1979). Note on a modification to the nonlinear Schrodinger¨ equation for application to deep water waves. *Proc. R. Soc London Ser. A. Math. Phys. Sci.* 369, 105–114. doi: 10.1098/rspa.1979.0154

Ellingsen, S.Å. (2014a). Initial surface disturbance on a shear current: The Cauchy-Poisson problem with a twist. *Phys. Fluids* 26, 082104. doi: 10.1063/1.4891640

Ellingsen, S.Å. (2014b). Ship waves in the presence of uniform vorticity. *J. Fluid Mech.* 742, R2. doi: 10.1017/jfm.2014.28

Ellingsen, S.Å., Abid, M., Kharif, C., and Li, Y. (2024). Dispersive wave focusing on a shear current: Part 1 — Linear approximations. *Water waves* 6, 367-411. doi: 10.1007/s42286-024-00085-3

Ellingsen, S., and Li, Y. (2017). Approximate dispersion relations for waves on arbitrary shear flows. *J. Geophys. Res.: Oceans* 122, 9889–9905. doi: 10.1002/2017JC012994

Flamarion, M. V., Castro, E. M., and Ribeiro-Jr, R. (2023). Pressure anomalies beneath solitary waves with constant vorticity. *Eng* 4, 1306–1319. doi: 10.3390/eng4020076

Ghantous, M., and Babanin, A. V. (2014). Ocean mixing by wave orbital motion. *Acta Phys. Slovaca* 64, 1–57. doi: 10.2478/apsrt-2014-0001

Higgins, C., van Den Bremer, T., and Vanneste, J. (2020). Lagrangian transport by deep-water surface gravity wavepackets: effects of directional spreading and stratification. *J. Fluid Mech.* 883, A42. doi: 10.1017/jfm.2019.877

Hsu, H.-C. (2013). Particle trajectories for waves on a linear shear current. *Nonl. Analy. Real World App.* 14, 2013-2021. doi: 10.1016/j.nonrwa.2013.02.005

Kenyon, K. E. (1969). Stokes drift for random gravity waves. *J. Geophys. Res.* 74, 6991–6994. doi: 10.1029/JC074i028p06991

Kharif, C., and Pelinovsky, E. (2003). Physical mechanisms of the rogue wave phenomenon. *Europ. J. Mech.-B/Fluids* 22, 603–634. doi: 10.1016/j.euromechflu.2003.09.002

Kirby, J., and Chen, T. (1989). Surface waves on vertically sheared flows: approximate dispersion relations. *J. Geophys. Res.: Oceans* 94, 1013–1027. doi: 10.1029/JC094iC01p01013

Lane, E. M., Restrepo, J., and McWilliams, J. C. (2007). Wave–current interaction: A comparison of radiation-stress and vortex-force representations. *J. Phys. Oceanogr.* 37, 1122–1141. doi: 10.1175/JPO3043.1

Larsen, B. E., Al-Obaidi, M. A. A., Guler, H. G., Carstensen, S., Goral, K. D., Christensen, E. D., et al. (2023). Experimental investigation on the nearshore transport of buoyant microplastic particles. *Mar. pollut. Bull.* 187, 114610. doi: 10.1016/j.marpolbul.2023.114610

Li, Y. (2018). Wave-interference effects on far-field ship waves in the presence of a shear current. *J. Ship Res.* 62, 37–47. doi: 10.5957/JOSR.170017

Li, Y., and Ellingsen, S. (2019). A framework for modeling linear surface waves on shear currents in slowly varying waters. *J. Geophys. Res.: Oceans* 124, 2527–2545. doi: 10.1029/2018JC014390

Li, Y. (2021). Three-dimensional surface gravity waves of a broad bandwidth on deep water. *J. Fluid Mech.* 926, 1–43. doi: 10.1017/jfm.2020.1076

Li, Y., and Chabchoub, A. (2024). How currents trigger extreme sea waves. The roles of Stokes drift, Eulerian return flow, and a background flow in the open ocean. *Geophys. Res. Lett.* 51, e2023GL107381. doi: 10.1029/2023GL107381

Li, Y., and Ellingsen, S. (2016a). Multiple resonances of a moving oscillating surface disturbance on a shear current. *J. Fluid Mech.* 808, 668–689. doi: 10.1017/jfm.2016.637

Li, Y., and Ellingsen, S. (2016b). Ship waves on uniform shear current at finite depth: wave resistance and critical velocity. *J. Fluid Mech.* 791, 539–567. doi: 10.1017/jfm.2016.20

Li, Y., and Li, X. (2021). Weakly nonlinear broadband and multi-directional surface waves on an arbitrary depth: A framework, Stokes drift, and particle trajectories. *Phys. Fluids* 33, 076609. doi: 10.1063/5.0057215

Li, Y., Smeltzer, B. K., and Ellingsen, S. A. (2019). Transient wave resistance upon a real shear current. *Europ. J. Mech.-B/Fluids* 73, 180–192. doi: 10.1016/j.euromechflu.2017.08.012

Longuet-Higgins, M. S. (1953). Mass transport in water waves. *Philos. Trans. R. Soc A* 245, 535–581. doi: 10.1098/rsta.1953.0006

McIntyre, M. (1981). On the'wave momentum' myth. *J. Fluid Mech.* 106, 331–347. doi: 10.1017/S0022112081001626

McWilliams, J. C. (2016). Submesoscale currents in the ocean. *P. R. Soc London. A.* 472, 20160117. doi: 10.1098/rspa.2016.0117

McWilliams, J. C., Sullivan, P. P., and Moeng, C. (1997). Langmuir turbulence in the ocean. *J. Fluid Mech.* 334, 1–30. doi: 10.1017/S0022112096004375

Mellor, G. (2015). A combined derivation of the integrated and vertically resolved, coupled wave–current equations. *J. Phys. Oceanogr.* 45, 1453–1463. doi: 10.1175/JPO-D-14-0112.1

Monismith, S., Cowen, E., Nepf, H., Magnaudet, J., and Thais, L. (2007). Laboratory observations of mean flows under surface gravity waves. *J. Fluid Mech.* 573, 131–147. doi: 10.1017/S0022112006003594

Myrhaug, D. (2015). Stokes drift estimation based on long-term variation of wave conditions. *Proc. Institution Mechanical Engineers Part M: J. Eng. Maritime Environ.* 229, 141–146. doi: 10.1177/1475090213506699

Myrhaug, D., Wang, H., and Holmedal, L. E. (2014). Stokes drift estimation for deep water waves based on short-term variation of wave conditions. *Coast. Eng.* 88, 27–32. doi: 10.1016/j.coastaleng.2014.01.014

Onorato, M., Proment, D., and Toffoli, A. (2011). Triggering rogue waves in opposing currents. *Phys. Rev. Lett.* 107, 184502. doi: 10.1103/PhysRevLett.107.184502

Peregrine, D. H. (1976). Interaction of water waves and currents. *Adv. Appl. Mech.* 16, 9–117. doi: 10.1016/S0065-2156(08)70087-5

Pizzo, N., Lenain, L., Rømcke, O., Ellingsen, S.Å., and Smeltzer, B. K. (2023). The role of Lagrangian drift in the geometry, kinematics and dynamics of surface waves. *J. Fluid Mech.* 954, R4. doi: 10.1017/jfm.2022.1036

Qiao, F., Yuan, Y., Ezer, T., Xia, C., Yang, Y., Lü, X., et al. (2010). A three-dimensional surface wave–ocean circulation coupled model and its initial testing. *Ocean Dynamics* 60, 1339–1355. doi: 10.1007/s10236-010-0326-y

Quinn, B., Toledo, Y., and Shrira, V. (2017). Explicit wave action conservation for water waves on vertically sheared flows. *Ocean Model.* 112, 33–47. doi: 10.1016/j.ocemod.2017.03.003

Shrira, V. I. (1993). Surface waves on shear currents: solution of the boundary-value problem. *J. Fluid Mech.* 252, 565–584. doi: 10.1017/S002211209300388X

Shrira, V., and Slunyaev, A. (2014). Nonlinear dynamics of trapped waves on jet currents and rogue waves. *Phys. Rev. E* 89, 041002. doi: 10.1103/PhysRevE.89.041002

Skop, R. A. (1987). Approximate dispersion relation for wave-current interactions. *J. Waterway Port Coastal Ocean Eng.* 113, 187–195. doi: 10.1061/(ASCE)0733-950X(1987)113:2(187)

Smith, J. A. (2006). Observed variability of ocean wave Stokes drift, and the Eulerian response to passing groups. *J. Phys. Oceanogr.* 36, 1381–1402. doi: 10.1175/JPO2910.1

Steer, J. N., Borthwick, A. G., Stagonas, D., Buldakov, E., and van den Bremer, T. S. (2020). Experimental study of dispersion and modulational instability of surface gravity waves on constant vorticity currents. *J. Fluid Mech.* 884, A40. doi: 10.1017/jfm.2019.951

Stewart, R. H., and Joy, J. W. (1974). HF radio measurements of surface currents. *Deep Sea Res. Oceanogr. Abstracts* 21, 1039–1049. doi: 10.1016/0011-7471(74)90066-7

Stokes, G. G. (1847). On the theory of oscillatory waves. *Math. Phys. Pap.* 1, 197-229.

Sullivan, P. P., and McWilliams, J. C. (2010). Dynamics of winds and currents coupled to surface waves. *Ann. Rev. Fluid Mech.* 42, 19–42. doi: 10.1146/annurev-fluid-121108-145541

Sutherland, B. R., DiBenedetto, M., Kaminski, A., and Van Den Bremer, T. (2023). Fluid dynamics challenges in predicting plastic pollution transport in the ocean: A perspective. *Phys. Rev. Fluids* 8, 070701. doi: 10.1103/PhysRevFluids.8.070701

Suzuki, N., and Fox-Kemper, B. (2016). Understanding Stokes forces in the wave-averaged equations. *J. Geophys. Res. C: Oceans* 121, 3579–3596. doi: 10.1002/2015JC011566

Thomas, R., Kharif, C., and Manna, M. (2012). A nonlinear Schrödinger equation for water waves on finite depth with constant vorticity. *Phys. Fluids* 24, 127102. doi: 10.1063/1.4768530

Touboul, J., Charland, J., Rey, V., and Belibassakis, K. (2016). Extended mild-slope equation for surface waves interacting with a vertically sheared current. *Coast. Eng.* 116, 77–88. doi: 10.1016/j.coastaleng.2016.06.003

Ursell, F. (1953). The long-wave paradox in the theory of gravity waves. *Math. Proc. Cambridge Philos. Soc.* 49, 685–694. doi: 10.1017/S0305004100028887

van den Bremer, T. S., and Breivik, Ø. (2018). Stokes drift. *Philos. Trans. R. Soc A* 376, 20170104. doi: 10.1098/rsta.2017.0104

van den Bremer, T., Whittaker, c., Calvert, R., Raby, A., and Taylor, P. (2019). Experimental study of particle trajectories below deep-water surface gravity wave groups. *J. Fluid Mech.* 879, 168-186. doi: 10.1017/jfm.2019.584

Van Dyke, M. (1982). *An album of fluid motion* Vol. 176 (California: The Parabolic Press).

Van Roekel, L., Fox-Kemper, B., Sullivan, P., Hamlington, P., and Haney, S. (2012). The form and orientation of langmuir cells for misaligned winds and waves. *J. Geophys. Res.: Oceans* 117, C05001. doi: 10.1029/2011JC007516

Webb, A., and Fox-Kemper, B. (2011). Wave spectral moments and Stokes drift estimation. *Ocean Model.* 40, 273–288. doi: 10.1016/j.ocemod.2011.08.007

Webb, A., and Fox-Kemper, B. (2015). Impacts of wave spreading and multidirectional waves on estimating Stokes drift. *Ocean Modell.* 96, 49–64. doi: 10.1016/j.ocemod.2014.12.007

White, B. S., and Fornberg, B. (1998). On the chance of freak waves at sea. *J. Fluid Mech.* 355, 113–138. doi: 10.1017/S0022112097007751

Xin, Z., Li, X., and Li, Y. (2023). Coupled effects of wave and depth-dependent current interaction on loads on a bottom-fixed vertical slender cylinder. *Coast. Eng.* 183, 104304. doi: 10.1016/j.coastaleng.2023.104304

Yang, Y., Li, Y., Li, J., Liu, J., Gao, Z., Guo, K., et al. (2021). The influence of Stokes drift on oil spills: Sanchi oil spill case. *Acta Oceanologica Sin.* 40, 30–37. doi: 10.1007/s13131-021-1889-9

Yang, Z., and Liu, P. L.-F. (2022). Depth-integrated wave–current models. part 2. current with an arbitrary profile. *J. Fluid Mech.* 936, A31. doi: 10.1017/jfm.2022.42

Zheng, Z., Li, Y., and Ellingsen, S.Å. (2023). Statistics of weakly nonlinear waves on currents with strong vertical shear. *Phys. Rev.Fluids* 8, 014801. doi: 10.1103/PhysRevFluids.8.014801

Zheng, Z., Li, Y., and Ellingsen, S.Å. (2024). Dispersive wave focusing on a shear current. part 2: nonlinear effects. *Water Waves.* 6, 413-449. doi: 10.1007/s42286-024-00097-z

Zippel, S. F., Farrar, J. T., Zappa, C. J., and Plueddemann, A. J. (2022). Parsing the kinetic energy budget of the ocean surface mixed layer. *Geophys. Res. Lett.* 49, e2021GL095920. doi: 10.1029/2021GL095920

Zippel, S., and Thomson, J. (2017). Surface wave breaking over sheared currents: Observations from the Mouth of the Columbia River. *J. Geophys. Res.: Oceans* 122, 3311–3328. doi: 10.1002/2016JC012498

Appendix

In this section, we validate the derivations used for the results presented in section 4. Appendix 1 shows the good agreement between the Stokes drift velocity evaluated using (20) and the analytical approach for the cases without a current and with a linearly sheared current. Appendix 2 depicts that the particle trajectories predicted by (38) agree well with the net mean displacement obtained from the predictions using the Stokes drift velocity given by (20) in both the x and y direction.

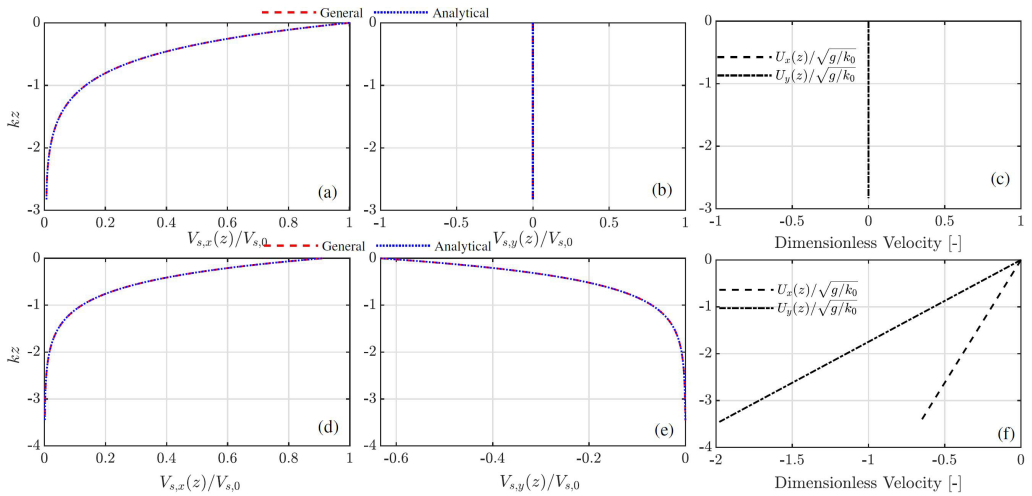

APPENDIX 1
Stokes drift velocity in the x and y direction for waves alone and in the presence of a linearly sheared current, where the analytical results for the case in the former and latter are based on (22) and (24), respectively.

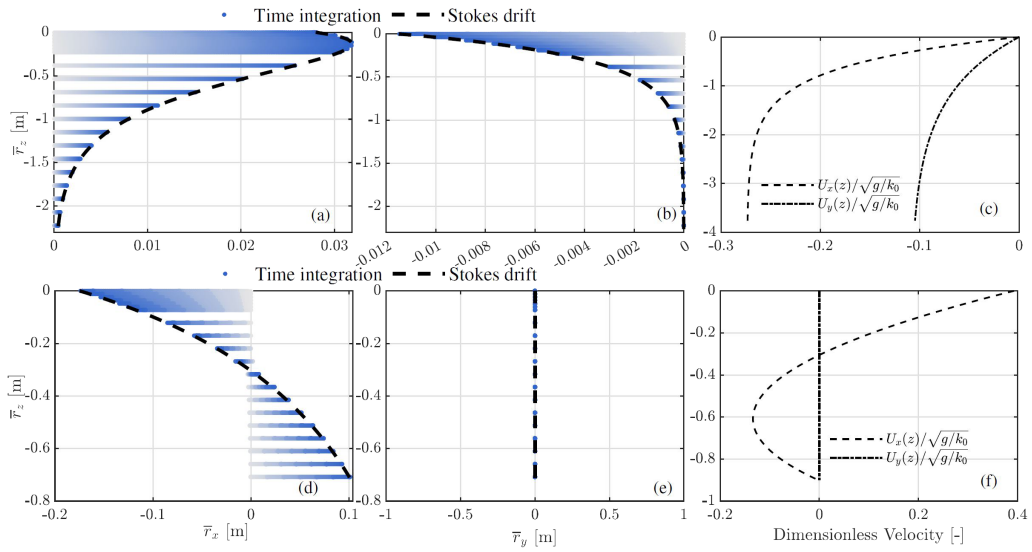

APPENDIX 2
Wave-induced particle trajectories in the xoz (panels **(A, D)** and yoz (panels **(B, E)** planes and the current velocity components varying with the dimensionless depth kz where k denotes the wavenumber of a monochromatic wave propagating in the positive x direction.

Frontiers in Marine Science

Explores ocean-based solutions for emerging global challenges

The third most-cited marine and freshwater biology journal, advancing our understanding of marine systems and addressing global challenges including overfishing, pollution, and climate change.

Discover the latest Research Topics

See more →

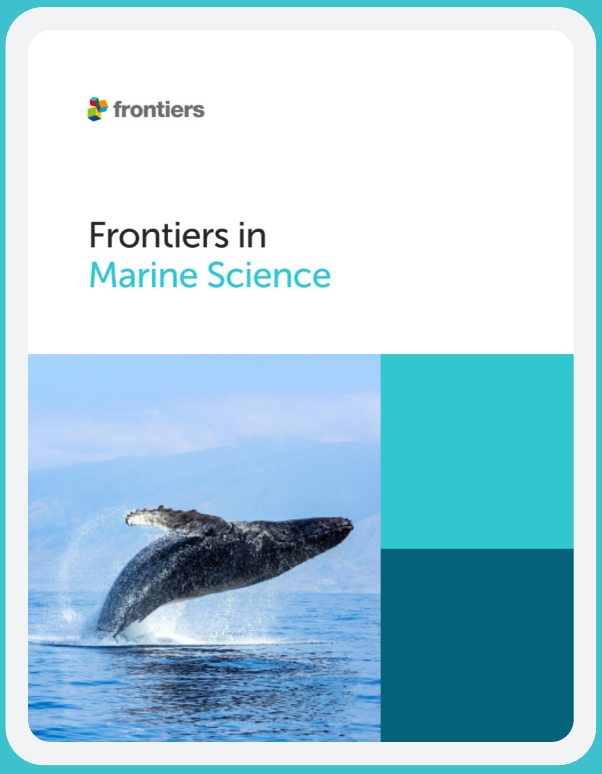

Frontiers

Avenue du Tribunal-Fédéral 34
1005 Lausanne, Switzerland
frontiersin.org

Contact us

+41 (0)21 510 17 00
frontiersin.org/about/contact